

**A Method for Optical Tracking of On-Orbit Servicing
Operations in Geostationary Orbit Using Speckle
Interferometry**

by

Robert L. Scott, M.S., P.Eng.

A thesis submitted to the Faculty of Graduate and Postdoctoral Affairs in
partial fulfillment of the requirements for the degree of

Doctor of Philosophy

in

Aerospace Engineering

Carleton University
Ottawa, Ontario

©Her Majesty the Queen in Right of Canada, as represented by the
Minister of National Defence, 2015

Abstract

On Orbit Servicing (OOS) is a class of space missions that could potentially extend the life of orbiting satellites by fuel replenishment, repair, orbital maintenance or satellite repurposing, and possibly reduce the rate of space debris generation. OOS performed in geostationary orbit poses a unique challenge for the optical space surveillance community. OOS satellites performing close proximity operations with separations less than 1 km in geosynchronous orbit subtend an angle comparable to the angular size of atmospheric seeing (turbulence) cells as viewed by a ground-based observer. This degrades the ability of a ground-based observer from resolving a geostationary satellite pair in order to perform astrometric measurements on the objects' relative positions.

In this research, a speckle-interferometric observational approach designed to detect and estimate the relative orbits of servicing satellites about their client is described. It was found that the use of the cross-spectrum of speckle imagery and extraction of its imaginary component provides unambiguous measurables useful for relative orbit estimation for closely-spaced satellites. This approach is enabled by the availability sensitive Electron Multiplying CCD (EMCCD) cameras which permit the detection of very faint speckles from an astronomical source. This thesis describes an observational model, the speckle-imaging acquisition process, an image-processing algorithm and experimental test results pertaining to the speckle measurement of very closely-spaced satellites.

Testing of the cross-spectrum technique was conducted by observing rare optical alignments (optical conjunctions) of co-located geostationary satellites using medium and small aperture telescopes configured to perform speckle interferometry. Satellite pairs of magnitudes of $M_{primary} = 10.3$, $\Delta m = 0.3$ and $M_{primary} = 9.0$, $\Delta m = 1.5$ were observed with the 1.6-m Mont-Mégantic telescope. Minimum detected separations between the two satellites of 1.5 arcseconds were achieved. A subsequent small aperture telescope test successfully detected a satellite pair of $M_{primary} = 9.67$, $\Delta m = 1.63$. It was found that in-track and cross-track relative orbit positions precise to 100 meters with respect to reference ephemeris provided by a satellite operator was achieved and evidence is shown that 50-meter precision is possible with longer observational periods.

It was also found that due to the satellites' relatively high relative motion rates that strong fringe rotation affected the separation measurements. This issue is less likely to affect real OOS satellite cases as the relative separation distances between them are much less than co-located satellites making their relative angular velocities much smaller in comparison. A technique to handle cases when the fringes are rotating at an excessive rate was developed and was found to be a more reliable approach to detecting the separation distance of the secondary satellite.

In order to use speckle interferometry to measure the relative orbits of satellites in close proximity to one another a visibility requirement must be respected. This is due to atmospheric turbulence where both satellites must fall within the isoplanatic patch (< 5 arcsecond conical radius) before speckle patterns can be reliably acquired. This angle sets an upper limit on the separation of the satellite pair of ~ 1 km in geosynchronous orbit. Further to this, the seeing conditions must be steady during observation in order to ensure that the fringe measurements are reliably correlated during image processing. Due to the dynamic coupling between the radial and in-track motion of a servicer about its client, the radial component requires ~ 3 hours of observations to reliably estimate it. This is due to a partial observability limitation where the near-alignment of the camera field of view and the radial direction of the client coordinate frame are nearly co-linear. While partial observability of the radial component of the servicer's motion is detectable the relative orbit is overall observable due to the dynamic coupling between the in-track and radial directions.

Acknowledgements

It is a pleasure to acknowledge the tremendous support of the women and men of the Canadian Armed Forces who watch the skies to maintain Canada's position as a leader in the emerging field of Space Situational Awareness. I am very grateful to Defense Research and Development Canada who provided funding support for this work while I worked on the development of the NEOSSat microsatellite project and the Ground Based Optical space surveillance system. Appreciation is extended to: Gary Geling, Malcom Vant, Maria Rey, Caroline Wilcox, Dr. Brad Wallace, Stefan Thorsteinson, Major Donald Bedard, Lt Colonel Aaron Spaans, Lt Colonel Pascal Tremblay, Lt Colonel Catherine Marchetti, Dr Scott McLelland, Paul Pulsifer, Brian Eatock, Chris McMillan, John Weaver who have all played a role helping me either build sensors or collect observational data when I needed it. I also wish to acknowledge the talented engineering teams at the Department of National Defence who built Canada's first space based space surveillance satellites *SAPPHIRE* and *NEOSSat*, without whom I would not have learned the technical boundaries about the field of space surveillance. It has been my privilege to play a part in the Canadian Armed Forces' role in Space Situational Awareness.

From Carleton University, I wish to acknowledge my thesis advisor Dr. Alex Ellery who also gave me the tremendous flexibility needed to accommodate both my graduate studies while working as a mission scientist on NEOSSat. Bruce Burlton provided tremendous insights into flight operations at Telesat Canada. Both of these professors' experiences led to the combined topic of space surveillance of robotic On-Orbit Servicing in GEO.

I would also like to acknowledge the talented staff of the Mont-Mégantic observatory in Mont-Mégantic, Quebec and the University of Montreal for their generous granting of observational time on the 1.6m telescope. This work would not have been possible without access to one of the highest performance EMCCD cameras available and appreciation to Nuvu Camera Inc.; Oliver Daigle, Felecien Legrand and Phillippe Richelet is extended. Tim Douglas at Telesat Canada provided tremendous support by supplying satellite orbital ephemerides, without which the experimental portions of this research would not have been possible.

My family has been so supportive and I also wish to extend a thank you to my mother Bonnie, father Lauchie and my partner Rebecca for their continued patience and encouragement. You have all been so generous and your kindness will not be forgotten. My grandfather once said that “education doesn’t cost anything to carry around”. This wise advice has always steered my endeavors in that knowledge is the best investment one can make in oneself and in others.

Per aspera ad astra.....

Robert Lauchlan Scott

Table of Contents

Abstract	ii
Acknowledgements	iv
Table of Contents	vi
List of Tables	xi
List of Illustrations	xii
List of Appendices	xviii
Chapter 1: Introduction	1
1.1 On Orbit Servicing as a space surveillance problem	1
1.2 A short overview of On-Orbit-Servicing missions	2
1.3 Geostationary orbit.....	5
1.4 Space surveillance and the problem of OOS in GEO	7
1.5 Motivation for this research: Space surveillance of closely-spaced objects. 10	
1.5.1 The OOS problem.....	14
1.6 Thesis problem statement	15
1.6.1 Initial exploration using light curve inversion	17
1.6.2 Speckle interferometry.....	22
1.6.3 EMCCDS	24
1.6.4 Other considered technologies: Adaptive optics.....	25
1.6.5 Other considered technologies: Space surveillance radars	27
1.6.6 Other considered technologies: Space based measurements	28
1.7 Thesis layout and section overview	28
1.8 Literature overview: Satellite speckle interferometry.....	30
1.9 Literature review: Differential angles for relative orbit estimation	31
1.10 Definitions and conventions for the client and servicer.....	32
1.11 Chapter summary and contributions	33
Chapter 2: Atmospheric turbulence and speckle interferometry	35
2.1 Atmospheric turbulence	35

2.2	Temporal nature of atmospheric turbulence	39
2.3	Number of speckles.....	40
2.4	Isoplanatic angle	41
2.5	Spatial frequency characteristics of a telescope and atmosphere	44
2.5.1	Diffraction limited transfer function.....	45
2.5.2	Labeyrie-Korff transfer function.....	46
2.6	Speckle interferometry.....	47
2.6.1	Image power spectrum.....	48
2.6.2	Stacking images	50
2.6.3	Power spectrum measurements.....	52
2.6.4	Autocorrelation	53
2.7	Directed vector autocorrelation.....	55
2.8	Cross-spectrum for satellite speckle interferometry	58
2.8.1	The cross-correlation	59
2.8.2	The cross-spectrum	60
2.8.3	Cross-spectrum of real speckle images.....	62
2.8.4	Metrics from the imaginary component of the cross spectrum.....	64
2.9	Other atmospheric effects: Chromatic dispersion.....	66
2.10	Other atmospheric effects: Atmospheric extinction	69
2.11	Chapter summary and contributions	70
Chapter 3: Reference frames, observational and relative motion models		71
3.1	Geocentric and relative orbit measurements.....	71
3.2	True of date reference frame convention for differential observations	74
3.2.1	Differential angles measurements.....	75
3.3	Transformation of observations from Hill frame to differential angles.....	75
3.3.1	Generalized rotation of the TOD frame to the Hill frame	76
3.4	Relative motion model.....	81
3.4.1	Linearized relative motion model.....	83
3.4.2	Solar radiation pressure adjustment.....	85
3.5	Relative orbit determination	88
3.6	Initial orbit determination for OOS satellites in proximity flight.....	88

3.6.1	Optimal Orbit determination for OOS proximity orbits	90
3.7	Chapter summary and contributions	91
Chapter 4:	Signal modelling, instruments, and image processing	92
4.1	Signal modelling for space surveillance sensors	92
4.2	Signal modelling for EMCCDs.....	94
4.3	Signal modelling for speckle interferometry	95
4.3.1	Estimating the minimum number of images to detect a secondary satellite	96
4.4	Speckle instrument configuration	99
4.4.1	Nyquist sampling of the speckles	99
4.4.2	General instrument arrangement.....	100
4.5	Small aperture telescope testing using binary stars	101
4.5.1	Instrument calibration, orientation angle and pixel scale	103
4.6	Image processing	105
4.6.1	Cosmic ray rejection algorithm.....	105
4.6.2	Isolation of the imaginary component of the fringes	107
4.6.3	Orientation angle.....	108
4.6.4	Fringe separation distance.....	110
4.6.5	Image timestamps	112
4.7	Chapter summary and contributions	112
Chapter 5:	Experimental findings	113
5.1	Mont-Mégantic observational campaign	115
5.2	Mont-Mégantic instrument description.....	116
5.3	Instrument calibration	118
5.4	Observations of satellites using speckle images	119
5.5	Observations of Anik G1 and Anik F1R.....	121
5.6	Observations of Anik F1 and Anik G1	127
5.7	Correcting the fringe rotation effect	133
5.8	Relative orbit estimation using track data.....	136
5.8.1	General filter setup.....	136

5.8.2	1 st track: Anik F1R and Anik G1 – Relative orbit state estimate.....	138
5.8.3	1 st track: Anik F1R and Anik G1 – Relative orbit covariance	140
5.8.4	2 nd track: Anik F1 and Anik G1 – Relative orbit state estimate	142
5.8.5	2 nd track: Anik F1 and Anik G1 – Relative orbit covariance.....	144
5.9	Mont Mégantic relative orbit track summary	145
5.10	Small aperture telescope observations of a visual conjunction	145
5.11	Chapter summary, contributions and recommendations.....	149
Chapter 6: Observability of relative orbits using differential angles		152
6.1	Prior work	153
6.2	Simulated observational test cases.....	154
6.2.1	Anik G1, Anik F1R.....	155
6.2.2	OOS simulated test case, in-track station-keeping of 200 meters	157
6.2.3	OOS simulated test case, co-elliptic drift of offset of -200 meters.....	159
6.2.4	Test Case Summary	161
6.3	Effects of increased measurement precision.....	161
6.4	Observability of the relative motion	163
6.4.1	Jordan Canonical form – Observability assessment	164
6.5	Chapter summary, contributions and recommendations.....	166
Chapter 7: Conclusions.....		168
7.1	Thesis summary	168
7.2	Significance of work and contributions	171
7.2.1	Contributions.....	172
7.3	Potential Applications.....	173
7.4	Recommendations for future research	174
List of Abbreviations.....		177
Appendices		179
Appendix A		179
A.1	Proximity Flight Missions.....	179
Appendix B		180
B.1	Orbit Estimation.....	180

1.1.2	Linearizing Orbital Motion.....	180
1.2	Batch Least Squares.....	182
1.3	Kalman Filter Implementation.....	183
1.4	Extended Kalman Filter Implementation.....	185
Appendix C.....		186
C.1	EMCCD Camera Parameters.....	186
Appendix D.....		187
D.1	Computing the cross-spectrum.....	187
D.2	Directed Vector Autocorrelation.....	189
References.....		190
Biographical Sketch.....		202

List of Tables

Table 1	DVA Computation Time.....	57
Table 2	Filter Effective Wavelengths and Bandwidths.....	68
Table 3	Extinction coefficients for various filters [73].....	69
Table 4	Initial relative orbit estimate for GEO On-Orbit Servicing	90
Table 5	Sequential Estimation Overview for OOS	91
Table 6	DRDC Ottawa Space Surveillance Observatory system configuration	102
Table 7	Mont-Mégantic Telescope Optical Parameters.....	117
Table 8	Binary Star WDS ES326 BC	119
Table 9	Autonomous On-Orbit Servicing and Proximity Flight Missions	179
Table 10	Table of Notation	181
Table 11	Andor iXon 888i Specifications.....	186
Table 12	Nuvu HNu LN EMCCD iXon 888i Specifications.....	186

List of Illustrations

Figure 1: (Left): DART (upper left) and MUBLCOM (two circular solar panels) (NASA).....	4
Figure 2 (<i>left</i>): Orbital Express Servicing Satellite (<i>Right</i>): NEXTSat client test target right (DARPA).....	5
Figure 3 Geostationary commercial satellites (Image credit: Boeing).....	6
Figure 4: Space Debris in Earth orbit (Image credit: NASA).....	8
Figure 5: Space Surveillance Network (Image credit: US Strategic Command).....	8
Figure 6: (<i>Left</i>): Anik G1, Anik F1, and Anik F1R. (<i>Right</i>): Optical conjunction (an alignment) of Anik F1 and Anik G1. Streaks are background stars trailed during the image’s exposure	10
Figure 7: Closely-spaced objects problem in GEO orbit. 1) Neighboring GEO station-keeping, 2) Co-located satellites, 3) On-Orbit Servicing.....	11
Figure 8: Satellite bus type differentiation by using light curves [18].....	13
Figure 9: Scale sizes of interest for the proximity of client satellite for OOS monitoring.....	17
Figure 10: Forward model reflectivity definitions for equation 1.1.....	19
Figure 11: Synthetic light curve output [36]. (<i>Inset</i>): Imported CAD geometry.	21
Figure 12: (<i>Top</i>): Combined light curve (blue) for client (green) and servicer (red) for co-elliptic drift relative orbit shown in the bottom frame. (<i>Middle</i>): Rotational phase of the servicer to track the client as it passes. (<i>Bottom</i>): Selected time steps of the servicer’s relative motion [36].....	21
Figure 13: Left: Speckle Image of a double Star. Right: Modulus of Fourier transform showing Fringes of the objects (Image credit: DRDC Ottawa).....	23
Figure 14 <i>Left</i> : GE-23 geostationary satellite. <i>Center</i> : De-convolved ground based image of GE-23, <i>Right</i> : Approximate model of GE-23 in detected orientation (Image credit reference [52]).....	26
Figure 15: Vertical Turbulence distribution as a function of altitude for the Mount Graham observatory (Image credit reference [78])	38

Figure 16: <i>(Left)</i> Long exposure profile of binary star. <i>(Center)</i> Profile exhibiting seeing width of the atmospheric point spread function. <i>(Right)</i> Speckle pattern from short exposure image.	39
Figure 17: Selected frames of various exposure lengths showing changes in speckle behavior.....	40
Figure 18: Atmospheric seeing cells of size r_0 forming speckles on the detector plane. Speckles are of size λ/D . The seeing disk is of size λ/r_0	41
Figure 19: Simplified model of the isoplanatic angle.	42
Figure 20: <i>(Left)</i> : Example of ideal diffraction limited object. <i>(Right)</i> : Example of speckle object where the ideal object is duplicated over the seeing disk	42
Figure 21: <i>(Left)</i> Bright binary STF 738AB showing speckle duplication.....	43
Figure 22: Diffraction Limited MTF for normalized spatial frequency u_n	45
Figure 23: Diffraction Limited (τ_{DL}), Low Frequency (τ_{LF}) , High-Frequency τ_{HF} and combined Labeyrie Korff transfer function τ_{LK}	47
Figure 24: Object model $O(x)$ modelled with Dirac delta functions.....	49
Figure 25: $O(x)$ with phase shift Δx	50
Figure 26: <i>(Left)</i> : Point source objects in spatial (x,y) plane. <i>(Right)</i> : Power spectrum Fringes in spatial frequency (u,v) plane.....	52
Figure 27: Measurements of separation distance ρ (or d) and the orientation angle θ	53
Figure 28: Speckle image of binary star, its power spectrum and autocorrelation	54
Figure 29: Example of Directed Vector Autocorrelation (x,y expressed in units of pixels).....	56
Figure 30: GEO satellites Anik F1R (Lower left) and Anik G1 (Upper right). Frame size is 512x512 pixels	58
Figure 31: <i>(Left)</i> : Object function $O(x)$ with point spread function (dashed) <i>(Right)</i> : Cross-correlation as expressed in equation 2.35.....	59
Figure 32: Speckle image, autocorrelation, cross-correlation, real cross spectrum, imaginary cross-spectrum and imaginary fringe profile. Notice that the imaginary component is positive in the direction of the true location of the secondary.	61
Figure 33: Speckle Image Example with North Reference Vector	65

Figure 34: (Left) Cross-spectrum imaginary component (Right) Profile of imaginary component showing gradient (slope) as positive at the center of the profile. The object is the right.	65
Figure 35: Chromatic dispersion for various filter bands. Note that the <i>I</i> filter has lower dispersion due to the narrow width of its filter band-pass.....	67
Figure 36: Filter bandpass used for speckle Interferometric measurements.....	68
Figure 37: Relative position vectors, geocentric and topocentric frames (not to scale)	73
Figure 38: Rotation of the sidereal angle α and declination δ to form the RSW frame	77
Figure 39: Hour angle ($\alpha-\alpha_t$) and δ_i angles with respect to the primary satellite.....	80
Figure 40: Looking along the line of sight from a ground based observer to client-servicer pair.....	89
Figure 41: Number of frames estimated from equation 4.6 required to achieve $SNR = 6$ for various aperture diameters and object magnitudes	97
Figure 42: (Not to scale) General arrangement for a speckle imaging instrument (1) secondary mirror, (2) primary mirror, (3) Sloan <i>i'</i> filter, (4) focuser, (5) focal length extension via barlow lens, (6) EMCCD detector	100
Figure 43: (<i>Left</i>): DRDC Ottawa Space Surveillance Observatory. (<i>Right</i>): 35cm telescope.....	102
Figure 44: (<i>Left</i>): EMCCD and filter wheel. (<i>Right</i>): Sloan <i>i'</i> , Cousins I filters.....	102
Figure 45: Drift method to determine the orientation angle of the camera.....	104
Figure 46: Image Processing Block Diagram	106
Figure 47: (<i>Left</i>): Cosmic ray strike. (<i>Right</i>): Unwanted fringing due to cosmic ray.	106
Figure 48: (<i>Top</i>): Raw Speckle Frame, (<i>Left</i>): Raw Imaginary fringes. (<i>Right</i>): Auto correlated imaginary fringes	107
Figure 49: Sobel filter applied to AC of imaginary fringes	108
Figure 50: (<i>Left</i>): Imaginary fringe profile. (<i>Right</i>): Profile showing positive slope (marked) indicating that the fainter secondary object is in the direction of the profile..	109
Figure 51: (<i>Left</i>): Raw fringe profile with Moffat fit envelope (semi-transparent). (<i>Right</i>): Deconvolved profile showing imaginary fringes.....	111

Figure 52: *(Left)*: Relative orbit trajectories of co-located GEO satellites Anik F1, Anik F1R, and Anik G1. *(Right)*: Anik G1, Anik F1R undergoing an optical conjunction. 114

Figure 53: *(Left)*: Mont-Mégantic Observatory *(Right)*: 1.6m telescope..... 116

Figure 54: *(Left)*: Nuvu EMCCD. *(Right)*: Fabric baffling to reduce stray light..... 117

Figure 55: Speckle image of WDS ES326BC..... 119

Figure 56: Anik G1 and Anik F1R during the optical conjunction (18 Feb 2014).... 121

Figure 57: Anik G1 and Anik F1R. Note that Anik F1R’s path is in the $-x_{\text{Hill}}$ direction relative to Anik G1 and is moving in the $+y_{\text{Hill}}$ (eastward) and $+z_{\text{Hill}}$ (northward) directions..... 122

Figure 58: *1st column*: Time, separation distance and measured orientation angle. Time is expressed in minutes past midnight (UTC), separation (d) arcseconds, and θ in degrees. *2nd column*: Selected frames during the optical conjunction. *3rd column*: Raw imaginary component of the cross-spectrum. White arrow indicates celestial north, black arrow indicates the direction to the secondary object, *4th column*: Autocorrelation (AC) of the imaginary fringes where the white line indicates the profile axis and red line indicates fringe orientation angle. *5th column*: Moffat normalized fringes. Cyan line indicates the center of the profile and vertical red lines indicate the first detected fringe minima. 124

Figure 59: *(Top left)*: Separation distance d , *(Right)*: orientation angle θ , *(Bottom)*: Seeing ε 125

Figure 60: Differential measurements $\Delta\alpha_t$, $\Delta\delta_t$ (red x, blue o) plotted against reference ephemeris 126

Figure 61: Previous processing of Anik G1, Anik F1R track $\Delta\alpha_t$, $\Delta\delta_t$ (red x, blue o). Declination biases and enhanced differential right ascension noise is visible at the start of the track. The $\Delta\alpha_t$ residuals have lower precision due to the lower stack sizes. 127

Figure 62: Anik F1 and Anik G1 selected speckle frames from the 2nd track. 128

Figure 63: Anik F1 (primary) and path of Anik G1 relative to Anik F1. FOV is 27 arcseconds. Note that Anik G1’s path is in the $+x_{\text{hill}}$ direction relative to Anik F1 and is moving in the negative in-track (westward) and negative cross-track (southward) direction. 128

Figure 64: *1st column*: Time, separation distance and measured orientation angle. Time is expressed in minutes past midnight (UTC), separation (d) arcseconds, and θ in degrees. *2nd column*: Selected frames during the optical conjunction. *3rd column*: Raw imaginary component of the cross-spectrum. White arrow indicates celestial north, black arrow indicates the direction to the secondary object, *4th column*: Autocorrelation (AC) of the imaginary fringes where the white line indicates the profile axis and red line indicates fringe orientation angle. *5th column*: Moffat normalized fringes. Cyan line indicates the center of the profile and vertical red lines indicate the first detected fringe minima. 130

Figure 65: (*Top left*): Separation distance d (arcseconds) (*Right*): Orientation angle θ , (*Bottom*): Seeing ϵ 131

Figure 66: Selected frames during the “seeing bloom”..... 131

Figure 67: Differential measurements $\Delta\alpha_t, \Delta\delta_t$ (red x, blue o) plotted against reference ephemeris 133

Figure 68: Effect of rapidly moving objects causing stacks to smear the fringes..... 134

Figure 69: Fourier transform of the cross-spectrum imaginary fringes resulting in two spikes separated by $2d$ 135

Figure 70: Differential measurements $\Delta\alpha_t, \Delta\delta_t$ using improved object detection approach..... 136

Figure 71: $\Delta\alpha, \Delta\delta$ measurements near-directly inferring state variables y_{Hill} and z_{Hill} 138

Figure 72: Anik F1R Relative Trajectory with respect to Anik G1. Green dot is track start. Red x is track end..... 139

Figure 73: Anik F1R relative trajectory with respect to Anik G1. Three-dimensional plot of measurements (purple points) versus reference ephemeris (white). Direction of motion is indicated..... 139

Figure 74: 1st track radial, in-track and cross-track error relative to reference ephemeris. Regions where observations were not processed by the filter are marked... 140

Figure 75: Anik G1, Anik F1R relative orbit uncertainty 141

Figure 76: (*Left*): Anik G1’s trajectory relative to Anik F1. Green dot is track start. Red x is track end..... 142

Figure 77: Anik F1 and Anik G1 estimated relative trajectory (blue) and reference trajectory (yellow) showing the westward track bias. Direction of motion is indicated.	143
Figure 78: RIC position error compared to operator ephemeris	144
Figure 79: Anik F1, Anik G1 relative orbit uncertainty.....	145
Figure 80: Anik F1, Anik G1 speckle images acquired on 2 Aug 2015	146
Figure 81: Path of Anik G1 relative to Anik F1 during the third track on August 2, 2015. Conical half radius is the isoplanatic angle of 5 arcseconds. Direction of motion is indicated.....	146
Figure 82: (<i>Top left</i>): Anik F1, Anik G1 separation distance d (arcseconds). Red is the new processing approach, blue points are d (ρ) measurements inferred from the fringe minima. The black line indicates the true separation distances from ephemerides (<i>Right</i>): Orientation angle θ , (<i>Bottom</i>): Seeing ε	147
Figure 83: Differential measurements $\Delta\alpha_i$, $\Delta\delta_i$ (red x, blue o) plotted against reference ephemeris	148
Figure 84: Measured trajectory of Anik G1 with respect to Anik G1.	149
Figure 85: The detector's coordinate axes (red EMCCD axes) showing near alignment with the radial direction of the Hill frame (white).....	153
Figure 86: Co-located satellite case with continuous measurements added to filter .	155
Figure 87: (<i>Left</i>): Simulated Mont-Mégantic track showing radial error. (<i>Right</i>): Simulated track rotated to the plane of observer to emphasize the smooth appearance of the track in this direction.....	157
Figure 88: Continuous measurements for +200 m in-track station-keeping.....	158
Figure 89: Convergence for the +200 m in-track station keeping case. The radial position of the observations spreads radially along the line-of-sight of the observer	159
Figure 90: Continuous measurements for -200 m co-elliptic drift.....	160
Figure 91: Convergence for the co-elliptic drift case. The spray of radial position estimates is along the line-of-sight of the observer	161
Figure 92: Converge time vs measurement noise	163

List of Appendices

Appendix A.....	179
A.1 Proximity Flight Missions.....	179
Appendix B.	180
B.1 Orbit Estimation.....	180
Appendix C.	186
C.1 EMCCD Parameters.....	186
Appendix D.	187
D.1 Computing the cross-spectrum.....	187
D.2 Directed Vector Autocorrelation.....	189

Chapter 1: Introduction

1.1 On Orbit Servicing as a space surveillance problem

On-Orbit-Servicing (OOS) and On-Orbit Inspection (OOI) offer exciting new possibilities for the delivery of interventional services to satellites in Earth orbit. Intervention can take the form of inspection (e.g. by optical imaging), satellite anomaly resolution such as freeing a stuck solar array, satellite repair, satellite refuelling, parts replacement and orbital or attitude maneuvering adjustment. Some inventive proposals include robotic disassembly, on-orbit construction or de-orbit services that could potentially limit the spread of space debris. While these new robotic servicing technologies offer many new and possibilities for satellite missions (see Annex A), they also pose new problems for the space surveillance community who is responsible to track space operations to maintain safety and security in the Earth orbital environment.

The research described in this thesis focuses on the observational problems inherent to monitoring OOS activities in Geosynchronous Equatorial Orbit (GEO)—a circular, equatorial orbit of 35,786 km altitude that is densely populated with satellites. GEO contains more than 400 [1] commercial and government satellites that share the same orbital plane, making it a particularly attractive orbit for future servicing missions. Ground-based observations of two OOS satellites in GEO—with a separation distance of 1 km or less—see an angular separation between the two satellites subtending less than 5 arcseconds ($< 25 \mu\text{rad}$). Tracking objects with tight separations like these is especially problematic since closely-spaced objects appear to blend due to atmospheric turbulence, making traditional tracking methods—such as pixel clustering—problematic.

Optical telescopes are widely available and are the primary passive means by which objects are tracked in GEO. When deciding on an approach for OOS tracking, sensor availability was a key consideration. Atmospheric turbulence is a limitation that all optical telescopes encounter when viewing closely-spaced astronomical objects or an upcoming OOS mission. The angular size of Earth's turbulence (seeing) cells is comparable to the angular size between the OOS satellite pair, which naturally blurs the position of two objects. This issue compounds the problem of measuring the position of closely-spaced OOS satellites.

This dissertation describes an approach designed to compensate for atmospheric turbulence and enable ground-based electro-optical space surveillance of OOS proximity flight in GEO. It is a practical, low-cost approach to tracking and measuring the relative orbit of larger objects ($>10 \text{ m}^2$) that perform OOS in GEO. Experimental results are shown using optical alignments of co-located geostationary satellites, acting as OOS proxies to test the approach. Relative astrometric measurements of the satellites closing to within 1.5 arcseconds of one another were achieved and their relative orbits estimated. Limitations of this approach were encountered and solutions to these problems are described.

1.2 A short overview of On-Orbit-Servicing missions

The reliability of spacecraft is a key consideration in the development of satellite systems and has been since the dawn of the space age. When anomalies occur on orbit they often leave satellite and spacecraft operators with little recourse for correction which encourages the development of complex and expensive engineering solutions (such as redundancy) to increase reliability [2]. The capability to physically interact with satellites is relatively rare but progressive steps have been taken to develop technologies needed to perform OOS.

The first space shuttle-based intervention repaired the Solar Maximum satellite [3] involving robotic-assisted captivation and astronaut enabled repairs to resurrect the spacecraft. Parts and instruments were replaced enabling its science mission to be continued. Subsequently, the Palapa B2 and Westar-6 satellite [4]—which were stranded in a useless orbit—were recovered after astronaut enabled captivation attempts. They were eventually returned to Earth for refurbishment and re-flight. More recently, the Canadian robotic arm (Canadarm 2) —equipped with the Dextre robotic module—performed a series of robotic refuelling tests aboard the International Space Station as a technology demonstration of robotic refuelling of satellites [4]. Technology development in OOS is continuing by a variety of nations for both civilian and security purposes.

The complexity, cost and risk of astronaut-enabled OOS inspired autonomous and semi-autonomous robotic satellite systems to be examined. The Engineering Test Satellite 7 (ETS-VII) [6] was developed and launched in 1997 by NASDA (Japan) to test

the viability of on-orbit servicing using a robotic manipulator. This mission consisted of a chaser (Hikoboshi) and target satellite (Orihime) in a 550 km Low Earth Orbit (LEO) of 35-degree inclination. The satellite was tele-robotically controlled via the TDRSS network; and robotic subtasks were executed autonomously. The result of these exercises showed that autonomous rendezvous and docking was possible within 2 meters, station-keeping and proximity flight up to six kilometres separation could be performed.

Small satellite missions¹ designed to perform proximity operations and On Orbit Inspection (OOI) were developed by the US in the early 2000s as low-cost technology demonstration flying as secondary payloads on US Air Force missions. The XSS-10 [8] (2003) and XSS-11 [9] (2005) both performed proximity flight operations to demonstrate close-approach formation flight necessary for orbital inspection. These small systems of 28 and 100 kg demonstrated that small satellite systems can perform proximity operations on low-cost platforms and that autonomous proximity operations could be enabled. These smaller missions are in contrast to ETS-VII which was a large satellite of nearly 3 tonnes mass.

The DART (Demonstration of Autonomous Rendezvous) mission [10] was launched in 2005 and performed autonomous proximity operations about the MUBLCOM (Multiple Paths Beyond Line of Sight Communications) satellite, a DARPA communications technology demonstration project (see Figure 1). DART was designed to perform a variety of approaches to MUBLCOM using both GPS and visible/near infrared visible cameras to estimate its relative position with respect to its client (MUBLCOM). For 11 hours, it performed several successful rendezvous with MUBLCOM. Then, unbeknownst to the satellite operators (or the navigation algorithms on DART), DART missed a navigation waypoint and collided [10] with MUBLCOM.

The DART collision highlights one of the key risks of performing close-proximity flight about a client satellite. Unintentional collision is a real possibility for close-proximity formation flight despite continuous sensor input feeding relative navigation information on-board a servicing satellite. In this case, an externally measured relative

¹ Technology development for small satellite LEO formation flight continues today. In 2014 the Canadian CanX-4 and CanX-5 mission performed a 50 meter projected circular relative orbit about one another using 6 kg cubesat platforms [7] but rendezvous and inspection was not performed.

orbit of the servicing satellite could have reduced the risk of collision between the two objects if external sensor measurements were possible. External orbital validation is used regularly by space operators to independently assess satellite conjunction risk (the chance risk of collision between two independent satellites) by collecting positional measurements and comparing them to operator ephemerides.

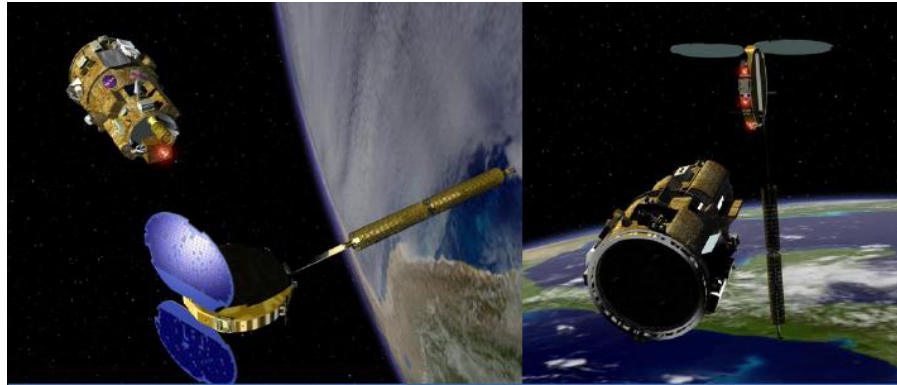


Figure 1: (Left): DART (upper left) and MUBLCOM (two circular solar panels) (Image credit: NASA)

Two years later, the Orbital Express Mission [11] (2007) demonstrated the full array of capabilities needed for true robotic OOS satellite intervention and built upon technology developments in prior microsatellite efforts. Orbital Express consisted of a robotic-arm and captivation mount equipped servicing satellite ASTRO (Figure 2 left) and the rendezvous target NEXTSat (Figure 2 right). The mission demonstrated autonomous rendezvous, proximity formation flight, the first autonomous inter-satellite fluid (hydrazine) transfer, battery replacement, and autonomous inspection fly-around. Although the Orbital Express performed its feats in LEO, the mission was designed to test robotic technologies needed to perform OOS in the more strategically important geostationary orbital regime.

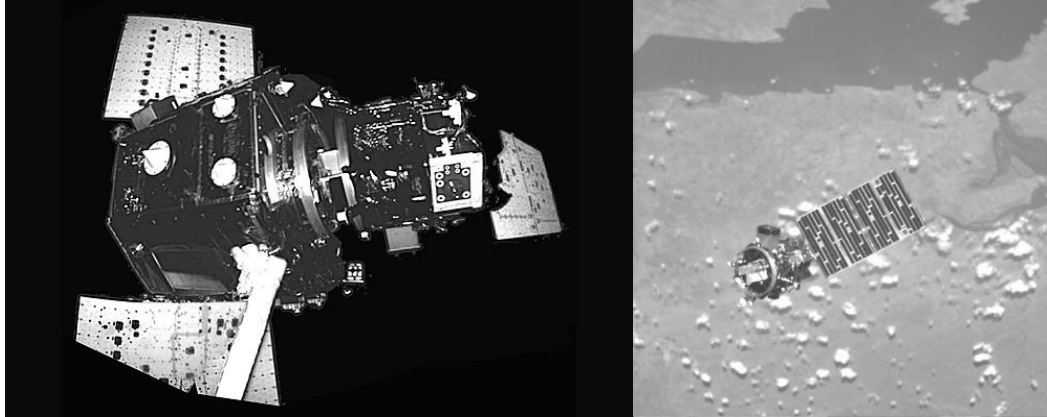


Figure 2 (left): Orbital Express Servicing Satellite (Right): NEXTSat client test target right (Image credit: DARPA)

1.3 Geostationary orbit

Geosynchronous Equatorial Orbit (GEO) or “geostationary orbit” is of particular interest to governments and commercial enterprise because of its value for global communication, weather monitoring and surveillance. GEO [12] is a circular orbit of 35,786 kilometers altitude (~5.61 Earth Radii) with a zero-degree inclination making GEO satellites fly over Earth’s equator. Satellites placed at this altitude with ~3.0 km/s velocity relative to the inertial frame have a mean motion that matches the rotational rate of the Earth causing GEO satellites to appear stationary with respect to the Earth fixed frame. Because of this, they easily maintain persistent radio tele-communication and visibility over a large area of the Earth.

At present, GEO hosts the greatest concentration of operating satellites in a single orbiting plane and altitude where all satellites maintain relative formation as they provide services to terrestrial-based customers. The commercialization of GEO provides direct broadcast television and international telephony for its commercial customers. The orbit is also strategically important for government organizations that use GEO for persistent air, sea and land force communications as well as persistent missile warning. GEO is now packed with more than 400 satellites [1] in station-keeping boxes—each of which is typically 0.1 degrees longitude wide by 0.1 degrees tall (approximately ~74 x 74 km in size and ~35 km deep).

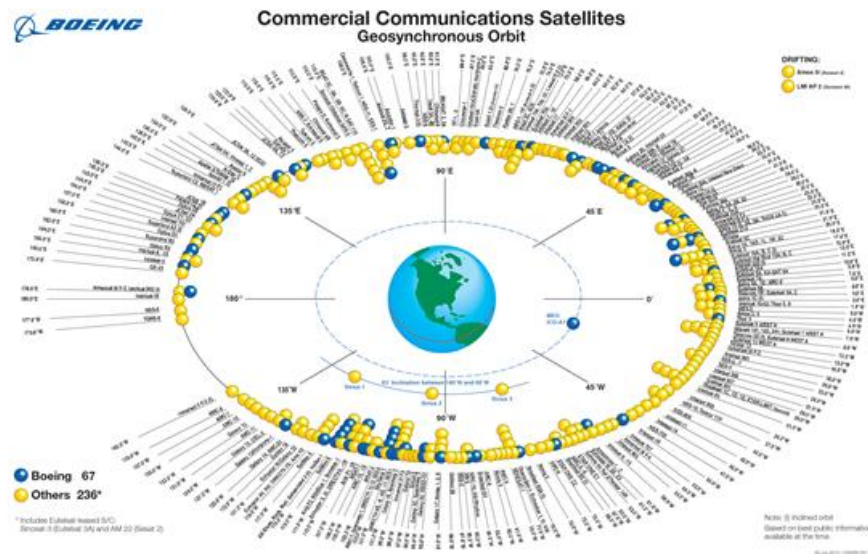


Figure 3 Geostationary commercial satellites (Image credit: Boeing)

Geostationary satellites perform routine orbital manoeuvres to maintain station-keeping [12] by North-South and East-West maneuvering to maintain inclination, eccentricity and altitude control. Without these maneuvers, the satellites would drift relative to the Earth due to perturbations from the Sun and other gravitational effect. The need for orbit maintenance is one of the leading factors why geostationary satellite lifetime is limited to approximately 15 years due to the finite amount of station-keeping propellant kept on board the satellite. At the end of the GEO satellite's life, a small reserve of propellant is kept such that its final maneuver moves the satellite into the geosynchronous graveyard orbit to reduce the likelihood of collision with operational satellites. This graveyard orbit should be [13] a minimum of 235 km above the geostationary belt with additional margin added depending on the solar radiation pressure properties of the satellite. Once the satellite has entered this orbit, the spacecraft is generally decommissioned.

Far in advance of this decommissioning, the satellite owner generally initiates the recapitalization of the asset by the acquisition of a new satellite and launch or, alternatively, lease services from another satellite already on orbit to maintain priority use of the satellite's longitude slot assigned by the International Telecommunications Union

(ITU). The finite fuel capacity of geostationary satellites limits their lifetime simply because this consumable cannot be replenished.

If these geostationary satellites could be refuelled (or repaired) this could lead to new economic possibilities for satellite operators. Proposals for such services have appeared (Annex A) but have yet to be flown. Should the next step of OOS servicing begin in GEO where satellites begin interacting with one another, the space surveillance community could be impacted.

1.4 Space surveillance and the problem of OOS in GEO

Space surveillance is any activity geared towards detecting, tracking and maintaining a catalog of objects orbiting the Earth. Space surveillance is normally achieved by the use of radar and optical sensors which measure the positions of objects orbiting Earth. These sensors then feed this data into an Orbit Determination (OD) system such as the one used at the Joint Space Operations Center (JSpOC) in Vandenberg California. JSpOC performs the role of sensor management for the Space Surveillance Network (SSN) [14]—an affiliation of sensors that consist of dedicated, contributing, and collateral systems which observe active and inactive Resident Space Objects (RSOs). Both civilian and military space flight safety is supported by maintaining a satellite catalog for orbital prediction. JSpOC computes predicted collision risks between satellites using the satellite catalog and performs re-entry warning assessments to reduce the risk of injury on the ground. Other nations also maintain their own space surveillance capabilities. The Russian Space Surveillance System (RSSS) and the Chinese maintain space surveillance capabilities to support their national programs. Likewise, European systems are being established to collectively contribute to the monitoring of the situation in space [14].

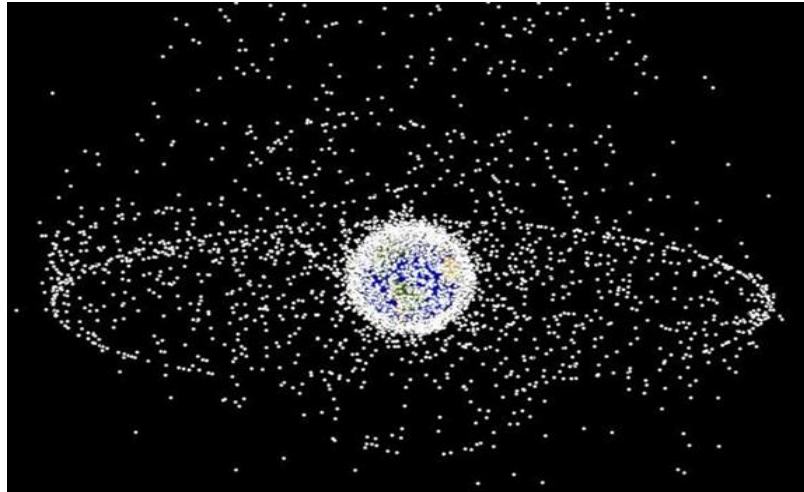


Figure 4: Space Debris in Earth orbit (Image credit: NASA)

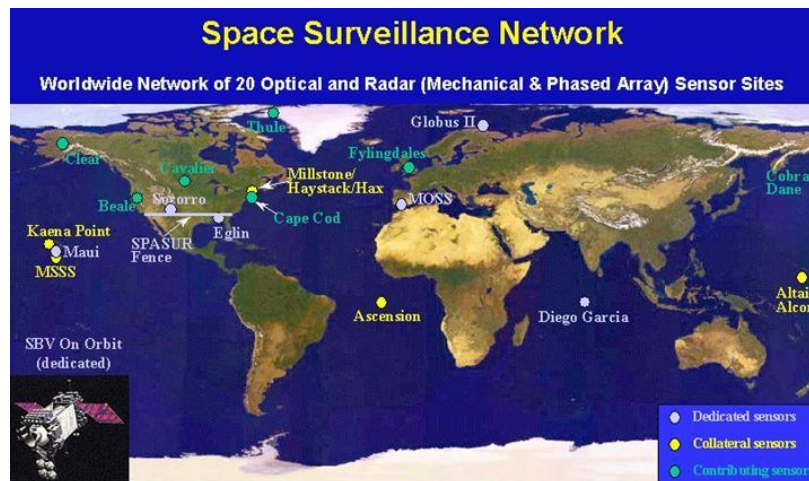


Figure 5: Space Surveillance Network (Image credit: US Strategic Command)

The SSN collects measurements primarily by two means—radars and optical telescopes. Radars—such as the Eglin Phased Array [15]—measure range and range rate on orbiting objects. A variety of ground-based radars have been distributed globally to perform this role. These radars primarily track LEO orbits, however, some radars—like the Millstone Hill [16] radar—also perform GEO tracking. In addition to ranging measurements, radar cross-section (RCS) measurements are also collected which provide a rough indication of the size of an object based on its radio reflectivity.

Optical telescopes—such as GEODDS [17]—principally collect “angles-only” measurements on deep space satellites (GEO), where such data may contain

right-ascension/declination measurements or azimuth/elevation measurements. Optical telescopes form images that can be used to determine the magnitude² or brightness of an object which can also be used as a coarse means of estimating object size.

Space surveillance generally treats orbiting objects as non-interacting—that is, objects independently follow trajectories under the influence of Keplerian motion that has been modified by natural perturbations such as atmospheric drag, luni-solar gravity and solar radiation pressure. “Unnatural” forces (for example, thrust, mass loss or satellite interaction) corrupt the orbit estimation process as these effects cause unnatural steps in satellite trajectories. Both natural and unnatural orbital forces can be modelled during orbit propagation however; limitations on their accuracy are present. Inaccuracies caused by the effects of sensor noise, lack of timing knowledge of impulsive thrust events, and extreme computational burden can limit propagation accuracy. It is a large computational enterprise to maintain and predict orbits for the more than 22,000 known objects in the satellite catalog.

Satellites in GEO are usually well-separated from one another. The orbital slot management approach for GEO orbit assigns narrow station-keeping boxes where many satellites neighbour one another by 0.1 degrees of longitude (~74 km at GEO altitude). At the other extreme, GEO satellites can also be co-located within the same geostationary satellite station-keeping box [12]. In such cases, satellites perform elliptical flight about one another, which permits them to safely occupy the same station-keeping box. The two satellites use different radio frequencies so they don’t interfere with other radio transmissions’ broadcasts to the same location in GEO orbit. Satellite co-location is achieved by inclination and eccentricity offsets which permit satellites to elliptically spiral about one another to reduce the risk of collision. Using this approach, more radio-frequency communications services can be provided within the limited amount of orbital

² Magnitude is a relative flux scale where larger numbers indicate that an object is fainter than a reference. The ratio of flux from two objects is $M_2 - M_1 = -2.5 \log_{10}(f_2/f_1)$. The Sun has a V-band apparent magnitude of -26.74 magnitudes as observed from the Earth. Many large GEO satellites’ apparent magnitude varies between magnitude 10-13. A dark adapted human eye is limited to detecting a magnitude 6 star at a dark sky location. Most satellite brightnesses are recorded in apparent magnitude whereas absolute magnitude denotes an object’s brightness corrected to a standard distance of 10 Parsecs from the observer which is commonly used in astrophysics.

real estate available in geostationary orbit. This tight orbital formation approach is experiencing increased usage in geostationary orbit [18].

Canada has used satellite co-location regularly. For instance, the Canadian geostationary satellites Anik F1, Anik F1R and Anik G1, operated by Telesat Canada, occupy the same orbital slot at 107.3° W. Ground-based images of the satellites are shown in Figure 6 where these satellites appear as dots in the imagery and background stars appear as streaks.

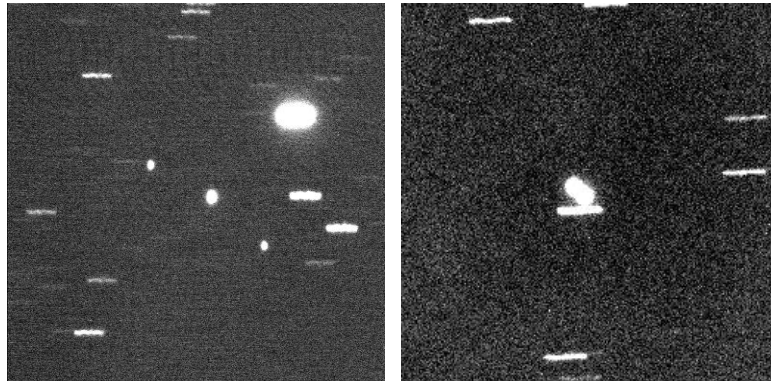


Figure 6: *(Left):* Anik G1, Anik F1, and Anik F1R. *(Right):* Optical conjunction (an alignment) of Anik F1 and Anik G1. Streaks are background stars trailed during the image's exposure

1.5 Motivation for this research: Space surveillance of closely-spaced objects

Studies of closely-spaced objects in geostationary orbit have usually focused on the tagging (identification) problem where a detected satellite must be tagged with a correct object identity (usually the SSN ID number). Images such as Figure 6 can often lead to ambiguous situations where the point-like satellites cannot be easily differentiated within a single image. Orbit determination systems rely on accurate satellite tagging to refine orbital estimates so that the correct orbital measurement information is propagated. Satellite tagging (also known as correlation [19]) is typically performed by way of coarse orbital information (e.g. general perturbation two-line-elements [20]) where the object's measured position from a sensor is compared to the object's predicted location. For GEO satellites neighboring one another in their station-keeping boxes, this simple association method works relatively well—general perturbation elements usually have positioning

errors of 1-10 km in GEO which permits unambiguous station-keeping box differentiation.

Figure 7 characterizes the three size-scale regimes of interest for optical detection of closely-spaced objects in GEO showing 1) the neighboring (cluster) GEO problem, 2) the co-located satellite problem and 3) the OOS problem. The OOS problem is a much more stressing detection case in comparison to the other two as neighboring GEOs and co-located satellites are still detectable as individual point source objects. The OOS case can exhibit separations within the seeing disk of the atmosphere appearing to blend the objects together.

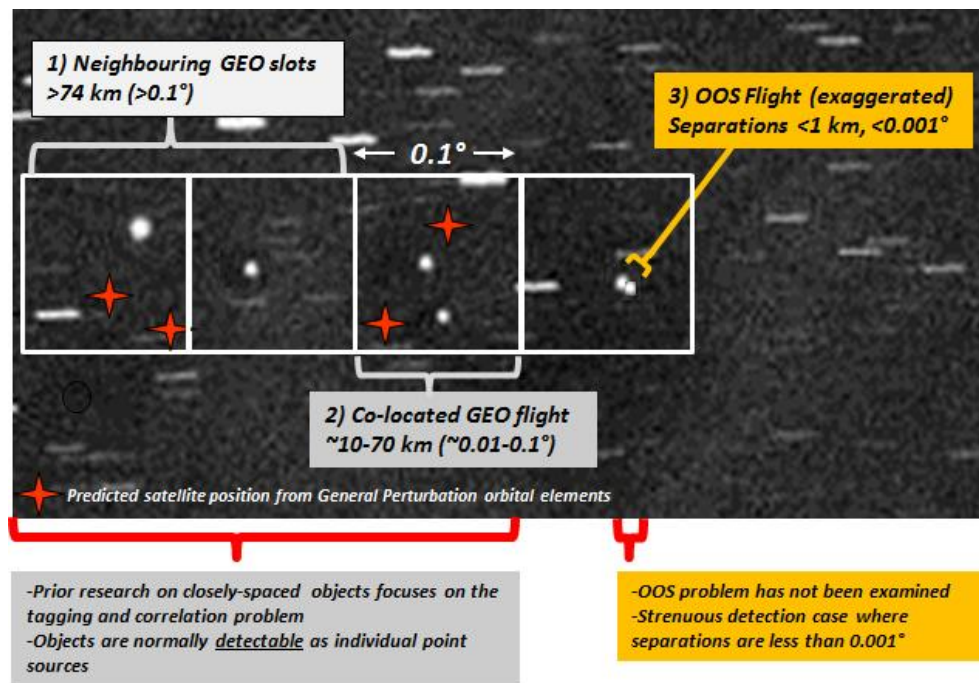


Figure 7: Closely-spaced objects problem in GEO orbit. 1) Neighboring GEO station-keeping, 2) Co-located satellites, 3) On-Orbit Servicing

In the case of clustered or co-located satellites, the use of general perturbation orbital data begins to break down as a means to tag the identity of the satellites. The tighter separations of co-located and clustered GEOs can be easily swapped as measured satellite separations become comparable to the error of the general perturbation orbital elements. This results in cross-tagging, a situation where a satellite is tagged with the wrong

satellite identification which can cause position measurements to be automatically rejected in the orbit association process.

To help resolve this problem, complementary information collected by space surveillance sensors can be inspected to resolve cross-tags. For instance, Space Object Identification (SOI) data, such as unfiltered photometry, filtered photometry or spectrometric data can be added to the positional data to alleviate cases of ambiguous tagging. In Figure 6 (left) Anik F1, which has very reflective solar array concentrators, makes its identification effortless as it is the brightest object in the cluster. Photometric data can be acquired simply by counting the measured flux from a detected object in an image (see Figure 8) or by measuring its radar cross section.

Unfiltered photometry uses the entire wavelength sensitivity of a CCD camera to detect the magnitude (brightness) of an orbiting object and can be inexpensively acquired by small telescopes [18]. Unfiltered telescopes are used to detect faint objects in GEO as their spectral detection range is not limited by filter transmission losses or bandpass cutoffs. Photometric data collected on orbiting GEO satellites is often contrasted with universal time or phase angle³ to characterize trends in the brightness (see Figure 8) which are unique to the satellite. This is due to the GEO satellite's motion changing the viewing geometry with respect to the observer and the Sun and the reflectivity and shape of the object. Differentiation of GEO satellite bus types can be performed in this manner.

³ Phase angle is a term used by the optical space surveillance community to coarsely describe the amount of illumination on a resident space object which can be observed by a ground based observer. The angle subtends sun-object-observer where phase angles of zero degrees indicate that the object's illuminated disk is fully observed by the observer.

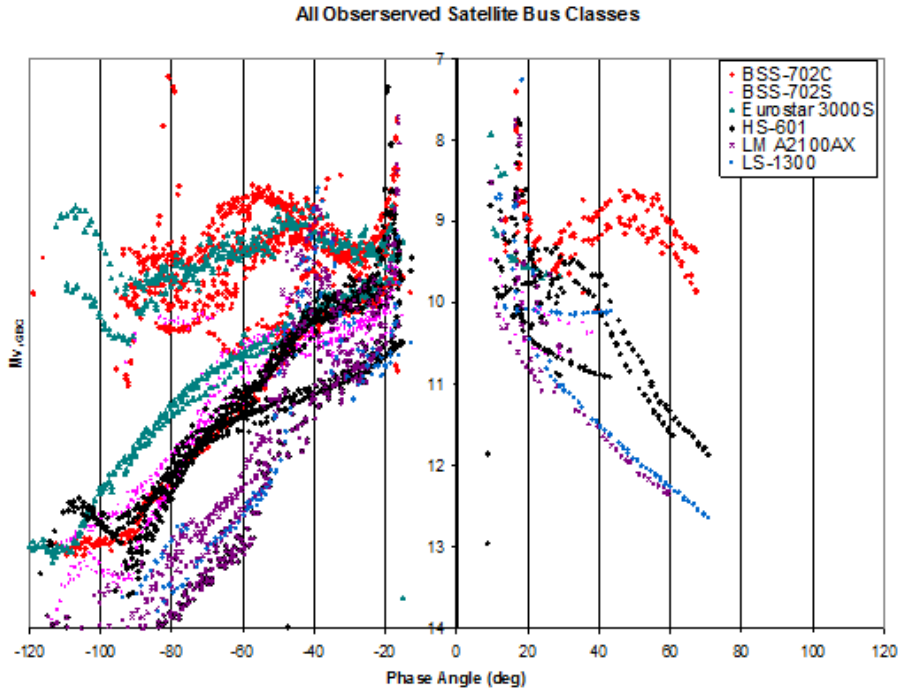


Figure 8: Satellite bus type differentiation by using light curves [18]

Broadband color filters, such as the astronomical Johnson U, B, V, R, I filters, can characterize satellites by measuring their filtered magnitudes with respect to time and phase angle or by measuring changes in their color index (such as B-V or V-R). Payne [21] used B-band photometric measurements to infer the offset angle of GEO solar arrays from the sun line as solar arrays tend to be more reflective in the B-band. Color indexes enable a more refined level of identification for closely-spaced satellites. Payne's [22] studies color monitoring of GEO satellites shows examples of object differentiation simply by taking color index measurements on them. Bedard [23] found that a related spectroscopy-derived color ratios technique offers a similar path to differentiate satellites to aid in their identification. Filtered photometry is relatively simple to implement, however, there is a small price paid with respect to sensitivity when introducing filters into the optical train of a telescope. As a filter bandpass tends to be relatively large in comparison to spectral techniques the sensitivity loss is often acceptable in comparison to the characterization benefits.

Satellite spectroscopy is a technical approach that uses the highest wavelength resolution (see example in reference [24]) to identify material composition on the

surfaces of satellites. Satellite materials have been shown to exhibit unique spectrometric fingerprints that allow them to identify common spacecraft materials such as aluminum, white paint, solar cells, etc. When combined with an inversion (unmixing) approach [25], both spectroscopic and broadband filtered measurements can be used to determine percentage material composition on the surfaces of satellites. Satellite spectral signatures also exhibit temporal changes [26] which can be used as markers to identify them. Other researchers have extended spectrometric approaches to thermal infrared to remotely measure the temperature of geostationary debris objects to help identify their state [27] as well as help to determine their origin. Since spectroscopy requires large telescopes, its usefulness is limited for most space surveillance applications but it is currently an active area of research for closely-spaced objects [28].

Filtered color photometry is favored for closely-spaced object differentiation since it is a good match between sensitivity and differentiation capabilities for moderately sized space surveillance telescopes. For closely-spaced satellite tracking however, this filtered photometry doesn't assist in the detection problem when the objects are very close together.

1.5.1 The OOS problem

The problem of clustered satellites in GEO is further complicated when analyzing proximity flight of very closely-spaced OOS missions (separations of 1 km or less). It is difficult to clearly differentiate satellites during close proximity flight in GEO (see Figure 6 left) because they are so close together. Likewise, their motion cannot be accurately analyzed. Filtered photometry and spectroscopy could possibly identify two satellites very closely-spaced together in GEO however their relative motion is not inferable from spectrometric measurements.

Two closely-spaced satellites in GEO orbit subtend a tiny angle when viewed from the ground. The angular size of interest in the OOS problem is two orders of magnitude smaller than the GEO cluster problem. Two OOS satellites separated by 200-1000 meters when viewed at geostationary ranges (~40,000 km) is comparable to the angular size of Earth's atmospheric turbulence cells which subtend angles between one to four arcseconds (~5-20 μ rad). Obtaining diffraction-limited (resolution set by the aperture of

the telescope) imagery becomes problematic in the face of this turbulence requiring other techniques to be explored.

OOS is a dual-use space technology having both civil space and security space applications. An ability to remotely monitor close proximity OOS flight in GEO can assist space operators in both regimes of use. In situations where a secondary satellite is expected (and desired) to be servicing a client, an ability to independently estimate the servicer's trajectory would benefit satellite operators by validating the servicer's relative orbit against its own internal guidance. From a space security perspective, remotely monitoring activities of an interloping satellite near one's own satellite can help determine the interloping object's intent. Inspecting the relative motion of the servicer about the client, one can infer whether a secondary satellite's motion is intentional (such as complicated rendezvous and fly around maneuvers) or if the object is benignly separating from a satellite (such as shredded space debris).

1.6 Thesis problem statement

New types of OOS space flight activities are beginning to occur in GEO orbit. Remotely monitoring such activities using traditional space surveillance means is becoming increasingly necessary to ensure flight safety, assist flight controllers and to maintain Space Situational Awareness (SSA).

Even though high-performance space surveillance systems can help measure such activities in GEO (see section 1.7.4), a method that can collect observational data using readily available optical telescopes has not been realized. This is a current research gap given the broader availability of small and medium class instruments globally. Optical telescopes with apertures less than 1 meter are more widely available and more affordable to operate than radars or large astronomical observatories. For these reasons, optical telescope technology is the technical path explored in this work.

To begin, this research explores how the presence of a secondary satellite located near a client is detected (the detection problem). Next, an approach to measure the relative position of an un-captivated OOS satellite so that a relative orbit can be estimated is developed. This step is particularly important since tracking—and the ability to monitor and measure the motion of objects—is the building block on which all SSA analysis is

built. Estimating a collision risk between objects or detecting servicing satellite maneuvers cannot occur without first estimating the relative motion between objects.

The goal of this research is to achieve arcsecond-level (equivalent to 200 meters separation distance) precise relative motion measurements between an OOS satellite pair as viewed from the ground. This work focuses on *uncaptivated* relative motion flight where the client and servicer are in proximity to one another but are not docked. In summary, the thesis goals are:

- devise a means to infer the presence of a servicer (secondary) object that is in close proximity to a client satellite in GEO;
- measure an object's position relative to a client satellite by forming differential positional measurements;
- estimate the relative orbit of the object about the client satellite; and
- determine limitations of this observational approach (observability and detectability).

Figure 9 shows the area of regard for close proximity OOS flight in GEO showing the 5 arcsecond (1 km separation at 40,000 km range) angular size projected in the proximity of a client satellite. It is assumed in this dissertation that for satellites separated by more than 1 km that traditional space surveillance techniques can locate and track them.

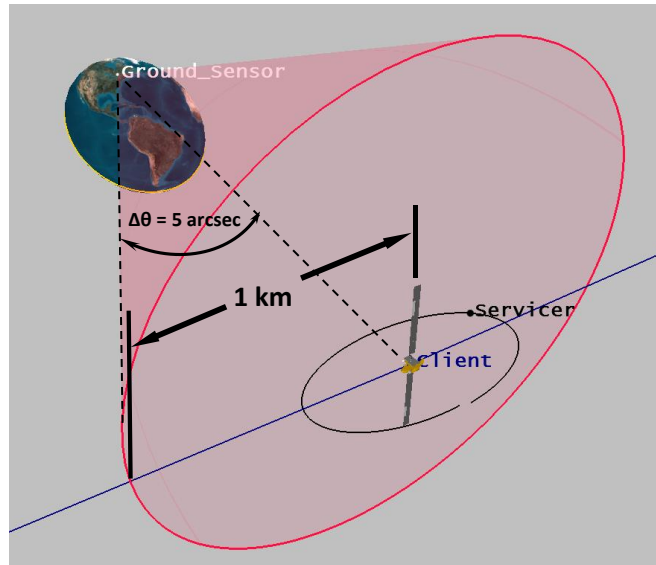


Figure 9: Scale sizes of interest for the proximity of client satellite for OOS monitoring

There is a challenge to overcome. Atmospheric turbulence is a key limitation for ground-based optical telescope resolution. The angular sizes of Earth’s atmospheric turbulence cells are comparable to the angular size of the relative motion between two spacecraft at geostationary ranges. As atmospheric turbulence is random, obtaining astrometric measurements of satellites is difficult in the presence of the blurring effects of turbulence. For this reason, a technical approach that accounts for turbulence is required.

1.6.1 Initial exploration using light curve inversion

In the early stages of this research, photometry (the measurement of the brightness of objects) was explored as a means to address the OOS problem. The appeal of this approach is that light curves, the time history of brightness of orbiting objects, are relatively insensitive to atmospheric turbulence.

The asteroid astronomy community (Ostro [29]) pioneered light-curve inversion to estimate the shape of distant, diffusely reflecting asteroids without directly resolving their surface features. By measuring repeating, periodic, photometric light curves, time-series photometric measurements can be inverted by way of a constrained minimization algorithm that can estimate the surface shape of a distant astronomical body. By

monitoring pulses of light from astronomical objects, it can be inferred that a particular surface facet on the body just rotated into view of the telescope.

Modelling light reflected from a satellite is similar to that reflected from an asteroid. The forward model of a satellite's light curve is expressed as [30]

$$\mathbf{F}'(t) = F_{Sun,i} \left(\frac{1}{O_i} \right)^2 \left(\frac{S_{Norm}}{S_i} \right)^2 \sum_k A_k \langle \hat{\mathbf{n}}_k \cdot \hat{\mathbf{o}}_i \rangle \langle \hat{\mathbf{n}}_k \cdot \hat{\mathbf{s}}_i \rangle \rho_k(\hat{\mathbf{n}}_k, \hat{\mathbf{o}}_i, \hat{\mathbf{s}}_i, \mathbf{p}_{BRDF}) \quad (1.1)$$

where $\mathbf{F}'(t)$ is a vector of range normalized brightness measurements, F_{sun} is the solar flux, $\hat{\mathbf{o}}_i$ and $\hat{\mathbf{s}}_i$ are the observer and sun vectors expressed in the body frame of the object. The subscript k denotes the k^{th} facet on the satellite, ρ_k is the band averaged bidirectional reflectance distribution (BRDF) for each facet normal $\hat{\mathbf{n}}$. The brackets $\langle \rangle$ are Macaulay brackets representing the non-negative operator⁴ [30]. Equation 1.1 ignores the contribution from object self-shadowing. For convex objects this effect can be safely ignored.

Figure 10 shows the facet geometry needed to perform forward modelling of satellite brightness estimation. The reflection vector \mathbf{u} , is the vector describing the direction of the extant ray of light off of the illuminated surface. It is required to calculate the amount of light scattered in the direction of the observer \mathbf{o} to account for the BRDF properties of the surface dA_k .

⁴ The non-negative operator is defined as $\langle x \rangle = x$ if $x \geq 0$ and $\langle x \rangle = 0$ if $x < 0$. The non-negative operator should not be confused with the ensemble average which uses the same notation in the following section

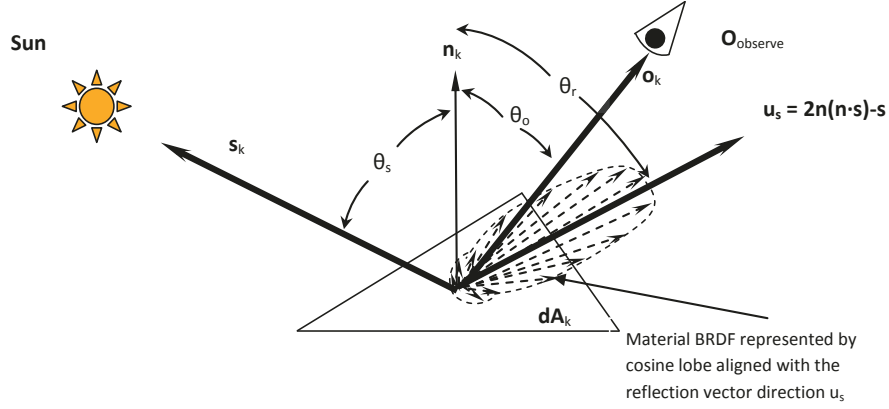


Figure 10: Forward model reflectivity definitions for equation 1.1

Equation 1.1 can be written more compactly for a diffusely reflecting (Lambertian) albedo or a_k where the BRDF is expressed as $\rho_k = a_k/\pi$

$$\mathbf{F}'_i = F_{Sun,i} \left(\frac{1}{O_i}\right)^2 \left(\frac{S_{Norm}}{S_i}\right)^2 \sum_k \left(\frac{a_k A_k}{\pi}\right) \langle \hat{\mathbf{n}}_k \cdot \hat{\mathbf{o}}_i \rangle \langle \hat{\mathbf{n}}_k \cdot \hat{\mathbf{s}}_i \rangle \quad (1.2)$$

$$= \mathbf{A}\mathbf{X}$$

\mathbf{A} is a matrix of bidirectional reflectance distribution functions and \mathbf{X} is a vector consisting of the facet normals $\hat{\mathbf{n}}_k$. Using this form, inversion of the light curve to estimate the shape (facet normal) of the space object can be performed by minimizing the function [31]

$$\chi^2 = \|\mathbf{F}' - \mathbf{A}\mathbf{X}\|^2 \quad (1.3)$$

where \mathbf{F}' is a time series of light curve measurement data. As \mathbf{X} is constrained to be non-negative (albedo-area products are non-zero), gradient descent methods can be used to determine the best-fit facet normals. Application of this approach to satellite shape estimation was first described by Lambert [32] and others [33],[34] using simulations of satellite light curves. These simulations exhibited promising results in the estimation of satellite shape.

For the OOS problem, it was envisaged that this inversion could be extended to include two objects where the attitude (rotational) motion of the servicer is assumed to be

continually slewed toward the client. By making shape and reflectivity assumptions about the satellite pair, synthetic light curves can be generated using the scattering behavior of equation 1.1, albeit modified by an additional secondary satellite. As satellite light curves are strongly influenced by attitude, it was initially believed that a photometric time-history of closely-spaced OOS satellites could be inverted to produce an estimate of the servicer's attitude (assuming the client maintained its nominal nadir-pointing orientation). Tools to estimate the brightness of a client GEO satellite (see Figure 11) based on computer-aided design models and BRDFs of common satellite materials [35] were created and synthetic light curves (see Figure 12) for prismatic client and servicing satellite were generated.

Testing revealed that simulated and OOS object pair light curves did exhibit some skew features (see Figure 12), providing some indication of the servicer's presence in proximity to the client [36]. It was later found that inversion was not promising as several issues hinder its application. First, this approach is heavily reliant on a-priori knowledge of the client's light curve, something which is unlikely to be available. Second, the simplified albedo models used are unreliable since specular highlights are commonly observed in geostationary satellite light curves [37]. Third, the assumption that the servicer is continually trained on the client is unrealistic as in-track station-keeping formation flight is a possibility in GEO orbit. This formation would not likely incur a detectable attitude change. All of these assumptions made this approach impractical and was subsequently abandoned.

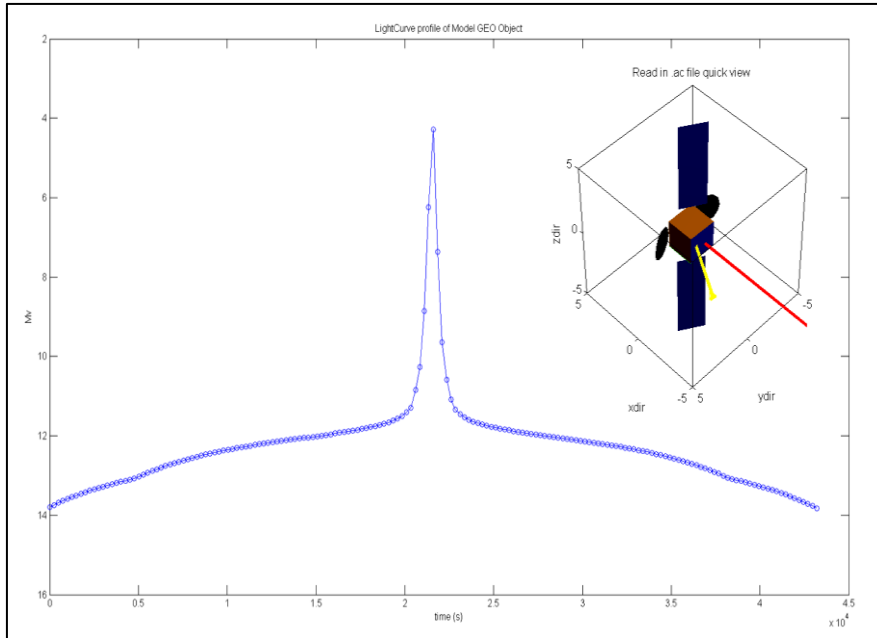


Figure 11: Synthetic light curve output [36]. (Inset): Imported CAD geometry.

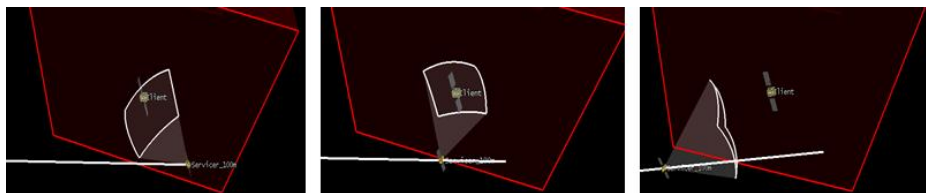
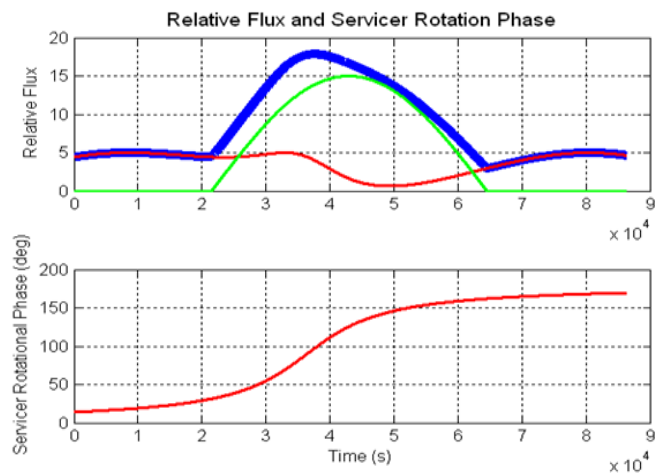


Figure 12: (Top): Combined light curve (blue) for client (green) and servicer (red) for co-elliptic drift relative orbit shown in the bottom frame. (Middle): Rotational phase of the servicer to track the client as it passes. (Bottom): Selected time steps of the servicer's relative motion [36]

1.6.2 Speckle interferometry

Antoine Labeyrie's observation [38] (1970) that short exposure speckle images of astronomical objects preserves the diffraction-limited⁵ characteristics of the astronomical object was a key finding prior to the advent of Adaptive Optics (AO). Labeyrie's algorithm averages a set of Fourier transformed, short-exposure, speckle images that are acquired in a way that preserves the diffraction-limited content in the imagery. The square modulus of these stacks is then taken which form interference fringes for binary (two point source) objects. This approach is sometimes referred to as a single-aperture interferometry [39] where the full aperture of the telescope is used to construct interference fringes on distorted wave fronts of an astronomical object observed through the atmosphere.

An image $i(x,y)$ is the convolution of the atmosphere and point spread function $s(x,y)$ with the astronomical object $o(x,y)$. It can be expressed as

$$i(x,y) = s(x,y) * o(x,y) \quad (1.4)$$

By taking the Fourier transform of equation 1.4 the convolution becomes a product of the spatial frequency content contained in the speckle image

$$I(u,v) = S(u,v) \cdot O(u,v) \quad (1.5)$$

where u,v are the spatial frequency (cycles per frame) of the speckle image.

By stacking the Fourier transforms of the short-exposure images and then taking the square modulus of the complex image information, the ensemble average results in

$$\langle |I(u,v)|^2 \rangle = \langle |S(u,v)|^2 \rangle \cdot |O(u,v)|^2 \quad (1.6)$$

⁵ The diffraction limit is the highest possible resolution of an ideal optical system. The Airy radius $1.22\lambda f/D$ characterizes this resolution for an optical system of aperture diameter D , focal length f and wavelength λ .

In equation 1.6, the symbol $\langle \rangle$ denotes the ensemble average of a series of astronomical images and $| \cdot |$ denotes the modulus of the complex data. For binary star measurements, the division of the speckle image in the spatial frequency plane by the Fourier transform of the telescope and point spread function $|S(u, v)|$ provides an estimate of the Fourier transform of the object $o(x, y)$. This amounts to a spatial high-pass filtering of the speckle image. Figure 13 shows an example of interference fringes formed after transforming a stack of speckle images of a binary star with a 2.9 arcsecond separation.

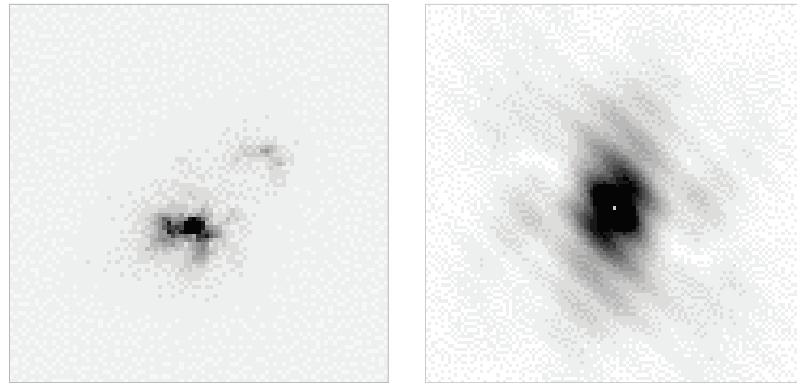


Figure 13: Left: Speckle Image of a double Star. Right: Modulus of Fourier transform showing Fringes of the objects (Image credit: DRDC Ottawa)

The binary star community exploited this approach enabling the measurement of gravitationally bound binary stars⁶ with separations less than the atmospheric seeing disk, allowing large aperture telescopes to take advantage of their full resolution capabilities. Binary star observation is an analogue to the OOS satellite problem as two closely-spaced stars, corrupted by turbulence, are difficult to measure precision angular separations in the face of turbulence. Measurements of the positions of astronomical objects, referred to as astrometry, are used by both the astronomical and the space surveillance community to understand and predict the motions of objects in space.

⁶ The Washington Double Star Catalog [40] is a comprehensive catalog of binary stars maintained by the US Naval Observatory. These stars served as calibration references for this research.

Initial application of speckle imaging required fast film-based acquisition systems or low light video cameras to acquire the short exposure imagery needed to freeze the boiling of the atmosphere. Slow frame-acquisition times coupled with relatively low detector quantum efficiencies limited speckle interferometry's use to larger telescopes and brighter stellar objects. Although the advent of Charged Couple Device (CCD) cameras increased the ability to detect faint objects, long readout times and high read noise of these devices remained a hurdle for most fast-imaging applications.

1.6.3 EMCCDS

In the past decade, high-speed EMCCDs (Electron Multiplied CCDs) or Low Light Level CCDs (L3CCDs) [41] have enabled high temporal resolution astronomy at lower cost with greatly reduced read noise levels. EMCCDs utilize charge amplification gates on the serial register to amplify detected photoelectrons prior to entry to the EMCCD's output amplifier and analog-to-digital register. Charge amplification increases the effective signal-to-noise ratio at the expense of some noise sources (see chapter 4) introduced by the stochastic nature [42] of the charge amplification process.

EMCCDs initially found use as reference star sensors due to their fast readout rates and high sensitivity, making them well-suited to adaptive optics systems. Initially, EMCCDs were only available with small pixel arrays suited for guide star acquisition and phase front measurement. Larger detectors—which operate rapidly and collect frames of up to 1024x1024 pixels at 20 Hz frame rates and higher—are more appealing for space surveillance. They ease the acquisition process required to center satellite targets within a telescope's field of view and enable image stacking for increased detection sensitivity for faint satellites.

EMCCDs are an excellent choice for speckle interferometry since they combine the qualities of a high speed read-out with the ability to sense very faint sources due to their low read noise. EMCCDs have found use in speckle interferometry at large aperture

telescopes (>2m aperture) [43], [44], [45] and for Lucky Imaging⁷ [46]. Moderate sized instruments have also employed them [47] providing precision measurements on astronomical objects with accuracies of 0.05 arcseconds or better. EMCCDs have enabled small aperture systems to play a role in speckle interferometry where high read-noise CCDs previously limited them to bright objects. Examples of measurements obtained via speckle interferometry using 0.5m [45] and even automated 25-cm portable systems [48] where double stars with separations of 1 arcsecond as faint as magnitude 9 were reported.

Scientific grade CMOS—an alternative camera technology—was also considered for use in this research since these cameras feature large pixel arrays, have fast readout rates and low readout noise. EMCCDs tend to be considered a better option since they are better able to detect faint signals, a necessary quality for geostationary satellite detection. For the detection of brighter objects there are few performance differences between EMCCDs and Scientific grade CMOS.

Generally, EMCCDs have limited lifetimes due to the use of high voltages in the serial register to achieve high charge amplification. Their lifetimes are further reduced by imaging brightly lit objects with high EM gains. Care must be taken to prevent illuminating the detector with a bright source when high EM gains are applied.

1.6.4 Other considered technologies: Adaptive optics

Adaptive Optics (AO) systems sense the wavefront distortion of incoming light and perform mechanical deformation of the primary (or secondary) mirror to compensate for the perturbed wavefronts. This correction process allows them to achieve diffraction-limited imagery. AO systems sense wavefront phase distortions by monitoring a reference star (or other object) close to the target astronomical object. There are two primary types of AO systems. The first type is a natural guide star AO where a bright star

⁷ There is a non-zero probability $p(\text{good image}) \approx 5.6 \exp(-0.1557 (\frac{\lambda}{r_0})^2)$ that a telescope acquiring images in a high speed manner observes a diffraction-limited image due to the random nature of atmospheric turbulence. A select set of these best “lucky images” can be extracted and stacked to reproduce a near diffraction limited image. This approach was not pursued in this research due to the likelihood that the objects were faint making centroiding, shifting and stacking problematic. Lucky imaging does hold appeal as there is no ambiguity object created during the stacking process (see section 2.6) and that small aperture systems are more likely to produce good images even though their diffraction limit is large.

is located within 20 arcseconds of the target of interest and is imaged at a high rate to issue corrections to a deformable mirror. The second type is a laser AO where a 589 nm laser produces an artificial star at an altitude of 90 km. This artificial star is used as a conveniently placed reference source [49] for issuing mirror deformations to correct for atmospheric turbulence.

AO systems acquired the first resolved ground-based images of geostationary satellites. The first such resolved set of images were obtained by Worden [50] who resolved large satellite structures using the 6.5 m Multiple Mirror telescope (MMT). Features of ~ 10 meters in size were just detected. Other work [51] examined the use of the large US Air Force AEOS telescope to perform imaging of GEOs with microsatellite-class objects in close proximity. Drummond [52] acquired images of the GE-23 satellite using the 10-m Keck telescope resolving major features such as bus, solar arrays and antenna reflectors (see Figure 14). It was found that imagery acquired from these systems benefited from post processing using Multi-Frame Blind Deconvolution (MFBD) to further refine the AO imagery to resolve major satellite features.

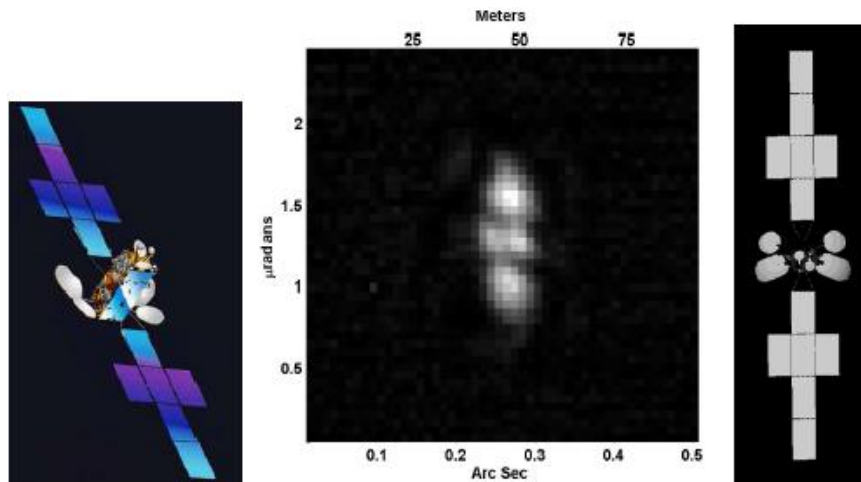


Figure 14 *Left: GE-23 geostationary satellite. Center: De-convolved ground based image of GE-23, Right: Approximate model of GE-23 in detected orientation (Image credit reference [52])*

Images such as Figure 14 are rare since large telescopes—such as the Keck—are not readily available to the space surveillance community. While direct satellite imaging

would certainly satisfy OOS monitoring needs, its application for real-time processing, and the lack of such large aperture telescopes, makes their use relatively unlikely. As the characteristic width of a GEO satellite solar panel is ~2 meters wide, a telescope with an aperture greater than 15 meters would be required to resolve this detail making direct imaging problematic to implement. Alternative approaches are being explored and is an active area of research. Sparse aperture interferometers are believed to hold promise to resolve fine scale detail in GEO using multiple small aperture telescopes configured as optical interferometers. DARPA has been exploring the development of proof of concept systems in this area [53].

For satellite tracking, AO systems that incorporate natural guide stars are impractical. Due to the high angular velocity of an Earth orbiting satellite with respect to the celestial sphere, it is unlikely that a satellite and a bright reference star will reside within a 20 arcsecond radius for an appreciable length of time. This makes Laser AO the preferred technique. AO systems are also expensive, complicated and hard to access since they are typically installed at the largest astronomical observatories [49] to take advantage of the resolving power of their large apertures. Due to the complexity, expense and accessibility of AO systems they were not considered for this research.

1.6.5 Other considered technologies: Space surveillance radars

Powerful space surveillance radars such as the Eglin [15] and Millstone Hill [16] radars provide all-weather, uninterrupted surveillance of deep space—a unique capability that helps address the OOS problem. These systems were not considered for use in this dissertation because of their cost and lack of availability (rarity).

Ranging radars are capable of providing resolution of the relative radial position. This research found that differential angles-only (plane of sky) measurements exhibit a shortcoming in that approximately three hours of observations are required for a relative orbit to converge on an estimate of the radial position error. This is due to a radial position observability issue (which is correctable) however large observation times are required. Differential ranging measurements added to a relative orbit estimation process could increase the observability of an OOS satellite pair. This could help converge a relative orbit solution much more quickly.

1.6.6 Other considered technologies: Space based measurements

Another solution to observe OOS is to place an in-situ space surveillance sensor in close proximity to the satellites performing OOS. Such a platform could perform relative measurements using an optical camera without the issues of turbulence or detectability. This approach was discounted as the expense and lead-time to develop an in-situ space-based mission would be unfeasible.

Relative orbit estimation from one satellite to another using angles-only (optical) data can be hindered by observability issues since the lack of range information does not provide a unique solution for estimating the relative orbit. Woffinden [54] found that relative orbit estimation from a space-based observer using angles-only information for one of the two OOS satellites was unobservable using the Linearized relative orbit equations. This problem indicated that a calibrated maneuver needs to be performed to observe relative orbits more easily.

This observability problem is not an issue if an alternate orbital reference system is used. Tombasco [55] developed a relative GEO element batch-estimator hybrid coordinate approach which was not limited by the type of restrictions mentioned above and it maintained the ability to observe objects in orbit. Two OOS satellites can be observed by a third/tertiary party as long as special techniques are used with the optical measurements.

1.7 Thesis layout and section overview

This thesis begins with an introduction to basic phenomenology of atmospheric turbulence, speckle imaging, the mathematical foundations of the cross-spectrum, and optical satellite observation. The adaptation of cross-spectrum observational technique to the closely-spaced satellite problem is then described by adapting celestial and telescope coordinate frames and by identifying a GEO relative motion model using solar-radiation-pressure adjusted Clohessy-Wiltshire [56] equations of motion. An observational approach is also described using small and medium aperture telescopes. A description of differential angles measurements, or “metric observations” [57] used to indirectly

measure the position and velocity of an orbiting object is also developed. A description of a general speckle instrument and image processing approach is described.

A key contribution of this work are experimental results using the 1.6-m Mont-Mégantic telescope [58] to observe co-located geostationary satellites acting as OOS proxy objects. These results provide great insight into the operational needs for image processing and data collection for such an instrument. Relative orbit estimation was performed and the findings are presented in chapter 5.

Some notable limitations were encountered with the cross-spectrum speckle interferometry method as adapted for satellite observation. The observational approach works usually with a limited angular radius (~ 5 arcseconds) from the client satellite. It requires steady seeing conditions better than 3.5 arcseconds for precise astrometry. It was also found that the differential angle measurements, produced by cross-spectrum speckle interferometry, provokes observability issues in the relative orbit determination—especially in the radial position between two closely-spaced objects. Speckle interferometry was also found to be limited in the range of relative brightness (relative size) of the objects in the OOS pair where the smallest counterpart satellite could be no fainter than $\Delta m = \sim 2.5$ magnitudes, or a relative size ratio of approximately $1/10$ as large as the client satellite. For a fully-equipped servicing satellite with a large bus and solar arrays to support robotic servicing, this may be a reasonable⁸ detection limitation. However, this relative size limitation is not likely permit the detection of microsattellites ($< 1 \text{ m}^2$) in close proximity to the client satellite in GEO. Their brightness in GEO (magnitude 16 and fainter) is not expected to be sufficient for detection in contrast to a bright GEO satellite of characteristic magnitude varying from 9-12.

Detectability is a concern since the short exposure approach used to produce speckle images is photon-starved for faint OOS satellite pairs. A treatment of this effect is also described in the signal-to-noise modelling portion of this thesis.

⁸ The Orbital Express ASTRO servicer had deployed dimensions of $\sim 10 \text{ m}^2$ [59]. At GEO ranges ASTRO would reach an equivalent magnitude of approximately $M_v \sim 11$ which is consistent with the detection range for speckle interferometry. Many GEO satellites have magnitudes between 10-12th magnitude indicating that detection of a robotic servicer of ASTRO's size in GEO is not unrealistic.

1.8 Literature overview: Satellite speckle interferometry

The first application of speckle interferometry for space surveillance was envisaged to assist in direct satellite imaging. The first such attempt was by Worden [60] who first attempted autocorrelation based images on a large Molniya satellite. Indications of larger structures on the object were obtained. Theoretical studies by Beavers [61] and experimental work by Lawrence [62] showed significant progress in the pursuit to image satellites using ground based sensors without AO. Lawrence obtained impressive images of the Hubble Space Telescope where solar panels, main body structure and satellite shape were resolved by use of bispectrum [62] methods.

Some related, and very compelling work in the tracking of a moving solar system object using speckle interferometry was performed by Knox [63] whose results were an inspiration for this research. Knox measured the astrometric motion of Pluto with respect to a background occultation star using the 3.67 m Advanced Electro-Optical System (AEOS) telescope [64]. Remarkable astrometric angular precision was achieved (~ 0.003 arcseconds) in measurement of the distance that Pluto *missed* the background star⁹. While the miss was a loss for astronomers who were attempting to measure the density of Pluto's atmosphere [63], this work showed that speckle interferometry could be applied to moving objects, defeating atmospheric turbulence, and that simple motion models could achieve remarkable astrometric precision using differential angles measured from speckle interferometry. The application to satellite tracking, especially the OOS case, was very promising.

Despite these successes, the application of speckle interferometry to measure the relative positions of moving, closely-spaced satellites in GEO does not appear in the literature. This research abandons a goal of resolving physical features of the closely-spaced satellites using speckle interferometry since only the largest observatories have shown the resolution necessary to accomplish this (such as the examples in [50]-[52]). This research does aim to preserve the relative position information of two objects contained within a speckle image while accommodating the blurring nature of

⁹ It was later confirmed that the Pluto-Charon center of mass actually traversed the occultation star [63]

atmospheric turbulence. This work has not been performed previously and is a new contribution to the area of space surveillance.

1.9 Literature review: Differential angles for relative orbit estimation

Soop [12] and Montenbruck [66] provided a detailed measurement approach for orbit determination of a geosynchronous satellite about its nominal longitude using Hill's equations of motion. In this case, the relative orbit of the satellite would be around a fictitious, ideal, satellite placed exactly at its nominal longitude at zero inclination. They show that a single ground station is unable to produce accurate orbits for geostationary satellites using angles-only measurements since there are fewer measurement equations than the number of state variables required to estimate the orbit. The addition of measurements from another geographically separated ground station, or by incorporating ranging data, can resolve this lack of observability where the measurements are not fully able to estimate the orbit of the satellite.

In contrast to the measurement of a single GEO satellite about its nominal station keeping location, the relative orbit of two satellites about one another using differential angles is shown to be observable. Kawase [67] [68] used differential angular measurements on cooperative co-located geostationary satellites to estimate their relative orbit using Hill's equations and differential azimuth and elevation measurements. This was a *cooperative* case where the two satellites involved in the close proximity flight beacon their positions to a ground station radio antenna. It was found that relative orbits accurate to 200 meters were possible with a differential angle measurement noise of 0.3 millidegrees (1.1 arcsecond) and for several days of tracking data. For a true OOS servicing case, it not expected that either the servicer or the client satellite cooperatively beacons a ground station in this way, however, the relative orbit estimation findings from Kawase were promising. Another study by Sawada and Kawase [69] examined differential angles measured from an optical telescope but did not examine the specific case of very closely- spaced satellites nor was the observability condition examined.

In contrast to Soop's work, Kawasse demonstrated [68] that the relative orbit of two clustered satellites in GEO are observable by developing partial derivatives of the Hill's equations and showing that they are mutually independent. Furthermore, Kawasse

computed mean estimates for the error in the separation, relative drift rate and periodic error in the satellite's relative motion.

Following on the cluster resolution problem mentioned in section 1.5, Sabol [70][71] used small telescopes to test the prediction accuracy of the COWPOKE (Cluster Orbits With Perturbations of Keplerian Elements) propagation routine which acted as a replacement for the Hill's equations of relative motion. COWPOKE is designed to accommodate relative orbits of objects with non-circular orbits (eccentricities > 0) by taking advantage of a curvilinear coordinate system to estimate relative orbits. Good results were achieved with optical measurements ($\sim 200\text{m}$ accuracy) of GEO satellites despite the coarse initialization approach using general perturbation orbital elements to initialize the relative orbit determination. COWPOKE was also found to better produce relative orbit estimates in both right ascension and declination in comparison to TLEs which could assist in the cross-tagging process by using orbital data only.

All of these above-mentioned studies focused on estimating the relative motion of clustered and co-located satellites in GEO with the primary aim to: a) generate precise orbit data to maintain station-keeping; and b) generate relative orbit data to fix the cross-tagging problem encountered at many space surveillance telescopes. In all of this work, the relative separation distance between objects was not the primary consideration as it was expected that objects would be separated by tens of kilometers or more. The effect of turbulence or refraction on a sensor's ability to measure motion in the case of very closely-spaced operations of two satellites in GEO was not a primary consideration in these works.

In contrast, this research contributes to the field of space surveillance by analyzing the problem inherent in the collection of observation data with respect to non-cooperative, closely-located satellites in GEO from the standpoint of sensor detection and relative orbit estimation.

1.10 Definitions and conventions for the client and servicer

Throughout this thesis the naming convention for the client and servicing satellite adheres to the brightness convention used by binary star community. The "primary" (client) satellite is defined as the brighter of the two objects as it is anticipated that the

“secondary” (servicing) satellite is likely to be smaller (therefore less reflective) than a large geostationary communications satellite (the client).

The brightness ratio (α_b) is the ratio of flux of the secondary object (f_2) to the primary object (f_1). Using the respective object magnitudes ($\Delta m = m_2 - m_1$), α_b is expressed as

$$\alpha_b = \frac{f_2}{f_1} = 10^{-0.4(m_2 - m_1)} \quad (1.7)$$

In cases where the servicer would be brighter than client satellite the relative position vector would be reversed after relative orbit estimation is performed.

When specifying the brightness characteristics of a tracked pair of satellites, the primary’s magnitude is then followed by Δm to indicate the brightness of the secondary relative to the primary. For instance, $m_1 = 10.7$, $\Delta m = 1.2$ indicates the primary satellite is magnitude 10.7 and the secondary is magnitude 11.9.

1.11 Chapter summary and contributions

Future OOS missions enabled by advances in autonomous space robotics and proximity flight could become a reality in the near future. Such missions in geostationary orbit offer new possibilities for satellite operators to extend the life of geostationary satellites designed to accommodate OOS servicing, to correct operational anomalies such as failed antenna deployments, or reduce the rate of space debris generation.

OOS missions in geostationary orbit creates a new tracking problem for space surveillance sensors as proximity flight between satellites with separation distances less than one kilometer has not been addressed. Tracking the relative position and motion of objects in close proximity is difficult with traditional space surveillance sensors making collision risk estimation and situational awareness problematic.

This chapter identified prior art in the areas of high resolution satellite imaging and relative orbit determination. While much work on relative orbit estimation using both optical and radio interferometric systems has been performed, these studies did not examine the specific case of proximity flight with separations less than one kilometer in

GEO. Great strides are being made in high resolution satellite imaging of objects in GEO orbit with a view toward microsatellite detection in proximity to large GEO satellites. While these works are promising and offer possibilities to detect very small objects, they require large astronomical observatories using adaptive optics approaches, or complex, sparse aperture systems to perform orbit estimation. These systems are complex and not readily available for general space surveillance usage.

A key barrier to high resolution astrometry of OOS satellites is atmospheric turbulence as turbulence cells are comparable in angular size to the separations between the objects being tracked. Initial attempts to address this problem using photometric inversion means were unproductive as this approach was too heavily reliant on assumptions. This approach was subsequently abandoned.

Speckle interferometry, using a cross-spectrum approach, was adopted for this research. It has been producing promising results insofar as the technique: 1) has the ability to track closely-spaced satellites in GEO; 2) are computationally efficient; and 3) can be adapted to small and moderate-sized telescopes making sensor availability a possibility. This research describes how speckle-interferometry can be adapted and used to remedy this OOS problem—a solution that contributes to the burgeoning field of Space Situational Awareness.

Chapter 2: Atmospheric turbulence and speckle interferometry

The optical detection of closely-spaced objects in geosynchronous orbit must overcome atmospheric turbulence in order to measure their close-proximity motion. The following is a précis of key atmospheric turbulence¹⁰ and other effects which influence the ability of space surveillance telescope to perform high precision relative astrometry while viewing astronomical sources through Earth's atmosphere. An overview of speckle interferometry is provided with a view toward performing space surveillance tracking of satellites using a technique originally conceived for binary star astronomy.

2.1 Atmospheric turbulence

The altitude dependent inhomogeneity of temperature, pressure, humidity and wind speed in Earth's atmosphere result in turbulence cells which refract rays of light from astronomical sources. The refractive index of air is a function of temperature, pressure and humidity, all of which influence the density of the media in which light transmits. The refraction of dry air n_s for a standard pressure of p_s of 1013.25×10^2 Pa and temperature T_s of 288.15 K is expressed [73] and detailed at length in [74] as

$$(n_s - 1) \times 10^6 = 64.328 + \frac{29498.1 \times 10^{-6}}{146 \times 10^{-6} - \sigma^2} + \frac{255.4 \times 10^{-6}}{41 \times 10^{-6} - \sigma^2} \quad (2.1)$$

where $\sigma = \lambda^{-1}$ where λ is the vacuum wavelength in nm. For other temperatures and pressures, equation 2.1 is adjusted by

$$n - 1 = (pT_s/p_sT)(n_s - 1) \quad (2.2)$$

¹⁰ An excellent description of optical and meteorological aspects of astronomical seeing is described by Coulman [72]

And the expression for the partial pressure of water vapor p_w in the air reduces the index of refraction by

$$43.49[1 - 7.956 \times 10^3 \sigma^2] \frac{p_w}{p_s} \quad (2.3)$$

Modelling energy variations of the turbulence of Earth's atmosphere is based on Kolmogorov's [75] turbulence models. Phase fluctuations of a turbulent field can be described in terms of the structure function

$$D_T(r) = \langle \Delta T(s+r) - \Delta T(s) \rangle \quad (2.4)$$

where T is the temperature, s is the line of sight distance and r is an arbitrary distance along that line of sight. The structure function is the measure of mean temperature deviation of along the line of sight. Kolmogorov turbulence for an isotropic turbulent field is shown to be proportional to $r^{2/3}$.

It can be shown [76] that temperature deviations influence the index of refraction n such that the structure function can be recast as equation 2.5 where C_n is the refractive index structure coefficient

$$D_n(r) = C_n^2 r^{\frac{2}{3}} \quad (2.5)$$

Fried [77] parameterized the phase structure function as

$$D_\phi(r) = 6.88 \left(\frac{r}{r_0} \right)^{5/3} \quad (2.6)$$

where r_0 is the Fried parameter or "coherence length" of the turbulence cell and the quantity 6.88 is an experimentally determined value set to equal a phase distortion of 1 radian. If the vertical profile of the refractive index distortions is known, then r_0 is defined as

$$r_0 = 0.185\lambda^{\frac{6}{5}}\cos^{\frac{3}{5}}(\xi) \left[\int C_n^2(z)dz \right]^{-3/5} \quad (2.7)$$

where ξ is the zenith angle (90-elevation angle) and h is the height above the ground. The Fried parameter is a measure of the equivalent atmospheric aperture where there is less than one radian of phase aberration incurred due to refractive distortion. The scale size of r_0 is approximately 10 cm in the visible band (~ 550 nm) and scales proportionally as $\lambda^{6/5}$ for different observation wavelengths. Larger values of r_0 indicate that the atmosphere is less turbulent and permits steadier observing conditions for a ground-based telescope.

Equation 2.7 indicates that the value of r_0 becomes smaller when turbulence increases (C_n^2 becomes large). The size of r_0 increases at longer wavelengths making them more favorable for use in speckle interferometry. There is also elevation (zenith angle) dependence where observations collected low on the horizon observe smaller r_0 due to the projection effect that occurs when looking through a thicker turbulence layer, increasing the number of atmospheric distortions observed. For satellite tracking applications, this limits the observable portion of sky for speckle interferometry as zenith angles of 60 degrees (30 degrees elevation) effectively decreases to $0.3 r_0$.

An example of a vertical profile of C_n^2 is shown in Figure 15. In this example, it is apparent that the majority of the refractive turbulence is resident near the ground layer where the C_n^2 profile approaches 10^{-15} . At higher altitudes, C_n^2 relaxes to less than 10^{-17} where steadier atmospheric fluid flow conditions prevail. In cases where high altitude winds contain most of the turbulence above the ground layer, the atmospheric properties at the 200 mbar ($z=12$ km) level are used to estimate r_0 . As most of the refractive turbulence is contained in the ground layer, it is common for many low altitude observatories to use the local surface weather conditions to estimate r_0 (see next section)

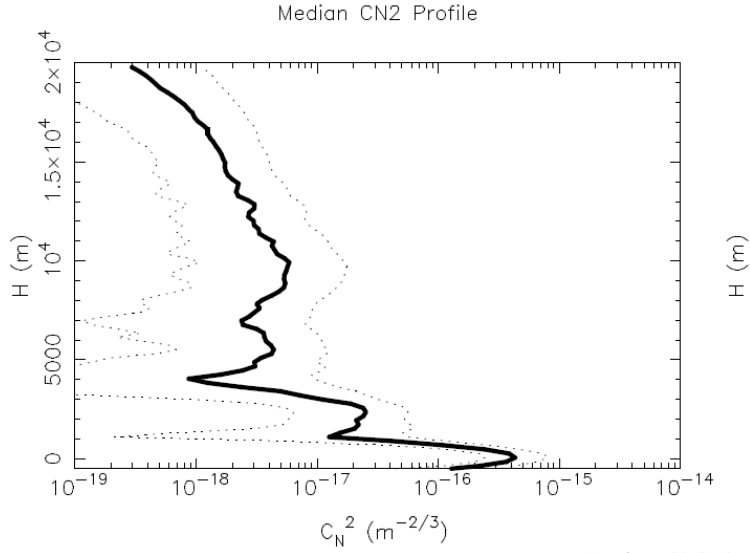


Figure 15: Vertical Turbulence distribution as a function of altitude for the Mount Graham observatory (Image credit reference [78])

A telescope’s diffraction limit is approximated by the Airy radius ($1.22\lambda/D$) where D is the aperture diameter of the telescope. Telescopes with an aperture D —which is smaller than r_0 —are limited to the Airy the telescope’s diffraction limit. In contrast, a telescope aperture much larger than r_0 can theoretically resolve much finer details on the astronomical object even-though it is limited to the atmospheric resolution aperture r_0 . In this case, the large light-gathering power of the instrument is preserved even while its ability to resolve fine scale detail is reduced due to the effects of the atmosphere.

Astronomical “seeing” is a commonly used term which describes the condition of the atmosphere for astronomical observing. Seeing is characterized by both r_0 and the observable wavelength of light.

$$\epsilon_{\text{seeing}} \approx 0.98 \frac{\lambda}{r_0} \quad (2.8)$$

In equation 2.8 ϵ_{seeing} is the size of the seeing disk of the atmosphere (radians) and is approximately a full width half maximum of a Gaussian function that describes the width of the atmospheric point spread function. Figure 16 shows a long-exposure binary star pair where atmospheric seeing has blurred the width of these stars beyond the diffraction limit of the telescope.

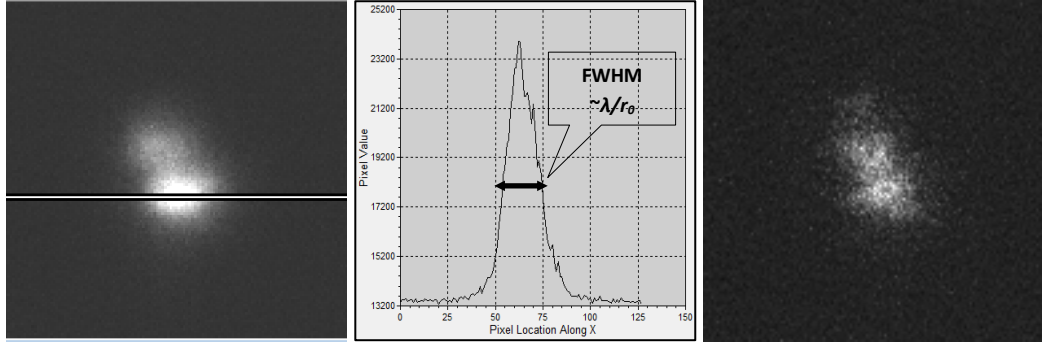


Figure 16: (Left) Long exposure profile of binary star. (Center) Profile exhibiting seeing width of the atmospheric point spread function. (Right) Speckle pattern from short exposure image.

2.2 Temporal nature of atmospheric turbulence

Seeing distortions (described previously) are not static—they rapidly change in time as turbulence cells move in front of a telescope’s aperture. The coherence time τ_0 parameterizes this timescale and is the time which a turbulence cell has a phase distortion less than 1 radian. This can be approximated by

$$\tau_0 = 0.31 \frac{r_0}{V_0} \quad (2.9)$$

where V_0 is the surface wind speed or the wind speed at the 200 mbar (20 kPa) level. The coherence time for a 5 km/hr surface wind with a seeing r_0 of 10 cm is approximately 22 milliseconds. Turbulence cells appear and disappear on this timescale for astronomical objects imaged with a ground based telescope. At some astronomical observatories experimental estimates of τ_0 (e.g. Lawrence [62]) reported coherence times of 1-2 milliseconds. While the precise value of τ_0 depends on the Fried parameter and wind speed, both techniques indicate that τ_0 varies on the scale of 1-10 milliseconds. This sets the required timescale of the imaging camera’s exposure needed to freeze the turbulence of Earth’s atmosphere.

Coherence time is used to set a camera’s optimal exposure time to increase the signal-to-noise ratio for speckle imaging. The integrating effect of a finite exposure time on short duration speckles blurs the fine-scale diffraction limited detail contained within a speckle image. Short exposure images capture fine-scale detail at the expense of a loss of signal-to-noise ratio. Long exposure images collect more photons and smooths fine-scale

detail by way of an averaging effect in the camera's exposure. In practice 10-20 millisecond images are usually acquired when performing speckle imaging of astronomical sources.

Figure 17 shows an example of varied exposure time impacting the ability to detect fine detail in speckle imagery. The first image is a short exposure (5 ms) capturing diffraction limited detail in the speckles where the binary object is just detectable. The medium-length exposure image (20 ms) shows more signal photons, but a blurring effect starts to appear. The long exposure (1000 ms) image incurs the full blurring effect of Earth's atmosphere. For exposure time $T_{exp} \gg \tau_0$, the smallest resolution detail is limited to the atmospheric point spread function of width ϵ . The fine scale speckle details are lost when the exposure time is much longer than the coherence time.

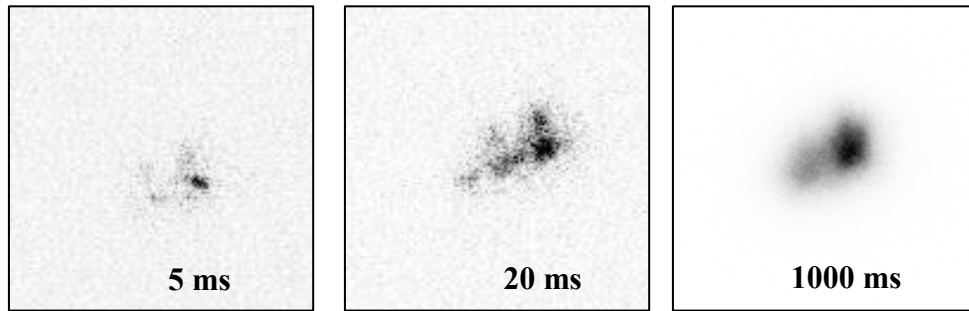


Figure 17: Selected frames of various exposure lengths showing changes in speckle behavior

2.3 Number of speckles

Turbulence cells within a perturbed atmospheric layer above the telescope creates a number of speckles that are proportional to the telescope aperture diameter divided by Fried parameter r_0 , such that

$$N_{speckles} \approx \left(\frac{D}{r_0}\right)^2 \quad (2.10)$$

A sketch of the formation of speckles on a detector is shown in Figure 18. It is apparent in equation 2.10 that smaller aperture D will exhibit fewer speckles for a given r_0 . The ratio D/r_0 (and its inverse) is used frequently in speckle interferometry. It is a key parameter for estimating the resolution behaviour of a telescope in the face of turbulence.

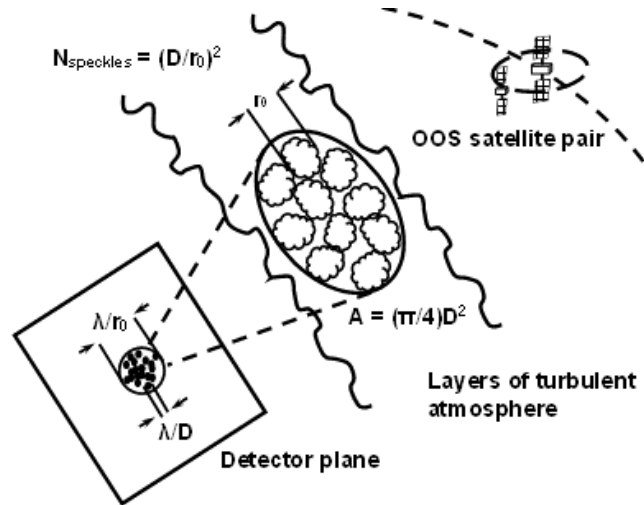


Figure 18: Atmospheric seeing cells of size r_0 forming speckles on the detector plane. Speckles are of size λ/D . The seeing disk is of size λ/r_0 .

2.4 Isoplanatic angle

Patterns of speckles that are produced by atmospheric turbulence will be repetitive over a small solid angle referred to as the *isoplanatic angle*. This angle is the limit where a phase aberration from a refractive turbulent medium has less than 1 radian of phase shift. This effect causes speckles to exhibit repeating patterns in a short exposure image. The isoplanatic angle is a necessary physical phenomenology for speckle interferometry as speckle patterns must be correlated in order for fringes to form and for autocorrelations to be computed (see section 2.6).

The isoplanatic angle can be conceptually visualized in Figure 19 where a distorting turbulence layer with cells of size r_0 is viewed by a telescope. The isoplanatic angle is the small angle subtended by the turbulence cell r_0 divided by the distance to the turbulence layer. The isoplanatic angle is a function of the seeing cell size r_0 and the distance to the characteristic turbulence layer at an altitude h above the observer.

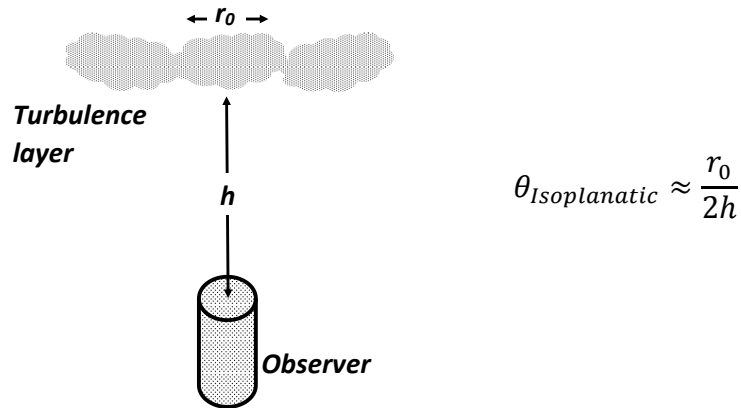


Figure 19: Simplified model of the isoplanatic angle.

Speckles from an astronomical source viewed through the turbulence cell r_0 exhibit a duplicative pattern. Figure 20 shows the duplicative behavior of a speckle image which replicates the pattern an ideal (undistorted) object due to the random phase variations.

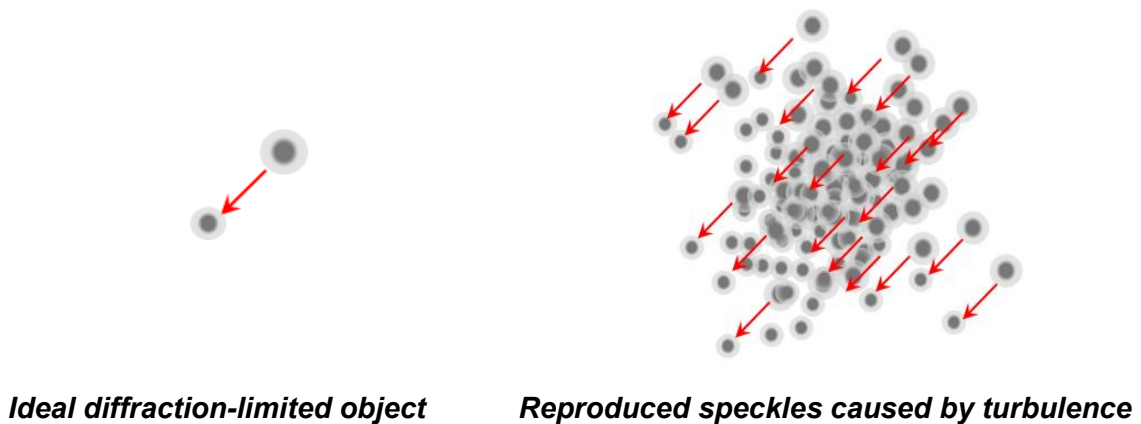


Figure 20: (Left): Example of ideal diffraction limited object. (Right): Example of speckle object where the ideal object is duplicated over the seeing disk

Figure 21 shows imagery collected on a bright binary star of 4.4 arcseconds separation which exhibits the duplicative nature of the atmospherically induced speckles when the objects are within the isoplanatic angle. Note that the speckle pattern observed in the brighter star is largely reproduced in the fainter star in the lower right of the frame.

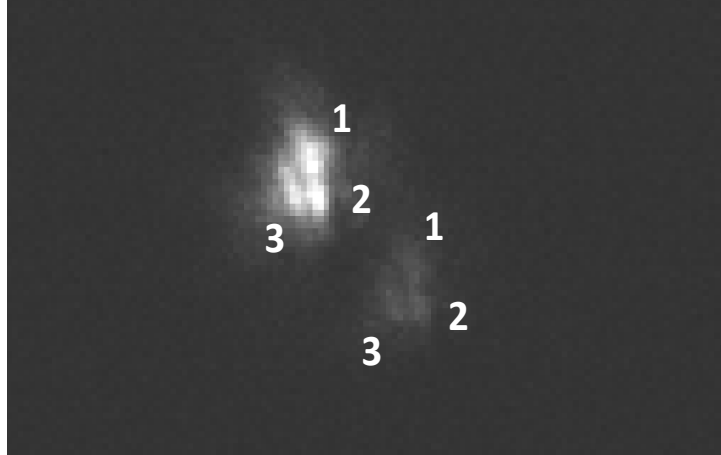


Figure 21: (Left) Bright binary STF 738AB showing speckle duplication

There is some debate regarding the size of the isoplanatic angle. This discrepancy is understandable given the fact that the size of the isoplanatic angle changes with respect to the altitude of the seeing layer. Roddier's analysis [79] examined the needs of speckle interferometry to determine the characteristic size of the isoplanatic angle. This work indicated that the angle is between 1-4 arcseconds and that others found that the angle can be as high as 6 arcseconds.

Experiments conducted on binary stars using a small aperture telescope found that speckle measurements could reliably produce autocorrelations with separations up to 5 arcseconds. This angular size is approximately 1 km in GEO orbit and is a good match between the close proximity flight cases for OOS versus the larger separations of several kilometers. This was set as the upper limit for the isoplanatic angle of for satellite speckle interferometry¹¹.

The isoplanatic angle can be estimated from knowledge of the C_n^2 profile by computing

$$\theta_{Isoplanatic} \approx 0.314 \cos(\xi) \frac{r_0}{\bar{h}} \quad (2.11)$$

¹¹ Objects separated further than 1 km radially in GEO could experience relative drift rates which would separate the objects considerably after a fraction of an orbital revolution. As such, these objects would meet the isoplanatic limit for only short periods of time in order to collect speckle measurements.

where

$$\bar{h} = \left[\frac{\int c_n^2(Z) |V(z)|^{5/3} dz}{\int c_n^2(Z) dz} \right]^{3/5} \quad (2.12)$$

\bar{h} is the altitude of the weighted average altitude of the seeing layer, ξ is the zenith angle (90°-elevation angle), V is the wind velocity profile and z is the vertical profile height. The zenith angle dependence will affect how this approach is used to track satellites at lower elevations since the isoplanatic angle will shrink by 50% for elevation angles of ~30 degrees. This limits speckle interferometry's use for general space surveillance since most space surveillance telescopes perform routine orbital tracking to elevation angles of 20 degrees. Speckle interferometry, which has additional atmospheric visibility limitations imposed requires zenith angles somewhat higher than that employed at typical space surveillance observatories.

2.5 Spatial frequency characteristics of a telescope and atmosphere

A telescope not only gathers and focuses light onto a detector plane, but also acts as a spatial frequency filter. The diffraction limit of telescope λ/D and the Airy radius $1.22\lambda/D$ are considered the highest degree of resolution possible with an unaberrated, clear-aperture telescope. For speckle imaging the spatial frequency information is usually of interest as the measurement of fringes, and other fine scale detail, is usually performed in the spatial-frequency domain rather than the spatial domain.

The spatial frequency u_n normalizes the spatial frequencies with respect to the diffraction limit λ/D . The normalized spatial frequency is defined as

$$u_n = \frac{f}{f_{\text{Diffraction Limit}}} = \frac{f}{D/\lambda} \quad (2.13)$$

The spatial frequency f is generally expressed in cycles/frame. To obtain the spatial frequency in cycles per frame, the number of pixels N is divided by the object distance d or $f(\text{cycles/frame}) = N (\text{pixels/frame}) / d (\text{pixels/cycle})$.

2.5.1 Diffraction limited transfer function

If the Airy function of a telescope diffraction pattern is Fourier transformed the Modulation Transfer Function (MTF) is produced. The MTF (see Figure 22) indicates the amount of transmission that various spatial frequencies will pass through a telescope aperture. It also indicates the relative strength of their attenuation or transmission. For an unaberrated (not optically flawed) circular aperture, the diffraction limited MTF (τ_{DL}) is expressed as

$$\tau_{DL} = \frac{2}{\pi} \{ \cos^{-1}(u_n) - u_n(1 - u_n^2)^{1/2} \} \quad (2.14)$$

Figure 22 shows a plot of τ_{DL} versus normalized spatial frequency u . The diagram shows that lower frequency content (wider separations in the spatial plane) are largely passed by a telescope ($u = 0 \dots 0.95$). A steep fall-off in a telescope's ability to pass higher spatial frequency information appears at the diffraction ($u_n \approx 1$). The ability of the telescope to pass high spatial frequency content is highly attenuated near the diffraction limit.

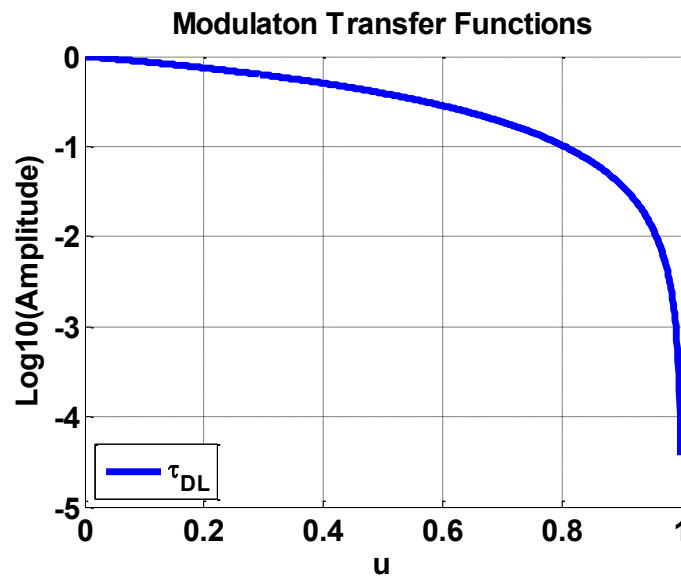


Figure 22: Diffraction Limited MTF for normalized spatial frequency u_n

2.5.2 Labeyrie-Korff transfer function

The Labeyrie-Korff transfer function [80] τ_{LK} is a model that describes the combined atmospheric and telescope spatial frequency transfer when subjected to turbulence (parameterized by r_0). The Labeyrie-Korff transfer function is composed of two parts: 1) a low frequency component that describes the seeing disk due to long-exposure characteristics of the telescope and 2) a high frequency component describing the transmission of high spatial frequency content which is needed for speckle interferometry.

The expression for the Labeyrie-Korff transfer function is:

$$\begin{aligned} \langle |\tau_{LK}(\mathbf{u}_n)|^2 \rangle \approx & \tau_{DL}^2(\mathbf{u}_n) e^{\left[-6.88 \left(\frac{D}{r_0} |\mathbf{u}_n| \right)^{\frac{5}{3}} \left(1 - |\mathbf{u}_n|^{\frac{1}{3}} \right) \right]} \\ & + \tau_{DL}(\mathbf{u}_n) \left(\frac{r_0}{D} \right)^2 \left[0.435 + 0.278 \left(\frac{D}{r_0} |\mathbf{u}_n| \right)^{-\frac{1}{3}} \right] \end{aligned} \quad (2.15)$$

where \mathbf{u}_n is the vector form of the spatial frequency content and can be considered as a one dimensional equivalent to u in this section. The first term in 2.15 describes the low spatial frequency transmission of a telescope. The second term models the higher spatial frequency transmission. Both components and their sum are plotted on Figure 23 for $r_0 = 10$ cm and $D = 1.6$ m.

The **low frequency** τ_{LF} component of equation 2.15 models long exposure image ($T_{exp} \gg \tau_0$) frequency transfer of the atmosphere and telescope and has a cutoff near $\sim u_n = 0.22$. The bulk of the transmission occurs at spatial frequencies less than this cutoff. During long exposure images the high frequency wing of Figure 23 collapses and follows the plot of τ_{LF} when the exposure times are much greater than the coherence time of the atmosphere.

The **high frequency portion** τ_{HF} preserves the short exposure ($T_{exp} \approx \tau_0$) spatial frequency content necessary for speckle interferometry to be performed. While the broad wing of τ_{HF} is approximately one-thousand times smaller than the transmission of τ_{LF} the spatial frequency transmission is nonzero. This high frequency wing of the Labeyrie

Korff transfer function is the spatial frequency regime in which speckle interferometry is performed. This region is between the seeing cutoff and the diffraction limit.

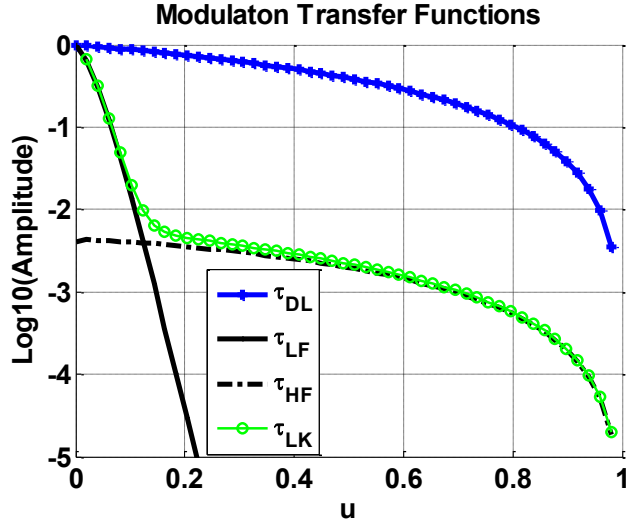


Figure 23: Diffraction Limited (τ_{DL}), Low Frequency (τ_{LF}), High-Frequency τ_{HF} and combined Labeyrie Korff transfer function τ_{LK}

When performing space surveillance of closely-spaced satellite objects ($u_n > r_0/D$) and when working with short exposures ($T_{exp} \approx \tau_0$), the second term of τ_{HF} in equation 2.15 with the coefficient 0.278 can be neglected. This simplifies the high frequency component to

$$\langle |\tau_{LK}(\mathbf{u}_n)|^2 \rangle \approx \langle |\tau_{HF}|^2 \rangle \approx \tau_{DL}(\mathbf{u}_n) \left[0.435 \left(\frac{r_0}{D} \right)^2 \right] \quad u_n > r_0/D \quad (2.16)$$

Expression 2.16 can be used to model the high frequency transfer function of spatial frequencies above the seeing cutoff. Note the appearance of the number of speckles $(D/r_0)^2$ in the simplified expression. This fact is used for signal to noise modelling in Chapter 4.

2.6 Speckle interferometry

The wave-like nature of light causes diffraction effects when a ray impacts a physical obstacle such as a telescope aperture or slits. Interference patterns can form due to the

constructive and destructive superposition of waves diffracted around the edges of objects. This interference helps infer physical properties about the source. In this section, the interference patterns generated by speckles of light observed through a telescope aperture are examined.

Antoine Labeyrie [38] devised an innovative means to measure diffraction-limited information about astronomical objects (such as a binary star) corrupted by atmospheric turbulence. His approach laid the foundation for the science of speckle interferometry—a family of techniques¹² that exploit high spatial frequency information content (contained in a short exposure astronomical image) — to overcome atmospheric turbulence and to enable high precision astrometry to occur. For binary star measurements, a measurement case analogous to OOS satellite monitoring, the separation distance and orientation angle can be directly measured from the fringes helping to determine the distance to astronomical object. The basis of Labeyrie Speckle Interferometry is described in the following sections.

2.6.1 Image power spectrum

A point source object $o(x)$ convolved with the instantaneous point spread function $s(x)$ of the combined atmosphere and telescope aperture forms an image $i(x)$ such that

$$i(x) = o(x) * s(x) = \int o(x) s(x - x') dx' \quad (2.17)$$

where $*$ denotes convolution and the object function is modelled as

$$o(x) = \delta(x) + \alpha_b \delta(x - d) \quad (2.18)$$

and α_b is the brightness ratio of the secondary object to the primary object (equation 1.7). The primary object is assumed to have a unitary brightness and $\delta(x-d)$ is a Dirac delta function that models the offset d that the object is displaced from the primary (see Figure 24).

¹² Autocorrelation, image-bispectrum, lucky imaging and Knox-Thompson image reconstruction techniques are examples of speckle interferometry inspired approaches developed prior to the availability of adaptive optics

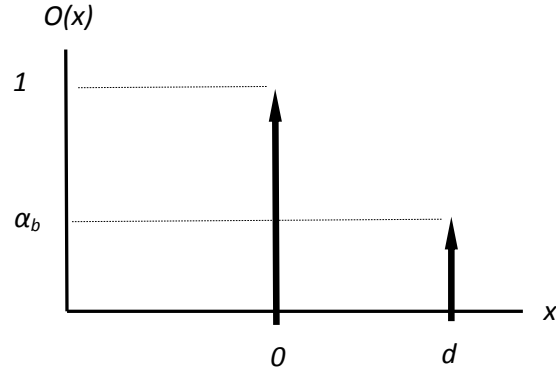


Figure 24: Object model $O(x)$ modelled with Dirac delta functions

The Fourier transform of the object function is

$$O(u) = e^{-i2\pi(0)u} + \alpha_b e^{-i2\pi ud} = 1 + \alpha_b e^{-i2\pi ud} \quad (2.19)$$

and the modulus of the object function is expressed as

$$O(u)O(u)^* = |O(u)|^2 = (1 + \alpha_b^2) + 2\alpha_b \cos(2\pi ud) \quad (2.20)$$

or equivalently, equation 2.20 can be expressed as

$$|O(u)|^2 = (1 - \alpha_b^2) + 4\alpha_b \cos^2(\pi ud) \quad (2.21)$$

Equation 2.20 and 2.21 describe a set of cosine fringes with wavelength $1/d$ with an amplitude offset of $(1 - \alpha_b^2)$. By measuring the spacing between the fringes, the separation distance between the objects can be found.

Note that if the object function is displaced by a small random offset Δx (such as a small speckle perturbation in Figure 25), the formulation then becomes:

$$o(x + \Delta x) = \delta(x + \Delta x) + \alpha_b \delta(x + \Delta x - d) \quad (2.22)$$

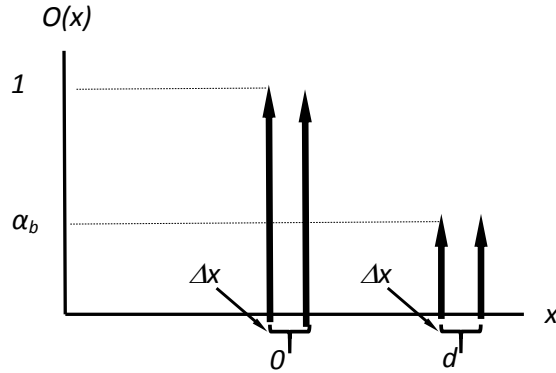


Figure 25: $O(x)$ with phase shift Δx

its Fourier transform is:

$$O(u) = e^{i2\pi\Delta xu} + \alpha_b e^{i2\pi\Delta xu - i2\pi ud} \quad (2.23)$$

The random phase shift Δx is removed after taking the square modulus of 2.23

$$\begin{aligned} |O(u)|^2 &= (e^{i2\pi\Delta xu} + \alpha_b e^{i2\pi\Delta xu - i2\pi ud})(e^{-i2\pi\Delta xu} + \alpha_b e^{-i2\pi\Delta xu + i2\pi ud}) \\ &= 1 + \alpha_b (e^{+i2\pi ud} + e^{-i2\pi ud}) + \alpha_b^2 \\ &= (1 + \alpha_b^2) + 2\alpha_b \cos(2\pi ud) \end{aligned} \quad (2.24)$$

Speckle patterns which duplicate over the isoplanatic angle (such as Figure 20) are tolerant to random phase incurred due to atmospheric turbulence and can be effectively cancelled forming interference fringes. As long as this duplicative nature is preserved a Fourier transform becomes sensitive to the repeating patterns contained within a speckle image. The fringe properties (separation distance and orientation) can then be used to measure the objects' relative positions.

2.6.2 Stacking images

Speckle images are acquired at a high frame rate due to the millisecond timescales of the atmospheric coherence timescale τ_0 . Labeyrie's method needs to stack multiple images to gather enough coherent signal as each image is inherently photon starved due to the short exposure times needed to freeze atmospheric effects. Typical exposure times

for Labeyrie speckle interferometry is between 10-20 milliseconds. Each individual exposure image is unlikely to contain enough signal photons to perform a fringe measurement unless the object is extremely bright. In practice, hundreds, or thousands of frames are stacked together in most speckle interferometry experiments in order to gather enough signal on faint astronomical targets.

The Fourier transform of a speckle image is described by

$$I(x) = O(x) \cdot S(x) \quad (2.25)$$

and the image power spectrum, after averaging many frames, is expressed as

$$\langle |I(u)|^2 \rangle = \langle |S(u)|^2 \rangle \cdot |O(u)|^2 \quad (2.26)$$

The measured image $\langle |I(u)|^2 \rangle$ is corrected by use of a nearby reference star to account for the Fourier transform of the shape of the atmospheric and telescope point spread function, such that

$$|O(u)|^2 = \frac{\langle |I(u)|^2 \rangle}{\langle |S(u)|^2 \rangle} \quad (2.27)$$

where $\langle |S(u)|^2 \rangle$ is the average modulus of the Fourier transform of an individual star which consists of spatial frequency information for both the atmosphere and telescope.

For satellite tracking applications, the normalization procedure using nearby stars is impractical as satellites move relative to them. There are other approaches to accomplishing this. Gili [81] indicates that either wavelet filtering or by dividing by a mean offset frame can achieve similar results without needing to observe calibration stars. Later in the image processing section, it will be shown that by taking the profile *parallel* to the fringes provides an approximate shape estimate for the point spread function $S(u)$ saving an observer from needing to observe a reference star during tracking of satellite objects.

2.6.3 Power spectrum measurements

Once fringes are formed, measurements are collected from the fringe profile. Figure 26 (left) shows an example of two bright satellite sources which are Fourier transformed and their power spectrum (Figure 26 right) reveals the fringe pattern created by taking the square modulus of the complex spatial frequency information.

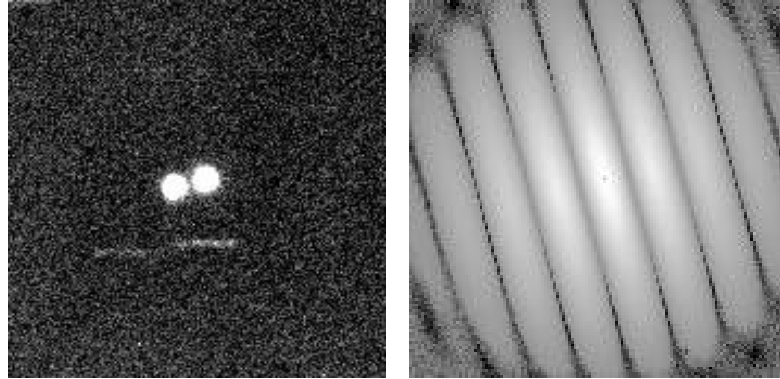


Figure 26: (Left): Point source objects in spatial (x,y) plane. (Right): Power spectrum Fringes in spatial frequency (u,v) plane

Note that in Figure 26 (right) the power spectrum fringes are symmetric about the center of the image (denoted by the central peak highlight). Also, the orientation angle of the fringes is perpendicular to the vector between the two objects in the spatial plane. The separation between fringe peaks (or the minima) is inversely proportional to the true separation distance on the image plane

$$d = Na_p/F_s \quad (2.28)$$

where N is the pixel dimension of the image, a_p is the pixel scale of the detector in arcseconds per pixel and F_s is the separation distance between fringes in cycles/frame.

Binary star observers usually record two pieces of information when observing positional metrics. These are the separation distance ρ and the orientation angle θ [82]. For example, Figure 27 shows two well separated binary stars such that their centroids

can be measured. The separation distance ρ (not to be confused with the autocorrelation¹³) is the angular distance between the centroids of the stars (measured in arcseconds). The orientation angle θ is the angle of the vector between two stars (red vector on Figure 27) and the direction to celestial North. Once these observations are formed with the epoch (time) of the observation the binary is described for orbit estimation.

The North orientation vector is found by using the star trail approach. It is described in the instrument description section 4.5.1.

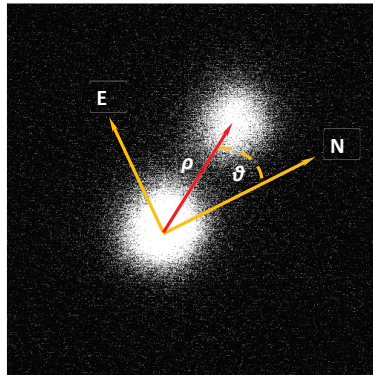


Figure 27: Measurements of separation distance ρ (or d) and the orientation angle θ

2.6.4 Autocorrelation

Autocorrelation of speckle images complements the image power spectrum. The astronomical community uses this technique regularly to measure binary stars and form quasi-images of objects (albeit with an ambiguous ghost object formed in the computation). Autocorrelation is a cross-correlation of a signal with itself computed using time or spatial shifts and is used to emphasize periodic information in a noisy signal. The autocorrelation of a two-dimensional image is computed as

$$AC(\rho_x, \rho_y) = \iint_{-\infty}^{\infty} \bar{I}(x, y) I(x + \rho_x, y + \rho_y) dx dy \quad (2.29)$$

¹³ The binary star community uses a convention where separation measurements use the notation ρ . In this manuscript, the separation distance will be expressed as a distance d to also help avoid confusion with the upcoming references to the slant range vectors in the relative orbit dynamics model in chapter 3.

A discretized form useful for image processing of astronomical images is

$$\rho_{ij} = \sum_{m=1}^M \sum_{n=1}^N I(m, n)I(m + i, n + j) \quad (2.30)$$

where the size of the pixel array is $N \times M$ and shifts of i, j pixels are performed over the entire image $I(m, n)$. Autocorrelation produces a matrix¹⁴ which is $2N \times 2M$ in size.

Figure 28 shows an example of a speckle image, its power spectrum and its autocorrelation. The first frame shows a speckle image of a bright binary star pair exhibiting the speckle pattern repetition. The center image shows the modulus of the power spectrum of the speckle image in the spatial frequency plane (u, v) . The third shows the autocorrelation formed by Fourier transforming the power spectrum.

Note that in the autocorrelation of Figure 28, the secondary object is highlighted as the two bright dots where the correct location of the secondary object is in the lower right. The quasi-image centers the bright primary star while two symmetrical, ambiguous objects appear on either side of it.

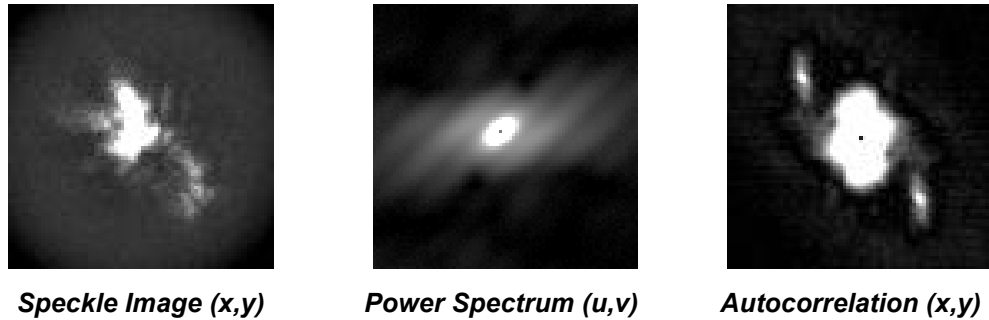


Figure 28: Speckle image of binary star, its power spectrum and autocorrelation

¹⁴ The autocorrelation expressed in equation 2.29 is equivalent to the modulus of the Fourier transform of the power spectrum. This result is described by the Weiner Khinchin theorem $\mathcal{F}|F(u)|^2(x) = \int_{-\infty}^{\infty} \bar{f}(\rho) f(x + \rho) d\rho$. The autocorrelation can be efficiently calculated using this property. The Fast Fourier Transform (FFT) requires $N \cdot \log(N)$ computations rather than the N^2 computations required by the multiple loop and summation approach implied by equation 2.30.

Boxcar subtraction approaches [83] can be used to correct the autocorrelation to remove the seeing disk width visible in Figure 28 as a “halo” around the points in the autocorrelation. This simple background fitting of an autocorrelation is often adequate to remove the embedded seeing disk effects. Others have used Gaussian high pass filters [84] in addition to reference stars normalization to remove the effects of the atmosphere on the point spread function.

Ambiguous objects—like the ones visible in Figure 28—are the result of the functional symmetry of the Fourier transform and its autocorrelation equivalent. Despite the elegance of these approaches, a 180-degree direction ambiguity appears in the location of the secondary object. While the speckle image in Figure 28 clearly shows that the true location of the secondary is in the lower right of the image, most speckle images do not exhibit an easy geometry that permits easy identification of the secondary’s true location. The primary object’s seeing disk often overlaps the secondary object. In this case, although fringes have been formed, it is not easy to determine true location of the secondary object. Inferring the true direction of the secondary object is not directly measureable using either the power spectrum or the autocorrelation alone.

In relative orbit estimation of satellites, this ambiguity effect is not acceptable since orbital measurements can be rejected during relative orbit estimation if positional measurements are inconsistent with a previous measurement of the secondary object’s location. A method to accurately pin-point the true direction to the secondary object is required for relative satellite measurements.

2.7 Directed vector autocorrelation

Directed Vector Autocorrelation (DVA) [83] can unambiguously compute the position of a secondary object by selectively switching the pixel values while computing the autocorrelation. The Directed Vector Autocorrelation is computed using the autocorrelation from equation 2.30 and is shown again here for clarity

$$\rho_{ij} = \sum_{m=1}^M \sum_{n=1}^N I(n, m)I(n + i, m + j) \quad (2.31)$$

While computing the DVA, the interior product of equation 2.31 is subjected to a selection rule [85] that forces the product's value to zero based on the following logic

$$\begin{aligned} & \text{if } I(n+i, m+j) > I(n, m) \\ & \text{then } I(n, m)I(n+i, m+j) = 0 \end{aligned} \quad (2.32)$$

Figure 29 shows an example of DVA applied to a speckle image of a binary star. In this image, both autocorrelation and DVA are computed.

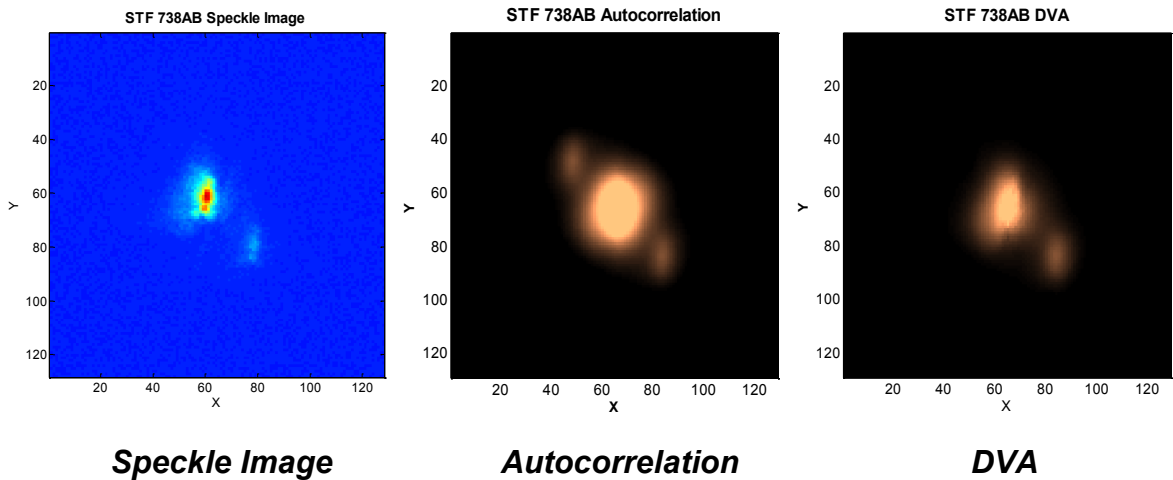


Figure 29: Example of Directed Vector Autocorrelation (x,y expressed in units of pixels)

In Figure 29 the autocorrelation preserved the secondary's position and maintained the ambiguity. The DVA highlighted the true location of the secondary object while suppressing the secondary object's presence below the color scale of the background.

While DVA is appealing to resolve the direction ambiguity, DVA's suitability for real-time satellite measurement is limited since large aperture telescopes tend to have longer focal lengths provoking smaller detector fields of view. Such telescopes' long focal lengths project the point spread function over a very large swath of pixels making the speckle patterns large in comparison to the detector size. Software implementations of DVA require four nested "for-loops" to scan and create a DVA matrix that will highlight

the position of a secondary object (See Annex C1). These embedded loops cause lengthy computational times to compute the DVA Matrix.

One test of DVA using a quad core Xeon workstation resulted in the processing times shown in table 1. It is clear that for even for small arrays that the computation of the DVA can be burdensome without the aid of parallel computing.

Table 1 DVA Computation Time

Image Array Size $N \times N$ (pixels)	Elapsed Processing Time (s)
32 x 32	0.0026
64 x 64	2.1
128 x 128	29.7
256 x 256	467
512 x 512	7867

According to the trend shown in table 1 an image of 1024 x 1024 pixels would take nearly 38.4 hours to compute using DVA. Clearly, DVA does not lend itself well to real time applications for larger fields of view—the processing times are far too long. Caloi [85] suggests that since DVA is symmetric, only half of the matrix needs to be computed, effectively halving computation times. Another approach is to selectively mask a small raster around the objects such that DVA can be performed on a smaller pixel region. This could work for bright objects but may be unstable when processing faint speckles as the object centroids can become unreliable at low signal levels.

During the Mont-Mégantic experiment (see Chapter 5), an 8X Barlow focal length extension was used to project the satellites’ optical point spread function across enough pixels to be Nyquist sampled by the detector (see section 4.4). Nyquist sampling is a necessary requirement for speckle imaging in order to accurately sample the point spread function of the speckles. An example speckle image from the Mont-Mégantic experiment is shown in Figure 30 where the speckled seeing disks are rather large on the imagery.

In this case, the width of the atmospheric point spread function was approximately 115 pixels wide—a size that requires a frame to be large enough to capture the position of both satellites. The width of the frame in Figure 30 is 512x512 pixels. Applying DVA to

single frame from the Mont-Mégantic experiment would have taken 1.9 hours to compute. Nearly 5000 images were acquired in a 15-minute interval when the satellites were within a 5 arcsecond radius from one another. Computing the position of the secondary using DVA would have taken nearly 1.1 years. Another approach¹⁵ was required to more efficiently compute the exact location of the secondary object.

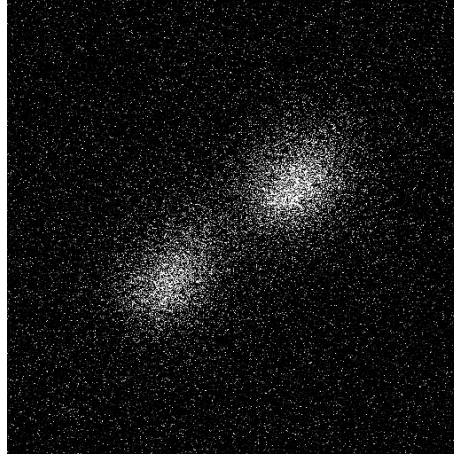


Figure 30: GEO satellites Anik F1R (Lower left) and Anik G1 (Upper right). Frame size is 512x512 pixels

2.8 Cross-spectrum for satellite speckle interferometry

Aristidi [86] published a description of the cross-correlation technique as applied to binary star measurement to unambiguously determine the location of the secondary star. Due to inherent processing advantages in the computation of the cross-spectrum, this technique was adapted to detect and measure the secondary satellite's location in a closely separated pair. The cross-spectrum, and its analog, the cross-correlation, can provide information on the true location of the secondary object while avoiding the computational burden of DVA.

¹⁵ For comparison, the cross-spectrum computation time for a 1024x1024 pixel image using the Xeon workstation described in section 2.7 is 0.036 seconds.

The mathematical description of the cross-correlation is similar to the autocorrelation and power spectrum. A description of the cross-correlation will be first described then its Fourier transform will be performed to obtain the cross-spectrum.

2.8.1 The cross-correlation

The cross-correlation is formed by integrating the object function $o(x)$ with its square $o^2(x)$, such that

$$K_0(\rho) = \int_{-\infty}^{\infty} o^2(x)o(x + \rho)dx \quad (2.33)$$

where ρ is the shift lag and $o(x)$ retains the same object definition from equation 2.18

$$o(x) = \delta(x) + \alpha_b \delta(x - d) \quad (2.34)$$

After integrating, the following product results:

$$K_0(\rho) = (1 + \alpha_b^3)\delta(\rho) + \alpha_b^2\delta(\rho - d) + \alpha_b\delta(\rho + d) \quad (2.35)$$

where α_b is the brightness ratio defined in equation 1.7. The cross-correlation produces a quasi-image where the central peak represents the primary object surrounded by two companions each spaced distance d apart. See Figure 31.

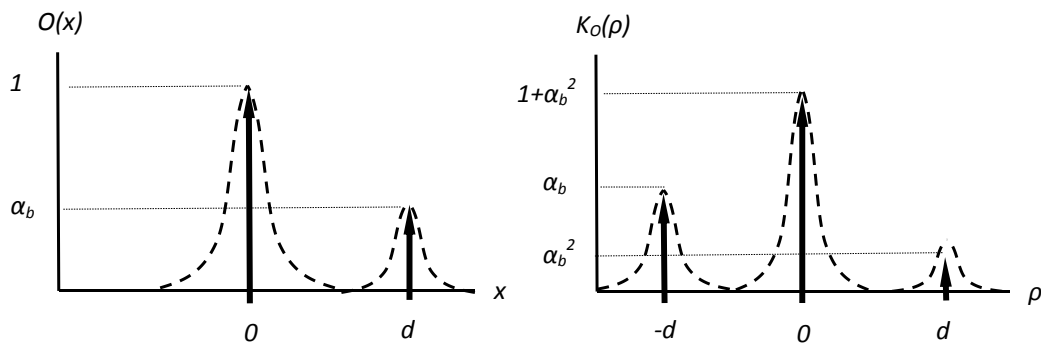


Figure 31: (Left): Object function $O(x)$ with point spread function (dashed) (Right): Cross-correlation as expressed in equation 2.35

Figure 31 shows that the true location of the secondary object (at location d) is located at the smaller peak of the computed cross-correlation. The suppressed height α_b^2 of the true location of the secondary compared the ambiguity's peak height α_b tends to make direct detection of the shorter peak awkward for image processing. The brighter peak can be used in image processing applications as long as the peak is rotated by 180 degrees in the spatial plane to correctly identify the true location of the secondary.

For image processing of satellite speckle images, the cross-spectrum is used rather than the cross-correlation in order to determine the distance and position of the two objects. By inspecting the properties of cross-spectrum fringes a direct path to determining the object separations can be found and is described in the following section.

2.8.2 The cross-spectrum

Taking the Fourier transform of the cross-correlation $K_0(\rho)$, one obtains

$$\mathcal{F}(K_0(\rho)) = K_0(u) = (1 + \alpha_b^3) + \alpha_b^2 e^{-2\pi i u d} + \alpha_b e^{i 2\pi u d} \quad (2.36)$$

where u is the spatial frequency. Partitioning the real and imaginary components of $K_0(u)$ identifies the components of the cross-spectrum as

$$\text{Re}(K_0(u)) = (1 + \alpha_b^3) + \alpha_b(1 + \alpha_b)\cos(2\pi u d) \quad (2.37)$$

and

$$\text{Im}(K_0(u)) = \alpha_b(1 - \alpha_b)\sin(2\pi u d) \quad (2.38)$$

Both the real and imaginary components are periodic in $1/d$. Examples of the cross-correlation, cross-spectrum and their real and imaginary components are shown in Figure 32. It should be recognized that the bright secondary object in the cross-correlation is the ambiguity object and the true location of the secondary is toward the lower right in Figure 32.

Aristidi [86] showed that the slope at the center of the imaginary component ($u = 0$) unambiguously points in the direction of the secondary object. The slope is

$$\text{slope} = \left[\frac{d}{du} \text{Im}(\widehat{K}_o(u)) \right]_{u=0} = 2\pi\alpha_b d(1 - \alpha_b) \quad (2.39)$$

With this convention, all of the information needed to compute the separation and orientation toward the secondary object is fully contained within the imaginary component of the cross-spectrum.

As it was assumed that the servicing satellite is fainter than the client satellite (section 1.10), the brightness ratio α_b is less than one. As per equation 2.39 the slope is positive in the direction of the fainter (secondary) object. Computing the gradient of the imaginary component of the cross-spectrum and taking value of the gradient at its center provides a direct indication of the direction toward the fainter servicing satellite.

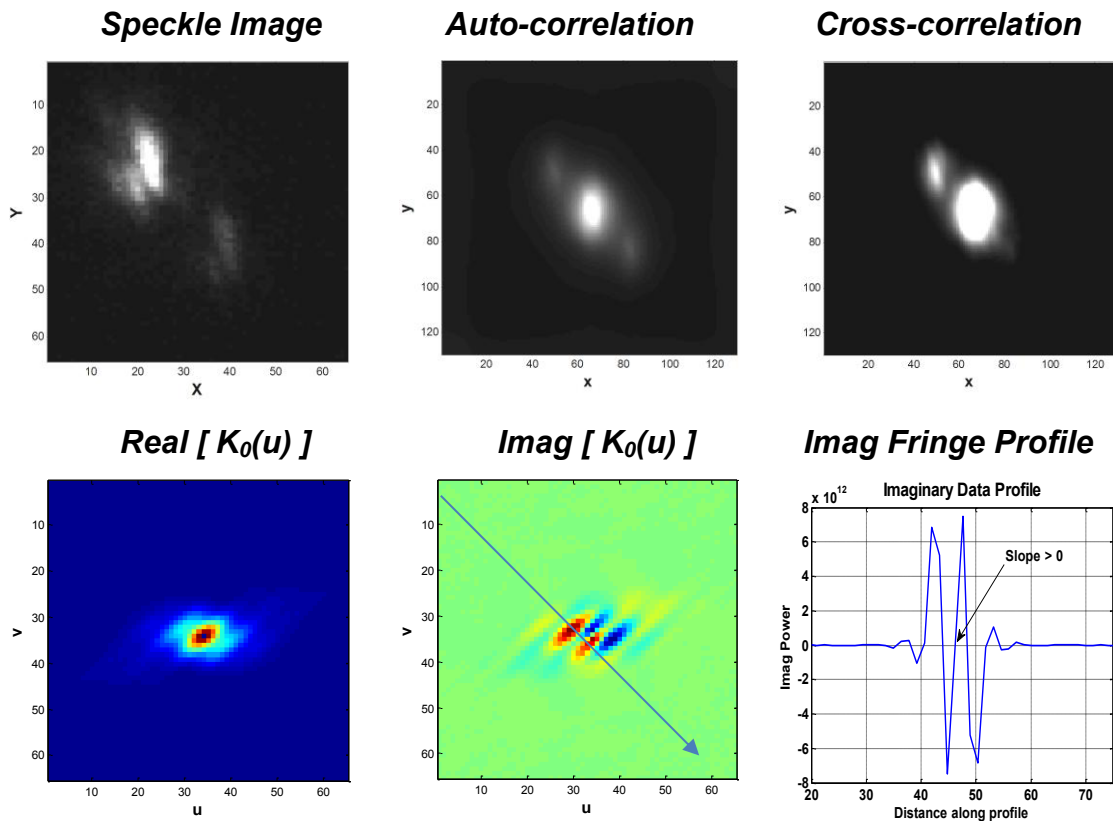


Figure 32: Speckle image, autocorrelation, cross-correlation, real cross spectrum, imaginary cross-spectrum and imaginary fringe profile. Notice that the imaginary component is positive in the direction of the true location of the secondary.

2.8.3 Cross-spectrum of real speckle images

Real speckle images with point spread functions $s(x)$ do not directly mimic Dirac delta functions. Approximations and assumptions are required to compute the cross-spectrum from an image composed of real speckles.

Aristidi [86] indicates that the cross-correlation for a real speckle image with Fourier transform K_s is

$$K_I(\rho) = \left(1 + \alpha_b^3\right) K_s(\rho) + \alpha_b K_s(\rho + d) + \alpha_b^2 K_s(\rho - d) + 2\alpha_b T_s(d, \rho) + 2\alpha_b^2 T_s(-d, \rho) \quad (2.40)$$

Equation 2.40 is nearly identical in form to equation 2.35 except for two bias terms $2\alpha_b T_s(d, \rho)$ and $2\alpha_b^2 T_s(-d, \rho)$ where $T_s(d, \rho)$ denotes the triple correlation. The triple correlation function $T_s(d, \rho)$ is equivalent to the mathematical expectation $E(\cdot)$ such that

$$\begin{aligned} T_s(d, \rho) &= \left\langle \int \hat{S}(x) \hat{S}(x + d) \hat{S}(x + \rho) dx \right\rangle \\ &= E[\hat{S}(x) \hat{S}(x + d) \hat{S}(x + \rho)] \end{aligned} \quad (2.41)$$

Aristidi shows that the ratio of brightness α_b is not known which makes the removal of these bias terms problematic. A proof [86] is offered that bias terms can be ignored if the cross-correlation is computed using a zero-mean image and zero-mean specklegram if the separation between objects is much larger than the speckle size¹⁶ such that $d \gg s$.

For image processing, raw images are zero-mean corrected by computing

¹⁶ Aristidi does not offer a ratio for how large d should be in proportion to the speckle size s but does show a simulated example where $d = 10s$. In this research, experimental observations on binary stars using a small-aperture telescope shown good results when the separation distance is greater than $3s$

$$\hat{S}(x) = S(x) - \bar{S} \quad \text{and} \quad \hat{I}(x) = I(x) - \bar{I} \quad (2.42)$$

where \bar{S} and \bar{I} are the mean level of the specklegram and the image. This permits the following approximation to be made for a zero-mean specklegram image

$$K_{\hat{I}}(\rho) = K_{\hat{S}}(\rho) * K_O(\rho) \quad (\text{condition } d \gg s) \quad (2.43)$$

where the bias terms of equation 2.40 are neglected. The Fourier transform of equation 2.43 recasts this expression into spatial frequency space as

$$\hat{K}_{\hat{I}}(u) = \hat{K}_{\hat{S}}(u) \cdot \hat{K}_O(u) \quad (2.44)$$

For image processing applications, the cross-spectrum is computed by term multiplication of the Fourier transforms of the zero-mean image's square and by its complex conjugate

$$\hat{K}_{\hat{I}}(u) = \mathcal{F}(\hat{I}^2) \cdot \mathcal{F}(\hat{I})^* \quad (2.45)$$

where \hat{I} is the zero mean image and * denotes the complex conjugate.

The “signal” equation for satellite speckle interferometry can be written as

$$\text{Im}(\hat{K}_{\hat{I}}(u)) = \hat{K}_{\hat{S}}(u) [\alpha_b (1 - \alpha_b) \sin(2\pi u d)] \quad (2.46)$$

In equation 2.46, $\hat{K}_{\hat{S}}(u)$ is a real-valued function that describes the cross-spectrum of the shape of the speckle. If a Gaussian speckle shape with a full width half max of 2.355σ is assumed, equation 2.46 can be written as

$$\text{Im}(\hat{K}_{\hat{I}}(u)) = \sqrt{2\pi}\sigma^2 e^{-\frac{3}{4}\sigma^2 u^2} [\alpha_b (1 - \alpha_b) \sin(2\pi u d)]$$

where

$$\mathcal{F}\left(e^{-\frac{x^2}{2\sigma^2}}\right) = \sqrt{2\pi}\sigma^2 e^{-\frac{\sigma^2 \pi^2 u^2}{2}} \quad (2.47)$$

Fringes formed in the cross-spectrum, or in the power spectrum, must be corrected (deconvolved) by the combined atmosphere and telescope point spread function $S(u)$. This is necessary to properly determine the fringe spacing of object $\widehat{K}_O(u)$ since the combined point spread function will move the position of the fringes by moving the maxima inward and the minima outward [87]. Correcting by $\widehat{K}_S(u)$ is equivalent to high-pass spatial filtering of the image—it reduces the impact of the atmospheric point spread function on the cross-spectrum. For satellite speckle interferometry, experiments show that a Moffat fit [88] taken along the profile parallel to the fringes works well during image processing of satellite speckles.

2.8.4 Metrics from the imaginary component of the cross spectrum

At this stage, the metrics (measurements) can be formed from the imaginary component of the cross-spectrum. The fringe orientation angle θ and separation distances between fringes F_s can be measured directly by inspecting the imaginary component of the cross-spectrum. Figure 33 shows an example of a speckle measurement of a binary star. Figure 34 shows imaginary fringes extracted from the cross spectrum.

The orientation angle¹⁷ θ is found by detecting the linear features of the fringes. Then, a 90-degree rotation is applied since the object axis is perpendicular to the fringes. Next, the gradient at the center of the imaginary fringe frame is used to determine the direction toward the fainter secondary object. Last, the offset angle to the North orientation (see Figure 33) is subtracted. This ensures that the measured orientation angle is referenced to celestial North for astrometric measurements intended for relative orbit determination.

The separation distance d is determined by finding the distance between the fringe minima¹⁸ closest to the center of the imaginary fringes. This distance in the frequency plane is F_s (the *Fringe Separation* in Figure 33). An estimate of the spatial separation is made according to equation 2.28 ($d = Na_p/F_s$) where the pixel pitch a_p and full-array frame size N is used to determine the separation distance d (arcseconds).

¹⁷ The orientation angle θ is measured counter-clockwise toward East and is valued between 0-360 degrees (see Figure 34).

¹⁸ For fast moving satellites, it was found that applying a second Fourier transform to the fringes was a more reliable means to determine the fringe separation. This is discussed in Chapter 5.

Images collected by a fast imaging camera are stacked sequentially. Fainter satellite objects require 100 (or more) stacked images to ensure consistency in the data processing approach. Timestamps t_i are taken as the average time of the stack.

The observation triplet then consists of

$$\mathbf{y}_i = [t_i \quad d \quad \theta]^T \tag{2.48}$$

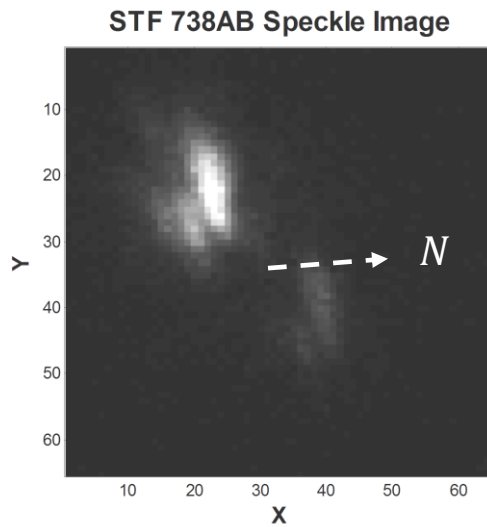


Figure 33: Speckle Image Example with North Reference Vector

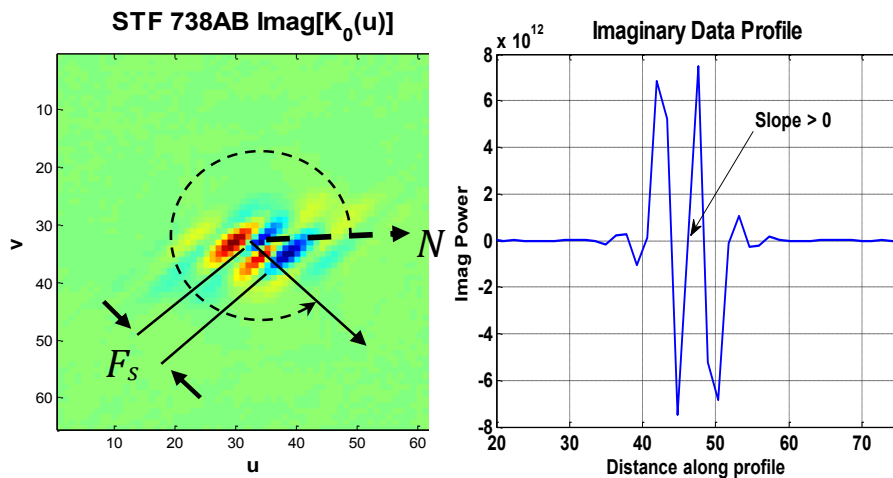


Figure 34: (Left) Cross-spectrum imaginary component (Right) Profile of imaginary component showing gradient (slope) as positive at the center of the profile. The object is the right.

2.9 Other atmospheric effects: Chromatic dispersion

Earth's atmosphere disperses different wavelengths of light similar to a prism. This effect chromatically elongates speckles in the direction of the zenith during speckle imaging. This effect is negligible at the zenith ($z = 0^\circ$) but can incur as much as 0.6 arcseconds of chromatic dispersion at elevation angles of 30° for a V-band filter (see Figure 35). Elongated speckles are a source of astrometric error and this chromatic dispersion effect needs to be controlled when speckle imaging near the horizon.

Chromatic dispersion can be controlled by 1) observing at higher elevation, 2) using narrow bandwidth filters, 3) observing at longer wavelengths and 4) using corrective optical elements.

Telescopes located at mid-latitudes view geostationary satellites with a maximum elevation of ~ 35 degrees. Satellite tracking favors viewing lower elevation angles to increase the number of satellites detectable from a given observatory. For speckle observations of satellites presented later in this dissertation, elevation angles of 29 degrees were necessary to conduct testing. As such, passive optical elements were explored to control dispersion.

Filters can be used to reduce chromatic dispersion by limiting the wavelengths of light passed through the telescope. Dispersion is proportional to the center wavelength λ and the bandwidth ($\Delta\lambda$) of the filter used to collect speckle images. Dispersion is strongest in blue wavelengths and weaker at longer, redder wavelengths (see Figure 35). While a narrowband infrared filter appears ideal, it is beneficial to use a broader infrared filter to increase the amount of signal detected from a satellite object. This increases the detectability of satellites while staying within the detector's quantum efficiency (spectral sensitivity) curve (see Figure 36).

Risley prisms can be incorporated into a telescope's optical train to directly control dispersion. Two such prisms are aligned in the optical path of a telescope and are rotated to vectorially cancel the chromatic dispersion effect. An excellent reference on the selection and use of Risley prisms is described by Mason [89] who recommends that chromatic dispersion be minimized to be less than $\frac{1}{2}$ of the speckle size for proper binary star measurement.

While Risley prisms add significant benefit, use of infrared filters was chosen in order to reduce the complexity of the optical train on the back of the instrument. Increasing the size of the optical path is problematic due to the increased counterweight needs and mechanical flexure of the cantilevered optical elements. The chromatic dispersion error incurred by use of filters-only to control dispersion was deemed to be acceptable for this work to simplify the mechanical design of the instrument.

During practice observations of binary stars using a small aperture telescope, it was found that the choice of Sloan *i'* filtered measurements lessened the need for dispersion corrective equipment as the dispersion error incurred by the use of this near-infrared bands is approximately 0.35 arcseconds. The Rayleigh limit for the small aperture telescope is 0.47 arcseconds at this wavelength (see table 2). While this did not fully meet the recommendation of [89] the error incurred was deemed acceptable for experimental needs for satellite tracking.

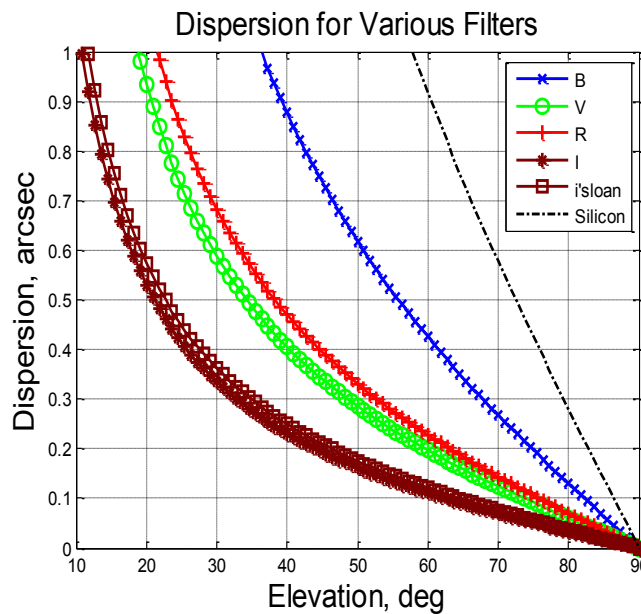


Figure 35: Chromatic dispersion for various filter bands. Note that the *I* filter has lower dispersion due to the narrow width of its filter band-pass

Table 2 Filter Effective Wavelengths and Bandwidths

Filter	Effective Wavelength λ (nm)	Effective Bandwidth $\Delta\lambda$ (nm)
U	366.3	65
B	436.1	89
V	544.8	84
R	640.7	158
I	798.0	154
i' (sloan)	743.9	123

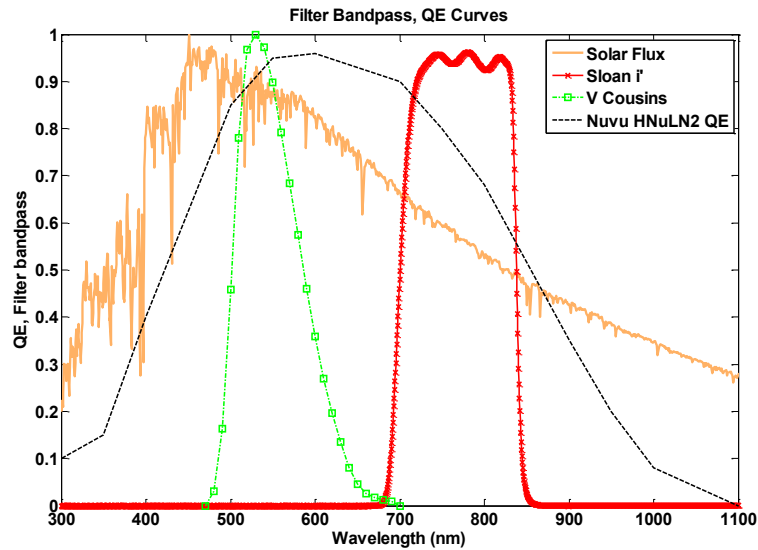


Figure 36: Filter bandpass used for speckle Interferometric measurements

Observing in Sloan i' filter is also beneficial for satellite observations during bright lunation (full moon) periods. Sydney [90] recommends a filter with a band-pass of 650-850 nm for full moon conditions to cut out bright lunar glow at 640 nm and atmospheric OH sky-glow emissions red-ward of at 880 nm. As chromatic dispersion increases for lower wavelengths, Sloan i' is a good compromise between the needs to minimize chromatic dispersion for speckle-interferometry while suppressing lunar and sky-glow noise sources for satellite detection.

2.10 Other atmospheric effects: Atmospheric extinction

An astronomical object detected by a ground based telescope observes an attenuated signal due to atmospheric gases, aerosols and other particles absorbing some of the incoming light during its passage through the atmosphere. In essence, all stars appear dimmer than they actually are due to the atmosphere's absorption. This effect is referred to as atmospheric extinction and corrections can be made to determine the true (exo-atmospheric) magnitude of an astronomical object. If one observes at lower elevation angles, the line of sight is oblique as it passes through a longer optical path of the atmosphere. This reduces the amount of signal detected by an imager.

A first order model of extinction uses a flat Earth and atmosphere of constant thickness to determine the number of air masses (equivalent thicknesses of Earth's atmosphere) that a telescope looks through. The air mass χ can be estimated as $\chi = 1/\sin(el)$. For elevations above 20 degrees, extinction can be estimated [91] as

$$\Delta M_v = k_{ext}\chi = \frac{k_{ext}}{\sin(el)} = \frac{k_{ext}}{\cos(\zeta)} \quad (2.49)$$

where k_{ext} is the extinction coefficient for the filter band of interest. Extinction coefficients are lower for longer wavelength filters (see table 3). As speckle images favor longer observation wavelengths to control chromatic dispersion, less extinction is incurred making longer wavelengths favorable for observation.

Table 3 Extinction coefficients for various filters [73]

Filter	Effective Wavelength λ (nm)	Extinction Coefficient (Magnitude/airmass)
U	366.3	0.6
B	436.1	0.4
V	544.8	0.2
R	640.7	0.1
I	798.0	0.08

2.11 Chapter summary and contributions

Atmospheric turbulence is a barrier to high precision optical astrometry of OOS satellites. Key parameters that characterize atmospheric turbulence are; the Fried parameter r_0 , the coherence time τ_0 , the seeing disk size ε and the isoplanatic angle $\Delta\theta$. The isoplanatic angle is the limit ($\Delta\theta < 5$ arcseconds) which speckle interferometry can be performed. It is argued in this chapter that speckle interferometry observations of OOS satellite operations in GEO require that the satellites' separation be less than 1 km to correspond with this limitation.

An overview of Labeyrie Speckle interferometry and related techniques were also described and an analogy between speckle observations of binary stars and satellite-tracking was made. Although speckle processing using either power spectrum or autocorrelation methods provide useful astrometric measurements for binary stars, a computationally fast method to unambiguously determine the true direction to the secondary object was required.

This chapter argued that Directed Vector Autocorrelation (DVA)—a standard approach used to resolve the quadrant ambiguity—is computationally prohibitive for real-time space surveillance measurements. In contrast, the cross-spectrum was identified as a more computationally efficient means of inferring the separation distance between two objects. Implementation of the cross-spectrum technique rests on an assumption that objects are separated by distances d larger than the speckle size s (where $d > 3s$).

Other atmospheric effects, such as chromatic dispersion and atmospheric extinction, have demonstrated elevation sensitivities which reduce the effectiveness of space surveillance sensors. Chromatic dispersion can be controlled by use of Sloan i' infrared-band observations as longer wavelengths experiences less dispersion. In addition, observations during bright lunation are possible as this filter rejects both lunar glow and sky glow from increasing background noise on a detector. In this way, a larger area of the sky, and more lunation periods, become available increasing the utility of speckle methods for a wider array of telescopes.

Chapter 3: Reference frames, observational and relative motion models

A transformation is required to convert separation and orientation angles generated by speckle interferometry into astrometric measurables needed for relative orbit determination. A dynamics model describing relative motion flight of two closely-spaced satellites is also needed along with a measurement model relating the state dynamics to the measurements. This chapter addresses coordinate frame selection, relative motion models and measurement models which link telescope measurements to relative orbit estimation.

3.1 Geocentric and relative orbit measurements

Space surveillance telescopes, such as GEODDS [17], collect angles-only measurements of Earth orbiting objects by measuring encoder angles on their telescope mounts (altitude/azimuth angles) or by registering an astronomical image by detecting background stars and matching star positions to a star catalog (astrometry). The latter measurement approach is also used with space-based observations such as those collected by the Space Based Visible (SBV) [92], Space-Based Space Surveillance satellite (SBSS) [93], and the Canadian Sapphire satellite [94]. Observations from telescopes usually consist of observer-centric time, right ascension, and declination (t, α, δ) of the position of an RSO. These observations are usually referenced to an observer's coordinate system (usually topocentric J2000 for right ascension, declination or the South-East-Zenith coordinate system for azimuth, elevation measurements).

These “angles-only” measurements are line-of-sight direction angles which enable *absolute* orbit estimation with respect to the geocentric Earth center. A unit direction vector $\hat{\mathbf{L}}_i$ from the observer to the detected object is modelled as

$$\hat{\mathbf{L}}_i = \begin{bmatrix} \cos(\delta_t) \cos(\alpha_t) \\ \cos(\delta_t) \sin(\alpha_t) \\ \sin(\delta_t) \end{bmatrix} \quad (3.1)$$

Orbit estimation is performed by contrasting an initial guess of the object's orbit against measurements. An optimal estimation algorithm—such as batch least squares

[65] or a sequential step or Kalman filter for orbit determination [65][95]—is used to estimate the orbit and create its covariance (uncertainty in the state vector). Orbits are referenced to Earth’s geocentric center and tied to a coordinate frame such as J2000 or the International Celestial Reference Frame (ICRF) [65].

Satellites performing OOS that are measured by differential speckle observations (d, θ) consist of *differential angles* measurements that describe the *relative angular position* of a secondary satellite with respect to its client. The trajectory that the servicing satellite follows is a *relative orbit* with respect to the client satellite. As the target orbit is mostly circular for geostationary satellites, the client’s radial, in-track and cross-track flight axes are used as a frame of reference for a relative orbit determination.

The Local Vertical Local Horizontal (LVLH) frame matches the Hill frame of reference which is centered on the client satellite has its principle axes directions defined by equation 3.2.

$$\hat{x} = \frac{\vec{r}}{|\vec{r}|} \quad \hat{y} = \frac{\vec{z} \times \vec{x}}{|\vec{z} \times \vec{x}|} \quad \hat{z} = \frac{\vec{r} \times \vec{v}}{|\vec{r} \times \vec{v}|} \quad (3.2)$$

In equation 3.2, \vec{r} and \vec{v} is the position and velocity vector of the client satellite, \hat{x} points in the radial direction away from the client, \hat{y} is in the direction of the client’s velocity vector and \hat{z} is the orbit normal. Within this frame, the relative position vector $\Delta\vec{r}$ and velocity $\Delta\vec{v}$ represent the servicer satellite’s state vector with respect to the client.

Topocentric optical measurements collected on the OOS satellite pair is taken from an observer’s ground-based position (*obs*). The observation geometry and the Hill frame $[\hat{x}, \hat{y}, \hat{z}]$ is shown in Figure 37. Note that the vectors $\vec{\rho}_1$ and $\vec{\rho}_2$ —representing line of sight vectors are multiplied by range ρ from the observer to the target—form the vector $\vec{\rho}_i = \rho \hat{L}_i$

The position of the servicing satellite relative to the client is the difference between the slant range vectors $\vec{\rho}$ and is equivalent to the difference between the absolute positional vectors of the satellite \vec{r} . This difference is written as

$$\vec{r}_2 - \vec{r}_1 = \vec{\rho}_2 - \vec{\rho}_1 = \Delta\vec{r} \quad (3.3)$$

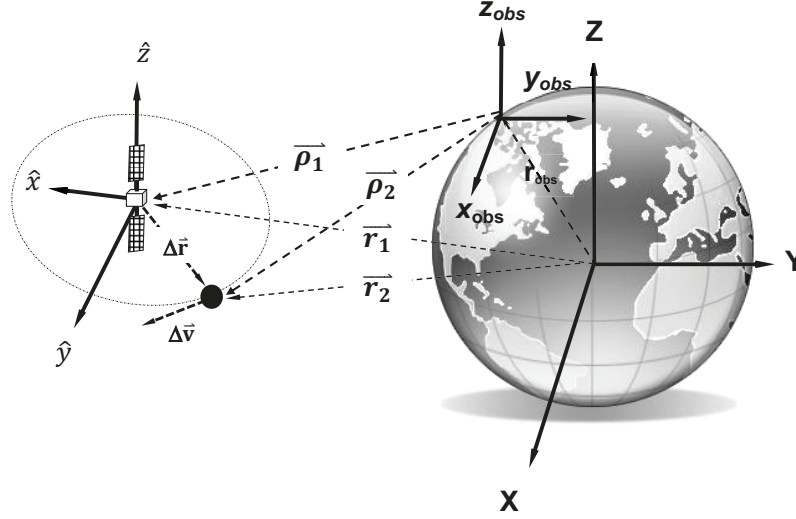


Figure 37: Relative position vectors, geocentric and topocentric frames (not to scale)

The geocentric position vector \vec{r}_1 of the primary satellite in geocentric coordinates is expressed as

$$\vec{r} = \begin{bmatrix} r_x \\ r_y \\ r_z \end{bmatrix} = r_{GEO} \begin{bmatrix} \cos(\delta)\cos(\alpha) \\ \cos(\delta)\sin(\alpha) \\ \sin(\delta) \end{bmatrix} \quad (3.4)$$

where r_{GEO} is the geostationary orbit semi major axis ($r_{geo} = 42,164.2$ km) and (α, δ) are the geocentric right ascension and declination of the client satellite.

The observer's slant range vector $\vec{\rho}$ is resolved into components expressed in the topocentric (*obs*) coordinate frame as

$$\vec{\rho} = \begin{bmatrix} \rho_x \\ \rho_y \\ \rho_z \end{bmatrix} = \rho \begin{bmatrix} \cos(\delta_t)\cos(\alpha_t) \\ \cos(\delta_t)\sin(\alpha_t) \\ \sin(\delta_t) \end{bmatrix} \quad (3.5)$$

and the magnitude of the components are the quadrature

$$\|\bar{\boldsymbol{\rho}}\| = \sqrt{\rho_x^2 + \rho_y^2 + \rho_z^2} \quad (3.6)$$

3.2 True of date reference frame convention for differential observations

Differential angles measurements collected from a ground based telescope are best matched to the “True¹⁹ Equator and Equinox of Date” or “True of Date” (*TOD*) frame [65]. Geostationary satellites fly in circular orbits about the true equator of date making this orbital frame convenient to model the motions of geostationary satellites. This coordinate frame is a natural match to the right ascension and declination axes of a telescope mount which are fixed to the Earth and are aligned to rotate about the true pole of date. This *TOD* frame also eases the determination of the North orientation on an image using the star trail method (see section 4.51 on detector calibration) as the stars trail in the westward direction about the true rotational axis of date. This compatibility between 1) the motion of a geostationary satellite in the equatorial plane and 2) the match of the alignment of the telescope axes with the true celestial pole makes the *TOD* frame convenient for collecting differential angular measurements.

The topocentric right ascension (α_t) and declination (δ_t) are resolved by the division of the various components in equation 3.7 and 3.8. These definitions adhere to the typical conventions of the astronomical community.

$$\alpha_t = \tan^{-1} \left(\frac{\rho_y}{\rho_x} \right) \quad (3.7)$$

$$\delta_t = \sin^{-1} \left(\frac{\rho_z}{\|\boldsymbol{\rho}\|} \right) \quad (3.8)$$

¹⁹ The context of “True” in astrodynamics refers to the actual Earth equator and equinox at the time of observation.

3.2.1 Differential angles measurements

Differential right ascension ($\Delta\alpha_t$) and differential declination ($\Delta\delta_t$) measurements are formed by converting fringe separation measurements d, θ (see Figure 27) to celestial coordinates

$$\Delta\alpha_t = \frac{d \sin(\theta)}{\cos(\delta_t)} \quad (3.9)$$

$$\Delta\delta_t = d \cos(\theta) \quad (3.10)$$

The measured differential right ascension in equation 3.9 must be corrected by the object's topocentric declination ($\cos \delta_t$) to accommodate the narrower separation of lines of right ascension at high declinations. When observing near the celestial equator (as in geostationary satellite observation) this correction can be neglected.

3.3 Transformation of observations from Hill frame to differential angles

For relative orbit estimation to occur, a transformation that relates the Hill state vector to the measured angles $\Delta\alpha$, $\Delta\delta$ is required. A series of transformations are required to convert from the topocentric TOD frame to the rotating (Hill) coordinate frame which flies with the primary satellite. This transformation can be achieved by creating differentials of equations 3.7, equation 3.8 and isolating the True of Date differential position vector $\Delta\vec{\rho} = [d\rho_x \quad d\rho_y \quad d\rho_z]^T$. The differentials are expressed as

$$\begin{bmatrix} \Delta\alpha_t \\ \Delta\delta_t \end{bmatrix} = \frac{1}{\|\boldsymbol{\rho}\|^2} \begin{bmatrix} -\rho_y & \rho_x & 0 \\ -\rho_x\rho_z & -\rho_y\rho_z & 1 \\ (\rho_x^2 + \rho_y^2) & (\rho_x^2 + \rho_y^2) & \end{bmatrix} \begin{bmatrix} d\rho_x \\ d\rho_y \\ d\rho_z \end{bmatrix} \quad (3.11)$$

where

$$\Delta\vec{\mathbf{r}} = \Delta\vec{\boldsymbol{\rho}} = [d\rho_x \quad d\rho_y \quad d\rho_z]^T \quad (3.12)$$

Equation 3.12 represents the vector from the client satellite to the secondary satellite.

Intermediate expressions for equation 3.11 are formed by recognizing that

$$\sin(\alpha_t) = \frac{\rho_y}{\sqrt{p_x^2 + p_y^2}} \quad \cos(\alpha_t) = \frac{\rho_x}{\sqrt{p_x^2 + p_y^2}} \quad \sin(\delta_t) = \frac{\rho_z}{|\boldsymbol{\rho}|} \quad (3.13) \quad (3.14) \quad (3.15)$$

which yield the equivalent angular expression for equation 3.11

$$\begin{bmatrix} \Delta\alpha_t \\ \Delta\delta_t \end{bmatrix} = \frac{1}{\rho} \begin{bmatrix} -\frac{\sin(\alpha_t)}{\cos(\delta_t)} & \frac{\cos(\alpha_t)}{\cos(\delta_t)} & 0 \\ -\cos(\alpha_t)\sin(\delta_t) & -\sin(\alpha_t)\sin(\delta_t) & \cos(\delta_t) \end{bmatrix} \begin{bmatrix} d\rho_x \\ d\rho_y \\ d\rho_z \end{bmatrix} \quad (3.16)$$

Equation 3.16 is referenced to the topocentric TOD frame. This expression now needs to be rotated to align with the Hill coordinate frame axes.

3.3.1 Generalized rotation of the TOD frame to the Hill frame

Likewise, to describe the state (position and velocity) of the servicer with respect to the client satellite, a transformation is needed. The Hill state vector is expressed as

$$\mathbf{x} = [x \quad y \quad z \quad \dot{x} \quad \dot{y} \quad \dot{z}]^T = [\vec{\mathbf{r}}_{Hill} \quad \vec{\mathbf{v}}_{Hill}]^T \quad (3.17)$$

$\vec{\mathbf{r}}_{Hill}$ and $\vec{\mathbf{v}}_{Hill}$ are the position and velocity of the servicer with respect to the client. Obtaining state estimates for these two vectors relative position vectors is needed in order to describe the motion of the servicer about the client satellite.

An intermediate frame is available which can be used to link the TOD frame with the rotating Hill frame. This can be achieved by use of the radial-transverse-normal $[RSW]$ frame [65] (see Figure 38) by the implementing the following rotation sequence

$$\vec{\mathbf{r}}_{RSW} = [\mathbf{R}|\mathbf{S}|\mathbf{W}]\vec{\mathbf{r}}_{TOD} \quad (3.18)$$

where the column vectors \mathbf{R} , \mathbf{S} , \mathbf{W} are expressed as

$$\mathbf{R} = \frac{\vec{\mathbf{r}}}{|\vec{\mathbf{r}}|} \quad \mathbf{S} = \frac{\vec{\mathbf{W}} \times \vec{\mathbf{R}}}{|\vec{\mathbf{W}} \times \vec{\mathbf{R}}|} \quad \mathbf{W} = \frac{\vec{\mathbf{r}} \times \vec{\mathbf{v}}}{|\vec{\mathbf{r}} \times \vec{\mathbf{v}}|} \quad (3.19)$$

where $\vec{\mathbf{r}}$ and $\vec{\mathbf{v}}$ are the position and velocity vectors of the primary satellite expressed in the TOD frame. If the geocentric right ascension and declination of the satellite is used, a set of rotations can be created such that

$$[\mathbf{R} \mid \mathbf{S} \mid \mathbf{W}] = \mathbf{R}_y(-\delta) \mathbf{R}_z(\alpha) \quad (3.20)$$

where α is the sidereal (geocentric) angle of the position of the satellite in the TOD frame (see Figure 38) and \mathbf{R}_y , \mathbf{R}_z are rotation matrices about the y and z axes respectively.

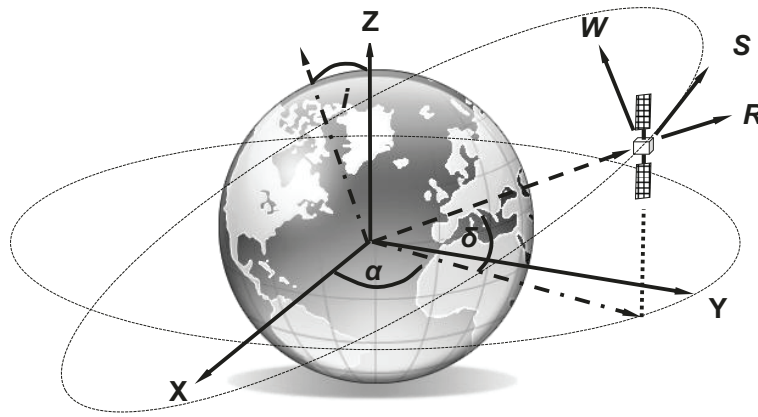


Figure 38: Rotation of the sidereal angle α and declination δ to form the RSW frame

The transformation then becomes

$$\begin{bmatrix} \Delta \vec{\mathbf{r}}_{TOD} \\ \Delta \vec{\mathbf{v}}_{TOD} \end{bmatrix} = [\mathbf{R} \mid \mathbf{S} \mid \mathbf{W}]^{-1} \begin{pmatrix} \mathbf{I}_{3 \times 3} & \mathbf{0}_{3 \times 3} \\ \mathbf{0}_{3 \times 3} & \mathbf{I}_{3 \times 3} \end{pmatrix} \begin{bmatrix} \Delta \vec{\mathbf{r}}_{RSW} \\ \Delta \vec{\mathbf{v}}_{RSW} \end{bmatrix} \quad (3.21)$$

where $\Delta \vec{\mathbf{r}}_{TOD}$ and $\Delta \vec{\mathbf{v}}_{TOD}$ are the inertial position, velocity of the differential position (equation 3.12), and velocity vectors and $\mathbf{I}_{3 \times 3}$ is the identity matrix. The $\Delta \vec{\mathbf{r}}_{RSW}$ vector is equivalent to the Hill position vector so no further transformations are required on this component of the Hill state vector. The velocity $\Delta \vec{\mathbf{v}}_{RSW}$ must be adjusted as the Hill frame rotates with respect to the RSW frame. This is compensated by adding the cross product of $\vec{\boldsymbol{\omega}}$ and $\vec{\mathbf{r}}_{Hill}$ where $\vec{\boldsymbol{\omega}}$ is the angular velocity of the Hill frame with respect to the RSW frame, or

$$\vec{\mathbf{v}}_{RSW} = \vec{\mathbf{v}}_{Hill} + \vec{\boldsymbol{\omega}} \times \vec{\mathbf{r}}_{Hill} \quad (3.22)$$

To represent the components more succinctly, the vector formulation of the components is used

$$\begin{bmatrix} \Delta \vec{\mathbf{r}}_{RSW} \\ \Delta \vec{\mathbf{v}}_{RSW} \end{bmatrix} = \begin{bmatrix} \vec{\mathbf{r}}_{Hill} \\ \vec{\mathbf{v}}_{Hill} + \vec{\boldsymbol{\omega}} \times \vec{\mathbf{r}}_{Hill} \end{bmatrix} = \begin{bmatrix} \mathbf{I} & \mathbf{0} \\ \boldsymbol{\omega}_{\times} & \mathbf{I} \end{bmatrix} \begin{bmatrix} \vec{\mathbf{r}}_{Hill} \\ \vec{\mathbf{v}}_{Hill} \end{bmatrix} \quad (3.23)$$

In equation 3.23, \mathbf{I} is the 3x3 identity matrix and the cross product of equation 3.22 is recast as the skew symmetric matrix

$$\boldsymbol{\omega}_{\times} = \begin{pmatrix} 0 & -\omega_z & \omega_y \\ \omega_z & 0 & -\omega_x \\ -\omega_y & \omega_x & 0 \end{pmatrix} \quad (3.24)$$

By substituting equation 3.20 into 3.16 and supplementing additional matrix columns to accommodate the Hill velocity, the following expression is obtained

$$\begin{bmatrix} \Delta \vec{\mathbf{r}}_{TOD} \\ \Delta \vec{\mathbf{v}}_{TOD} \end{bmatrix} = [\mathbf{R}|\mathbf{S}|\mathbf{W}]^{-1} \begin{pmatrix} \mathbf{I}_{3 \times 3} & \mathbf{0}_{3 \times 3} \\ \boldsymbol{\omega}_{\times} & \mathbf{I}_{3 \times 3} \end{pmatrix} \begin{bmatrix} \vec{\mathbf{r}}_{Hill} \\ \vec{\mathbf{v}}_{Hill} \end{bmatrix} \quad (3.25)$$

After performing the algebraic manipulations needed to reduce equation 3.25 into a more workable form, the following set of equations is produced which relate $[\vec{\mathbf{r}}_{Hill}, \vec{\mathbf{v}}_{Hill}]^T$ to the measurement vector $\mathbf{y}_i = [\Delta \alpha_t \quad \Delta \delta_t]^T$

$$\begin{bmatrix} \Delta \alpha_t \\ \Delta \delta_t \end{bmatrix} = \frac{1}{\rho_t} \begin{bmatrix} h_1 & h_2 & h_3 & 0 & 0 & 0 \\ h_4 & h_5 & h_6 & 0 & 0 & 0 \end{bmatrix} \begin{bmatrix} \vec{\mathbf{r}}_{Hill} \\ \vec{\mathbf{v}}_{Hill} \end{bmatrix} \quad (3.26)$$

where the terms h_i are defined as:

$$h_1 = \frac{\sin(\alpha - \alpha_t - \delta) + \sin(\alpha - \alpha_t + \delta)}{2\cos(\delta_t)} \quad (3.27)$$

$$h_2 = \frac{\cos(\alpha - \alpha_t)}{\cos(\delta_t)} \quad (3.28)$$

$$h_3 = \frac{\cos(\alpha)\sin(\alpha_t)\sin(\delta) - \sin(\alpha)\cos(\alpha_t)\sin(\delta)}{\cos(\delta_t)} \quad (3.29)$$

$$h_4 = \cos(\delta_t)\sin(\delta) - \cos(\alpha)\cos(\alpha_t)\cos(\delta)\sin(\delta_t) - \sin(\alpha)\cos(\delta)\sin(\alpha_t)\sin(\delta_t) \quad (3.30)$$

$$h_5 = \sin(\alpha - \alpha_t)\sin(\delta_t) \quad (3.31)$$

$$h_6 = \cos(\delta_t)\cos(\delta) + \cos(\alpha)\cos(\alpha_t)\sin(\delta)\sin(\delta_t) + \sin(\alpha)\sin(\alpha_t)\sin(\delta)\sin(\delta_t) \quad (3.32)$$

If the client satellite is in a true geostationary equatorial orbit, then $\delta = 0$ and the slant range ρ_t from the observer to the client can be assumed to be constant. Equation 3.26 can then be simplified to

$$\begin{bmatrix} \Delta\alpha_t \\ \Delta\delta_t \end{bmatrix} = \frac{1}{\rho_t} \begin{bmatrix} \frac{\sin(\alpha - \alpha_t)}{\cos(\delta_t)} & \frac{\cos(\alpha - \alpha_t)}{\cos(\delta_t)} & 0 & 0 & 0 & 0 \\ -\cos(\alpha - \alpha_t)\sin(\delta_t) & \sin(\alpha - \alpha_t)\sin(\delta_t) & \cos(\delta_t) & 0 & 0 & 0 \end{bmatrix} \begin{bmatrix} \bar{\mathbf{r}}_{Hill} \\ \bar{\mathbf{v}}_{Hill} \end{bmatrix} \quad (3.33)$$

The term $(\alpha - \alpha_t)$ denotes the hour angle for the geostationary satellite and as geostationary satellites are, to first order, motionless on the sky this term is also taken as constant. Figure 39 depicts the observation geometry for a client and servicing satellite using the angular definitions from equation 3.33.

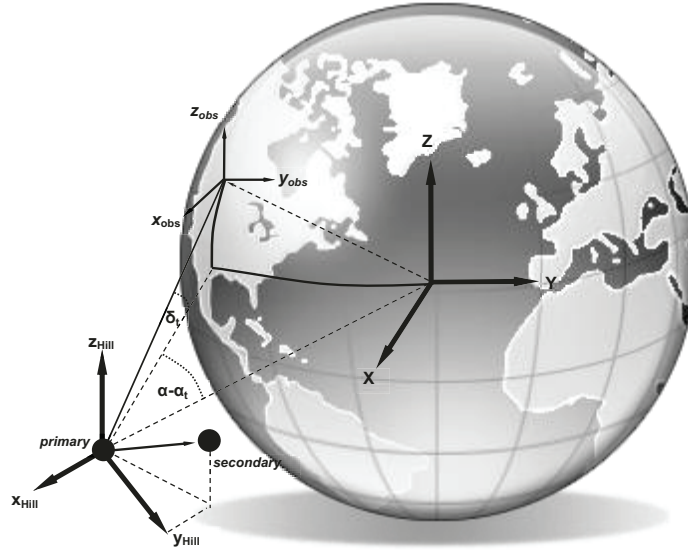


Figure 39: Hour angle ($\alpha - \alpha_t$) and δ_t angles with respect to the primary satellite

For observations of geostationary satellites both $(\alpha - \alpha_t)$ and δ_t do not exceed $\pm 8.5^\circ$ as a geostationary satellite cannot be viewed from a ground-based location at elevation angles lower than the horizon. These angles are usually smaller as geostationary satellites are observed well above the horizon due to atmospheric extinction and high refraction. For geostationary satellites which are relatively high in the sky (elevations greater than 25 degrees), a small angle approximation to equation 3.33 can be made

$$\begin{bmatrix} \Delta\alpha_t \\ \Delta\delta_t \end{bmatrix} = \frac{1}{\rho_t} \begin{bmatrix} (\alpha - \alpha_t) & 1 & 0 & 0 & 0 & 0 \\ -\delta_t & \delta_t(\alpha - \alpha_t) & 1 & 0 & 0 & 0 \end{bmatrix} \begin{bmatrix} \vec{r}_{Hill} \\ \vec{v}_{Hill} \end{bmatrix} \quad (3.34)$$

The observation transformation from Hill state variables to observed differential angles in equation 3.34 is directly sensitive to changes in the y, z components of the Hill position vector \vec{r}_{Hill} and partially sensitive to changes in the x position of \vec{r}_{Hill} . The parameters $(\alpha - \alpha_t)$ and δ_t are radian quantities each of having a maximum extent of ~ 0.07 radians. A discussion of observability of the relative orbit is presented in Chapter 6 as these small quantities impact the convergence of an orbital solution.

Figure 39 and equation 3.34 show that if the ground station and the satellite are at the same longitude ($\alpha - \alpha_t = 0$) then $\Delta\alpha$ measurements become insensitive to changes in the radial position x of the servicer. Likewise, if the observer is on Earth's equator ($\delta_t = 0$) then $\Delta\delta$ measurements are insensitive to both radial and in-track motion of the client.

3.4 Relative motion model

Relative motion for satellite intercept, rendezvous and docking has been extensively studied for both LEO and GEO space flight. Most analysis begins by an examination of the inertial equations of motion for a satellite about the Earth center. For a satellite undergoing two-body motion, and under the influence of perturbation accelerations, the differential equation of motion is

$$\ddot{\vec{r}} = -\mu \frac{\vec{r}}{|\vec{r}|^3} + (\vec{a}_{grav} + \sum \vec{a}_{3rdBody}) + (\vec{a}_{drag}) + (\vec{a}_{SRP}) + (\vec{a}_{Thrust}) \quad (3.35)$$

where \vec{r} is the position vector of the object, \vec{a}_{grav} is perturbation due to non-spherical forces such as J_2 and or sectoral/tesseral gravitational influence, $\sum \vec{a}_{3rdBody}$ are gravitational accelerations from the Sun, Moon or large planetary bodies in the solar system, \vec{a}_{drag} is atmospheric drag deceleration usually applicable to low earth orbits, and \vec{a}_{SRP} is solar-radiation pressure force, a strong acceleration affecting deep space satellite orbits.

For relative motion flight the difference between the servicer and the client satellite is desired

$$\vec{r}_{rel} = \vec{r}_{servicer} - \vec{r}_{client} \quad (3.36)$$

Differentiating twice gives the accelerations in order to use equation 3.36.

$$\ddot{\vec{r}}_{rel} = \ddot{\vec{r}}_{servicer} - \ddot{\vec{r}}_{client} \quad (3.37)$$

Taking the difference between the dynamics model of equation 3.35 for two satellites and using subscript $_{2-1}$ to denote the difference between the two perturbative accelerations of the servicer (2) and client (1) objects, yields a general expression for the relative position between the satellites

$$\begin{aligned}
\ddot{\vec{r}}_{rel} &= \ddot{\vec{r}}_{serv} - \ddot{\vec{r}}_{client} \\
&= -\mu \frac{\vec{r}_{serv}}{|\vec{r}_{serv}|^3} + \mu \frac{\vec{r}_{client}}{|\vec{r}_{client}|^3} + (\vec{a}_{grav} + \vec{a}_{3rdBody})_{2-1} \\
&\quad + (\vec{a}_{drag})_{2-1} + (\vec{a}_{SRP})_{2-1} + (\vec{a}_{Thrust})_{2-1}
\end{aligned} \tag{3.38}$$

For a client satellite located in GEO orbit, atmospheric drag can be safely ignored. If client and servicer are both satellites in close proximity, Earth's aspheric gravitational perturbation and third-body gravitational forces $(\vec{a}_{grav} + \vec{a}_{3rdBody})_{2-1}$ can also be ignored [67] as their vector magnitudes and direction are comparable. Thrust from the primary satellite is ignored in this analysis, however, servicer satellite thrust can be included by modelling thrust acceleration and numerically integrating equation 3.38. Solar Radiation Pressure (SRP) is a strong perturbation in GEO orbit and closely-spaced satellites would experience a differential SRP acceleration due to their different cross-sectional areas and reflectivity. Differential SRP will be analyzed in more detail in the next section.

Using the assumptions above, equation 3.38 can be simplified for closely-spaced geostationary satellites. The relative motion equation becomes

$$\ddot{\vec{r}}_{rel} = \mu \left(\frac{\vec{r}_{client}}{|\vec{r}_{client}|^3} - \frac{\vec{r}_{serv}}{|\vec{r}_{serv}|^3} \right) + (\vec{a}_{SRP})_{2-1} + (\vec{a}_{Thrust})_2 \tag{3.39}$$

The key dynamics of the relative motion in equation 3.39 is contained within the first bracketed term which described the two-body dynamics of the satellite and servicer. A linearized solution is possible for the two-body dynamics assuming a circular orbit and small separation distances between the two objects.

3.4.1 Linearized relative motion model

The Clohessy Wiltshire [56], or Hill's equations [96] describe a linearized case of equation 3.39 ignoring solar radiation pressure and thrust. They can be used to describe the baseline of formation flight for near-circular orbits. One key assumption is that the separation distance between satellites \vec{r}_{rel} is much smaller than the semi-major axis size of the primary. For an OOS case where the servicer is within 1 km of the client, the ratio of the maximum separation to the semi-major axis size is $\sim 0.002\%$ which makes Hill equations a good approximation to model the relative motion of close proximity satellites.

The equations of relative motion of a secondary object relative to its primary satellite are described by equation 3.40 which is a coupled, second-order differential equation

$$\begin{bmatrix} \ddot{x} \\ \ddot{y} \\ \ddot{z} \end{bmatrix} = \begin{bmatrix} 2\omega\dot{y} + 3\omega^2x \\ -2\omega\dot{x} \\ -\omega^2z \end{bmatrix} + \begin{bmatrix} a_x \\ a_y \\ a_z \end{bmatrix} \quad (3.40)$$

Equation 3.40 shows that the radial direction (x) and the in-track direction (y) are dynamically coupled. The cross-track coordinate (z) is uncoupled from the other two coordinate directions in this model. This uncoupling of the cross-track component of motion is a simplification as satellites with cross-track separations actually incur a tiny radial component [97]. This is due to the curved geometry of real orbits departing from the idealized Cartesian frame representation of the Hill equations. This effect will be neglected for relative orbit estimation of very closely-spaced GEO satellites.

Expressed in state space form, equation 3.40 is recast as

$$\dot{\mathbf{x}} = \mathbf{A}\mathbf{x} + \mathbf{f} \quad (3.41)$$

where the matrices \mathbf{A} and \mathbf{f} are defined as

$$\mathbf{A} = \begin{pmatrix} 0 & 0 & 0 & 1 & 0 & 0 \\ 0 & 0 & 0 & 0 & 1 & 0 \\ 0 & 0 & 0 & 0 & 0 & 1 \\ 3\omega^2 & 0 & 0 & 0 & 2\omega & 0 \\ 0 & 0 & 0 & -2\omega & 0 & 0 \\ 0 & 0 & -\omega^2 & 0 & 0 & 0 \end{pmatrix} \quad \mathbf{f} = \begin{pmatrix} 0 \\ 0 \\ 0 \\ a_x \\ a_y \\ a_z \end{pmatrix} \quad (3.42)$$

and the state vector, with the Hill subscript removed, is

$$\mathbf{x} = [x \quad y \quad z \quad \dot{x} \quad \dot{y} \quad \dot{z}]^T \quad (3.43)$$

A closed-form solution can be obtained from 3.40 [65] and is expressed as:

$$\begin{bmatrix} x(t) \\ y(t) \\ z(t) \\ \dot{x}(t) \\ \dot{y}(t) \\ \dot{z}(t) \end{bmatrix} = \begin{bmatrix} 4-3\cos(\omega_{\oplus}t) & 0 & 0 & \frac{1}{\omega_{\oplus}}\sin(\omega_{\oplus}t) & \frac{2}{\omega_{\oplus}}(1-\cos(\omega t)) & 0 \\ 6(1-\cos(\omega_{\oplus}t)) & 1 & 0 & \frac{2}{\omega_{\oplus}}(\cos(\omega_{\oplus}t)-1) & \frac{4}{\omega_{\oplus}}(\sin(\omega_{\oplus}t)-3t) & 0 \\ 0 & 0 & \cos(\omega_{\oplus}t) & 0 & 0 & \frac{1}{\omega_{\oplus}}\sin(\omega_{\oplus}t) \\ 3\omega_{\oplus}\sin(\omega_{\oplus}t) & 0 & 0 & \cos(\omega_{\oplus}t) & 2\sin(\omega_{\oplus}t) & 0 \\ 6\omega_{\oplus}(\cos(\omega_{\oplus}t)-1) & 0 & 0 & -2\sin(\omega_{\oplus}t) & 4\cos(\omega_{\oplus}t)-3 & 0 \\ 0 & 0 & -\omega_{\oplus}\sin(\omega_{\oplus}t) & 0 & 0 & \cos(\omega_{\oplus}t) \end{bmatrix} \begin{bmatrix} x_0 \\ y_0 \\ z_0 \\ \dot{x}_0 \\ \dot{y}_0 \\ \dot{z}_0 \end{bmatrix} \quad (3.44)$$

where ω_{\oplus} is the mean angular rate of geostationary orbit (7.29×10^{-5} radians/second) and t is referenced to a suitable epoch.

Equation 3.44 can be written compactly using state transition matrix notation. The initial state $\vec{\mathbf{x}}(\mathbf{t}_0)$ and final state $\vec{\mathbf{x}}(\mathbf{t})$ are related via the state transition matrix $\Phi(\mathbf{t}, \mathbf{t}_0)$. The state transition matrix is the interior 6x6 matrix from equation 3.44.

$$\vec{\mathbf{x}}(\mathbf{t}) = \Phi(\mathbf{t}, \mathbf{t}_0)\vec{\mathbf{x}}(\mathbf{t}_0) \quad (3.45)$$

where $\Phi(\mathbf{t}, \mathbf{t}_0)$ is

$\Phi(\mathbf{t}, \mathbf{t}_0)$

$$= \begin{bmatrix} 4-3\cos(\omega_{\oplus}t) & 0 & 0 & \frac{1}{\omega_{\oplus}}\sin(\omega_{\oplus}t) & \frac{2}{\omega_{\oplus}}(1-\cos(\omega t)) & 0 \\ 6(1-\cos(\omega_{\oplus}t)) & 1 & 0 & \frac{2}{\omega_{\oplus}}(\cos(\omega_{\oplus}t)-1) & \frac{4}{\omega_{\oplus}}(\sin(\omega_{\oplus}t)-3t) & 0 \\ 0 & 0 & \cos(\omega_{\oplus}t) & 0 & 0 & \frac{1}{\omega_{\oplus}}\sin(\omega_{\oplus}t) \\ 3\omega_{\oplus}\sin(\omega_{\oplus}t) & 0 & 0 & \cos(\omega_{\oplus}t) & 2\sin(\omega_{\oplus}t) & 0 \\ 6\omega_{\oplus}(\cos(\omega_{\oplus}t)-1) & 0 & 0 & -2\sin(\omega_{\oplus}t) & 4\cos(\omega_{\oplus}t)-3 & 0 \\ 0 & 0 & -\omega_{\oplus}\sin(\omega_{\oplus}t) & 0 & 0 & \cos(\omega_{\oplus}t) \end{bmatrix} \quad (3.46)$$

3.4.2 Solar radiation pressure adjustment

It is well-established that Solar Radiation Pressure (SRP) perturbs active geostationary satellites by causing eccentricity variations in their orbits [12]. SRP causes a differential acceleration as the area-to-mass ratio and objects' reflectivity and cross-sectional area are not likely to be equal. The relative motion model (equation 3.44) must be adjusted to compensate for this effect.

The differential solar radiation pressure acceleration ($\vec{\mathbf{a}}_{SRP}$) is modelled as the difference between the sunward-projected area-to-mass ratios of the objects and their coefficients of reflectivity C_r . This acceleration is expressed as:

$$\vec{\mathbf{a}}_{SRP} = -P_{Sun} \left(\left(\frac{C_{RA}}{M} \right)_2 - \left(\frac{C_{RA}}{M} \right)_1 \right) \frac{\vec{\mathbf{r}}_{Sun}}{|\vec{\mathbf{r}}_{Sun}|^3} \quad (3.47)$$

where

$$\vec{\mathbf{a}}_{SRP} = -P_{Sun} \gamma \frac{\vec{\mathbf{r}}_{Sun}}{|\vec{\mathbf{r}}_{Sun}|^3} \quad (3.48)$$

where the vector $\vec{\mathbf{r}}_{Sun}$ is the position vector from the object to the sun and the solar range normalization $|\vec{\mathbf{r}}_{Sun}|^3$ creates a unit vector away from the satellite in the anti-solar direction. The SRP constant P_{Sun} ($4.56 \times 10^{-6} \text{ Nm}^{-2}$) is normalized to one AU. The SRP state parameter γ is the difference between the solar reflectivity, cross sectional area and mass

$$\gamma = \left(\frac{C_{RA}}{M} \right)_2 - \left(\frac{C_{RA}}{M} \right)_1 \quad (3.49)$$

Observation of OOS satellites using optical telescopes is not likely to exceed 12 hours due to the day-night cycle. This permits some simplifications to be made enabling the analytic integration of equation 3.41. The Sun's apparent motion on the celestial sphere for a 12 hour observing period is less than 0.5 degrees. Therefore, the position vector of the Sun in the inertial frame can be assumed to be nearly constant for short (nightly) observational intervals.

The equations of motion are integrated by taking the convolution of the perturbation \mathbf{f} with the unforced state transition matrix $\Phi(\mathbf{t}, \mathbf{t}_0)$ described in equation 3.41. This integration follows the form detailed by Kawasse [67]. Assuming that the sun's position is constant, the perturbation acceleration with respect to the satellite pair is expressed as

$$\begin{bmatrix} a_x \\ a_y \\ a_z \end{bmatrix} = \begin{bmatrix} -\gamma P_{sun} \cos(\delta_{sun}) \cos(\alpha - \alpha_{sun}) \\ -\gamma P_{sun} \cos(\delta_{sun}) \sin(\alpha - \alpha_{sun}) \\ -\gamma P_{sun} \sin(\delta_{sun}) \end{bmatrix} \quad (3.50)$$

where α_{sun} and δ_{sun} are the constant right ascension and declination of the sun²⁰ and α is the geocentric right ascension of the primary satellite. The state transition, accommodating the solar radiation pressure perturbation, is expressed as

$$\mathbf{x}(t_1) = \Phi(t_1, t_0)\mathbf{x}(t_0) + \gamma \mathbf{p}(t_1, t_0) \quad (3.51)$$

The convolution between the initial and final sidereal angles is expressed as

$$\gamma \mathbf{p}(\alpha_1, \alpha_0) = \int_{\alpha_0}^{\alpha_1} \Phi_u(\alpha_1 - \alpha) \mathbf{f}(\alpha) d\alpha \quad (3.52)$$

Remembering that the right ascension of a geostationary satellite rotates at the sidereal rate of rotation of the Earth (e.g. $\alpha(t) = \alpha_0 + \omega_{\oplus}(t - t_0)$) the following set of equations are obtained.

²⁰ A simple formula for computing the geocentric coordinates of the sun with accuracies of 0.01 degrees is available from Meeus [98]

$$p_1 = \frac{\gamma P_s \cos(\delta_{sun})}{4\omega} [(5 \cos(\alpha_{sun} - \alpha_1) - 8 \cos(\alpha_{sun} - \alpha_0) + 3 \cos(\alpha_{sun} - 2\alpha_0 + \alpha_1) - 2(\alpha_0 - \alpha_1) \sin(\alpha_{sun} - \alpha_1))] \quad (3.53)$$

$$p_2 = \frac{-\gamma P_s \cos(\delta_{sun})}{2\omega} [(2 \sin(\alpha_{sun} - \alpha_0) - 5 \sin(\alpha_{sun} - \alpha_1) + 3 \sin(\alpha_{sun} - 2\alpha_0 + \alpha_1) + 6(\alpha_0 - \alpha_1) \cos(\alpha_{sun} - \alpha_0) + 2(\alpha_0 - \alpha_1) \cos(\alpha_{sun} - \alpha_1))] \quad (3.54)$$

$$p_3 = \frac{\gamma P_s \sin(\delta_{sun})}{\omega} [\cos(\alpha_0 - \alpha_1) - 1] \quad (3.55)$$

$$p_4 = \frac{-\gamma P_s \cos(\delta_{sun})}{4} [(3 \sin(\alpha_{sun} - 2\alpha_0 + \alpha_1) - 3 \sin(\alpha_{sun} - \alpha_1) + 2(\alpha_0 - \alpha_1) \cos(\alpha_1 - \alpha_{sun}))] \quad (3.56)$$

$$p_5 = \frac{-\gamma P_s \cos(\delta_{sun})}{2} [(3 \cos(\alpha_{sun} - \alpha_1) - 6 \cos(\alpha_{sun} - \alpha_0) + 3 \cos(\alpha_{sun} - 2\alpha_0 + \alpha_1) - 2(\alpha_1 - \alpha_0) \sin(\alpha_1 - \alpha_{sun}))] \quad (3.57)$$

$$p_6 = \gamma P_s \sin^2(\delta_{sun}) (\sin(\alpha_1 - \alpha_0)) \quad (3.58)$$

Now the state must be adjusted to accommodate the presence of the new state parameter γ in the estimation process. The state is adjusted by adding the parameter:

$$\mathbf{x} = [x \quad y \quad z \quad \dot{x} \quad \dot{y} \quad \dot{z} \quad \gamma]^T \quad (3.59)$$

The state transition matrix is then augmented with the solar radiation pressure equations $p_1 \dots p_6$ [67]:

$$\Phi_{(s_1, s_0)} = \begin{pmatrix} \Phi_u & p_1(\alpha_1, \alpha_0) \\ & \vdots \\ & p_6(\alpha_1, \alpha_0) \\ \hline 0 \dots 0 & \mathbf{I} \end{pmatrix} \quad (3.60)$$

The state transition matrix in equation 3.60 model the dynamics of the state (equation 3.59) capturing both the linearized motion from the Hill equations and the differential SRP dynamics.

3.5 Relative orbit determination

Orbit determination is segmented into two primary areas 1) Initial Orbit Determination (IOD) and 2) Optimal orbit determination (OD). Initial orbit determination is a coarse estimate designed to yield a good starting point for optimal orbit estimation routines such as Least Squares or a Sequential filter to converge on an estimate. Optimal orbit determination is designed to produce the best state estimate by minimizing the mean square residual error from the fitted trajectory and the measurements. Optimal orbit estimation can produce estimates of much higher fidelity than IOD as they process all available information adhering to a proper force model.

3.6 Initial orbit determination for OOS satellites in proximity flight

IOD does not produce an orbit of suitable quality for precise orbit propagation or other analysis as it is intended to initialize least squares estimation algorithms or a sequential filter. Common methods of obtaining IOD using a set of angular data include: Laplace's method and Gooding's Angles Only Algorithms [65]. Each of these algorithms uses a short arc of measurement data—usually three sets of observations—to solve for a coarse initial state estimate $[\bar{\mathbf{r}} \quad \bar{\mathbf{v}}]^T$.

For OOS monitoring, a simple IOD was created based on the assumption that the objects' relative in-track drift rates are zero. This is a reasonable assumption as satellite pair would rapidly separate from one another after a few orbital revolutions if the radial offset between the two satellites were large. The simple algorithm described below creates a coarse state estimate based on simple forward difference equations on the measurement data.

To start, a slant-range distance ρ_t from the observer to the client satellite is required. This can be easily obtained from general perturbation two-line-elements²¹ by propagating the orbit using a variety of astrodynamics tools such as STK™ or Freeflyer™. A timespan of differential angles data is required but in this case a pair of observations can be used $(t_1, \Delta\alpha_1, \Delta\delta_1)$ and $(t_2, \Delta\alpha_2, \Delta\delta_2)$.

The key assumption for close-proximity flight is that the relative drift rates between the two objects are near zero. This approximation constrains the initial in-track velocity to initial radial position, such that

$$\dot{y}_0 = -2\omega_{\oplus}x_0 \quad (3.61)$$

As the detector's image plane is roughly aligned with the in-track and cross-track directions of the primary satellite's motion it can be assumed that the in-track motion is directly coupled to $\Delta\alpha$ measurements. Similarly, the cross-track direction is directly coupled to $\Delta\delta$ measurements (See Figure 40).

Computing the quantities in table 4 provides a coarse estimate for the initial relative orbit of the client about the servicer. The radial velocity \dot{x}_0 is not observable from these equations and it is assumed that this velocity is small for close proximity flight by setting it to be half of the initial in-track (\dot{y}_0) velocity.

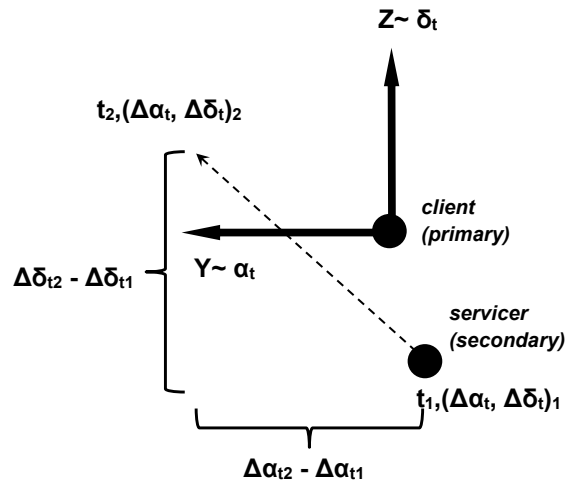


Figure 40: Looking along the line of sight from a ground based observer to client-servicer pair.

²¹ Two line element sets are available from SpaceTrack.org , <https://www.space-track.org> [99]

Table 4 Initial relative orbit estimate for GEO On-Orbit Servicing

Initial Hill State Variable	IOD Approximation	Equation
x_0	$\approx -\frac{\rho(\Delta\alpha_2 - \Delta\alpha_1)}{2\omega_{\oplus}\Delta t}$	(3.62)
y_0	$\approx \rho(\Delta\alpha_1)$	(3.63)
z_0	$\approx \rho(\Delta\delta_1)$	(3.64)
\dot{x}_0	$\approx -\omega_{\oplus}x_0$	(3.65)
\dot{y}_0	$\approx \frac{\rho(\Delta\alpha_2 - \Delta\alpha_1)}{\Delta t}$	(3.66)
\dot{z}_0	$\approx \frac{\rho(\Delta\delta_2 - \Delta\delta_1)}{\Delta t}$	(3.67)

3.6.1 Optimal Orbit determination for OOS proximity orbits

With the dynamics model expressed in equation 3.60, and the measurement model for a near zero inclination geostationary satellite (equation 3.33), a Kalman²² Filter implementation was selected for relative orbit estimation. The linearized dynamics and measurement model was well suited for relative orbit estimation and provides insight into the time varying aspects of the covariance.

The relative orbit estimation process used for this research is outlined in Table 5. The definitions of the state variables appear in the table of notation in Appendix B.1. The initial state and covariance for the estimation process used for the experimental stages later in this research was set directly using the state estimate from the satellite operator and using a large initial covariance of 1 km position error.

²² An overview of Batch Least Squares, the Kalman filter and Extended Kalman filter algorithms used for orbit determination is provided in Appendix B.

Table 5 Sequential Estimation Overview for OOS

Initialize state and covariance	$\hat{\mathbf{x}}(t_0) = \hat{\mathbf{x}}_0$	(3.68)
Predict	$\bar{\mathbf{x}}_{k+1} = \Phi_{k+1,k} \hat{\mathbf{x}}_k$	(3.69)
	$\bar{\mathbf{P}}_{k+1} = \Phi \mathbf{P}_k \Phi^T + \mathbf{Q}$	(3.70)
Compute Kalman Gain	$\mathbf{K}_k = \bar{\mathbf{P}}_k \mathbf{H}_k^T [\mathbf{H}_k \bar{\mathbf{P}}_k \mathbf{H}_k^T + \mathbf{R}_k]^{-1}$	(3.71)
Compute State Update	$\hat{\mathbf{x}}_{k+1} = \bar{\mathbf{x}}_k + \mathbf{K}_k (\mathbf{y}_k - \mathbf{H} \bar{\mathbf{x}}_k)$	(3.72)
	$\bar{\mathbf{P}}_{k+1} = (\mathbf{I} - \mathbf{K}_k \mathbf{H}) \bar{\mathbf{P}}_k$	(3.73)

3.7 Chapter summary and contributions

This chapter's detailed the development of a generalized measurement matrix (equation 3.26) for differential angles observations on closely-spaced OOS satellites in GEO orbit. While the measurement approach shares similarities with Kawase's work [67], an observational frame definition meeting the practical observational needs for 1) the use of optical telescopes to measure small (arcsecond level) differential angles on satellites; and 2) a transformation relating celestially referenced, differential angles to the motion of geosynchronous satellites, has not been published previously. Prior art in this area focuses on the use of azimuth-elevation measurements using radio ranging systems. While these techniques are similar, altitude-azimuth measurements are not practical to implement on with optical speckle imagery. Optical detection has the added benefit of not requiring cooperation from either satellite during observation.

This chapter adapted a relative motion model based on the Clohessy-Wiltshire (Hill) equations of motion using Kawase's modification for solar radiation pressure. This model is an appropriate, linearized and compact dynamics description suited for single-evening optical observations of satellites performing OOS. A coarse estimate for initial relative-orbit determination based on a short track of differential angles measurements is provided along with a description of the Kalman Filter approach used for relative orbit estimation.

Chapter 4: Signal modelling, instruments, and image processing

This chapter provides an overview of satellite detectability modelling and its adaptation for speckle interferometric measurements of satellites performing OOS. As EMCCD detector technology was selected for high frame rate, low light detection of closely-spaced satellites the expression for the EMCCD signal-to-noise ratio is also provided. Estimates for the signal-to-noise model for speckle imaging based on the interplay of atmospheric and telescope effects are also presented and adapted to the OOS problem.

4.1 Signal modelling for space surveillance sensors

Silicon Charged Couple Device (CCD) detectors sense photons by registering photoelectrons raised on a semiconductor after a photon impacts the crystal lattice of the CCD. The probability that a photon is converted into a photoelectron during this impact is referred to as Quantum Efficiency (QE). QE varies with wavelength (see example in Figure 36). Most modern, visible band CCDs have QE peaking at ~90% QE for 550 nm wavelengths and are generally have sensitivity over a range of wavelengths varying from 300 nm to 1100 nm. Different detector chemistry can be used to detect the near infrared (Indium Gallium Arsenide) or far infrared (Mercury Cadmium Telluride) in order to operate in different detection wavebands.

The detection of astronomical objects using CCDs is modelled using the CCD equation [100]. Hejduk [91] presented a slightly modified CCD equation intended for the detection of deep-space orbiting satellites for both inertially fixed (sidereal stare) and for rate-track (analogous to stellar imaging) modes of tracking. Hejduk's equation ignores shot noise and models the mean signal of the satellite above the background noise in order to estimate the probability of detection for a given false alarm rate. Shell [101] provided a similar detection model albeit excluding dark noise on CCDs (a reasonable assumption for modern CCDs).

The rate \dot{S} that photoelectrons are generated on a CCD is

$$\dot{S} = A_{eff} \langle QE \rangle F_0 10^{-0.4T M v} \tau_{atm} \quad (\text{photoelectrons/sec}) \quad (4.1)$$

where A_{eff} is the effective light gathering area of the telescope, $\langle QE \rangle$ is the solar weighted quantum efficiency of the optical detector, F_0 is the flux of a zero magnitude²³ star in photons/meter²/s and τ_{atm} is the atmospheric transmittance (approximately 0.65 for low altitude sites). To determine the number of photons per second that impacting a detector the $\langle QE \rangle$ term simply needs to be removed from equation 4.1.

For point-source objects the integrated signal intensity on the best pixel²⁴ of a CCD detector is

$$S_T = \dot{S}T_{exp}k_f = A_{eff}\langle QE \rangle F_0 10^{-0.4T_{Mv}}\tau_{atm}T_{exp}k_f \quad (4.2)$$

where T_{exp} is the integration time of the CCD camera and k_f is the ensquared energy, or the percentage of energy from the object which illuminates the best pixel on the CCD array. For most wide-field space surveillance telescopes, k_f is between 0.3-0.5. Systems that prefer centroid accuracy over sensitivity will reduce this factor to a scale of 0.1 or less as this increases the effective number of pixels across the point spread function.

Noise sources from a CCD and the sky background are added in quadrature

$$\sigma = \sqrt{N_{sys}^2 + BT_{exp} + N_{DC}T_{exp}} \quad (4.3)$$

where N_{sys}^2 is the read noise of the CCD (a function of the CCD read-out rate), B is the background sky surface flux and N_{DC} is the dark current.

The sky background generation rate is estimated by

$$B = (10^{-0.4B_{vm}})A_{eff}\langle QE \rangle F_0 \alpha_p^2 \quad (4.4)$$

where the surface brightness of the sky B_{vm} is expressed in magnitudes per square arcsecond and α_p is the pixel pitch of the detector in arcseconds/pixel. In the visual band, the background sky brightness for a dark astronomical site is approximately 21.5

²³ The flux from a zero magnitude star in the visual band is approximately 5.67×10^{10} photons/s/m². For the infrared bands where most of the speckle interferometry observations are collected, the flux rate of 1.15×10^{10} photons/s/m² is used (equivalent to 4760 Jy with $\Delta\lambda/\lambda=0.16$ at 1.51×10^7 photons/s/m²/Jy)

²⁴The “best pixel” is the detector pixel which senses the largest fraction of energy in a point spread function.

magnitude/arcseconds² whereas a bright urban area can experience deleterious sky brightness of <19 magnitude /arcseconds².

4.2 Signal modelling for EMCCDs

EMCCDs are gaining popularity for the detection of faint astronomical sources due to their high frame rates, and low read noise. The use of charge amplification on the output serial register enables very high signal to noise ratios to be achieved. Their wavelength sensitivity range and high quantum efficiencies are comparable to standard CCDs albeit they can operate at much higher frame rates.

The CCD equation for EMCCDs is adjusted slightly due of the use of the mean EM gain G which reduces the read noise N_{sys} . There are other EMCCD-unique noise terms which must be included in the CCD equation to compute the signal-to-noise ratio. The expression for the EMCCD SNR equation is

$$\frac{S}{N} = \frac{S_T}{\sqrt{\left(\frac{N_{Sys}}{G}\right)^2 + F^2(BT_{Exp} + N_{DC}T_{Exp} + N_{CIC} + S_T)}} \quad (4.5)$$

The equation is modified with the clock induced charge signal N_{CIC} which is the spurious generation of electrons that result from high frequency clocking of pixels on the EMCCD array. F^2 is the multiplicative noise term caused the statistical amplification nature of the EMCCD ($F^2=2$). EM gain for most EMCCDs is user selectable between 2 to 1000 (or more) depending on the camera architecture. The pixel readout rate of the EMCCD is also user selectable which also sets the readout noise of the detector.

DRDC's Ottawa small aperture telescope (described later in this chapter) has EM gain range spanning 2-1000. The selection of the read rate depends on the size of the pixel array being read out, and the desired read noise on the detector. For most small aperture detections, a readout rate of 10 MHz was selected which corresponds to a read noise level of 40 e⁻/pixel. Applying an EM Gain of ~300 for most speckle measurements the read noise is effectively reduced to 0.1 e⁻/pixel.

4.3 Signal modelling for speckle interferometry

Signal modelling determines the detectability of an OOS satellite pair when viewed using speckle imaging. Several authors [102],[103],[104] have examined the signal to noise ratio for speckle interferometry for both speckle imaging of binary stars or to enable Knox Thompson image reconstruction. The signal modelling that follows adheres to the work by Miller [102] and notations are adopted corresponding to the work of Lawrence [62],Welsh [105] and Hoffman [106]. For the satellite tracking case, the convention where the signal-to-noise ratio is modelled at $\frac{1}{2}$ of the diffraction limit is upheld. This is consistent with the modelling approach by Miller [102].

The signal-to-noise ratio for speckle interferometry [105] is expressed as

$$\text{SNR} = \sqrt{m} \frac{\overline{S_T}^{-2} |O_n(u)|^2 \overline{|\tau_j(u)|}^2}{\overline{S_T}^{-2} |O_n(u)|^2 \overline{|\tau_j(u)|}^2 + \overline{S_T} + N_{pix} \sigma_r^2} \quad (4.6)$$

where $\overline{S_T}$ is the number of detected photo-electrons per frame, $\tau_j(u)$ is the optical transfer function for exposure time T_{exp} and spatial frequency u , $|O_n(u)|$ is the normalized object spectrum, m is the number of images in the measurement stack, N_{pix} is the number of pixels in the image and σ_r^2 is the variance of the detector noise in e^-/pix .

The finite integration time of a fast imaging camera image averages the fast changing nature of the speckles. O'Donnell [104] and Parry [107] identified that the temporal correlation of the speckles, assuming a stationary process, adheres to an exponential decaying process where the modulus of the instantaneous optical transfer function can be expressed as

$$\overline{|\tau_j(u)|}^2 = \frac{1}{T_{exp}} \int_{-T_{exp}}^{T_{exp}} \left(1 - \frac{|t|}{T_{exp}}\right) R_\tau(t) dt \quad (4.7)$$

where t is a dummy integration variable and $R_\tau(t)$ is the temporal autocorrelation function.

The temporal autocorrelation $R_\tau(t)$ has $1/e$ decay rates proportional to T_{exp}/τ_0 where τ_0 is the coherence time of the atmosphere. Parry [107] found that a decaying Gaussian model best fitted temporal autocorrelation data and modelled $R(t')$ as

$$R(t') = e^{\left(-\frac{t'}{\tau_0}\right)^2} \quad (4.8)$$

This effect of the temporal autocorrelation is primarily used for determining the optimal exposure time for a given set of atmospheric conditions. Lawrence shows the optimum exposure time is typically between $1.6\tau_0$ and $10\tau_0$ for photon counting detectors ($N_{sys} = 0 \text{ e}^-/\text{pix}$) and typical CCD cameras ($N_{sys} = 12 \text{ e}^-/\text{pix}$) respectively.

We now examine the case of the signal-to-noise ratio for two satellites in close proximity to one another detected at $1/2$ of the diffraction limit of a telescope.

4.3.1 Estimating the minimum number of images to detect a secondary satellite

An estimate for the minimum number of images m to obtain a given signal-to-noise ratio of for the detection of a primary satellite of magnitude M and its servicer of relative magnitude Δm is now described. Signal modelling uses the high frequency wing of the Labeyrie-Korff transfer function (equation 2.16) and assumes that the spatial frequencies of interest are above the seeing cutoff r_0/λ .

$$\langle |\tau(\mathbf{u})|^2 \rangle \approx \tau_{DL}(\mathbf{u}) \left(0.435 \left(\frac{r_0}{D} \right)^2 \right) \quad (4.9)$$

where the diffraction-limited transfer function $\tau_{DL}(\mathbf{u})$ is expressed as equation 2.14 and is the spatial frequency with respect to the diffraction limit. For this signal-to-noise estimation the normalized spatial frequency is set to $\mathbf{u} = 1/2$ which is the center of the high frequency wing in equation 4.9.

The number of signal photons impacting the detector in an exposure time T_{exp} is

$$\overline{S_T}(T_{exp}) = \frac{\pi}{4} D^2 F_0 T_{exp} (10^{-0.4M1} + 10^{-0.4M2}) \quad (4.10)$$

and $|O_n(|\mathbf{u}|)|^2$ is the normalized object function which is set to equal unity when $u = 0$ requiring equation 2.20 to be divided by $1 + 2\alpha_b + \alpha_b^2$. The mean signal level of equation 2.20 ($|\overline{O(u)}|^2 = 1 + \alpha_b^2$) is used to estimate the signal in equation 4.6, thus

$$|O_n(|\mathbf{u}|)|^2 \approx \frac{1 + \alpha_b^2}{1 + 2\alpha_b + \alpha_b^2} \quad (4.11)$$

The required number of stacked frames to achieve SNR=6 is shown in Figure 41. This simulation assumes $r_0 = 10$ cm, $QE = 0.65$ in the infrared, $T_{exp} = 10$ ms, $N_{pix} = 512^2$ pixels and read noise of $0.1e^-$. Plots for various aperture diameters are shown

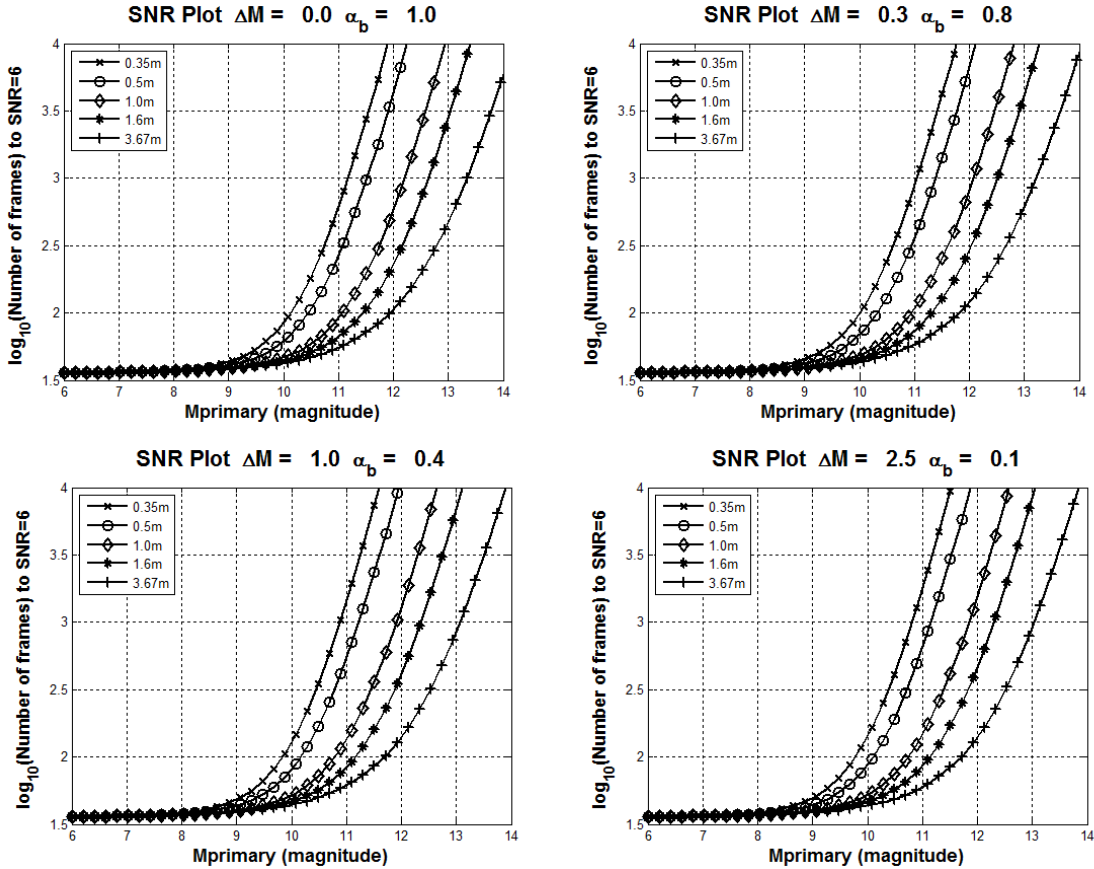


Figure 41: Number of frames estimated from equation 4.6 required to achieve $SNR = 6$ for various aperture diameters and object magnitudes

The plots show an interesting feature in that bright objects (less than magnitude 9) have similar requirements for the number of frames to achieve SNR=6. The effect is known and was explained by Miller [102]. At these high target signal levels, equation 4.6 saturates according to $SNR = \sqrt{m}$. In contrast, at low signal levels, the signal-to-noise

ratio of equation 4.6 is dominated by the number of photons per speckle $(D/r_0)^2$. This causes the quasi-exponential appearance to the plots in Figure 41.

These results suggest that a small aperture telescope stacking between 300-500 speckle images can detect large a geostationary satellite of $M_{primary} \sim 10.5$ with a neighboring servicer of $\sim 13^{\text{th}}$ magnitude separated by ~ 180 meters²⁵. In practice, small aperture telescope measurements performed in this research on binary stars and satellites were not successful at detecting objects much fainter than magnitude 11 indicating that the plots are somewhat optimistic. This is likely due to the effect where the temporal autocorrelation of the atmosphere is ignored (equation. 4.7). In addition, the effective light gathering area of the telescope is assumed to be using a full unobstructed aperture whereas real telescopes usually have a secondary mirror which reduces the light gathering power of the telescope. More complex approaches to signal to noise ratio modelling (Welsh [105]) can possibly account for the difference between theoretical and observed signal-to-noise estimates.

The plots do suggest that there is a preferred time frame to observe GEO satellites undergoing OOS. Most geostationary satellites tend to be brightest when viewed with phase angles of ± 30 degrees or less (see Figure 8). Figure 41 indicates that small to medium aperture telescopes can detect an object $1/10$ the size (e.g. $\alpha_b = 0.1$) of the primary satellite with ~ 100 frames per stack over a primary satellite magnitude range of 9.5 to 10.5. Most geostationary satellite bus light curves (Figure 8) tend to have these magnitudes when the satellite is within 30 degrees of the anti-solar direction. This suggests that in order to detect a servicer $1/10$ the size of the primary satellite the observations need to occur when the phase angle effects brighten the primary and secondary satellite.

In chapter 6 it will be shown that relative orbit estimates need approximately 3 hours of tracking data in order to estimate of the radial position of the secondary satellite. This result, coupled with the need to track the satellites within the anti-solar direction,

²⁵ The small aperture telescope's diffraction limit described later in this chapter is 0.47 arcseconds. Twice the diffraction limit corresponds to a projected separation between objects in GEO of ~ 182 m.

encourages this type of observation to occur within 30 degrees of the anti-solar direction; unless larger aperture telescopes are available to collect observations.

4.4 Speckle instrument configuration

A speckle imaging instrument designed to track satellite OOS activities in GEO requires harmonization between the competing needs of detectability of satellites and high rate imagery “freezing” of the fast moving atmosphere. Most space surveillance telescopes use 1 to 5 second exposures to detect faint satellites using moderate-sized aperture telescopes ($D < 1m$). Freezing the turbulence of Earth’s atmosphere forces the instrument to expose for shorter intervals resulting in lower signal. Harmonizing signal detection with the speckled nature of the telescope is problematic when exposure times are $\sim 10^{-2}$ seconds or less. The signal-to-noise expression (see section 4.3) shows that some degree of optimization is possible. The detectors must collect imagery at very high frame rates, where collection rates of 20 Hz and higher are common.

4.4.1 Nyquist sampling of the speckles

The instrument must ensure that the detector properly samples the width of a telescope’s speckle point spread function (psf). This is achieved by ensuring more than two pixels subtend the Airy radius in order to Nyquist sample²⁶ the psf. The size of the telescope’s psf can be estimated as $psf = \lambda f/D$ where f is the focal length of the telescope. Since most CCD and EMCCD detector pixels are available in sizes from 3-13 micrometers, a focal length extension is often required for a detector to properly sample the psf.

The cross-spectrum approach was tested with the DRDC Ottawa space surveillance telescope. Nyquist sampling for this instrument required that the telescope focal length (3.91 m) be extended using Barlow lenses. The telescope has a primary mirror diameter of 35 cm and has a focal ratio (f/D) ratio of 11. The observation wavelength of interest is the Sloan i’ filter band (744 nm). In this case the width of the psf is

²⁶ Shannon-Nyquist sampling requires that a periodic signal is sampled at a sampling frequency be greater than twice the highest frequency present the signal.

$$psf = (744nm)(11) = 8.2 \mu m \quad (4.12)$$

Detector pixels for the Andor iXon EMCCD [108] attached to the prime focus of the telescope has a pixel pitch of 13 μm . Barlow lenses—a commonly available focal length extension option—are available in 2X or 4X focal extensions. In this case, a 4x focal length extension was selected yielding an effective focal length of 15.64m and an Airy radius of 32.8 μm . With the pixel sampling of the EMCCD of 13 μm , a sampling ratio of 2.52 is obtained. This is greater than the Nyquist frequency and measurements were taken using this 4x Barlow arrangement (see section 4.5).

4.4.2 General instrument arrangement

Figure 42 shows the general arrangement of a typical speckle telescope. Speckle telescopes often use narrow band filters in addition to a focuser, a Barlow extension and an EMCCD camera. To detect satellites, a wider bandwidth filter (i') is used to admit more signal photons onto the detector while alleviating chromatic dispersion at lower elevation angles.

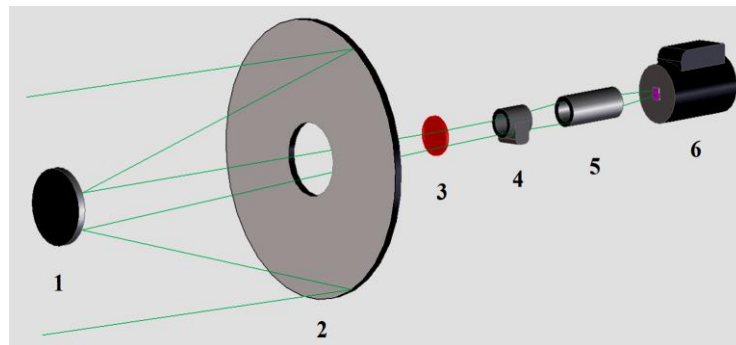


Figure 42: (Not to scale) General arrangement for a speckle imaging instrument (1) secondary mirror, (2) primary mirror, (3) Sloan i' filter, (4) focuser, (5) focal length extension via barlow lens, (6) EMCCD detector

Risley prisms (not shown in Figure 42) can be used to correct the chromatic dispersion of light passing through the telescope. To simplify the speckle instrument optical design Risley prisms were not incorporated as the small aperture speckle telescope (see next

section) was predicted to experience ~ 0.35 arcseconds of dispersion, which is less than the telescope's Airy radius of 0.47 arcseconds. This amount of uncompensated dispersion was deemed a reasonable compromise for remote telescope observation without needing an observatory attendant to manually reconfigure Risley prisms to compensate the dispersion effect. Adding another optical element to the backplane of the telescope would have further cantilevered the EMCCD increasing the likelihood of optical elements flexing under their own weight causing unwanted optical aberrations. For these reasons, Risley prisms were not incorporated in the small aperture telescope system.

4.5 Small aperture telescope testing using binary stars

DRDC Ottawa's small aperture space surveillance telescope [109] was configured²⁷ to perform speckle interferometry testing using binary stars as calibration objects. Test objectives were to configure and calibrate the cross-spectrum image processing algorithm so that speckle instrument testing could proceed without needing to wait for rare alignments of geostationary satellites. The binary stars selected for testing had separations between 0.5 to 5 arcseconds, magnitudes brighter than magnitude 11, and magnitude differences Δm of 3 magnitudes or less. These stars were selected from the Washington Double star catalog [40].

The small aperture telescope (see Figures 43,44 and Table 6) consists of a 35 cm Schmidt-Cassegrain reflecting telescope, a computerized focus ram, a filter wheel with Cousins I, Sloan i', and open filter slots. A 4X parfocal barlow lens and a thermoelectrically cooled Andor iXon 888i EMCCD with a 1024x1024 pixel array was affixed to the visual back of the telescope completing the optical assembly. The telescope is remotely computer controlled and slews to astronomical objects (and satellites) using a Software Bisque Paramount METM robotic telescope mount.

The instrument acquires 256x256 pixel images at a rate of 20 frames per second using the 10 MHz readout mode of the EMCCD. The EMCCD can operate at higher readout rates (>95 frames/sec) but higher read noise is incurred. These images are read-out to a

²⁷ An excellent reference on how to configure a speckle interferometer is described by Schneiderman and Karo [110]



Figure 43: (Left): DRDC Ottawa Space Surveillance Observatory. (Right): 35cm telescope



Figure 44: (Left): EMCCD and filter wheel. (Right): Sloan i', Cousins I filters

Table 6 DRDC Ottawa Space Surveillance Observatory system configuration

Parameter	Value	units	Notes
<u>Observatory location</u>			
latitude	45.45579°	° N	Geodetic WGS 84 coordinates
longitude	75.89101°	° W	
altitude	90	m	
<u>Optical system</u>			
Primary diameter	0.35	m	
Focal length	3.910	m	
Diffraction limit	0.43"	arcsec	
Focal extension	4x	15.64m	
<u>Detector</u>			
EMCCD pixel scale	0.171	arcsec pixel ⁻¹	
EM gain range	2-1000	-	
Instr. fov at 4X	2.9	arcmin	
Pixel pitch	13	µm	
Array dimensions	1024x 1024 (13x 13)	pixels (mm)	
Dark current	0.001	e ⁻ pix ⁻¹ sec ⁻¹	@-85°C
Full frame rate	20	Hz	
Read noise	40	e ⁻ @10 MHz	
Read noise with EM Gain	< 1	e ⁻	

data acquisition computer via a USB3 serial bus. Each image is referenced to the computer system clock which itself is steered to within 0.1 milliseconds of UTC using a GPS receiver installed in the acquisition computer PCI port. The instrument is network controlled permitting off-site observers to remotely acquire data.

A 300mm camera lens and Apogee Alta U42 CCD are affixed to the main telescope tube acting as a wide field finder to help center satellites for speckle imaging. As the main instrument has a narrow field of view (2.9 arcmin^2), pointing the telescope toward moving satellites was problematic. While the main instrument's pointing accuracy was often much better than 1 arcminute, satellites are not always located where their orbital estimates (two line elements) claim they are forecasted to be due to satellite maneuvering and sparse tracking data on their orbits. Some searching was occasionally required in order to center satellites on the EMCCD to acquire images.

4.5.1 Instrument calibration, orientation angle and pixel scale

To determine the North angle orientation angle of the detector the approach used by the binary star community was employed. The North orientation was found by exposing the detector on a bright, well separated double star for 10 seconds then abruptly turning off the mount's sidereal tracking during mid-exposure (see Figure 45). This technique resulted in a set of streaks which points west on the detector. Using the lit, streaked pixels the North orientation can be readily inferred by subtracting 90 degrees from the streak direction. To ensure that the image frame was not optically "flipped", the position angle and separation of the binary star was compared to the Washington Double Star catalog [40] to confirm the orientation angle was consistent with the measured west direction from the streaks.

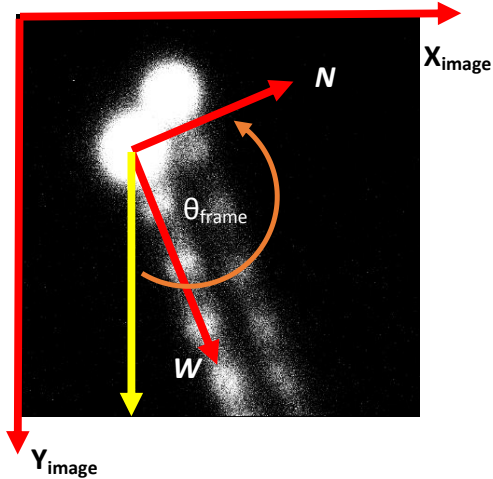


Figure 45: Drift method to determine the orientation angle of the camera

To calibrate the pixel scale a coarse estimate was made using the focal length of the instrument and the pixel size of the detector. The coarse estimate was

$$ap = 206265 \left(\frac{d_{pix}}{fl} \right) = 206265 \left(\frac{13\mu m}{4 \times 3.910m} \right) = 0.1714'' \quad (4.13)$$

Measurements of the centroids of long period binary stars were performed to confirm the pixel scale of the detector. The pixel scale was consistent with the estimate of 0.171 arcseconds. A diffraction mask was manufactured in order to attempt to precisely measure the pixel spacing of the detector. However, the diffraction mask did not produce useful fringes to measure the true pixel scale of the camera and was abandoned in favor of using binary stars as calibration references.

4.6 Image processing

Careful image processing is key to achieving cross-spectrum measurements of Earth orbiting satellites. The following sections describe the image processing steps which cross-spectrum was applied to satellite speckle observations. Image processing software was developed in Matlab using imported speckle images recorded on FITS (Flexible Image Transport System) [111] imagery. Figure 46 shows the main image processing flow diagram.

The processing begins by acquiring bias and dark frames to remove pixel-to-pixel sensitivity variations and dark (thermal) current from the EMCCD detector. Next, subtraction of the mean background from each frame is performed once a FITS speckle image is loaded into memory in MATLAB. Next, the cross-spectrum of each zero-mean image is computed using equation 2.45. Each image's cross-spectrum is added (stacked) sequentially as complex data and divided by the number of speckle images in the stack. In practice, 100 image stacks were used for the satellite tracking experiments described in the next chapter.

4.6.1 Cosmic ray rejection algorithm

A frequent issue encountered during data processing of speckle EMCCD images is rejection of images corrupted by cosmic rays. Cosmic rays are high-energy charged particles which impact the EMCCD during acquisition. These particles substantially increase the number of photoelectrons during their impact (see Figure 47, left). The cosmic ray causes a large “splash” of photoelectrons and is often higher intensity than the two speckle objects. The Fourier transform of these corrupted images resulted in additional, unwanted third object fringes (see Figure 47, right) which caused the fringe measurement algorithm to fail.

An effective way to remove frames corrupted by cosmic ray hits is to simply monitor the background standard deviation of the stacks. A cosmic ray hit can provoke a background standard deviation more than 5 times the mean of a stacks' background noise level. By monitoring the background standard deviation, cosmic ray corrupted images

were rejected from the stack making the cross-spectrum more resilient to these single events.

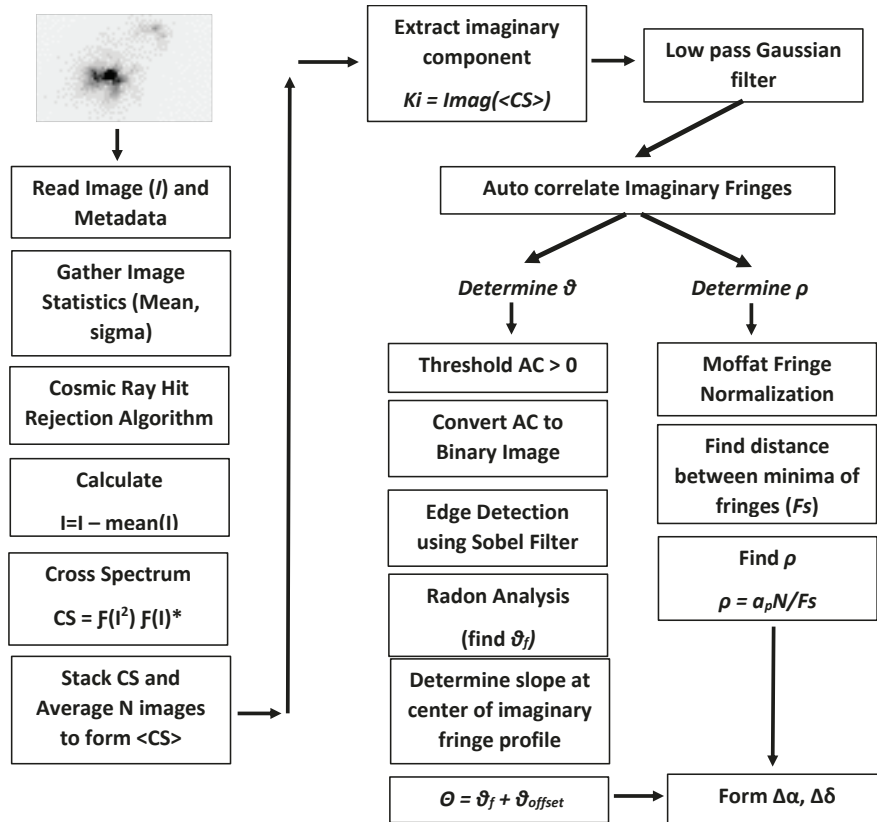


Figure 46: Image Processing Block Diagram

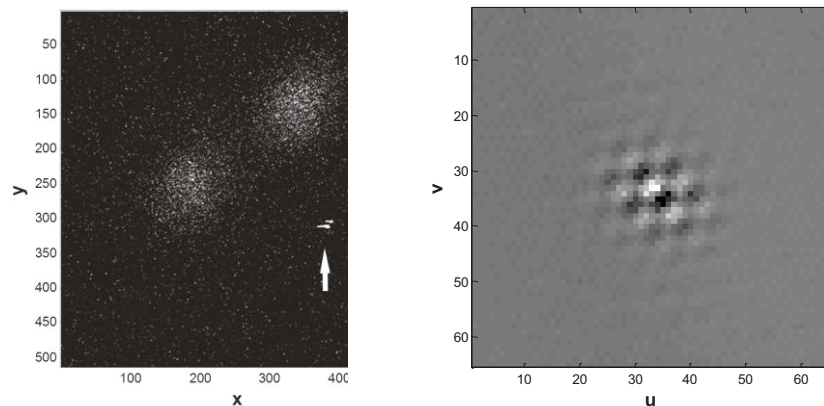


Figure 47: (Left): Cosmic ray strike. (Right): Unwanted fringing due to cosmic ray.

This simple algorithm had the additional benefit of rejecting bright background stars which occasionally appeared on the detector field of view as the satellite pair flew in front of them.

4.6.2 Isolation of the imaginary component of the fringes

The imaginary component of the cross-spectrum is extracted from each image stack and this matrix is analyzed to detect the orientation angle and the Fringe separation distance. Figure 48 shows a sample image, and the imaginary component of its cross-spectrum extracted. To remove the effects of noise near the center of the image a Gaussian low pass filter of 1-pixel radius was applied to remove single spike artifacts. The imaginary fringes are then auto-correlated (AC) to emphasize the periodic nature of the fringes.

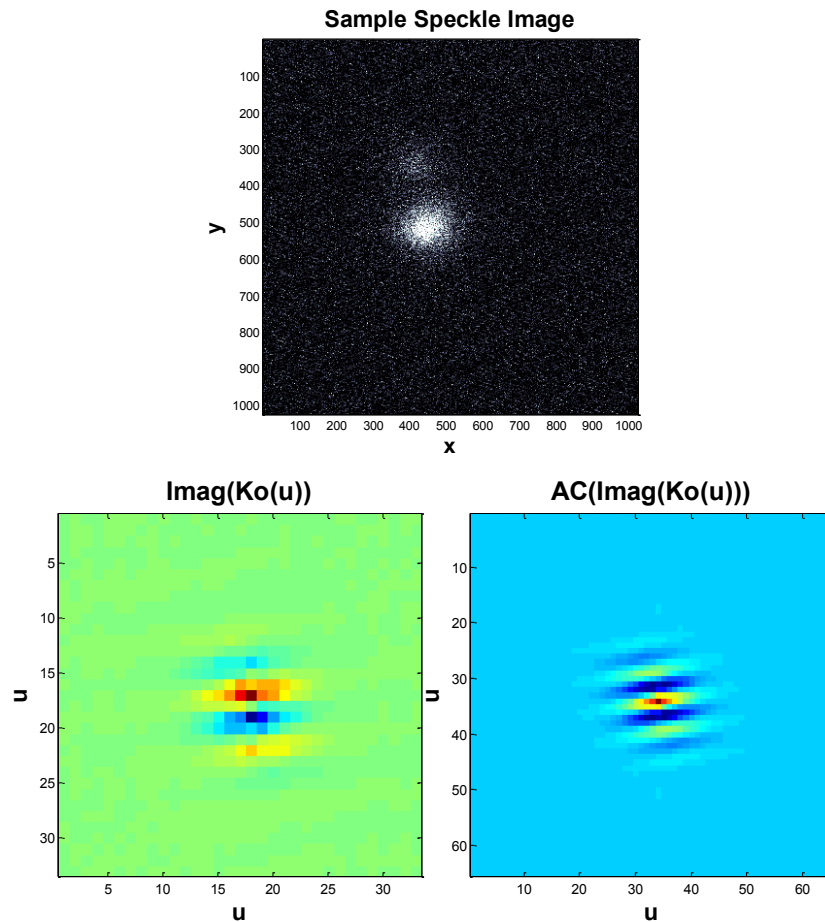


Figure 48: (Top): Raw Speckle Frame, (Left): Raw Imaginary fringes. (Right): Auto correlated imaginary fringes

At this stage, the auto-correlated fringe array is copied so that two processes can now occur separately. These processes determine 1) the fringe orientation angle and 2) the fringe separation (F_s) distance.

4.6.3 Orientation angle

The orientation angle is measured by detecting linear fringe features on the auto-correlated fringes. The auto-correlated fringes are binary thresholded and a Sobel edge detection kernel to detect fringe edges is applied (see Figure 49). A circular mask is also applied to “zero” any non-fringe content in this frame. This zero thresholding assists the subsequent Radon transform.

Sobel Filtered Imaginary Fringes

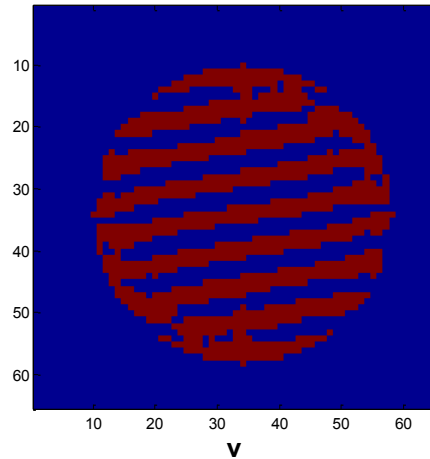


Figure 49: Sobel filter applied to AC of imaginary fringes

The Sobel filter is a convolution tool which emphasizes edges (gradients) in an image. It is structured with vertical \mathbf{G}_y and horizontal \mathbf{G}_x convolution kernels. The Sobel filter \mathbf{G} is computed as the quadrature of the directional convolutions (equations 4.14-4.16).

$$\mathbf{G}_x = \begin{bmatrix} -1 & 0 & +1 \\ -2 & 0 & +2 \\ -1 & 0 & +1 \end{bmatrix} * \mathbf{A} \quad \mathbf{G}_y = \begin{bmatrix} -1 & -2 & -1 \\ 0 & 0 & 0 \\ +1 & +2 & +1 \end{bmatrix} * \mathbf{A} \quad \mathbf{G} = \sqrt{\mathbf{G}_x^2 + \mathbf{G}_y^2} \quad (4.14) (4.15) (4.16)$$

The Radon transform is applied on the Sobel filtered image to determine the frame orientation angle with the strongest linear features. The use of a circular mask eliminates unwanted fringing effects at the edges of the cross-spectrum pattern which can corrupt the Radon transform from detecting the correct orientation angle. The circular mask ensures that the dominant fringe orientation is detected by elongating the longest fringe making it easier for the Radon transform to seek the correct orientation angle.

Once the fringe orientation angle is found, the profile perpendicular to the fringes is inspected using the original imaginary fringes (see Figure 50 left). The gradient at the center of the image points in the direction of the secondary in accordance with Aristidi's convention. This direction is then referenced to the North vector on the frame to identify the North-referenced orientation angle θ .

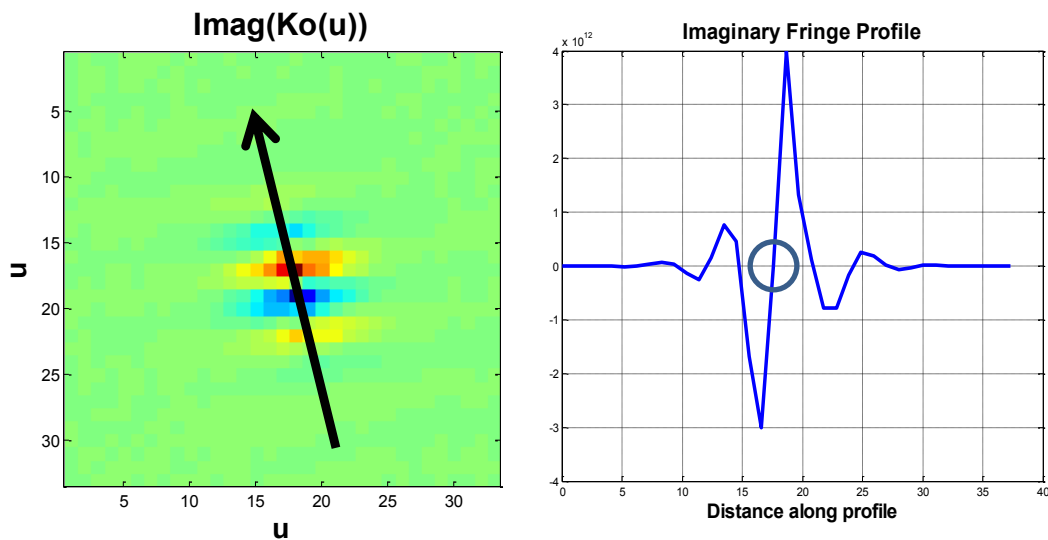


Figure 50: (Left): Imaginary fringe profile. (Right): Profile showing positive slope (marked) indicating that the fainter secondary object is in the direction of the profile.

During image processing the frame zero-reference angle direction is reckoned along the +y (downward) axis on an image. This is due to an odd programming convention in the use of Matlab's Radon transform which defines the zero-angle as being coincident with the image's +y axis, rather than the usual mathematical convention of defining the zero direction along the positive +x axis direction.

4.6.4 Fringe separation distance

The fringe separation distance (F_s) is used to determine the spacing between the objects. Direct measurement cannot be performed as image fringes are convolved with the object and atmosphere point spread function. This convolution displaces the true locations of the fringe minima and deconvolution using reference stars is usually performed to eliminate this effect.

Rather than interrupting satellite tracking to acquire cross-spectrums on single reference stars the deconvolution approach of Law [46] was used²⁸. The profile parallel to the fringes is used to approximate the cross-spectrum of a single unresolved point source. While this approach assumes circular symmetry of the point source, this approach was found to work well despite some asymmetry of the point spread function in the experimental observations. A Moffat [88] fit parallel to the auto-correlated imaginary fringes was used for this correction (see Figure 51 right) and the waist parameter α was broadened by 41% as an autocorrelated Gaussian full-width-half-maximum waist width is $\sqrt{2}$ wider than the full-width-half-maximum of a typical Gaussian profile.

The Moffat profile has a slowly expanding waist which helps fit fringes further from the center of the profile. The Moffat profile is modelled as

$$I(r) = A_0 + \frac{I_0}{\left[1 + \left(\frac{r}{\alpha}\right)^2\right]^\beta} \quad (4.17)$$

where I_0 is the peak intensity of the profile, r is the distance from the profile's centroid and α , β are parameters of the fit. A_0 is a constant vertical offset that is not usually included in the Moffat profile but is included in this model. It was empirically found that setting A_0 to approximately 25% of the standard deviation of the background of the imaginary data resulted in better profile fits.

²⁸ Telescopes with a high degree of aberration would require reference cross-spectrums in order to properly deconvolve the atmosphere and telescope point spread function.

The imaginary fringes (Figure 51 left) are then deconvolved using the best fit Moffat point source profile. The resulting fringes are then auto-correlated to emphasize the periodic content in the imaginary fringes (Figure 51 right).

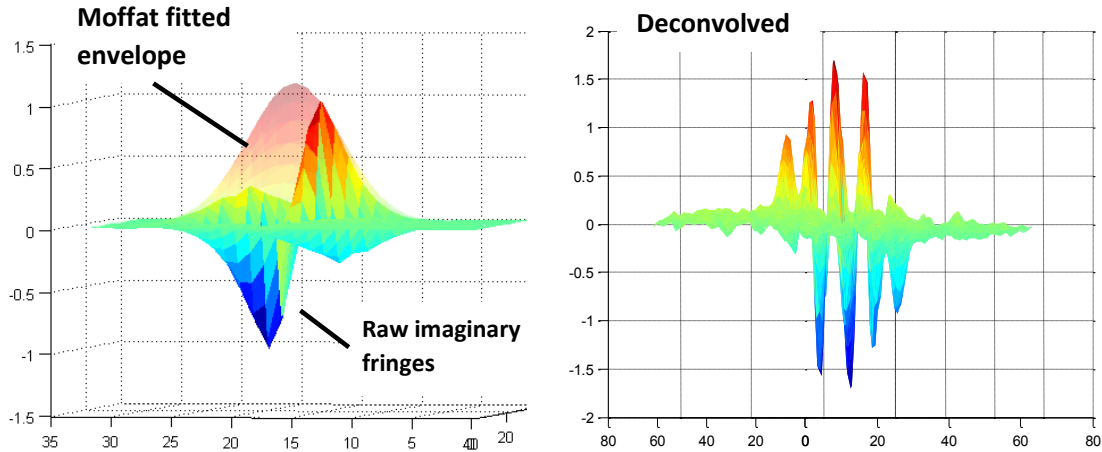


Figure 51: (Left): Raw fringe profile with Moffat fit envelope (semi-transparent). (Right): Deconvolved profile showing imaginary fringes.

A copy of auto-correlated fringes is kept in memory to identify the central peak in the fringe profile. This peak is used as a fiducial point that enables the Matlab image processing algorithm to search for closest local minima to the central peak. Once these minima are found, a quadratic fit is applied to the valley of the minima to refine the minima's true location. Then, the separation distance between the two minima is estimated using equation 2.28. Differential angles measurements $\Delta\alpha$, $\Delta\delta$ are then formed by using the orientation angle θ .

During speckle measurements on real, moving satellites (see chapter 5) an issue was encountered where high fringe rotational rates distorted the fringe stacks. These peak fringe rotational rates correspond to times of closest approach between the satellites which causes the fringes to smear during the stacking process. The test observation cases shown in the next chapter highlight two examples where warps in the separation distance measurements occur. This problem was resolved by taking a subsequent Fourier

transform of the deconvolved imaginary fringes stacks and extracting the peak frequencies directly. This technique is detailed in section 5.7 of the next chapter.

4.6.5 Image timestamps

Each image's FITS date header was extracted during image processing and the average time of the image stacks was used to timestamp of each $\Delta\alpha$, $\Delta\delta$ measurement. All times were referenced to UTC. A separate computation of the Julian date, which is needed for the solar radiation pressure adjustment, was also computed.

4.7 Chapter summary and contributions

A description of signal modelling as applied to speckle interferometry for satellites in close proximity in GEO is described in this chapter. Performance curves for small, moderate and large aperture telescopes are also computed to estimate the number of frames needed to detect closely-spaced satellites in GEO based on the primary and secondary satellite's magnitude. The results show that small and moderate aperture telescopes can perform speckle interferometry on primary objects in GEO with magnitudes between 9.5-10.5 with a secondary object of $1/10$ of the size of the primary. These objects should be detectable as long as the objects are observed at low phase angles within ~ 30 degrees of the anti-solar direction.

A description of the small-aperture space surveillance sensor configured for speckle satellite tracking is also provided and key design considerations are described. The instruments are configured to work in the near infrared to minimize chromatic dispersion error and to simplify the mechanical arrangement of the optics at the back plane of the telescope.

A description of the image processing approach for satellite speckle observations is also detailed including a description of the cosmic ray rejection routine. A means to sample, estimate and deconvolve the point spread function is also detailed. While this approach relies on rotational symmetry of the sampled psf it is found to work well for the experimental satellite tracking cases shown in the next chapter.

Chapter 5: Experimental findings

Observing a pair of closely-spaced objects in GEO orbit that are performing OOS is a challenge—observing them with speckle interferometry is even more challenging. This chapter describes experimental work undertaken to observe rare circumstances when geostationary satellites nearly mimic the motion of an OOS satellite for short intervals (< 15 minutes) of time.

On-Orbit Servicing missions are not currently performed in GEO which limits the ability to test the cross-spectrum measurement approach. Although binary stars can be used, they are dynamically static in comparison to satellites as they lack the relative motion intrinsic to this class of space mission. An ideal test would speckle satellites performing proximity operations within one kilometer of one another in GEO. While such a mission is not currently available for observation, the pursuit of a geosynchronous testing proxy would provide key insight that simulations alone cannot provide.

An alternate testing proxy using geosynchronous satellites is possible but requires planning, care and good weather for testing to occur. Geostationary satellite operators occasionally place more than one satellite within a single geostationary satellite slot. This flight-control strategy is known as GEO satellite co-location [12] (an example of such co-location is shown in Figure 52). Periodically, these co-located satellites appear to line-up along the line of sight with respect to a ground-based observer (see Figure 52 right). This alignment is rare; it only occurs once or twice a month, and rarely occurs during night-time conditions. Optical conjunctions [112] (as this type of alignment is known) occasionally exhibit a line-of-sight trajectory where satellites appear to be within 5 arcseconds of one another with respect to the observer. This particular geometry meets the isoplanatic condition for speckle interferometry. While the satellites visually appear to be very close to one another, they are in fact radially separated by ~10 km or more making the risk of collision between the two satellites negligible. These alignments offer the possibility to test the cross-spectrum approach for short intervals of time when the satellites appear to line up on the sky.

Co-located satellites fly in relative motion ellipses at much longer ranges and higher relative velocities in comparison to true OOS satellite pair motion. Co-located satellites' have high relative speeds with respect to one another due to the ~10 km radial offset between the spacecraft. This causes the observational windows to be brief (~10-15 minutes) where the satellites are within the isoplanatic limit. While these events are astrodynamically fleeting, these time periods are sufficient for experimental observations to evaluate the image processing and relative orbit estimation algorithms.

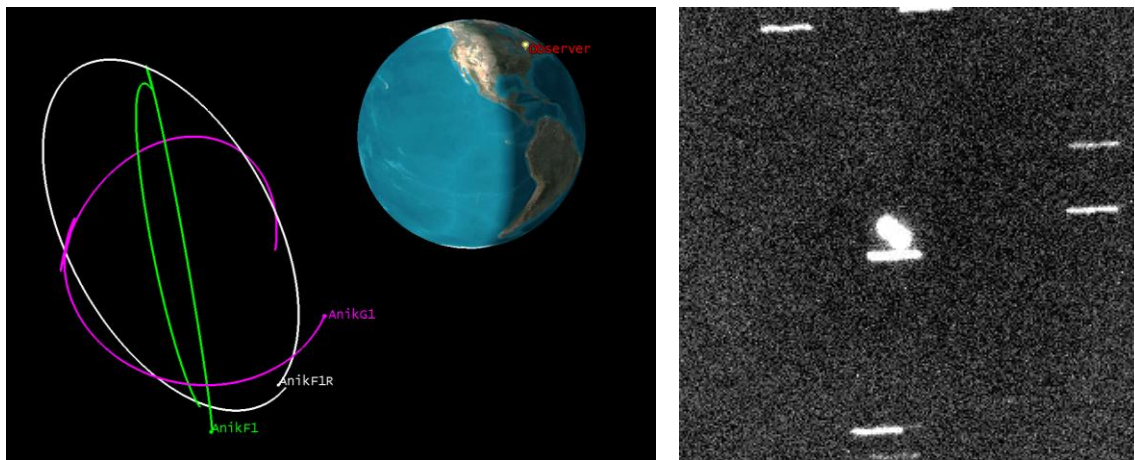


Figure 52: (Left): Relative orbit trajectories of co-located GEO satellites Anik F1, Anik F1R, and Anik G1. **(Right):** Anik G1, Anik F1R undergoing an optical conjunction.

To forecast when these alignments occur, satellite operator ephemerides are required. Telesat Canada operates three satellites at 107.3°W which fly in co-located formation and were selected as observational test candidates. With support from the flight dynamics team at Telesat Canada, predicted orbital ephemerides derived from the ranging measurements on Anik F1, Anik F1R and Anik G1 were inspected for geometric conditions meeting:

- 1) two satellites must align within 5 arcseconds of one another with respect to a ground observer
- 2) the alignment must occur at night and the satellites must be illuminated by the sun, and
- 3) the alignments occur when the weather forecast is expected to be clear.

These requirements reduced the number of opportunities to observe these events to one every 2-4 months. Forecasting these events beyond 1.5 weeks was difficult since the error in the operator ephemerides limits the ability to accurately predict these events to ~10 days. Likewise, unforecasted, satellite station-keeping maneuvers reduce the trustworthiness of the predictions beyond one week into the future. While it is relatively common for these co-located GEO satellites to align within 20-60 arcseconds from one another, the preferred event—where their angular separation is perceived to be less than 5 arcseconds—is rare. Support from the satellite operator was critical in predicting observational opportunities of these events.

General Perturbation Two Line Element (TLE) orbital element sets are a commonly available orbit product available from the Joint Space Operations Centers (JSpOC) [99]. These orbit estimates could be used to forecast these events however; it was found that this data source could only roughly forecast the time of the close approaches with an accuracy of ~4 hours making observational planning impractical. For speckle interferometry operator ephemerides were essential in order to ensure that the time of the event could be effectively forecasted and planned.

5.1 Mont-Mégantic observational campaign

Geostationary satellites are known to exhibit diurnal variations in their brightness profiles (see Figure 8) due to the constantly changing viewing geometry of the Sun, satellite and observer as the geostationary satellite flies in its orbital trajectory. Observing optical conjunctions using speckle imaging required access to a larger, more sensitive instrument in order to increase the likelihood of detecting faint satellite satellites due to high phase angle conditions which could fade the objects' brightness during alignment.

For this reason, an observation proposal was submitted to the University of Montreal (UoM) to use the Mont-Mégantic 1.6-meter telescope [58] configured with an EMCCD detector available at the observatory. UoM granted access to their equipment for two weeks in early February 2014—which was an optimal time of the year for the type of observation work planned. February has long, winter night skies and the geostationary belt is always illuminated by the sun as Earth's shadow is “above” the GEO belt at that

time of year. Observations planned for the 1.6 m telescope consisted of wide field imaging with the EMCCD and later magnified imaging for speckle observations.

5.2 Mont-Mégantic instrument description

The Mont-Mégantic telescope is an $f/8$ reflector (Figure 53) with a primary mirror of 1.55 m diameter. The diffraction limit λ/D is accordingly 0.073 arcseconds in the visible and 0.1 arcseconds in I-band. This corresponds to a 4.4 μm and 6.0 μm psf radius at the prime focus. Instrument details are provided in Table 7.

The detector selected for the observations was a 1024x1024 Nuvu EM LN2 liquid nitrogen-cooled EMCCD, (see Figure 54 left and specifications in Annex C). The detector was affixed to the telescope's prime focus using a focal length extension. The pixel pitch of the EMCCD subtended 13 μm which required a focal length extension in order to properly Nyquist sample the psf. An arrangement of 2X and 4X TelevueTM parfocal Barlows were affixed to the EMCCD and a set of standoff rings was assembled to accommodate the extra length of the Barlow lenses in order to meet focus for the telescope. A fabric light shroud was wrapped around the standoff rings to reduce stray light from entering the EMCCD optical path (see Figure 54 right).

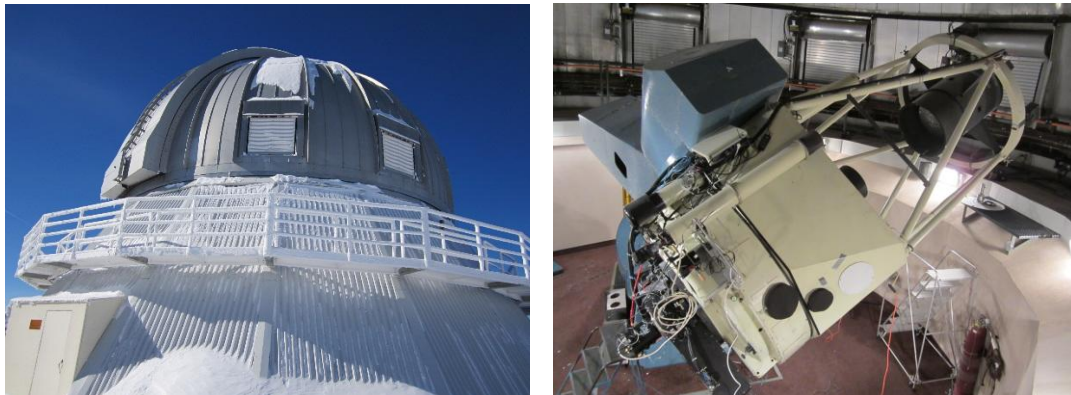


Figure 53: (Left): Mont-Mégantic Observatory (Right): 1.6m telescope

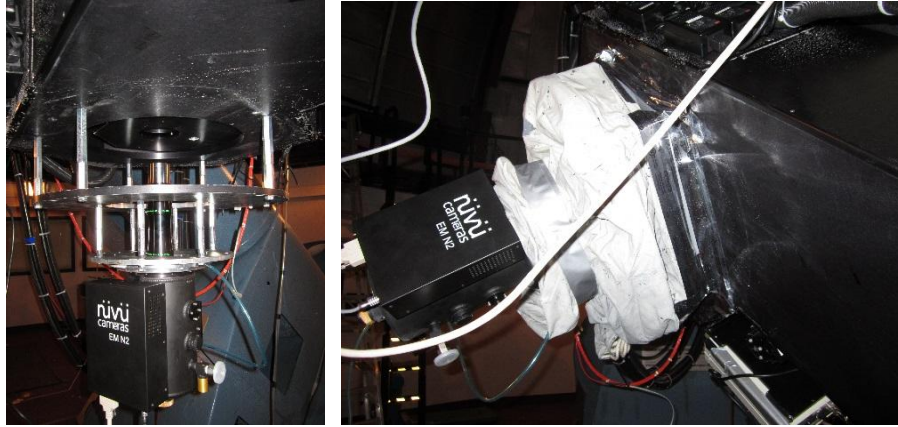


Figure 54: (Left): Nuvu EMCCD. (Right): Fabric baffling to reduce stray light.

Table 7 Mont-Mégantic Telescope Optical Parameters

Parameter	Value	units	Notes
<u>Observatory location</u>			
latitude	45.45579°	° N	Geodetic WGS 84 coordinates
longitude	71.15274°	° W	
altitude	1059	m	
<u>Optical system</u>			
Primary diameter	1.55	m	
Focal length	12.8	m	
Diffraction limit	5.4 (0.09")	μm (arcsec)	
Focal extension	8x	-	2x & 4x barlows
<u>Detector</u>			
EMCCD pixel scale	0.0271	arcsec pixel ⁻¹	
EM gain range	1-5000	-	
Instr. fov at 8X	26.8	arcsec	
Pixel pitch	13	μm	
Array dimensions	1024x 1024 (13.3x 13.3)	pixels (mm)	
Dark current	0.001	e ⁻ pix ⁻¹ sec ⁻¹	@-85°C
Full frame rate	16	Hz	
Read noise	0.1	e ⁻	
Read noise w/ EM gain	< 3	e ⁻	

The 8x focal extension achieved a psf pixel sampling of 2.8 pixels per psf radius meeting the Nyquist sampling requirement. Due to the long focal length of this optical system a narrow (27x27 arcsecond²) field of view formed making the process of centering stars, and satellites difficult on the main detector. A separate low light camera

and finder telescope attached to the main telescope tube was used to center stars and satellite targets on the primary instrument.

Telescope command used the observatory's telescope control computer where the Anik cluster's TLE's were loaded into the planetarium software used to point the telescope. Once the satellites were found using the low-light, wide field acquisition camera the satellites were centered in the main instrument and the mount's sidereal tracking was turned off. As geostationary satellites rotate in unison with Earth's rotational rate the satellites appear nearly motionless in the EMCCD's field of view.

Although geostationary satellites' orbital velocity corresponds to the mean rotation rate of the Earth, these rates are not perfectly matched which results in the satellites slowly drifting in the telescope's field of view. This causes both satellites to slowly drift off of the field of view. Non-sidereal rates of ~ 0.01 arcseconds/second in RA and DEC and were manually commanded into the telescope controller in order to eliminate slow relative drift of the satellite pair prior to imaging.

The Nuvu EMCCD streams FITS imagery at rates of ~ 16 images/second during acquisition. These images were serially acquired using a camera-linkTM gigabit Ethernet connection linked to the camera. The data was then sent to the Nuvu camera control computer and stored in memory.

5.3 Instrument calibration

The detector's North orientation was found using the star trails approach described in section 4.5.1. The North reference angle was 111.595 ± 0.1 degrees counter-clockwise from the +y axis.

It was not possible to use a diffraction mask with a large 1.6m telescope, so calibration of the pixel scale and North orientation angle of the detector was performed using widely spaced binary stars. *WDS 326BC*—an example of a long period double star selected from the Washington Double Star Catalog [40]—is detailed in Table 8 and Figure 55. This double star was imaged using normal integration times and was also speckle imaged.

The pixel scale was validated by measuring the centroid locations of binary star pair and cross-checking the recent measurements of the separation between the pair (see Table 8). The last set of measurements—taken in 2010—indicated that the separation distance

between the pair was 4.3 arcseconds—a markedly slow change considering the last measurement taken on the pair occurred in 1899 and indicated a separation distance of 4.1 arcseconds. The pixel scale was determined to be 0.0251 arcseconds per pixel, just slightly less than the 0.027 arcseconds per pixel estimate using the optical parameters of the telescope.

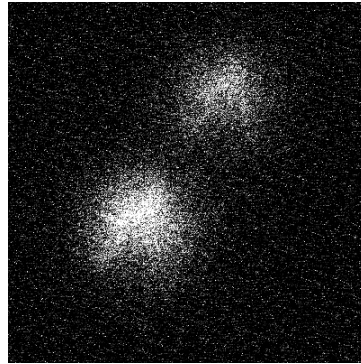


Figure 55: Speckle image of WDS ES326BC.

Table 8 Binary Star WDS ES326 BC

Parameter			units
WDS Identifier	03058+3202ES326BC		
Years of measurement	1899	2010	
ρ	4.1	4.3	arcsec
θ	34	34	degrees
Magnitudes (pri.,sec.)	10.99 pri.	12.0	Vmag

5.4 Observations of satellites using speckle images

During the observing time granted, Mont-Mégantic experienced nine days of heavy clouds, wind and snow which prevented observation activities for the majority of the grant period. During the first couple of evenings, some wide field imaging of satellites using the EMCCD occurred but no speckle imaging occurred.

On February 18, 2014, clear skies provided an opportunity to view two predicted optical conjunctions between satellite pairs Anik G1, Anik F1R and Anik F1, Anik G1.

The first optical conjunction was between Anik G1 and Anik F1R which was predicted to close to within 1.2 arcseconds of one another. The second optical conjunction with a wider separation of 7 arcseconds was forecasted for Anik F1 and Anik G1. Despite the fact that the second optical conjunction had a larger forecasted separation, it was selected for observation to make up for lost observational time due to heavy cloud cover during the previous week.

Weather conditions on the evening of 18 Feb 2014 were clear, however winds of 17 km/h (with gusts of up to 35 km/h) were experienced. This led to variable seeing conditions between 2 and 3.5 arcseconds. Highly degraded seeing conditions of up to 5 arcseconds were observed for a short 2-minute interval during the second satellite track when very gusty wind conditions were experienced. The typical median seeing conditions at Mont-Mégantic are normally between 1.5-2.0 arcseconds [113] signifying that the satellite speckle observations were collected during less-optimal seeing conditions. For comparison, pristine astronomical sites, such as the San Pedro Mártir Observatory in Mexico, routinely enjoys median seeing between 0.47 and 0.7 arcseconds [114]. The rarity of the GEO satellite alignments forced the use of these tracks despite the seeing conditions. Fortunately, the Mont-Mégantic telescope's south-west look direction permitted the dome to shield the telescope from the northerly wind minimizing telescope wind shake from further affecting the images.

Telescope setup was normal with a verification of the acquisition computer clock's time, check of the telescope focus and loading of satellite TLEs into the telescope control computer. The telescope was slewed to the area of the sky where the satellites were about to close on one another. Once the brighter satellite was acquired in the instrument, the mount's sidereal tracking rate was shut off and non-sidereal rates were applied. When both satellites were estimated to be within 6 arcseconds of one another, the EMCCD was set to continuously acquire 10 millisecond exposures at 16 frames per second and the FITS images were stored on the acquisition computer. This process continued until the satellites separated from one another.

5.5 Observations of Anik G1 and Anik F1R

On February 18, 2015 at 02:05 the satellite pair Anik G1 (the primary) and Anik F1R (the secondary) began an optical conjunction relative to the Mont-Mégantic observatory. The pair was observed for 10 minutes before and after their closest apparent approach (see Figure 56). This track was analyzed and results presented at the International Astronautical Congress 2014 [115] and the work was subsequently accepted for publication in the journal *Acta Astronautica* [112].

The relative motion and geometry of the optical conjunction is shown in Figure 57 where the small conical region is the isoplanatic radius of 5 arcseconds and the larger square field of view is the 27 arcsecond wide EMCCD detector. When Anik F1R entered this 5 arcsecond conical radius, the speckle imaging conditions were met. Anik F1R was radially inside of *Anik G1* during the track and was moving northward.

The magnitude difference of the two objects was $\Delta m = 0.36$ corresponding to absolute visual magnitudes of 10.23 and 10.59 magnitudes for Anik G1 and Anik F1R respectively. The brightness ratio was $\alpha_b = 0.72$ and their brightness's varied by no more than 0.2 magnitudes during the 15-minute observational period.

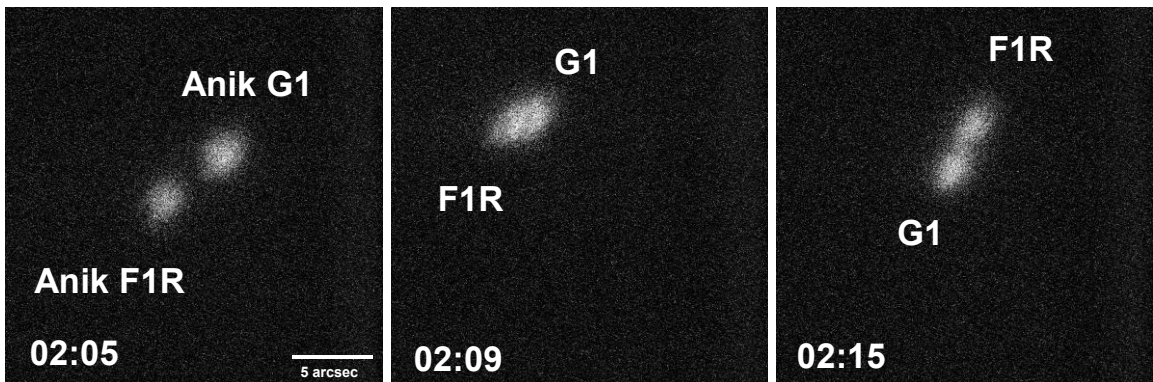


Figure 56: Anik G1 and Anik F1R during the optical conjunction (18 Feb 2014)

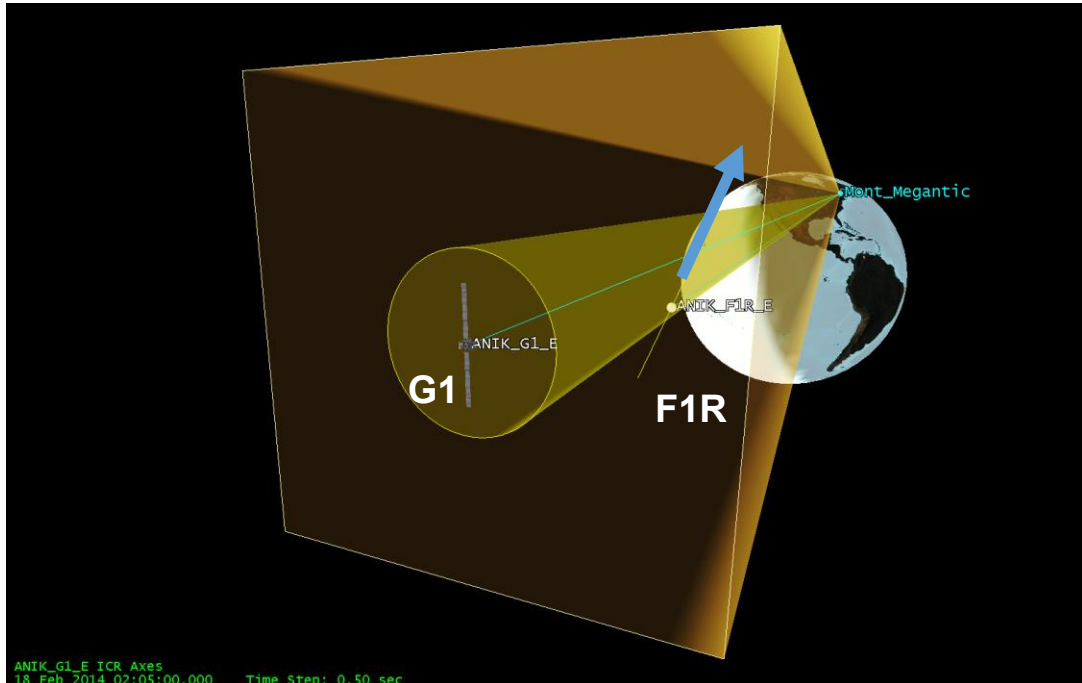


Figure 57: Anik G1 and Anik F1R. Note that Anik F1R's path is in the $-x_{Hill}$ direction relative to Anik G1 and is moving in the $+y_{Hill}$ (eastward) and $+z_{Hill}$ (northward) directions.

During the experiment, considerable photon noise was detected within the speckled psf of both satellites. Setting the gain of the EMCCD too high (10,000-11,000) may have caused this noise as the high gain emphasized the seeing disk *and* the speckles, not just the speckles themselves. The contrast and brightness level of the acquisition computer was set relatively low which caused the instrument operator to increase the gain in order to visually see both objects on the acquisition computer. By changing the brightness and contrast of the display this could have been avoided. Moderate EM gains (5000 or less) are recommended for future experiments as this setting will produce speckle images that more accurately reflect the speckled nature of the detections. Despite the photon noise, the data did not corrupt the detection process during the image processing stage.

For this optical conjunction, Figure 58 shows selected data processing frames and its columns display the following information

- 1st column: frame time t and d, θ measurements
- 2nd column: raw speckle image frames

- 3rd column: raw cross spectrum plots of $Im\{K_o(u)\}$,
- 4th column: the auto correlated fringes
- 5th column: Moffat normalized fringe profile with the first minima locations marked with vertical red lines. The distance between the fringe minima is F_s and is used to compute the separation distance between the satellites.

Figure 59 details the measured separation distance and orientation angle of Anik FIR relative to Anik G1. The satellites closed to 1.2 arcseconds of one another at $t = 131.5$ minutes past midnight UTC. The atmospheric seeing was computed during image processing by a separate Fourier transform analysis to estimate the full-width-half-max of the atmospheric point spread function. The seeing was approximately ~ 3.5 arcseconds for the majority of the observations in this track and is considered to be marginal (at best) seeing conditions for speckle interferometry. Figure 59 also shows that the cross-correlation approach detected the motion of the two spacecraft relatively well and tracking to within 1.5 arcseconds separation of the satellites was achieved.

Weakness in the detection algorithm was observed at the time of closest approach at $t = 131.5$ and $t = 132.1$ minutes as the orientation angle (Figure 59, right) exhibited spurious results. The reason for this is the high rotational rate of the fringes at the time of closest approach. The stacking and autocorrelation process smears the fringes and displaces the fringe minima inward at closest approach. As these fringes are smeared, the orientation angle is not chosen well by the Radon detection step as the fringes rotate at ~ 0.6 degrees per second. As the 100 image stacks are equivalent to a ~ 6 second exposure, fringes at the start and end of the stack are oriented nearly 3.6 degrees differently (~ 32 pixels). The subsequent autocorrelation process smears the fringes and the minima move inward (see section 5.7).

Anik G1 (primary), Anik F1R (secondary)
Observation Epoch 18 Feb 2014 02:05:00 UTC, $\alpha = 0.72$

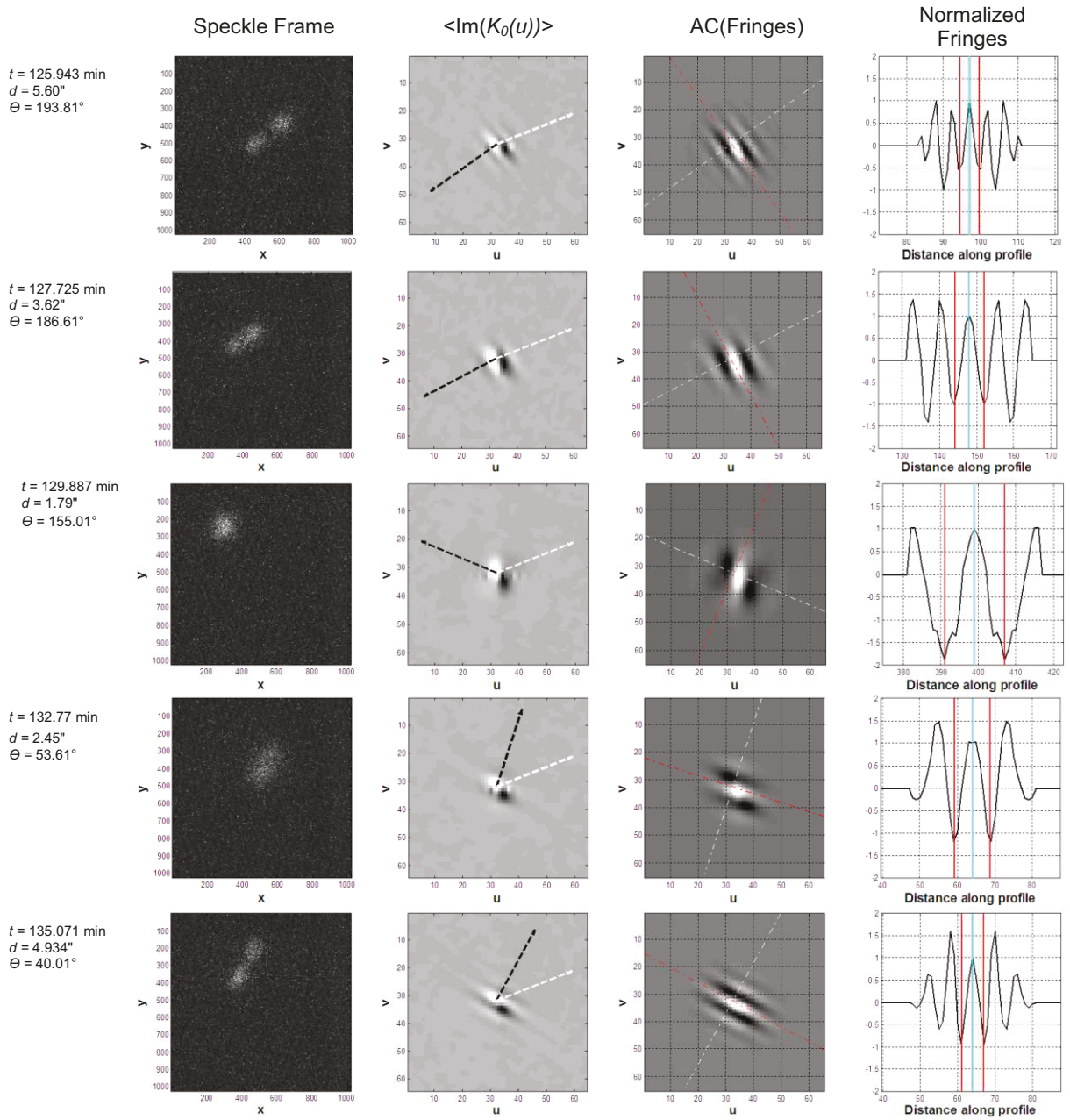


Figure 58: *1st column:* Time, separation distance and measured orientation angle. Time is expressed in minutes past midnight (UTC), separation (d) arcseconds, and θ in degrees. *2nd column:* Selected frames during the optical conjunction. *3rd column:* Raw imaginary component of the cross-spectrum. White arrow indicates celestial north, black arrow indicates the direction to the secondary object, *4th column:* Autocorrelation (AC) of the imaginary fringes where the white line indicates the profile axis and red line indicates fringe orientation angle. *5th column:* Moffat normalized fringes. Cyan line indicates the center of the profile and vertical red lines indicate the first detected fringe minima.

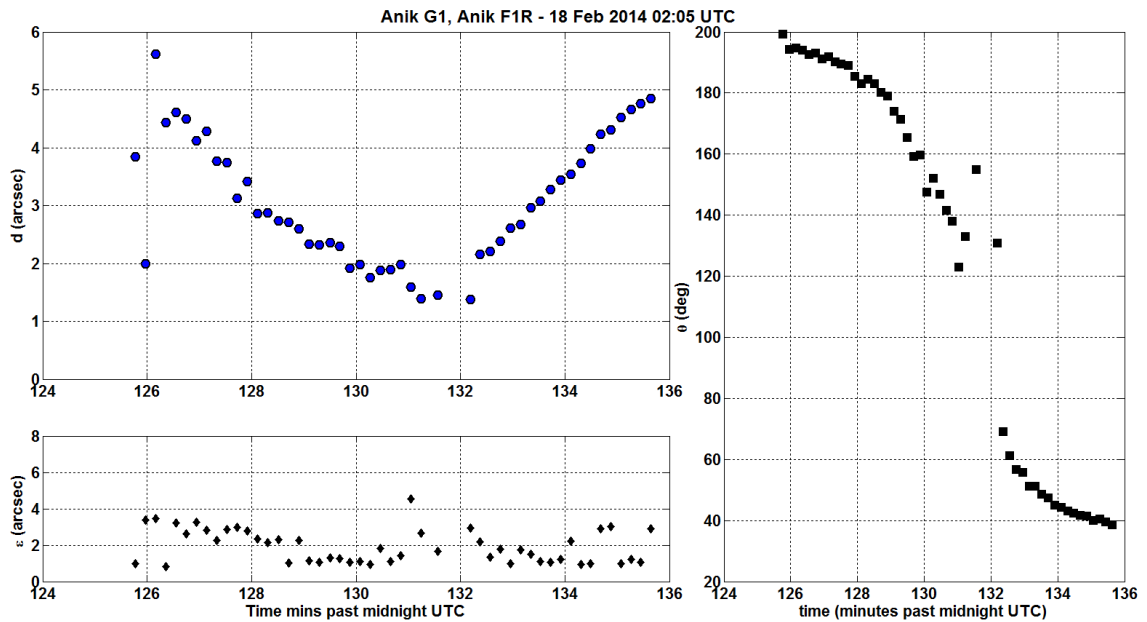


Figure 59: (Top left): Separation distance d , (Right): orientation angle θ , (Bottom): Seeing ϵ

Outside of the closest approach region, the ρ, θ measurements were transformed into differential angles ($\Delta\alpha, \Delta\delta$) and were compared to reference ephemerides provided by Telesat Canada (see Figure 60). This track closely adhered to the predicted differential angles with exceptions at the start and end of the track and at the point of maximum fringe rotation.

It should be emphasized that the isoplanatic limit is key to performing speckle interferometry and this limitation becomes visible in the large residuals at the start and finish of the plot in Figure 60 where the residuals curl with respect to the linear portion of the plot. At these times the track was acquired when the object overall separations exceeded 5 arcseconds making the correlation of the speckles less likely and the measurement process less trustworthy. Wider separations > 5 arcseconds also creates the narrowest fringes in the cross-spectrum, which makes it difficult for the Sobel and Radon transforms to identify linear fringe features.

The use of the imaginary fringe deconvolution approach described in section 4.64 improved the accuracy of data processing. Compared to a previous attempt to process this data [112], (see Figure 61) the additional processing steps of auto-correlating the imaginary fringes, and fitting a Moffat profile to approximate the psf of an unresolved

point source improved the measurement residual performance giving the results in Figure 60. This processing exhibited measurement noise in $\Delta\alpha$, $\Delta\delta$ (outliers removed) of 0.18 and 0.38 arcseconds respectively in each axis. The previous processing exhibited biases of +0.5 arcseconds or more in declination with $\Delta\alpha$ noise of ~ 1 arcsecond occurring frequently during the track. Increasing the stack size to 100 images per stack measurement also yielded additional measurement improvements (shown in Figure 60). The previous processing attempt used only 20 images per measurement. The two-fold increase in signal content from the additional stacked images improved the precision of the differential right ascension residuals from 0.35 arcseconds to less than 0.2.

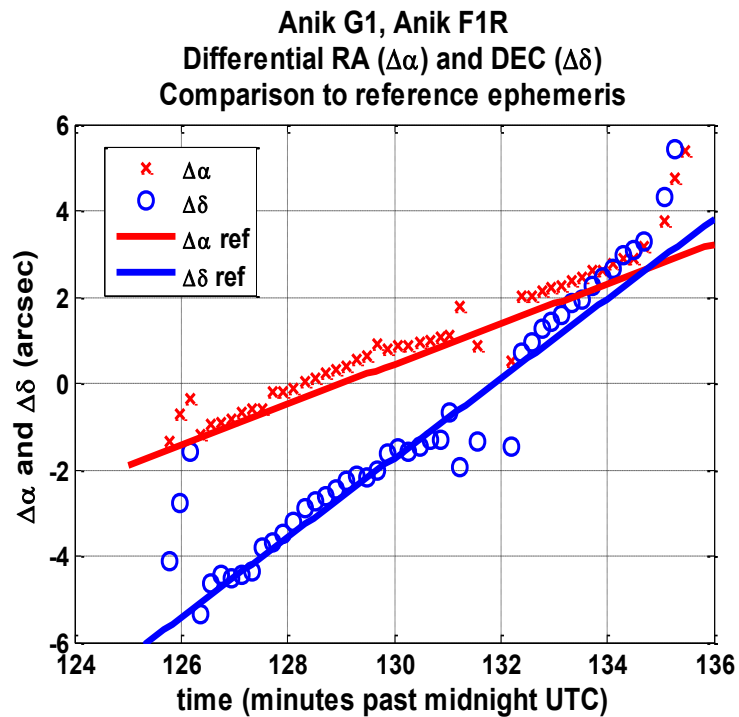


Figure 60: Differential measurements $\Delta\alpha_t, \Delta\delta_t$ (red x, blue o) plotted against reference ephemeris

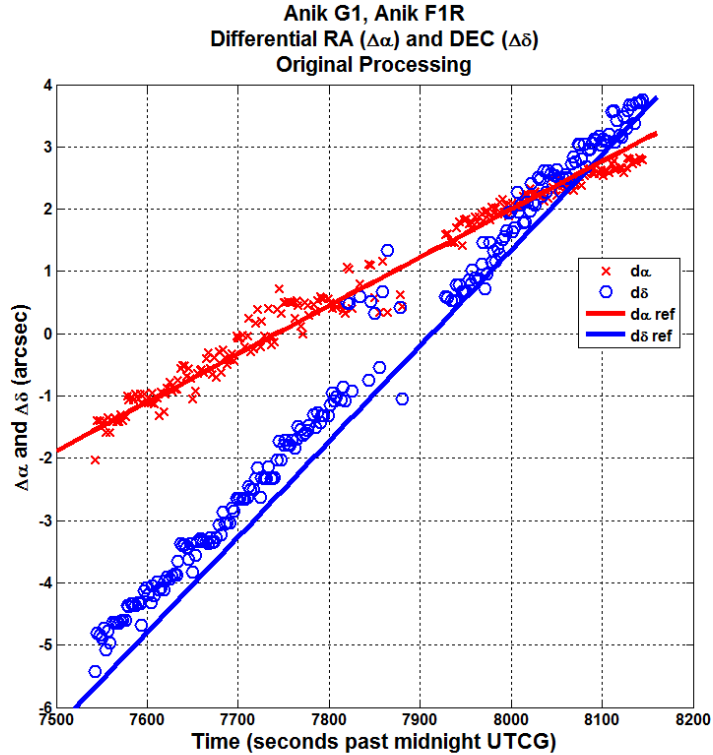


Figure 61: Previous processing of Anik G1, Anik F1R track $\Delta\alpha_t$, $\Delta\delta_t$ (red x, blue o). Declination biases and enhanced differential right ascension noise is visible at the start of the track. The $\Delta\alpha_t$ residuals have lower precision due to the lower stack sizes.

5.6 Observations of Anik F1 and Anik G1

A second serendipitous optical conjunction occurred on the evening of 18 Feb 2015 04:43 between Anik F1 and Anik G1. This was a unique opportunity as Anik F1 is known to be considerably brighter than Anik G1 which permitted a new test case for the cross-spectrum processing approach on a larger magnitude difference (see Figure 62). The brightness difference was $\Delta m = 1.53$ magnitudes ($\alpha_b=0.24$) corresponding to primary and secondary object magnitudes of 9.03 and 10.56 respectively. In contrast to the first track, Anik G1's motion was radially outside of Anik F1 (see Figure 63) and was moving southward.

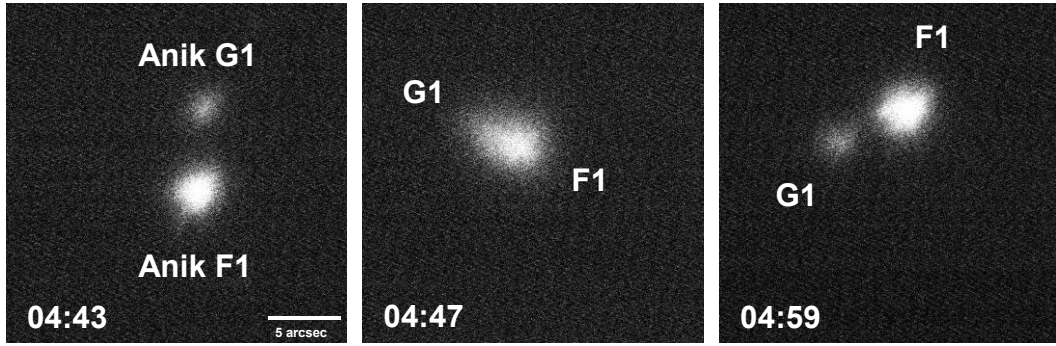


Figure 62: Anik F1 and Anik G1 selected speckle frames from the 2nd track.

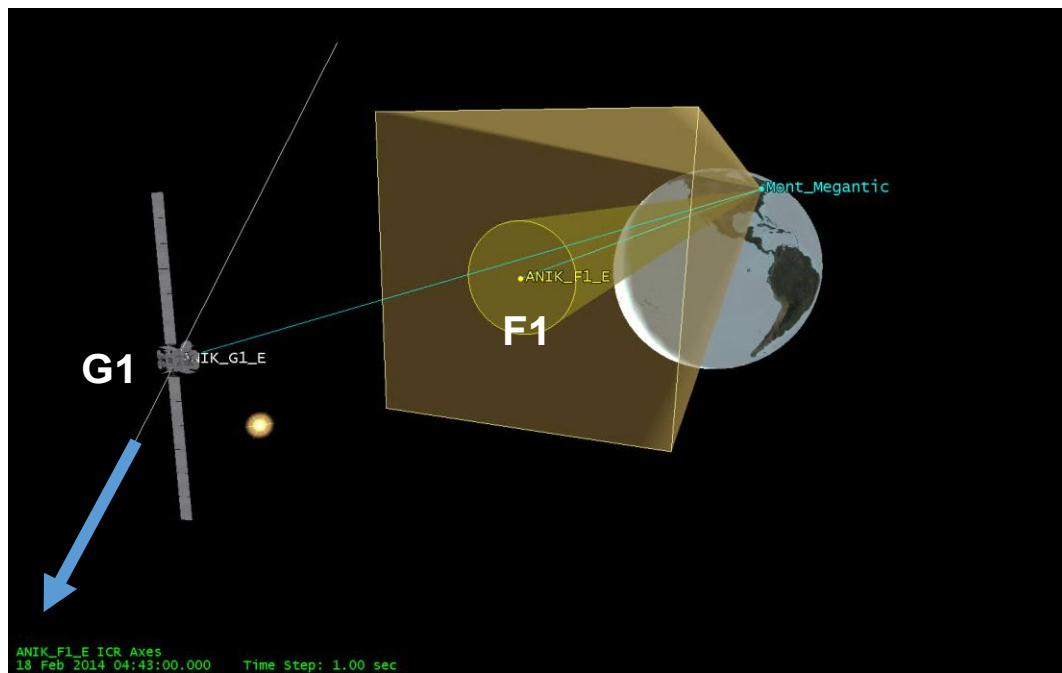


Figure 63: Anik F1 (primary) and path of Anik G1 relative to Anik F1. FOV is 27 arcseconds. Note that Anik G1's path is in the $+x_{\text{hill}}$ direction relative to Anik F1 and is moving in the negative in-track (westward) and negative cross-track (southward) direction.

This second track's angular separation was predicted to close within 7 arcseconds and was not expected to meet the isoplanatic limit for speckle interferometry. As the objects were known to have a larger brightness difference, imaging was attempted anyway as optical conjunctions are rare and any additional field data would help test the image processing software. Fortunately, the satellites actually closed within 3.4 arcseconds of one another permitting a rare second test case meeting the isoplanatic limit.

Figure 64 shows a selected set of cross-spectrum d, θ measurements from the second track. A very interesting feature was observed during this track (see the middle row in Figure 64). The seeing suddenly degraded at $t=292$ minutes which was attributed to high wind-gust conditions at the observatory that evening. The degraded seeing was experienced for a 3.5-minute interval centered at $t = 292$ minutes. Coincidentally, the separation measurements d exhibited an odd behavior where the separation measurements swelled near the time of the “seeing bloom” (see Figure 65, separation measurements and seeing plot).

Initially it was believed that the “seeing bloom” (see sample frames in Figure 66) decorrelated the speckles during this interval causing the sporadic separation distance measurements. After further investigation, it was found that the degraded seeing of the speckles had no noticeable effect on the image processing algorithm. The sporadic separation deviation was actually due to the fringe rotation effect due to the satellite’s close separation and apparent motion, not the degraded seeing.

As the closest separation distance between the two satellites in this track was ~ 3.5 arcseconds, the fringe rotation effect distorts the fringe minima for a longer interval causing the “bump” feature in the separation measurements in Figure 65. As these two co-located satellites have radial separations of ~ 10 km, very high relative angular rates are observed which provokes this fringe rotation effect. This is not expected to be a problem for real OOS cases where the satellites are within 1 km of one another as their apparent, relative angular velocities are much lower in comparison to the co-located satellite test cases examined here.

In contrast to the behavior of the separation distance d , the orientation angle θ (Figure 65 right) exhibited minor deviation and appears to have been largely unaffected by the degradation in the seeing. The Sobel filter and Radon transforms were able to detect and maintain a relatively smooth, continuous track of the orientation angle between the two objects even though the seeing conditions were degraded at that time.

Anik F1 (primary), Anik G1 (secondary)
Observation Epoch 18 Feb 2014 04:43:38 UTC, $\alpha = 0.24$

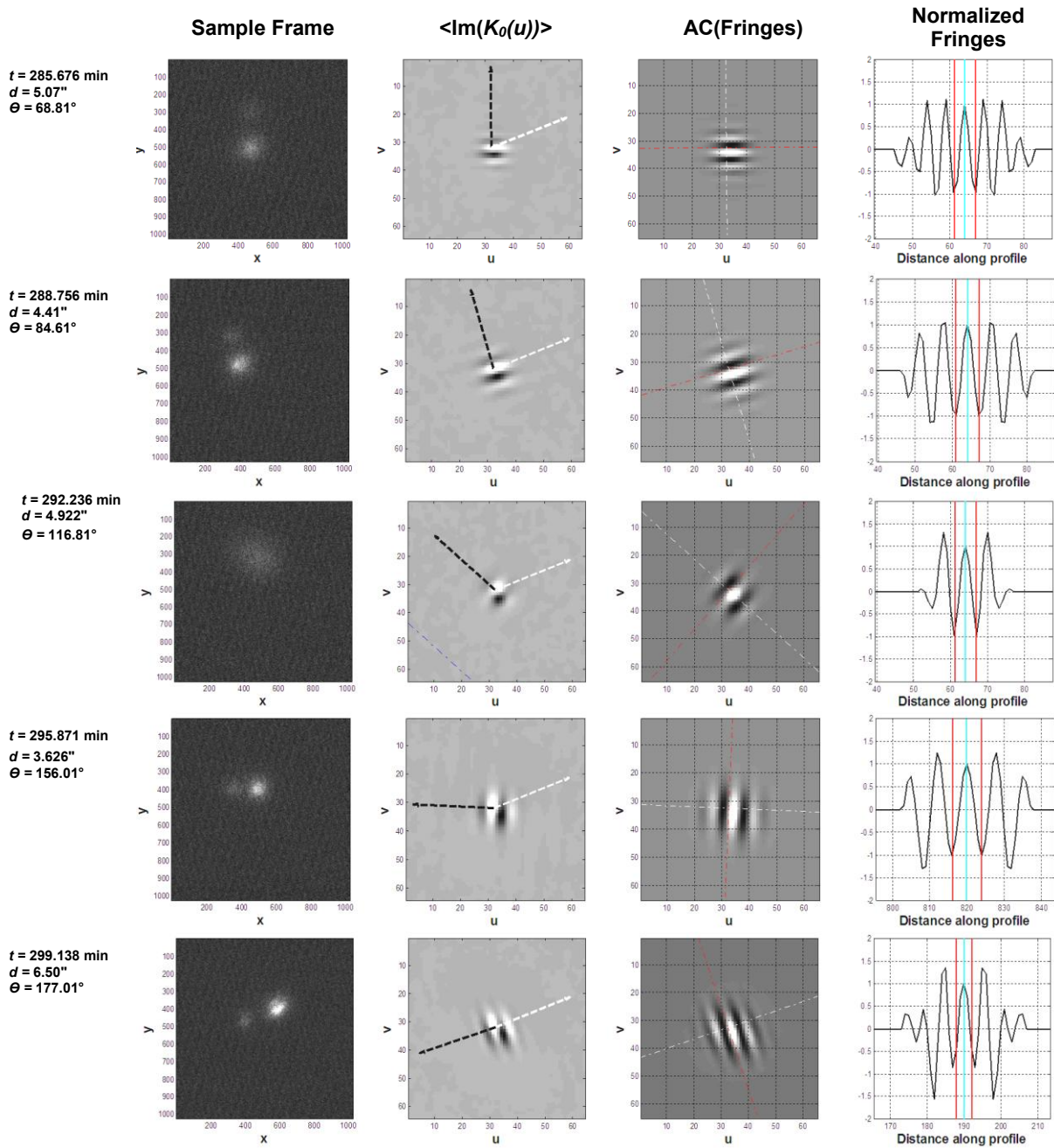


Figure 64: *1st column:* Time, separation distance and measured orientation angle. Time is expressed in minutes past midnight (UTC), separation (d) arcseconds, and θ in degrees. *2nd column:* Selected frames during the optical conjunction. *3rd column:* Raw imaginary component of the cross-spectrum. White arrow indicates celestial north, black arrow indicates the direction to the secondary object, *4th column:* Autocorrelation (AC) of the imaginary fringes where the white line indicates the profile axis and red line indicates fringe orientation angle. *5th column:* Moffat normalized fringes. Cyan line indicates the center of the profile and vertical red lines indicate the first detected fringe minima.

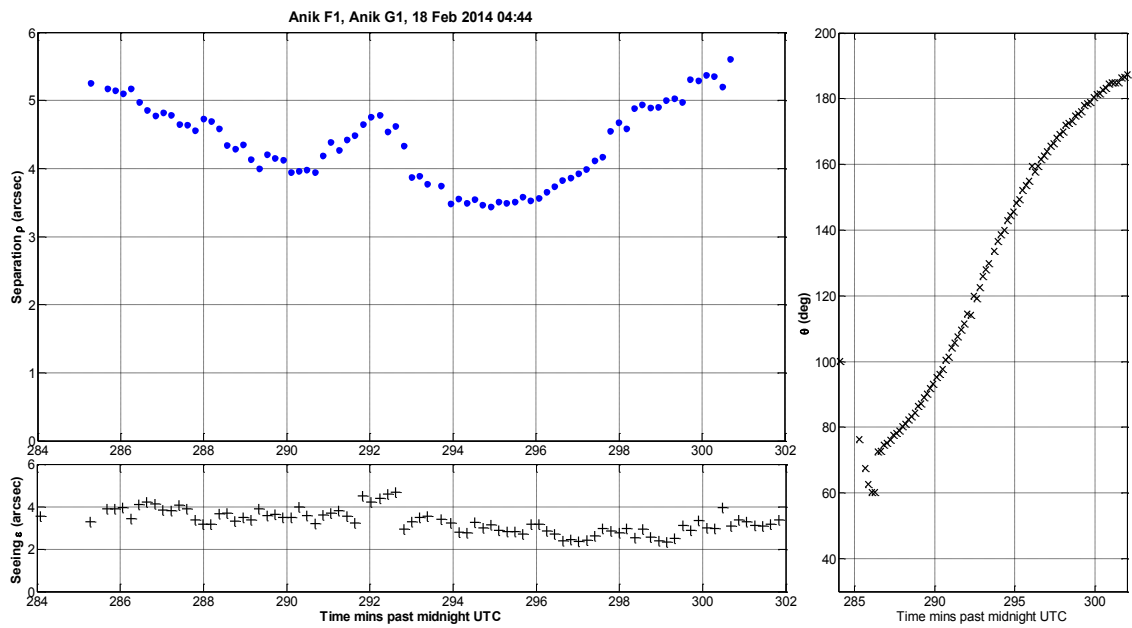


Figure 65: (Top left): Separation distance (arcseconds) (Right): Orientation angle θ , (Bottom): Seeing ε

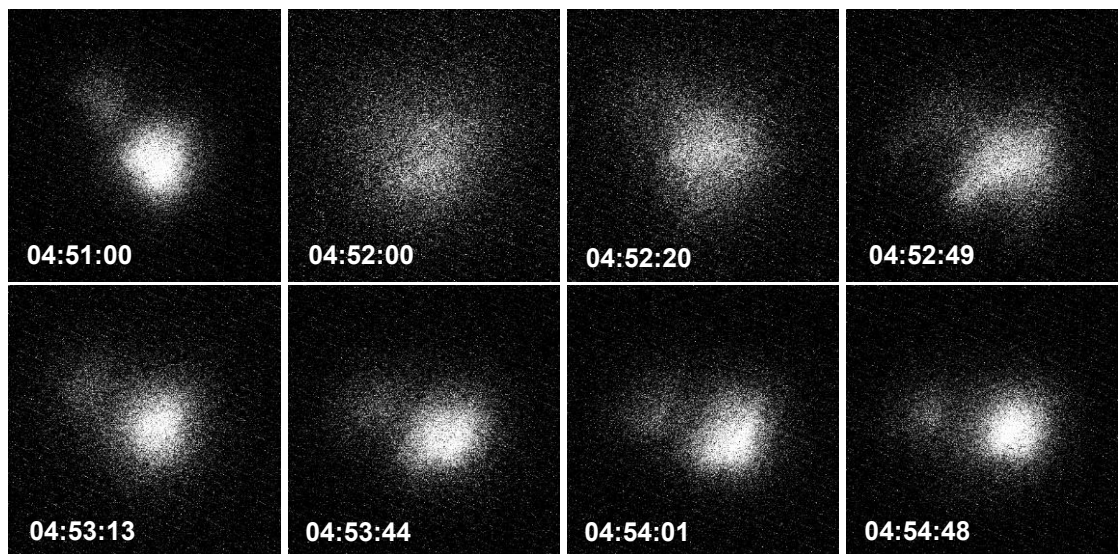


Figure 66: Selected frames during the “seeing bloom”

Figure 67 compares the differential measurements $\Delta\alpha$, $\Delta\delta$ with the reference ephemeris for these two satellites. There was a strong differential right ascension bias (unrelated to the fringe rotation and seeing bloom effects) which predicted the location of Anik F1 to be nearly 1 km eastward than where it was actually observed. Several speckle frames were manually inspected to ensure that the speckle algorithm's separation measurements were consistent with manual speckle centroid measurements and this was found to be the case.

Upon learning of this discrepancy, a request for a reprocessed post-fit orbital ephemeris for both Anik G1 and Anik F1R was placed with Telesat Canada. The post-fit ephemeris still exhibited some eastward bias of ~ 550 meters, but not to the extent originally shown in the predicted ephemeris. Figure 67 shows that a bias subtraction of 2.5 arcseconds was applied to the differential right ascension reference measurements. This bias subtraction emphasizes the consistency and adherence of the track with the satellite operator ephemerides. No correction was required for the differential declination measurements as no bias was visible.

Ranging systems on geostationary satellites are periodically calibrated for range bias which manifests as an in-track error in the geocentric orbit ephemerides. Some brief qualitative discussion²⁹ about this effect is presented in references [116][69]. Without additional measurements it is not possible to further isolate this bias using the short 15-minute relative orbit track available for these two satellites.

The fringe rotation effect is prominent in the $\Delta\alpha$, $\Delta\delta$ measurements as a warp in the trajectory centered at $t = 292$ minutes. Relative orbit measurements processed later in this manuscript was set to reject measurement data between $t = 291$ and $t = 294$ minutes to minimize the fringe rotation's impact on the relative orbit estimation. In addition to this exclusion, measurement data collected prior to $t = 288$ minutes was not processed as the isoplanatic angle condition was exceeded at the start of the track.

This track exhibited precise measurement residuals (with exception of the track start and the peak fringe rotation rate) with scatter of $\sigma_{\Delta\alpha} = 0.06$ arcseconds and $\sigma_{\Delta\delta} = 0.16$

²⁹ Telesat Canada's flight dynamics manager indicates that calibration of range bias occurs "every few months".

arcseconds. Compared with the first track, there was a slight improvement in measurement precision.

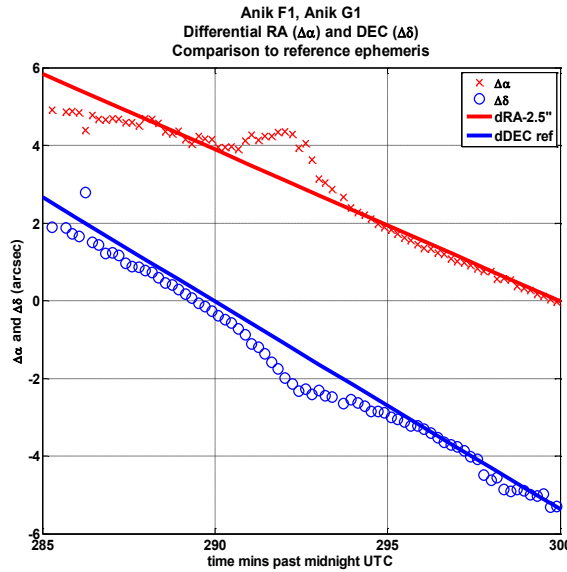


Figure 67: Differential measurements $\Delta\alpha_t, \Delta\delta_t$ (red x, blue o) plotted against reference ephemeris

5.7 Correcting the fringe rotation effect

It was realized that the location of the “bump” in the separation measurements was at the time of closest approach between the two satellite objects. The fringes exhibit their peak rotational rate when the objects are closest together and the width between the fringe minima is the broadest. The algorithm used to measure the positions of the fringe minima in the u, v plane at this time was found to cause spurious fringe separation measurements.

The “bump” feature in Figure 65 and Figure 67 is due to the stacking of differently oriented fringes and fringe widths. Figure 68 shows a 3-image stack example for two point sources moving rapidly past one another mimicking the effect observed in the second track. Initially, the fringes are vertical and broad (see Figure 68 step 1). When the objects separate the fringe rotation rate slows and the fringe separation narrows (step 2). Later, the fringe rotation rate further slows and the fringes are broadest (step 3). When multiple cross-spectrum frames are stacked the averaging of multiple, variously rotated fringes of various separations smears the stack’s average (see Figure 68 CS Stack). This

smearing causes the dark minima detection algorithm to preferentially weight fringes where the fringe rotation rates are slower, tending to artificially weight the narrower fringes at steps 2 and 3 of Figure 68. This preference for narrower fringes causes the spatial separation ($1/F_s$) to artificially swell outward. This effect is less pronounced when the objects are well separated (3-5 arcseconds) and is why the behaviour is less noticeable for the first satellite track and at the extremities of the second.

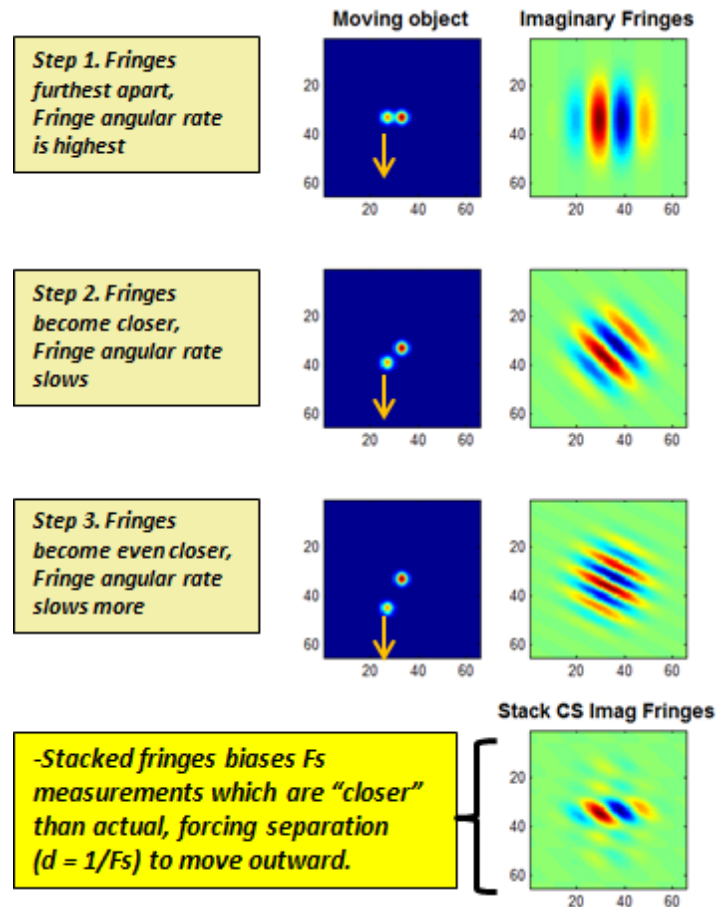


Figure 68: Effect of rapidly moving objects causing stacks to smear the fringes

After examining various techniques to mitigate this effect, it was found that passing the imaginary component of the cross-spectrum again through a Fourier transform was much more reliable at identifying the true fringe separation distance between the satellites. Equation 5.1 shows that a Fourier transform taken on the imaginary component of the

cross-spectrum fringes reveals two peaks separated by twice the distance between the objects

$$\begin{aligned} \mathcal{F}\{Im(K_o(u))\}(x) &= \mathcal{F}\{\alpha_b(1 - \alpha_b) \sin(2\pi ud)\} \\ &= \frac{\alpha_b(1 - \alpha_b)}{2} i\{\delta(x - d) + \delta(x + d)\} \end{aligned} \quad (5.1)$$

These peaks appear in the spatial plane making their identification and centroiding relatively easy to isolate (see Figure 69). A MATLAB routine was written to track the motion of the two spatial plane spikes and their relative position recorded.

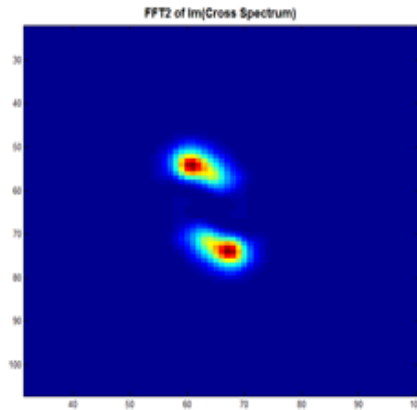


Figure 69: Fourier transform of the cross-spectrum imaginary fringes resulting in two spikes separated by $2d$

Applying this measurement approach to the second track's imaginary fringes shows improved measurement residuals with better adherence to the track's path. This technique also achieved better measurement precision and differential angles residuals of 0.1 arcseconds or less (see Figure 70) were found. These improved residuals, and overall better adherence to the actual satellite tracks, indicate that despite the high fringe angular rotation rate and deterioration of seeing at $t = 292$ minutes, the technique was more resilient to detecting the motion of moving objects when the objects closed on one another.

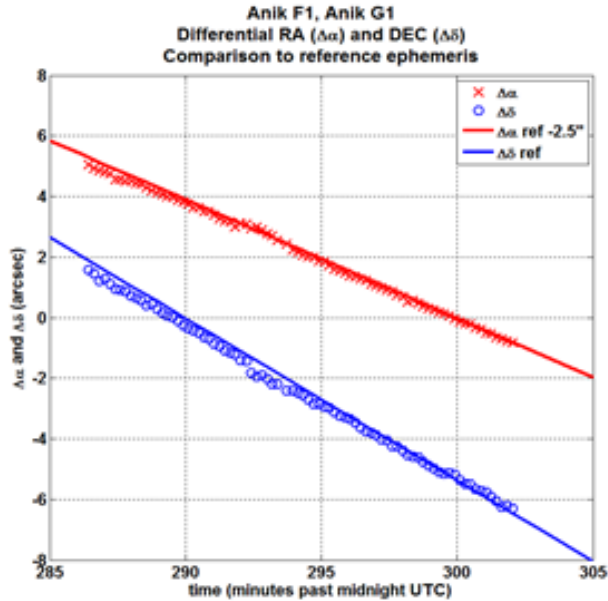


Figure 70: Differential measurements $\Delta\alpha_t, \Delta\delta_t$, using improved object detection approach

5.8 Relative orbit estimation using track data

Speckle measurements provide a means to infer the presence of the secondary object and measure “plane of sky” angular separations between them. Space surveillance’s primary role is to predict future activities of objects in orbit to support collision warning and other activities. For this reason, generating a relative orbit estimate creates additional value for operators since information about the relative trajectory of a secondary satellite about a client satellite can indicate status, and possibly its intent. In this sub-section, the relative orbit findings (based on the tracking data collected during the Mont-Mégantic experiment) are described.

5.8.1 General filter setup

Relative orbit estimation was performed using a Kalman filter by applying the linearized measurement and dynamics models described in Chapter 3. The linearized form of the measurement (equation 3.33) was used. Both tracks’ initial states were set using the operator’s orbital ephemerides with an initial position covariance set broadly so that observations would be accepted by the filter.

Based on the measurement noise $\Delta\alpha$, $\Delta\delta$ residuals from Figure 60 and Figure 70, the measurement noise matrix was set to a diagonal of

$$\mathbf{R} = \begin{bmatrix} (0.2)^2 & 0 \\ 0 & (0.2)^2 \end{bmatrix}^{30} \quad (\text{arcseconds}^2, \text{arcseconds}^2)$$

The initial state covariance was also set broadly to span the width of the isoplanatic angle (5 arcsec \sim 1 km in GEO) to ensure that the measurements are accepted by the filter. The covariance \mathbf{P} was set to

$$\mathbf{P} = \text{diag} [1^2, 1^2, 1^2, 0.0001^2, 0.0001^2, 0.0001^2, 1e-9] \quad (\text{km}^2, \text{km}^2/\text{s}^2, \text{km}^2/\text{kg})$$

where the final covariance term on the diagonal is the initial uncertainty of the differential SRP constant.

Initial experimentation involved the tuning of the filter and found that convergence³¹ was best achieved with the process noise \mathbf{Q} set to a diagonal of small values such that

$$\mathbf{Q} = \text{diag} [(10^{-6})^2, (10^{-6})^2, (10^{-6})^2, (10^{-6})^2, (10^{-6})^2, (10^{-6})^2, (10^{-10})^2] \quad (\text{km}^2, \text{km}^2/\text{s}^2, \text{km}^2/\text{kg})$$

Filtering of data was performed sequentially after each image processing stack was processed and measurements collected. All observations were included in the orbital fit excepting when the objects were greater than 5 arcseconds apart or during times of high turbulence (as in the second track) or high fringe rotation rate.

The filter was set to reject spurious observations that exceeded the 3- σ level. Observations were filtered by comparing the norm of the measured and the predicted observation matrix \mathbf{dy} to the innovation of the observations according to the logic

$$\begin{aligned} & \mathbf{if} \ \mathbf{norm}(\mathbf{dy}) > \mathit{SigmaLimit} \times \sqrt{\text{Tr}(\mathbf{H}\bar{\mathbf{P}}\mathbf{H}^T + \mathbf{R})} \\ & \mathbf{then} \ \dots \ \text{propagate the state and covariance, (do not update)} \end{aligned}$$

³⁰ During processing the arcsecond values are converted to radian equivalents. 1 radian \approx 206265 arcseconds

³¹ Simulations were required in order to determine convergence behavior of the filter. This is detailed in section 6.2

If the norm of the measurement residuals exceeded the 3-sigma limit of the innovation matrix, then the state and covariance are propagated according to equations 3.69 and 3.70. No state or covariance updates would be issued at those times.

5.8.2 1st track: Anik F1R and Anik G1 – Relative orbit state estimate

The initial state of Anik F1R relative to Anik G1 was initialized a state vector of epoch 18 Feb 2014 at 2^h05^m UTC and a relative state $\mathbf{x}_0 = [-9.936, 0.328, -0.038, 0.248, 1.446, 2.895, 0.001]^T$ (km, m/s, m²/kg). Differential tracking data was processed by the filter.

Processing precise differential angle observations significantly reduced the initial state covariance of in-track and cross-track measurement uncertainties. Both of these state variables are detectable with differential angles measurements $\Delta\alpha$, $\Delta\delta$. Because of measurement uncertainties of 0.2 arcseconds per axis—as specified in the measurement noise matrix \mathbf{R} —this state roughly translates to an immediate ~ 40 m positioning knowledge in both the y_{Hill} and z_{Hill} components of the relative position vector. The radial direction x_{Hill} , (while dynamically coupled to y_{Hill}) is not updated immediately. It requires longer tracking intervals to arrive at its estimate.

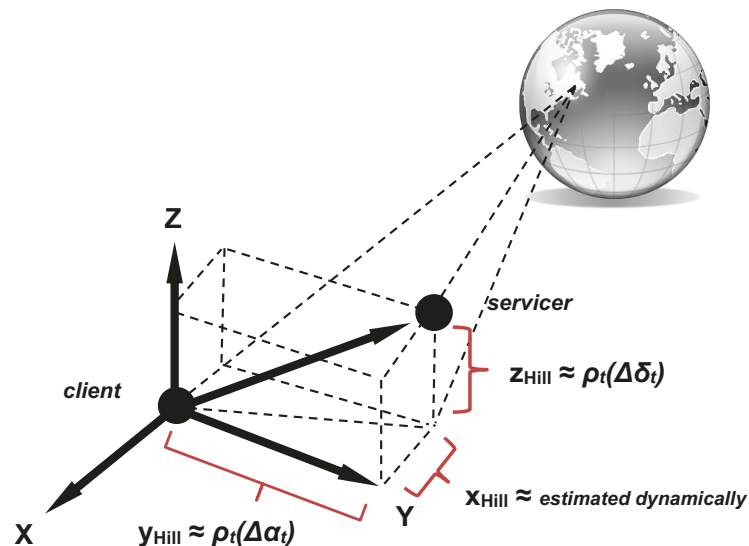


Figure 71: $\Delta\alpha$, $\Delta\delta$ measurements near-directly inferring state variables y_{Hill} and z_{Hill} .

Figure 72 shows the estimated relative orbit of Anik F1R with respect to Anik G1. This estimate was derived from the tracking measurements produced by the filter. A three dimensional projection (see Figure 73), roughly aligned with the Hill trajectory plot, is also shown to emphasize the manner that the estimated relative orbit adheres to the reference ephemeris. The track is relatively smooth over the short tracking arc and adheres to reference positions within 100 meters.

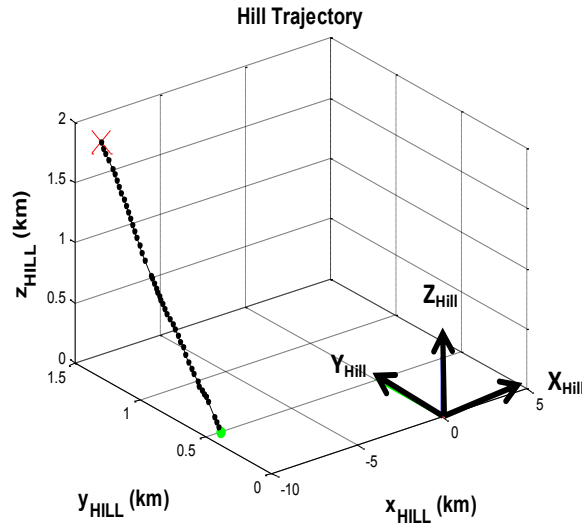


Figure 72: Anik F1R Relative Trajectory with respect to Anik G1. Green dot is track start. Red x is track end.

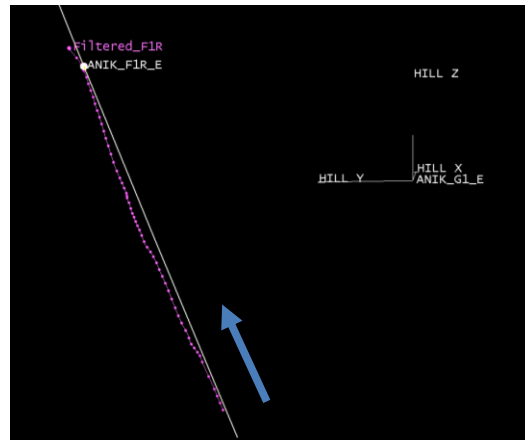


Figure 73: Anik F1R relative trajectory with respect to Anik G1. Three-dimensional plot of measurements (purple points) versus reference ephemeris (white). Direction of motion is indicated.

Sporadic θ measurements were encountered at the center of this track. The sporadic data points were properly rejected by the filter at $t \sim 132$ minutes according to the logic in section 5.8.1 and the state was propagated until good measurements were obtained.

Figure 74 shows the Radial, In-Track, Cross-Track (RIC) error between the filtered estimate of Anik F1R and the reference ephemeris of Anik F1R. Very good consistency of the estimated relative orbit was found and it adhered to the reference ephemeris within 100 meters per axis. Time spans where measurement data were rejected by the filter are shown.

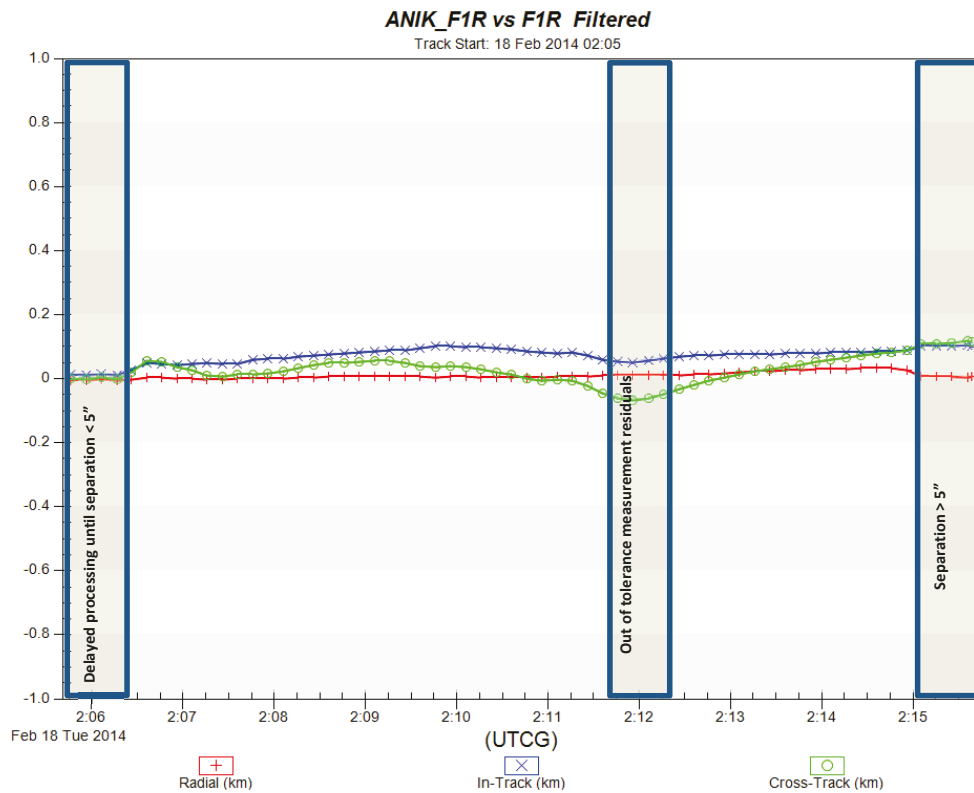


Figure 74: 1st track radial, in-track and cross-track error relative to reference ephemeris. Regions where observations were not processed by the filter are marked

5.8.3 1st track: Anik F1R and Anik G1 – Relative orbit covariance

Figure 75 shows the uncertainty of the radial, in-track and cross-track position for the 13 minutes of observational data processed by the filter. A slight but noticeable growth in

the radial position uncertainty (σ_R) is visible. In the next chapter, this uncertainty is linked to the incomplete observability of the x_{Hill} state variable. The in-track (σ_I) and cross-track (σ_C) directions largely coincide with the plane-of-sky measurements $\Delta\alpha, \Delta\delta$ and show a rapid reduction in position uncertainty when observations at $t \sim 126.3$ minutes is added to the filter. This reflects the relatively high precision of the $\Delta\alpha, \Delta\delta$ measurements of ~ 0.2 arcseconds accuracy which can be used to directly estimate the y_{Hill} and z_{Hill} components of the relative position vector. Although it is less noticeable, Figure 75 shows a slight growth of in-track and cross-track uncertainties which suggests that the filter is still estimating the radial position and radial velocity to complete a state estimate.

The $\Delta\alpha, \Delta\delta$ measurements are nearly direct measures of the y_{Hill} and z_{Hill} state components as these components are near-fully projected onto the plane of the detector. The radial component is not as observable due to the Hill frame's near alignment with the detector axes due to the viewing geometry from the ground. The estimate of this component relies on the measurement of the dynamic coupling between the in-track y_{Hill} and radial dynamics expressed in equation 3.40.

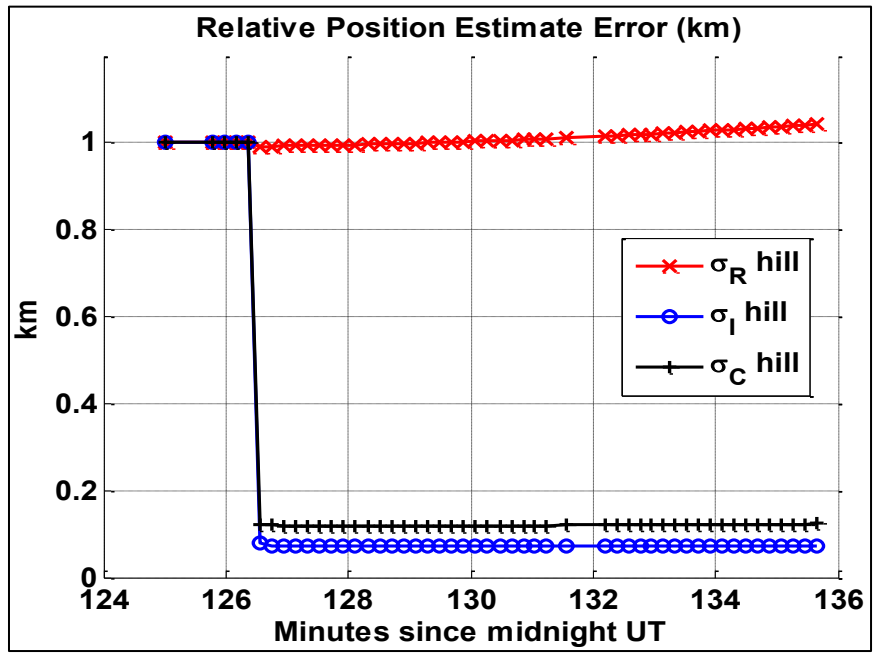


Figure 75: Anik G1, Anik F1R relative orbit uncertainty

5.8.4 2nd track: Anik F1 and Anik G1 – Relative orbit state estimate

The second track of Anik F1 and Anik G1 was initialized with state vector with epoch 18 Feb 2014 at 4^h43^m UTC with an initial relative position vector $\mathbf{x} = [8.082, 1.561, -0.320, 0.022, -1.222, -1.717, 0.001]$ (km, m/s, m²/kg). Due to the high fringe rotation at $t = 292$ minutes the filter was set to reject observations for the timespan between 290.7 and 293.4 minutes. The observations at the start of the track were also ignored as they did not meet the isoplanatic limit of 5 arcseconds.

Two key features were found in the processing of the data for this track (see Figure 76). The first feature was the immediate westward offset when the first observations were accepted by the filter in the estimated position of Anik G1 compared to its reference ephemeris. As mentioned in section 5.6, this offset of ~ 2.5 arcseconds westward of Anik G1's predicted location is believed to be due to ranging bias on board Anik F1.

The second feature is the slight warp in the track of Anik G1. While the filter was set to reject measurements around $t = 292$ minutes it appears that some of the distortion continued to impact the relative orbit estimate. This is likely caused by some residual fringe rotation effect and manifests as a radial error.

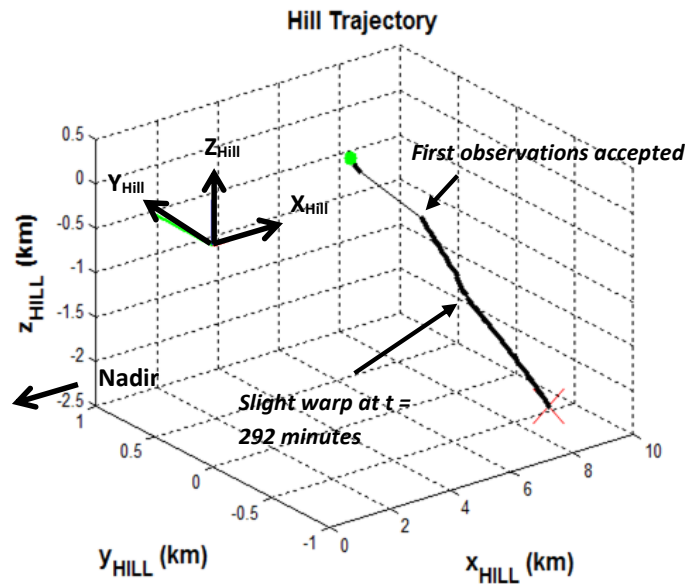


Figure 76: (Left): Anik G1's trajectory relative to Anik F1. Green dot is track start. Red x is track end

Figure 77 shows a 3-dimensional perspective of the estimated relative orbit of Anik G1 emphasizing the westward offset as soon as new relative position measurements were accepted by the filter. Except for the westward offset, the remainder of the track remained consistent with the reference ephemeris.

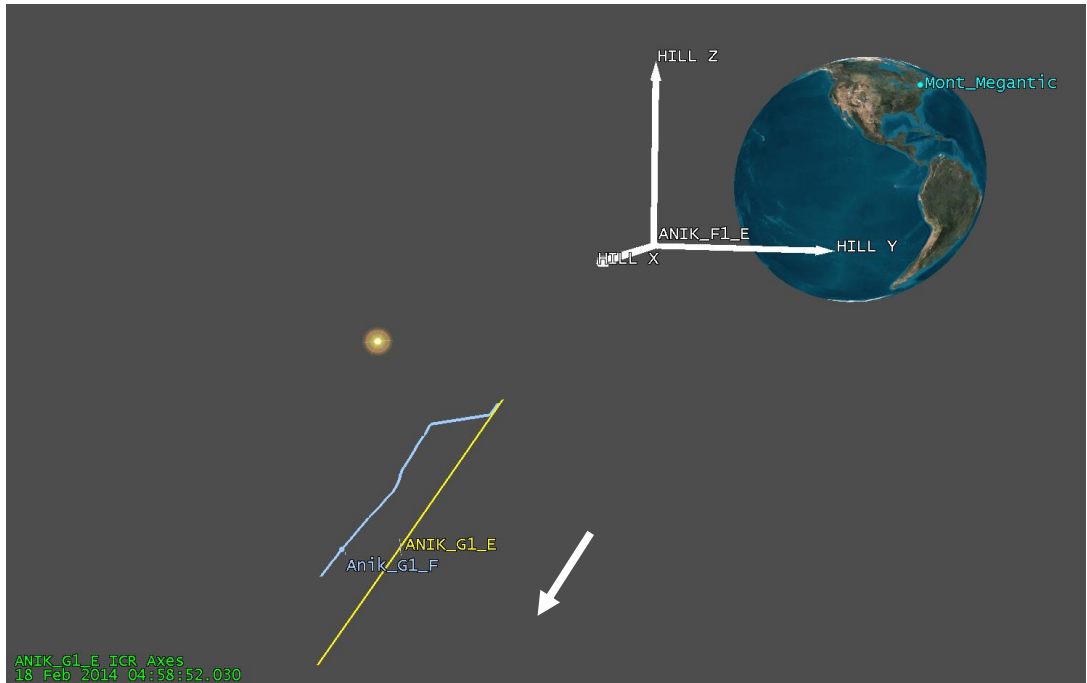


Figure 77: Anik F1 and Anik G1 estimated relative trajectory (blue) and reference trajectory (yellow) showing the westward track bias. Direction of motion is indicated.

The RIC plot shown in Figure 78 shows the consistency of Anik G1’s estimated relative orbit with respect to operator ephemeris. The westward bias is visible as the immediate westward negative offset in the in-track position error as soon as observations were accepted by the filter. Despite this bias, the in-track error appears bounded within a 100-meter region for the entire duration of the track.

After the peak fringe rotation at closest approach, the radial position error in Figure 78 grows indicating that the filter was converging on a relative orbit estimate different than the initial state used to initialize this track. As further measurement data is not added past 05:02 UTC, no further filtering ensues.

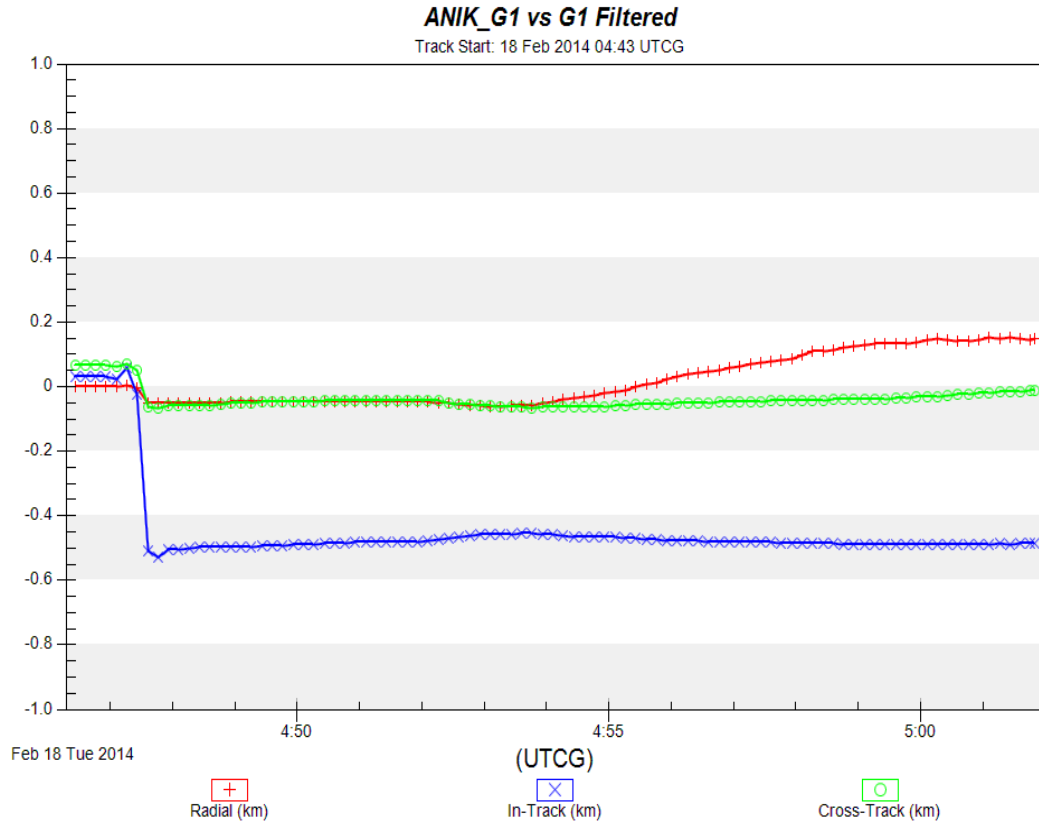


Figure 78: RIC position error compared to operator ephemeris

5.8.5 2nd track: Anik F1 and Anik G1 – Relative orbit covariance

Radial position uncertainty σ_R shows noticeable growth during the 15-minute observation timespan (see Figure 79) which is consistent with the behavior observed in the first track. The observing geometry is nearly identical to the first track with continued low observability with respect to the radial direction. Uncertainties σ_I, σ_C , exhibit growth in their covariances albeit at a much smaller rate compared to that observed in the radial direction.

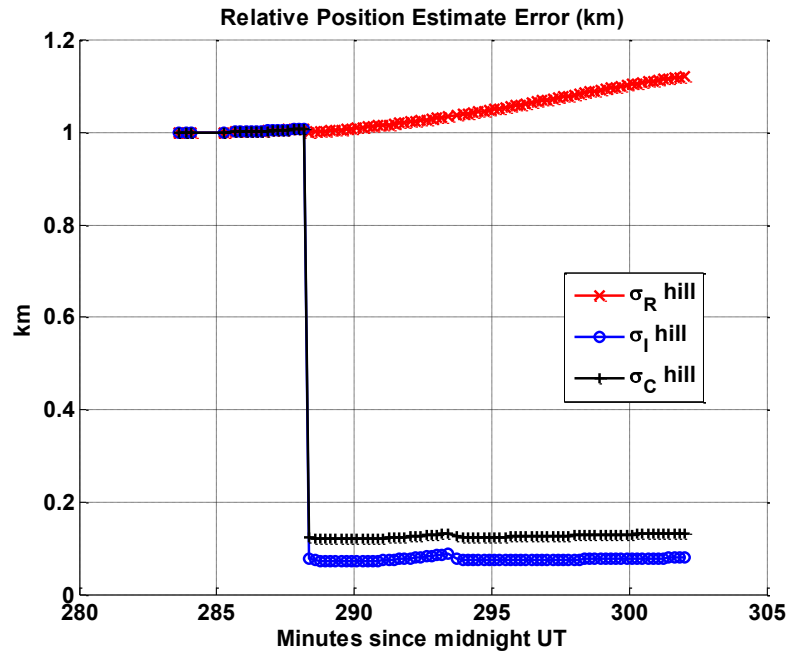


Figure 79: Anik F1, Anik G1 relative orbit uncertainty

5.9 Mont Mégantic relative orbit track summary

The findings of the relative orbit processing indicate that the in-track and cross-track measurements provided good relative orbit estimates however the radial uncertainty grew during the short tracking intervals. This was a cause for concern as relative orbit estimates requiring several days of observations would be of limited use from an operational space surveillance perspective. An investigation of the relative orbit estimation processes' observability and convergence is performed in the following chapter to address this concern.

5.10 Small aperture telescope observations of a visual conjunction

One of the goals of this research was to investigate if small-aperture telescopes are a viable option to perform OOS monitoring. Small aperture telescopes are relatively inexpensive (< \$250k) and are readily available to the space surveillance community. A prototype satellite speckle interferometer was developed at the DRDC Ottawa Space

Surveillance Observatory to investigate the viability of speckle measurements on binary stars and optically conjuncting satellites for OOS detection.

A third optical conjunction between Anik F1 and Anik G1 was speckle imaged on August 2, 2015 using the small aperture telescope at DRDC Ottawa. As in the previous cases, Anik F1 was the brighter satellite in the pair. The satellite magnitudes were $M_{primary} = 9.67$, $\Delta m = 1.63$ or $\alpha_b = 0.22$. This track was the largest magnitude difference attempted with the cross-spectrum speckle imaging approach making it a very good test case for the image processing algorithm. Sample speckle images are shown in Figure 80 and the path of Anik G1 relative to Anik F1 is shown in Figure 81.

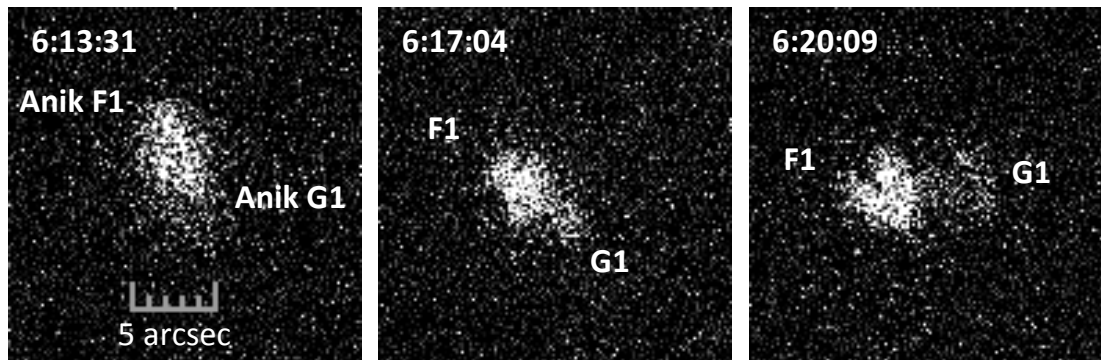


Figure 80: Anik F1, Anik G1 speckle images acquired on 2 Aug 2015

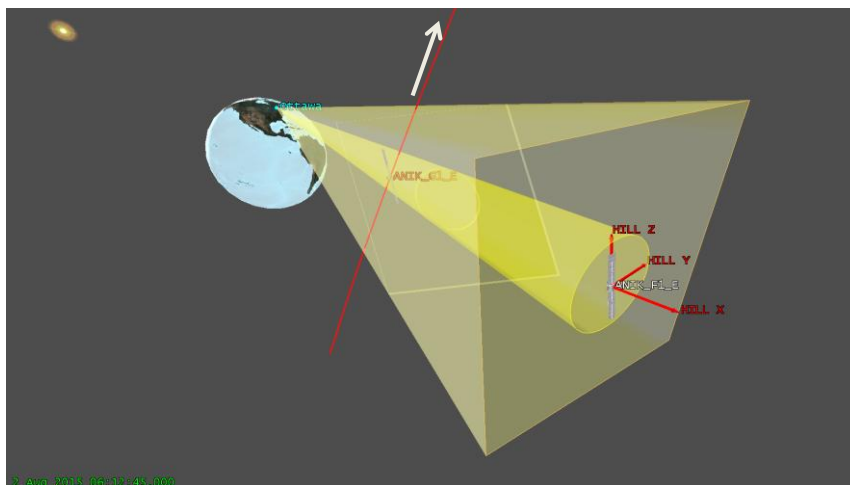


Figure 81: Path of Anik G1 relative to Anik F1 during the third track on August 2, 2015. Conical half radius is the isoplanatic angle of 5 arcseconds. Direction of motion is indicated.

It was found that the separation measurements (d) derived from the new fringe separation measurement approach continued to be more reliable than the original (fringe-minima detecting) technique. Figure 82 shows the separation measurements compared against one another where the original technique (blue circles) and the new technique (red squares) are contrasted. When the fringe rotational rate was highest at closest separation the excursions in d were again observed (see Figure 82 at $t = 376.5$ minutes). The original approach also continued to show higher measurement scatter whereas the new technique again exhibited better measurement residuals. A short tracking interruption is visible at $t = 378-379$ minutes where the telescope mount lost tracking on the target and a short period to reacquire the satellite pair was needed.

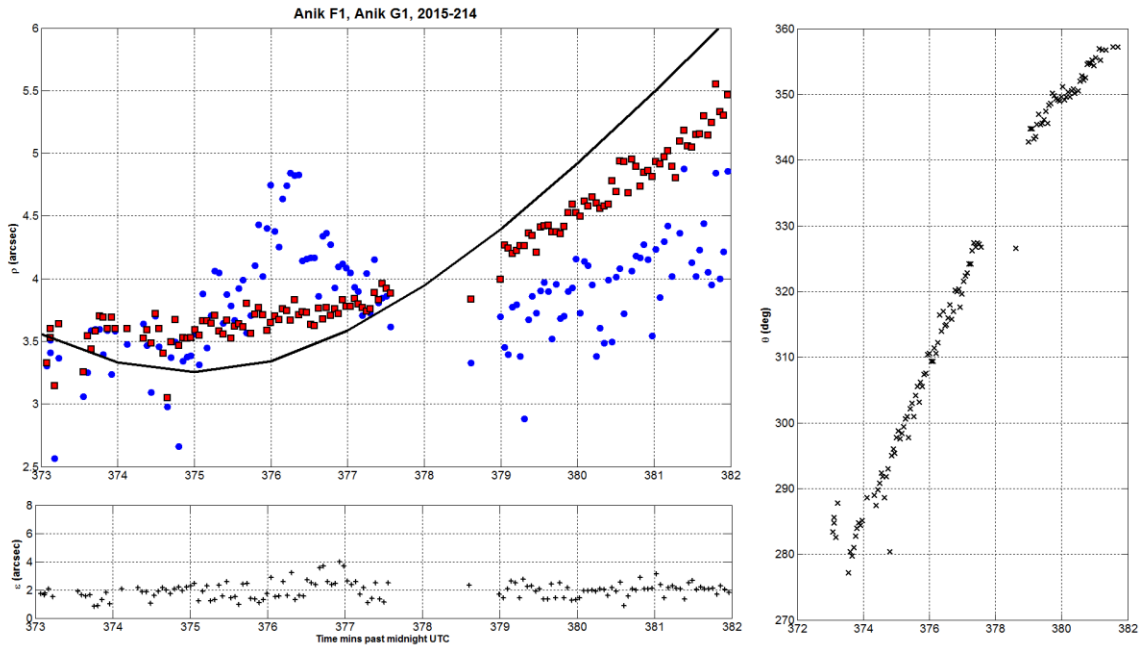


Figure 82: (Top left): Anik F1, Anik G1 separation distance (arcseconds). Red is the new processing approach, blue points are d (ρ) measurements inferred from the fringe minima. The black line indicates the true separation distances from ephemerides (Right): Orientation angle θ , (Bottom): Seeing ε

A quadratic trend for both speckle-measured and operator ephemeris derived separation distances was observed. The speckle measurements tend to exhibit a shallower trend than the reference ephemeris and it is difficult to assess whether or not this is a

measurement effect or if the error is embedded in-track bias existing within the operator ephemerides as described in section 5.6

Figure 83 shows this track's difference between the the differential angles measurements $\Delta\alpha, \Delta\delta$ compared against operator reference ephemeris. Good linear trend behaviour is observed but a bias of ~ 0.5 arcseconds is seen primarily in the $\Delta\alpha$ measurements. Some curvature is observed in the differential declination measurements at the start of the track between $t = 374.5$ and $t = 376$ minutes. No evidence of a maneuver in the orbital ephemerides was found indicating that the observations between these times are anomalous. While the $\Delta\alpha$ measurements do not exhibit the large 2.5 arcsecond bias observed during the second Mont-Mégantic track, it suggests that a systematic bias effect in the ranging system is possibly occurring on Anik F1.

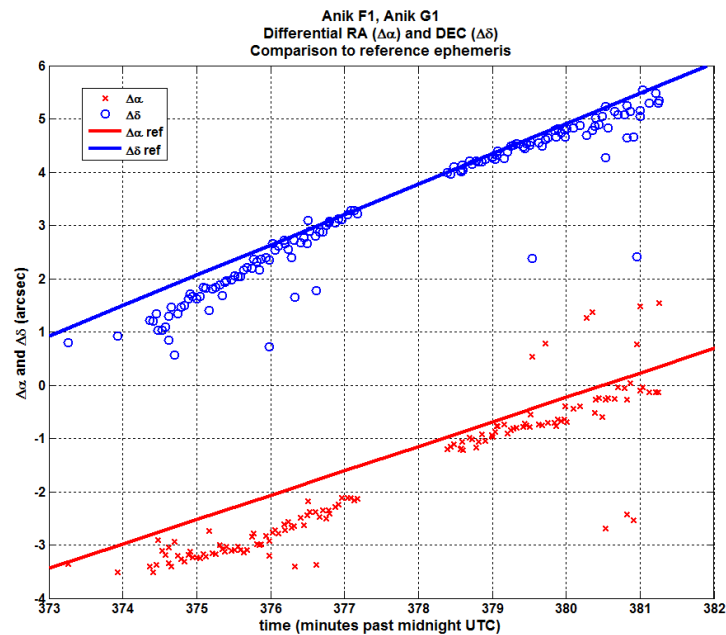


Figure 83: Differential measurements $\Delta\alpha_t, \Delta\delta_t$ (red x, blue o) plotted against reference ephemeris

Figure 84 shows the estimated relative orbit using the new measurement approach. The track exhibits some radial deviation and was expected given the findings from the Mont-Mégantic observations. The track largely adheres to the reference ephemeris indicating that the new approach to measuring the separation distances is much more robust even during times of high fringe rotation. The covariance (not shown) exhibited

similar behaviour to the Mont-Mégantic tracks where a slight growth in the radial uncertainty was observed. This effect is discussed in the following chapter.

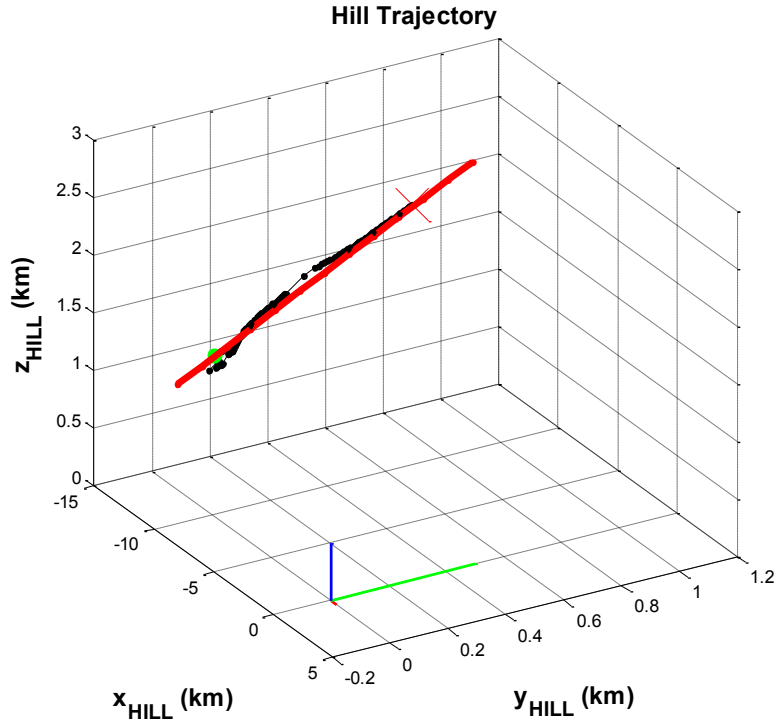


Figure 84: Measured trajectory of Anik G1 with respect to Anik G1.

5.11 Chapter summary, contributions and recommendations

Rare optical alignments of co-located geostationary satellites provided observational opportunities to test the cross-spectrum measurement approach on real satellite targets. While co-located satellites undergo much faster relative motion than what would be expected in real OOS mission scenarios, the lessons learned in these experiments provide real-world insight into practical issues of the speckle measurement approach.

During the Mont-Mégantic experiment, a medium aperture (1.6m) astronomical telescope was configured to perform speckle observations on co-located geostationary satellites that appeared to close within 5 arcseconds of one another. Anik G1 and Anik F1R were detected with magnitudes of $M_{primary} = 10.23$, $\Delta m = 0.36$ and speckle images were obtained. A second serendipitous track—where Anik F1 and Anik G1 closed to within 3.5 arcseconds of one another—was also speckled with magnitudes of $M_{primary} =$

9.03, $\Delta m = 1.53$. Tracking of the objects was achieved by deactivating the sidereal drive of the telescope mount and applying small non-sidereal rates to follow the motion of the brightest satellite of the pair. Over 5000 images per track were collected using an EMCCD during the ~ 15 minute observational periods for each satellite.

Differential angles measurements produced by image processing the cross-spectrums of the speckle images were found to have precisions of 0.2 arcseconds or better. Exceptions were made at times of maximum fringe rotational rate where unrealistic separation measurements were encountered. When the satellites have a high relative velocity (as they did in the co-located satellite proxy case) and the satellite closes to their point of closest approach, the reliability of the fringe detection algorithm is reduced due to highly rotated fringes being stacked on one another. This effect is less likely to be observed in a real OOS cases as their lower relative velocities (due to their closer proximities) would not provoke such high angular rates invoking fringe rotation. The improved fringe minima detection technique of Fourier transforming the imaginary component of the cross-spectrum was ground to largely address this issue and offers improved measurement precision.

The relative orbit estimations show very good performance of the in-track and cross-track position estimates. Time-exclusions for some observational data was used to increase the dependability of the filter's state estimate due to the isoplanatic angle limit being exceeded and times when the fringes were undergoing high angular rotation. It was found that if the fringe rotation rate was slower than 0.5 degrees per second the differential angles measurements were more trustworthy for the relative orbit estimation. Monitoring the fringe rotational rate could enable a filter in a real-time environment to automatically reject differential angle measurements as they are deemed less reliable. In addition, monitoring of the seeing condition would also be of benefit as degraded seeing conditions reduces r_θ , which reduces the probability of correlated speckles and obtaining good cross-spectrum measurement data.

One key limitation in the relative orbit estimation approach is that the initial states were based on a-priori operator ephemeris knowledge. In a true uncooperative OOS case, where the relative position of the servicer is unknown to the observer, the initial state will need to be determined by an initial relative orbit determination process. Section 3.6

provided a coarse estimate approach that can be used to perform this function. To initialize a blind relative orbit estimate, a short track of data (15 minutes to 1 hour or so) is required to create a coarse initial state estimate in order to seed optimal orbit determination.

While orbit estimates were made on data collected during the ~15-minute tracking intervals, convergence of the orbital estimates did not occur. This is attributed to the partial observability of the radial component of the Hill frame position and velocity. This effect warranted further examination and is discussed in more detail in the following chapter. While convergence was not achieved, very good in-track and cross-track estimation did occur indicating that the measurements were providing corrections which agreed with the reference operator ephemeris.

A small-aperture telescope was successful at collecting speckle measurements on Anik F1 and Anik G1 and produced good relative orbit estimates for the short tracking arc. The satellite magnitudes acquired with the small aperture telescope were $M_{primary} = 9.67 \Delta m = 1.63$ ($\alpha_b=0.22$). This track used the improved technique to determine the separation measurements between the two satellites based the use of the Fourier transform of the imaginary fringes. The measurements were found to be much more reliable (and less variable) especially when the objects neared their point of closest approach.

While relative orbit estimation of co-located satellites has been analyzed by various authors [55][67][68][69][71], there is no literature indicating that very closely-spaced relative orbit estimation on satellites in GEO has been performed, nor speckle interferometry applied to this particular problem. The good performance of the differential angles measurements indicates that this approach is viable for usage provided that lower latitude ground observing locations are used and they experience steady seeing conditions.

Chapter 6: Observability of relative orbits using differential angles

The tracks collected during the experimental observations demonstrated three cases where the relative orbit estimates did not converge within the 15-minute observational timespan. This finding called the speckle satellite observation approach into question as there were two possibilities regarding the orbit estimation using differential angles: 1) The filter would continue to diverge, or 2) the filter requires days of continuous observations for convergence to be achieved. It was known that relative orbits between two satellites were observable [68], therefore convergence of the orbital estimates is implied. However, the *transient behavior* of the covariance was not discussed in prior literature.

This transient behavior raised questions about this technique's viability. As visual-band optical telescopes are limited to operating only at night under favorable weather conditions a speckle observational approach requiring days to converge on a relative orbit estimate is of little value. In addition, conjunction estimation or tracking the motion of unexpected OOS objects requires timely orbital estimates in order to plan maneuvers. A need for timeliness of the filter's convergence is required.

This section examines the transient convergence behavior of the filter using the differential angles approach. Several avenues are explored to validate the convergence of the filter:

- 1) examining the transient behavior of the filter for simulated OOS tracking cases;
- 2) assessment of the impact that observation accuracy (precision) on the convergence;
- 3) an assessment of the observability of the system.

The Hill coordinate frame's radial direction is nearly collinear with the line of sight from the ground based observer. This viewing geometry provides good "plane-of-sky" measurements (See Figure 85) for the secondary object's y (in-track) and z (cross-track) position. The radial position x is considerably less observable due to this near collinearity of the camera boresight and the radial direction of the Hill coordinate system. The estimation of this component is then reliant on the dynamic coupling between the in-track

and radial components in Hill's equations. If in-track measurements are collected, an estimate of the radial position of the secondary can be achieved. The relationship between the measurements and the relative orbit's convergence will be examined in this chapter.

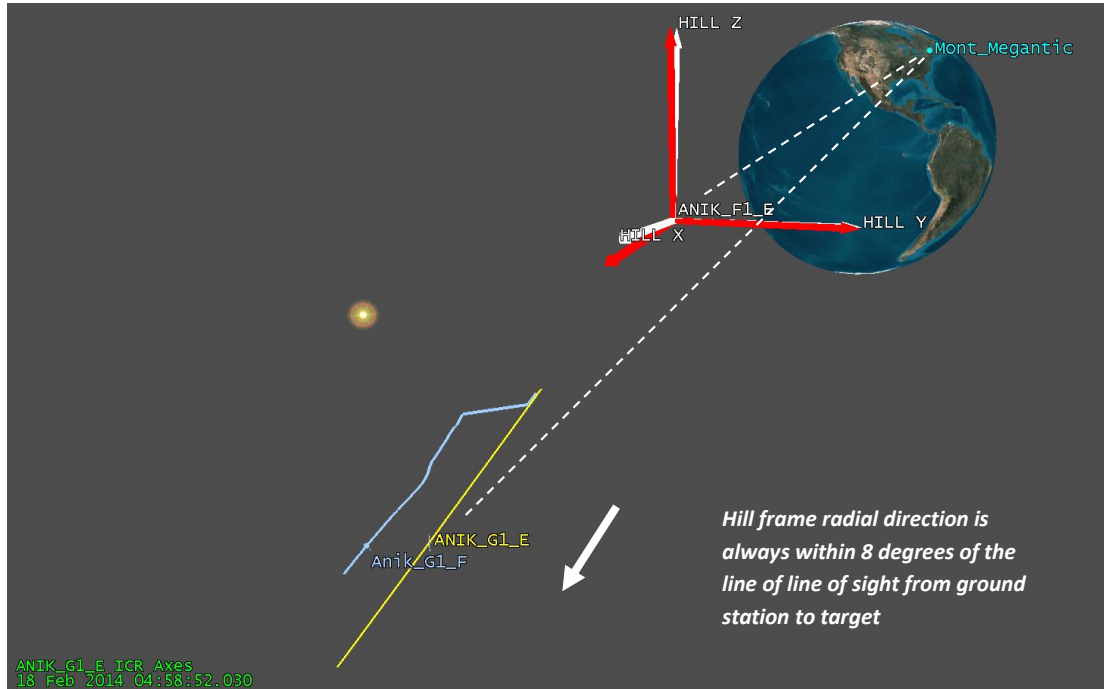


Figure 85: The detector's coordinate axes (red EMCCD axes) showing near alignment with the radial direction of the Hill frame (white)

6.1 Prior work

Kawase [67] studied the steady state convergence performance for differential angles tracking of clustered geostationary satellites and indicated that convergence occurred on the timespan of one day with a steady state error of ~100-200 meters for observation noise of ~0.39 to 0.35 millidegrees (approximately ~1.3 arcseconds). The hourly measurement cadence used in Kawase's study tended to mask the fine-scale transient convergence behavior of his filter but the overall convergence was shown to occur within one day.

Kawase tested the observability of his estimation approach [68] and it was shown to be fully observable. In addition, he provided mean error estimates for the number of

observations processed during estimation. While this indicates that the system is overall observable and that a steady state error condition is also possible, the transient behavior of the filter was not specifically examined.

Sabol [71] examined relative orbit estimation on clustered geostationary satellites in a manner similar to Kawase's work with exception that a specialized relative orbit dynamics model was employed (known as COWPOKE). His findings show that the perturbation algorithm worked well for medium accuracy applications but indicated that the large errors encountered were likely tied to the size of the prediction interval and the limited observability conditions. A specific examination of the time to converge was not expressed in this work.

These analyses emphasized the steady state relative orbit determination accuracy using differential angles measurements on neighboring geostationary satellites. The transient nature of the estimate was not examined nor was the case of very closely-spaced satellites addressed.

6.2 Simulated observational test cases

A series of simulations were created for three relative motion cases using the relative orbit model described in section 3.4.1 and by generating synthetic measurement data by adding measurement noise to the propagated reference orbit. These simulations would test if filter convergence would occur if a continuous, uninterrupted set of observations were provided to the filter for up to 12 hours (the maximum likely time to observe with an optical telescope). These tests examined the particular co-located satellite case of Anik G1 and Anik F1R³² and two conceptual OOS cases where the separation between the servicer and the client is approximately 200 meters. The conceptual cases are intended to test filter converge for inter-satellite separation cases much closer the co-located geostationary satellite cases to better mimic OOS.

³² It is physically unrealistic to observe two co-located satellites for several hours as their relative motion quickly breaches the isoplanatic limit. It is possible however to use wide-field instruments to measure their relative positions using typical space surveillance means. This test is to understand how long it takes for convergence to occur.

6.2.1 Anik G1, Anik F1R

This co-located geostationary satellite simulation accepted differential angles measurements continuously to the simulated filter for six hours. This simulation would examine if the filter converged within a short observing session corresponding to observing timeframes corresponding to a summer season observing session.

Figure 86 shows the error between the simulated estimated relative orbit and the reference trajectory. The uncertainties are plotted as the blue envelopes and are scaled to the 2-sigma uncertainty level. It is clear that the radial position covariance diverges slightly for the first 30 minutes and is followed by convergence after approximately 3 hours. Similar behavior is also observed in the in-track and cross-track directions.

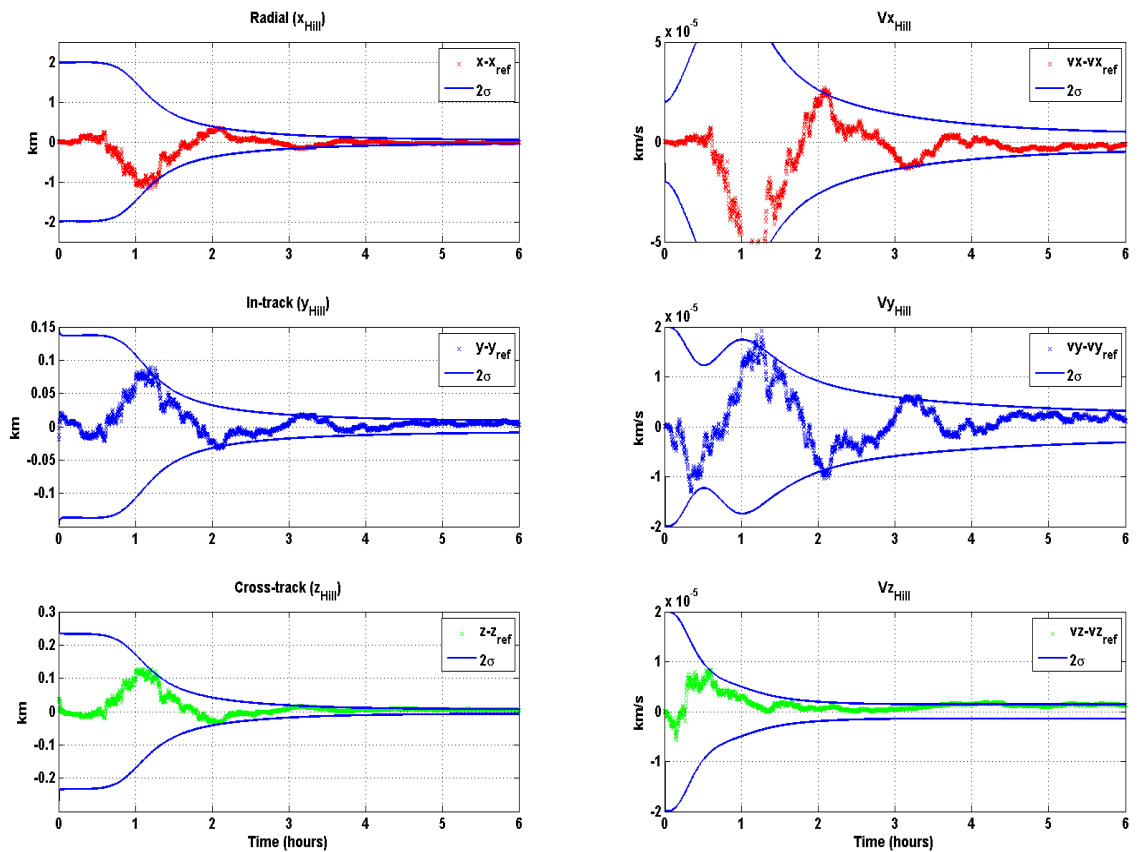


Figure 86: Co-located satellite case with continuous measurements added to filter

Differential angles measurements are insensitive to the secondary object's relative velocity and the estimated relative velocities exhibit strong, coupled divergence behavior

for both radial velocity v_{xHill} and a converging-diverging behavior for the in-track velocities v_{yHill} over the first hour then converges toward steady state after three hours.

It is apparent that while all three relative position measurements show a slight divergence, the radial velocity shows a strong divergence until enough measurements are collected to converge on its estimate. This is expected as the measurement matrix described by equation 3.33 implies no ability to sense the relative velocities of the satellites.

It is notable that the v_z plot exhibits convergence much more directly and doesn't experience the transient divergence/convergence coupling between the v_x and v_y directions. This behavior reflects that the cross-track (z and v_z) state variables are uncoupled from the radial and in-track positions and velocities in the linearized Hill equations. Differential measurements collected in the cross-track plane directly estimate the z and v_z components.

Figure 87 shows two plots of the estimated relative orbit rotated to emphasize the radial convergence behavior compared to the true trajectory. For ~ 3 hours the filter attempts to estimate the radial component causing the jagged appearance of the trajectory in the radial direction (Figure 87 left). Another view of this track aligned with the observer's line of sight is shown in Figure 87 (right). This view emphasizes the relative smoothness of the track in the plane of the detector reflecting the precision of the differential angles measurements in the in-track and cross-track direction. This view suppresses the radial position being estimated continuously by the filter.

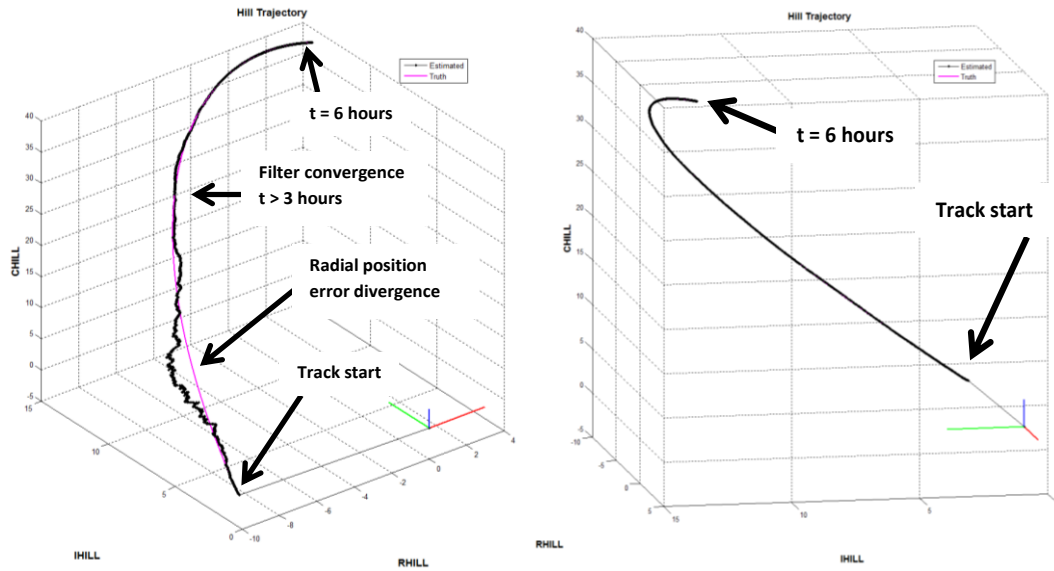


Figure 87: (Left): Simulated Mont-Mégantic track showing radial error. (Right): Simulated track rotated to the plane of observer to emphasize the smooth appearance of the track in this direction

6.2.2 OOS simulated test case, in-track station-keeping of 200 meters

A more realistic OOS scenario where a servicing satellite perched $y_0 = +200$ meters in-track with respect to the client satellite is examined in this simulation. The initial state was set to $\mathbf{x} = [0, y_0, 0, 0, 0, 0]^T$ (km, km/s). The same observing geometry and measurement noise was used in this simulation as in the previous run.

Similar convergence behavior is observed in this case as observed in the co-located satellite simulation (see Figure 88). A slight growth in the radial position (\mathbf{x}_{Hill}) error is observed for $t < 1$ hour. The filter then begins to converge after $t > 0.75$ hours and converges within 10% of the initial state error after 3 hours. The cross-coupling between the v_x and v_y velocities is again observed.

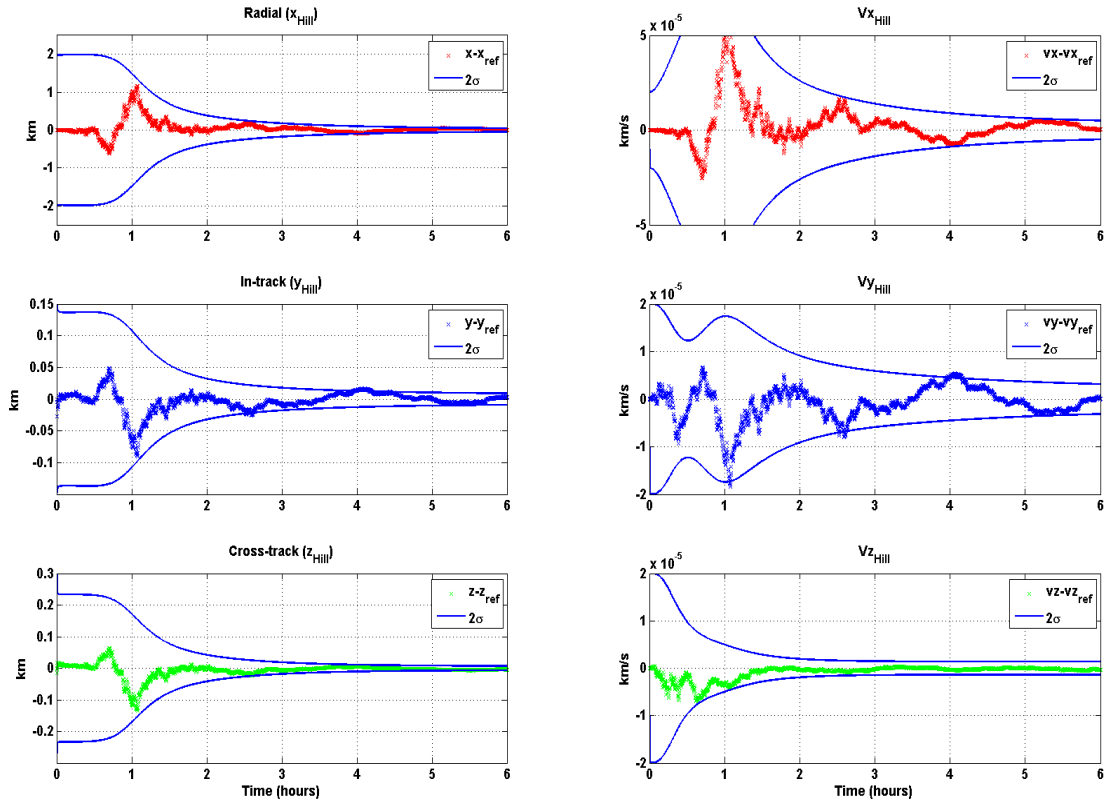


Figure 88: Continuous measurements for +200 m in-track station-keeping

Figure 89 exhibits a spray of radial position estimates as the filter attempts to converge on the estimate for the +200 meter in-track case. The radial position estimate spray is aligned with the line-of-sight of the ground-based observer reflecting the filter's radial position estimation. Eventually the position measurements converge on the +200 meter in-track station keeping location after >3 hours of observations and is marked in Figure 89.

It should be noted that there is a change of scale on in Figure 89 in comparison to the Figure 87. This causes a perceived effect that the radial uncertainty is much higher in this simulation compared to Figure 87. The size of the radial spray is the same between this test case and the first at ~1 km radial uncertainty.

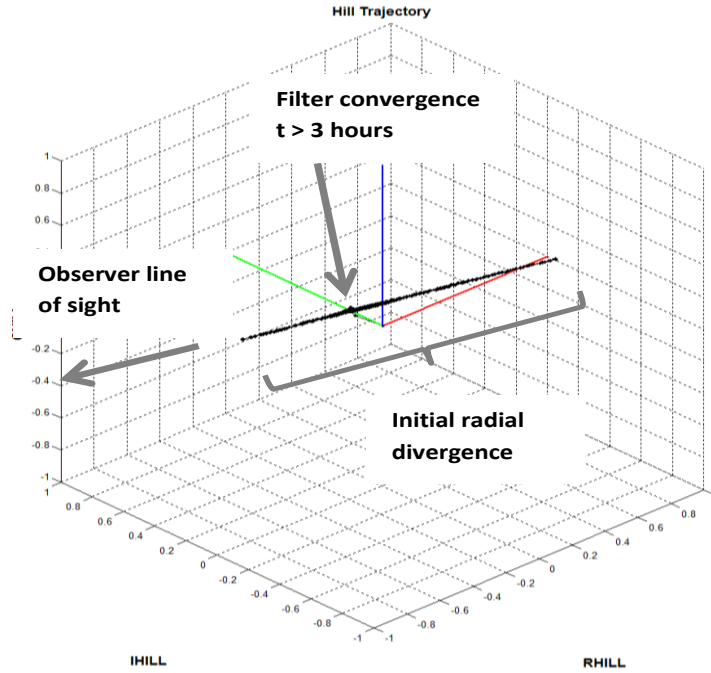


Figure 89: Convergence for the +200 m in-track station keeping case. The radial position of the observations spreads radially along the line-of-sight of the observer

6.2.3 OOS simulated test case, co-elliptic drift of offset of -200 meters

A simulation where the OOS servicing satellite performs $x_0 = -200$ m radial co-elliptic drift relative to the client is analyzed in this case. Co-elliptic drift orbits are relative motion orbits where a servicing satellite moves in a near-linear manner with respect to the client satellite. In contrast to the other two simulation test cases, the mean drift rate between the two satellites is non-zero and the servicer moves continuously with respect to the client satellite.

To compute the in-track relative velocity necessary for co-elliptic drift the initial state couples the radial offset position x_0 and in-track velocity \dot{y}_0 such that

$$\dot{y}_0 = -(3/2)\omega x_0 \quad (6.1)$$

where ω is the mean orbital rate of geostationary orbit (7.29×10^{-5} rad/sec) and x_0 is the radial offset distance. The state is then set as $\mathbf{x}_0 = [x_0, -0, 0, 0, \dot{y}_0, 0]^T$ (km, km/s). The linear in-track speed³³ of the secondary is approximately ~ 1.88 km/orbital revolution.

Figure 90 shows similar convergence behavior as in the previous two cases. At $t = 1$ hour the filter begins to converge and the filter converges after $t > 3$ hours.

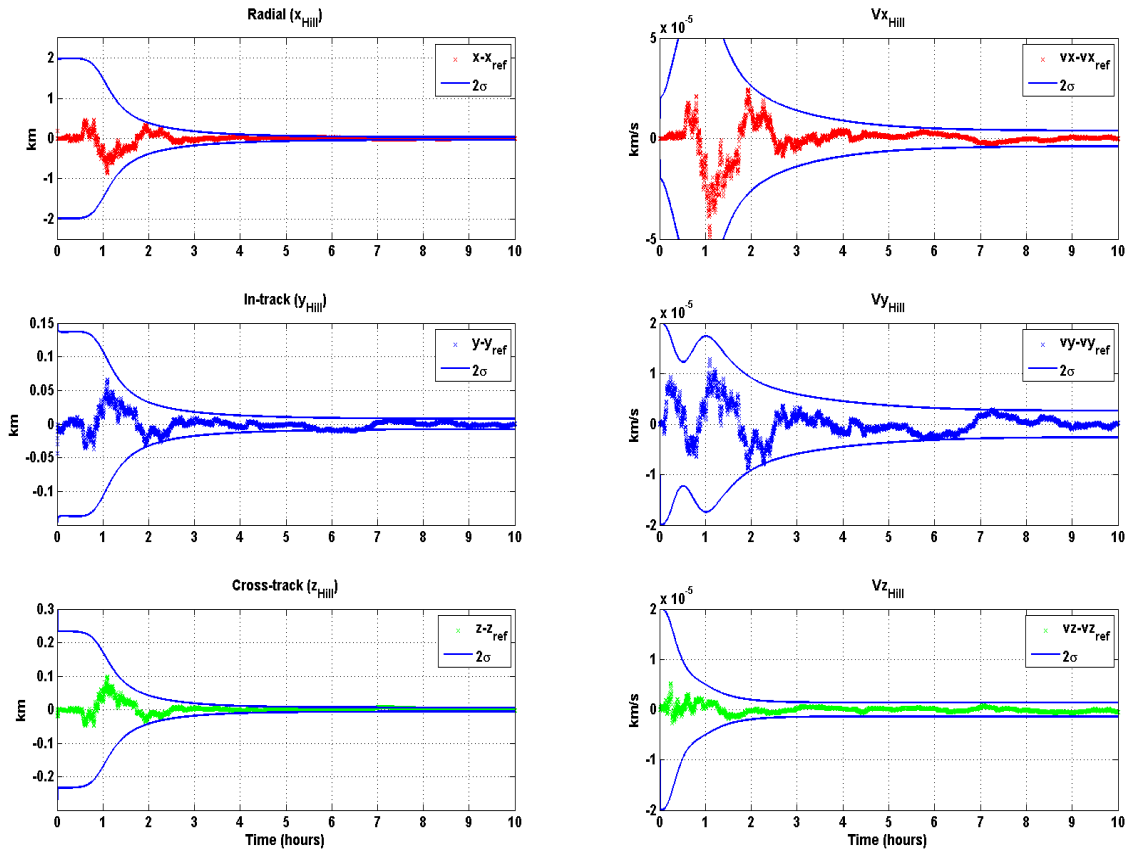


Figure 90: Continuous measurements for -200 m co-elliptic drift

Figure 91 shows the radial position estimates as the filter converges. At the start of the track the radial position measurements spray in the direction along the line-of-sight of the observer and large radial errors are shown. At the end of the track, the relative orbit begins to show a linear trajectory shape consistent with the co-elliptic drift motion.

³³ An estimate for the distance a servicing satellite moves in GEO during co-elliptic drift can be estimated as $d(\text{km}) = 9.43 (\Delta h(\text{km}))$ where Δh is in kilometers.

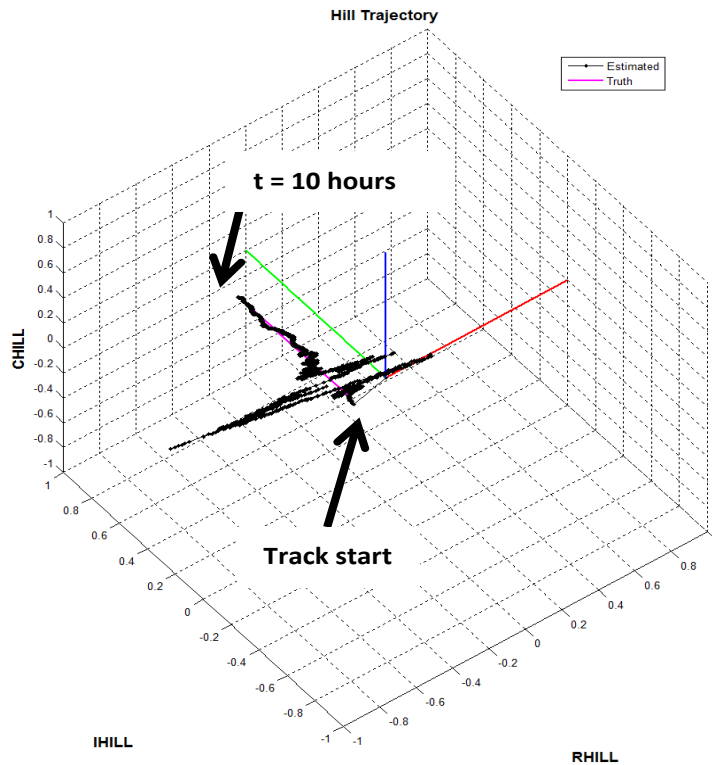


Figure 91: Convergence for the co-elliptic drift case. The spray of radial position estimates is along the line-of-sight of the observer

6.2.4 Test Case Summary

Overall, the simulations show that the filter generally requires three hours or more to converge on the relative orbit estimate assuming a sensor noise of 0.2 arcseconds. Strong cross-coupling between the v_x , and v_y components was observed due to the filter requiring more observational data to estimate their magnitude. All three cases did converge, but required several hours to do so. The radial offset distance size x_0 did not play a strong role in the time to converge the estimate. The co-elliptic drift test case also converged despite the objects having a non-zero relative drift rate.

6.3 Effects of increased measurement precision

The three simulations presented in section 6.2 used a measurement precision of 0.2 arcseconds. This section examines the impact of higher precision measurements on the

transient behavior of the filter. Two test cases are examined, the co-located case for Anik G1 and Anik F1R and +200 m in-track station-keeping case of the servicer.

The same simulation software used to test the three previous test cases was adapted to vary the sensor noise variance $\mathbf{R}_k = \text{diag} [\sigma_{A\alpha}^2, \sigma_{A\delta}^2]$. The span of sensor noise was set to vary from 0.01 arcseconds to 0.5 arcseconds and the amount of time required for the radial component to converge to less than 10% of its initial uncertainty was monitored to determine if the filter converged.

Figure 92 shows that the convergence time improves when higher precision data is processed by the filter. The amount of time required to converge on the orbital estimate mimics a power law of $t_{conv} \sim 4.7\sigma^{0.33}$. Interestingly there was no difference between the co-located satellite test case and the 200 m in-track station-keeping case (both plots overlaid one another).

The measurement noise from the Mont-Mégantic experiments varied from ~ 0.2 to 0.25 arcseconds. If it were possible to collect the observations on the co-located satellites for three hours, rather than the 15-minute period that met the isoplanatic condition, convergence of the orbital estimate would have likely occurred.

Even with sensor noise better than 0.05 arcseconds more than 1.75 hours of observation time is required for a converged relative orbit estimate. Higher precision in-track measurements can improve the rate of convergence. Increasing the number of pixels to sample the psf of the speckles is one way to achieve this. Larger aperture telescopes to produce more sharply defined speckles can also provide increased resolution necessary for fine scale measurement. However, a diffraction limit of 0.05 arcseconds corresponds to an aperture of $\sim 3\text{m}$ so larger aperture systems may not be a viable means to increase sensor precision in order to reduce convergence time due to expense and availability.

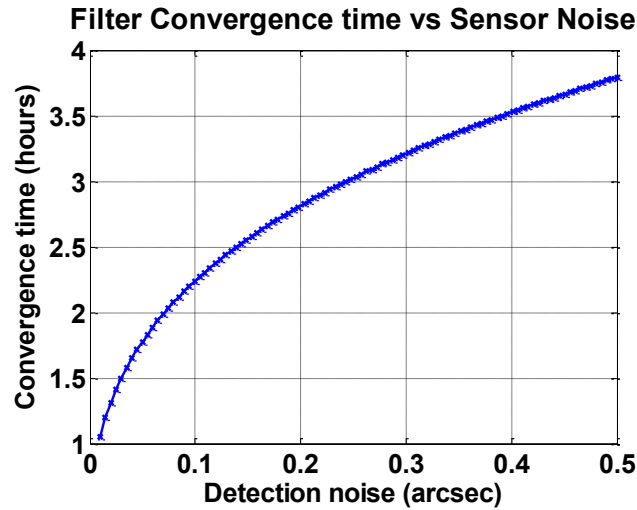


Figure 92: Converge time vs measurement noise

6.4 Observability of the relative motion

Observability determines if the internal state of system can be found by examination of its external (measureable) outputs [118]. If the initial state of the system, based on the indirect measurements, can be found within a finite period of time the system is *observable* [119]. Testing for system observability is generally achieved by an examination of the measurement matrix \mathbf{H} and the state dynamics matrix \mathbf{A} .

In the field of orbit estimation, it is impossible to directly measure the absolute position and velocity of an orbiting object (*the state*) with respect to the center of the Earth. Indirect measurements such as range, range-rate or angles must be collected and the geocentric orbit must be estimated via least squares or other sequential estimation means. Due to this indirect sensing requirement, non-optimal viewing geometries can occur where sensors cannot infer the motion of satellites. For instance, angles-only (camera) observations on a satellite moving directly toward an observer provides no information on the rapid closing rate between the two objects; however cross-track and in-track motion would be directly measurable as these can be inferred from the camera field.

Observability tests can be performed to determine if a system is observable. Vallado [65] indicates that observability can be evaluated by testing the measurement partial derivative matrix product $\mathbf{H}^T\mathbf{H}$ and ensuring that its value is positive definite. This is necessary for least squares applications as the $\mathbf{H}^T\mathbf{H}$ matrix product needs to be invertible in least squares applications.

In control engineering, a general test of observability requires an examination of the linear state dynamics matrix \mathbf{A} and the measurement matrix \mathbf{H} . By forming a compound matrix \mathbf{Q}_0 a test for observability can be performed by forming

$$\mathbf{Q}_0 = \begin{bmatrix} \mathbf{H} \\ \mathbf{HA} \\ \dots \\ \mathbf{HA}^{n-1} \end{bmatrix} \quad (6.2)$$

where n is the number of state variables. If $\text{rank}(\mathbf{Q}_0) = n$ then the system is observable [119]. If insufficient rank³⁴ is found, then the system is not observable.

For the OOS case using the linearized measurement partials matrix from equations 3.33 and the state dynamics from equation 3.42, \mathbf{Q}_0 is found to be full rank. Unfortunately, this insight doesn't lead to understanding of the relative weighting of each measurable on the overall observability of the system. Another test is required in order to examine these characteristics.

6.4.1 Jordan Canonical form – Observability assessment

Partial observability is a case where one or more states cannot be sensed by the output measurements. For the differential angles observations case, it is clear in equation 3.34 that the zeroed columns indicate that the servicer's velocity has no influence on the output measurements $\Delta\alpha, \Delta\delta$. The first column of equation 3.33 contains relatively small

³⁴ The rank of a matrix tests for the maximum number of linearly independence rows and column vectors in a matrix [120].

values³⁵ in comparison to the other two columns which respond to y_{Hill} and z_{Hill} . This is indicative that the measurements are relatively insensitive to changes in x_{Hill} .

An alternative means to assess observability can be achieved by recasting the dynamics equations into the Jordan Canonical Form [119] (JCF). The Jordan Canonical form is a linear transform which represents the state-space equations in block diagonal form useful for controllability and observability analysis [121]. Analyzing observability in the JCF offers an ability to infer the relative detectability of the states from the measurements.

The state and measurement equations requires the state dynamics and measurement equations to be recast as

$$\bar{\mathbf{x}} = \mathbf{V}\mathbf{x} \quad (6.3)$$

$$\bar{\mathbf{A}} = \mathbf{V}^{-1}\mathbf{A}\mathbf{V} \quad (6.4)$$

$$\bar{\mathbf{B}} = \mathbf{V}^{-1}\mathbf{B} \quad (6.5)$$

$$\bar{\mathbf{H}} = \mathbf{H}\mathbf{V} \quad (6.6)$$

such that the state dynamics and measurement equations are cast as

$$\dot{\bar{\mathbf{x}}} = \bar{\mathbf{A}}\bar{\mathbf{x}} + \bar{\mathbf{B}}\bar{\mathbf{u}} \quad \bar{\mathbf{y}} = \bar{\mathbf{H}}\bar{\mathbf{x}} \quad (6.7)(6.8)$$

The matrix \mathbf{V} is a transformation which is the solution of

$$\mathbf{A}\mathbf{V} = \mathbf{V}\mathbf{J} \quad (6.9)$$

where \mathbf{J} is the diagonal matrix containing the eigenvalues of the solution.

³⁵ α - α_i and δ_i are small angles not exceeding 8 degrees. For the Mont-Mégantic experiments α - $\alpha_i = 3.922^\circ$ and $\delta_i = -6.92^\circ$. Converting to radian equivalents are 0.0684 and -0.1208 radians.

Computing the $\bar{\mathbf{H}}$ matrix provides insight into the relative degree of observability of each of the states. By inspecting the values in the columns in $\bar{\mathbf{H}}$ the sensitivity of the output measurements as influenced by the state can be directly compared [121].

Using the observational parameters for the Mont-Mégantic observations ($\alpha - \alpha_t = 3.92^\circ$) and $\delta_t = -6.69^\circ$) the canonical form of the observation matrix is expressed as

$$\bar{\mathbf{H}} = 1 \times 10^{-6} \begin{bmatrix} 0.011 & 6.887 & 75.382 & 75.382 & 0 & 0 \\ 0.0001 & 11.622 & 4.399 & 4.399 & 12.415 & 12.415 \end{bmatrix}$$

$\bar{\mathbf{H}}$ shows that the first column consists of small numbers in comparison to the other columns indicating that both measurements $\Delta\alpha, \Delta\delta$ are relatively insensitive to the state of the radial component x_{Hill} . Thus, the observations using the differential angles on closely-spaced satellites is observable overall based on the test in equation 6.2. However, the JCF analysis shows that the measurements are less influenced by changes in the radial state of x_{Hill} indicating that a partial observability condition exists for the radial state variable using differential angles measurements.

6.5 Chapter summary, contributions and recommendations

The Mont-Mégantic observation campaign produced a good set of measurement data to attempt relative orbit estimation on closely-spaced objects in geosynchronous orbit. While good relative orbit estimates were obtained the results did contain a surprise as the estimate for the Hill position vector did not converge despite filtering the full 15 minutes of observations collected for each track. This convergence issue prompted an examination of the transient convergence behavior of the filter. If a relative orbit cannot be estimated based on data collected within one night-time observing session (< 12 hours), the approach would have little value.

Work by others [55][68][71] who investigated the relative orbit estimation problem using differential angles on geostationary satellites did not indicate a fundamental problem of convergence. While this was promising, these works did not specifically address the problem of convergence for very closely-spaced satellites in GEO orbit.

This chapter's contribution examined the specific case of very closely-spaced satellites in GEO with an eye toward the transient convergence behavior of the filter. This was

addressed in three ways; 1) simulation to examine the time to converge 2) variation of sensor noise effects on convergence and 3) an examination of observability.

Simulations were conducted where continuous differential angles data were added to the filter for fit-spans longer than the Mont-Mégantic observations. All simulation results showed that convergence was achieved after >3 hours of differential angles observations. This convergence was achieved for both co-located geostationary satellite test cases and two test cases mimicking 200m OOS formation flight. This was promising as a three-hour time-span is reasonable for a ground-based electro-optical sensor to operate and multiple tracking sessions do not appear to be required.

By varying the measurement noise it was found that there was direct reduction in the convergence time by using more precise measurement data. For the Mont-Mégantic experiments, the simulation results show that the 0.2 arcseconds of measurement noise experienced at Mont-Mégantic would have required ~2.8 hours to converge on a relative orbit solution. Improving the measurement noise to 0.1 arcseconds would reduce this time by ~0.6 hours in accordance with a power law sensitivity (Figure 92). This is practical to implement from an engineering perspective as higher sampling of the optical point spread function or by stacking more images to increase the signal to noise ratio can result in better measurement noise performance for astrometry.

Observability analysis confirmed that two closely-spaced satellites are observable overall, however only partial observability of the radial component was obtained by inspecting the Jordan Canonical Form of the observation matrix. This was expected due to the near alignment of the detector axes with the in-track and cross-track directions of the client satellite's motion.

Chapter 7: Conclusions

This research developed a ground-based electro-optical observational approach to detect the presence of very closely-spaced satellites performing OOS in geostationary orbit and measure their relative positions. Given the likelihood of future, close-proximity flight space missions in this orbital regime, this work represents a new contribution to the art of astrodynamics and space surveillance. The speckle interferometric (cross-spectrum) technique for satellite tracking developed in this research offers a means to measure the relative orbit between a client and moderately-sized servicing satellite in very close proximity to one another. This research made contributions by identifying: observational and equipment requirements, image processing and relative orbit estimation requirements and limitations for observing very closely-spaced satellites in geosynchronous orbit. The cross-spectrum technique was also validated using experimental test cases on geosynchronous satellites using a medium and a small aperture telescope. This research offers a new space surveillance tracking approach to support future OOS missions or complement sparse aperture or adaptive optics imaging approaches.

This chapter provides a recap of key findings, contributions, applications, and recommended future research avenues.

7.1 Thesis summary

Prior art in the optical tracking of closely-spaced objects in geostationary orbit emphasized techniques to assist in the observation association problem on geosynchronous satellites residing in neighboring, or the same, station-keeping boxes. The problem of detection and tracking of objects performing proximity operations about geosynchronous satellites with separations less than 1 km (5 arcseconds in GEO orbit when viewed from the ground) has not been addressed.

Attempting astrometric measurements between two satellites subtending angular sizes less than 5 arcseconds is a new area for space surveillance. Atmospheric turbulence cells subtend angles comparable to the size of the measurements which are being collected on two objects in geosynchronous orbit. While remarkable achievements have been made in

geosynchronous satellite imaging community, these approaches require very large, complex adaptive optics systems or dispersed sensing arrays to detect and infer the presence of the secondary satellite and to form high resolution imagery. These approaches also use deconvolution algorithms which do not lend itself well to real-time relative orbit estimation due to computational overhead. As typical geostationary satellites solar panel widths are ~ 2 meters, the necessary aperture diameter needed to resolve (or image) fine scale detail would require apertures much greater than ~ 15 meters in diameter.

Recognizing the complexity and computational limitations of direct imaging, this work examines a novel adaptation of speckle interferometry to measure differential angles between the satellites. These differential astrometric measurements enable relative orbit estimation without needing to reconstruct an image. A cross-spectrum speckle interferometry approach, adapted to overcome atmospheric turbulence is detailed with a view toward taking advantage of the availability of small to medium aperture telescopes. While the data acquisition approach mimics the techniques used by the binary star community, it was found that the use of the cross-spectrum, rather than Directed Vector Autocorrelation, is a more computationally efficient means to unambiguously determine the location of the secondary satellite in proximity to the client. This reduction in computational expense can pave the way to enable real-time detection possibilities.

This research was performed when high frame rate and very low read noise EMCCDs are becoming commercially available making speckle techniques a renewed possibility for small and medium aperture telescopes. This is in contrast to the photographic and video detector technologies used in the 1970s and 1980s when speckle interferometry was in its infancy. These older detector technologies limited speckle interferometry to brighter objects and to the use of larger aperture telescopes. EMCCD detector technology, coupled with small to medium aperture telescopes, adds additional freedom to detect objects in geosynchronous orbit.

A relative orbit determination approach for very closely-spaced geostationary satellites was devised in this work. A derivation of the observational model is shown and a form of the solar radiation pressure adjusted Hill's equations for short observational arcs are identified. Raw speckle images are of little value without an image processing approach

to transform the imagery into measurables needed for relative orbit determination. An image processing algorithm using the cross-spectrum of the square of a zero-mean image is described and some functional limitations (such as cosmic rays) in the use of this algorithm are also identified.

The configuration of small and medium aperture telescopes to perform satellite speckle interferometry is also provided. It was found that the use of the Sloan i' filter is a good compromise to reduce the effects of chromatic dispersion and to reduce background noise due to lunar or atmospheric sky glow. Signal-to-noise modelling for small and medium aperture telescopes indicated this approach is best suited for when the primary satellites brightness is between 9.5 to 10.5 magnitude. Image stacks up to 300-500 images could theoretically detect a small satellite approximately $\sim 1/10$ the size of the client spacecraft. While the estimates were somewhat optimistic, stack sizes of this scale are practical for data acquisition and provide an indication of the number of frames needed to detect the objects.

A key contribution of this research was experimental observations using both small aperture (0.35m) and larger aperture (1.6m) instruments to validate this observational technique on both binary stars and co-located proxy geostationary satellites. As no OOS satellite missions are currently available for study, the observation of rare “optical conjunctions” of co-located geostationary satellites was performed to mimic the angular separation between OOS satellites. Three optical conjunctions with separations less than 5 arcseconds were observed providing real test data for image processing and relative orbit determination testing.

The cross-spectrum approach was found to produce differential angle measurements with precisions of ~ 0.2 arcseconds on satellites with brightness differences of $\Delta m = 0.33$ and $\Delta m = 1.5$. While very good relative orbit measurements were collected on satellites with apparent separations down to ~ 1.5 arcseconds, the technique was shown to have three key limitations for OOS monitoring; 1) the satellites must both be resident within the isoplanatic angle which should not exceed 5 arcseconds, 2) the local seeing should be less than 3 arcseconds (and steady), 3) the rotational rate of the fringes produced by the cross-spectrum approach should be monitored for high fringe rotation rates. High fringe rotation rates (> 0.5 deg/sec) were found to provoke unrealistic separation measurements

as the fringe minima falsely move inward due to the autocorrelation and stacking process during image processing.

Relative orbits estimated using cross-spectrum speckle data produced tracks comparable to operator provided reference ephemerides within 100 m. A key finding in these measurements is that the radial component of the orbit state did not converge within the 15 minutes tracking timeframes for all satellite tracking experiments. Recognizing that orbit estimates must be achievable within the timespan of less than one evening's observation, simulations were performed to examine the behavior of filter convergence. The results show that convergence is achieved on timespans of three hours or more where relative orbit estimates of ~50 meters or less are possible. Simulations also show that the time to converge a relative orbit fit is dependent on the measurement precision where higher precision data (~0.05 arcseconds) converges an orbit estimate within ~1.7 of hours of observations.

An examination of the observability for closely-spaced geostationary satellites problem reaffirmed that the motion of the secondary satellite about the client is observable overall. However, only partial observability of the radial component of the servicer's motion can be achieved. This is due to the viewing geometry from ground to geosynchronous orbit where the detector plane is largely aligned with the client satellite's in-track and cross-track directions. This alignment causes low sensitivity to the radial position changes of the servicer. This partial observability points to the cause of the lengthy period of time required to obtain convergence of a relative orbit. Despite this shortcoming, it is shown that the servicer's relative orbit is observable overall.

7.2 Significance of work and contributions

Research in closely-spaced objects in geostationary orbit is a new area for space surveillance. Prior work in closely-spaced objects generally considers separation distances between the objects to be greater than 1-10 km. This research is original in that the objective is to remotely determine the relative orbit of the servicing satellite with respect to its client using an optical-only technique, where telemetry from either of the satellites is not required to perform relative orbit estimation.

7.2.1 Contributions

The following contributions to the field of space surveillance of closely-spaced objects in geostationary orbit using speckle interferometry have been made:

1. The adaptation of the speckle interferometry to overcome atmospheric turbulence enabling precision measurements of client and servicer within the seeing disk (<2.5 arcseconds). The ambiguous location of the secondary object, commonly encountered with speckle techniques, was resolved by the use of the cross-spectrum enabling the direct determination of the secondary object's location relative to the primary.
2. The development of a novel optical observational technique and derivation of a coordinate transformation between the relative orbit of the servicer to the differential angles measurements generated by speckle interferometry.
3. The development of computationally efficient image processing software based on cross-spectrum speckle interferometry measurements to estimate the relative orbit of closely-spaced geostationary objects.
4. Observational testing of the technique on geostationary proxy objects collected in a manner similar to an OOS scenario was performed to validate the image processing software. This was achieved using medium aperture (Mont-Mégantic 1.6-m) and small aperture (DRDC Space Surveillance Observatory 0.35-m) telescope observations of co-located geostationary satellites temporarily mimicking the angular separations of OOS satellites. The observational technique was successful at detecting active GEO satellites with separations less than 1.5 arcseconds. This has not been performed previously.
5. An assessment of this speckle interferometry technique's differential angles measurement precision was performed by comparing speckle measurement data with satellite operator orbital ephemerides. A precision of 0.1 arcseconds or better was shown to be achievable indicating that very good accuracy is possible.
6. An observability assessment of the servicer's relative orbit was performed due to the use of optical cameras (chapter 6). Both the in-track and cross-track

components of the servicer's motion are directly observable. However, the radial component is shown to be only partially observable due to the near alignment of the camera boresight with the radial ordinate of the client coordinate frame.

7. The establishment of detection limitations where optical speckle interferometry can be applied to the OOS problem in GEO were explored. The isoplanatic limit of ~ 5 arcseconds was established where the client and servicer satellites must be performing relative motion within 1 km of one another when viewed from the ground. For OOS satellite separations larger than this, speckle interferometry would not likely be employed. In addition, the minimum elevation that GEO objects should not be considerably less than 30 degrees due to chromatic dispersion and extinction effects. These limitations for the OOS observation problem have not been previously highlighted.

This research has been presented or published in forums relating to Space Situational Awareness and Space Surveillance. These works take the form of conference proceedings [36], [115], two journal papers [112], [122] and three lectures [123],[124],[125].

7.3 Potential Applications

Aside from the direct utility of detecting a close-proximity satellite and measuring its relative orbit, there are potential mission applications for speckle interferometry measurement of OOS flight in GEO.

OOS missions occurring in geostationary orbit do not have direct visibility to the L1 radio ranging signal available from the GPS constellation³⁶. As such, a geostationary or servicing satellite must rely on the ground ranging systems used to reckon its position. Ranging systems are known to exhibit in-track biases which can be immediately detectable by a speckle differential approach as shown in section 5.6. Speckle

³⁶ While much work continues on the use of GPS signal side-lobes to measure satellite positions in GEO [126] is ongoing, most systems still rely on laser or radar ranging and optical cameras to infer the position of a servicing satellite with respect to its client.

interferometry measurements can help initialize a relative orbit of the servicer with respect to the client satellite during proximity operations. Servicing satellites rely on on-board cameras to perform shape estimation in order to infer range. This is problematic if the satellites are at long range from one another. Satellite speckle interferometry differential measurements offer a complementary tool for initializing a relative orbit estimate for proximity operations.

The DART-MUBLCOM collision [10] highlighted the reality that satellites performing close-proximity flight can unintentionally collide as navigation safety algorithms are not flawless. An unintentional collision in GEO between a servicer and its client, while likely to be of low relative velocity, could be highly damaging to fragile solar panels spreading thin glass debris on orbit. The envisioned practice of using passively safety ellipses [127] between client and servicer can reduce the risk of collision however continuous assessment of collision probability is required. Proximity flight conjunction analysis is inherently a non-linear problem and is best calculated using Monte Carlo approaches [128]. However, Monte Carlo approaches place a heavy computational burden on on-board flight computers. Simplified covariance propagation approaches to determine collision probability [129] are practical for implementation on small spacecraft which can lead to increased safety. Satellite speckle interferometry can provide independent and complementary relative orbit state information, in addition to the on-board estimate, to assist a servicing satellite safely perform its mission.

7.4 Recommendations for future research

This research is an initial examination of a non-adaptive optics means to infer the presence and measure the relative motion of an OOS satellite in very close proximity to a geostationary client satellite. This research's contributions include the development of a speckle observational approach for closely-spaced satellites, an image processing algorithm and experimental measurements used to validate the quality of the data collection process. During this research several avenues of exploration were encountered which would add significant value as follow-on research topics.

Experimental Observations on Actual OOS Missions in GEO Orbit: The first natural extension to this research is to perform actual experimental observations on satellites which are performing OOS in geostationary orbit. While this research was fortunate to observe occasional, short-lived, alignments of co-located geostationary satellites their relative motions are very high in comparison to a true OOS mission. Future OOS missions are currently under consideration for flight making future experimental testing a possibility. It is possible that the first commercial OOS missions may occur in the 2019 [134] timeframe.

Short Wave Infrared (SWIR) Detection Approaches: These experiments were performed using near-infrared waveband bands in order to limit the effects of chromatic dispersion. The use of longer observation wavelengths enlarges the isoplanatic angle which could permit observations with wider separation angles. If a telescope and detector combination is available to collect observations in the K or K -short filters additional freedom to acquire observations during daylight could be achieved. Such functionality, in addition to night-time tracking, could offer new capabilities for relative orbit estimation. It has been long known that the daytime sky experiences considerably degraded seeing due to daytime heating. Understanding whether or not short-wave infrared observations could be performed using satellite speckle interferometry would be an interesting addition to this work.

Examination of the use of photo-detected measurements: The objects studied in the Mont-Mégantic observations were relatively bright (large) in comparison to the smaller satellite platforms which are now becoming more commonly available. Fainter (smaller) objects in geostationary orbit may become a reality in the near future which would impose a much reduced photon signal detectable on the ground. An examination of the use of photon detecting technologies should be considered as this could extend the detection range of this speckle approach. Image processing approaches for photo-detected speckle images exists (e.g. [86],[130]) however application to relative flight of two closely-spaced satellites does not appear in the literature. An examination of the detectability and metric accuracy of the satellite measurements would be a useful

extension to this research. Many EMCCD cameras feature photon-counting modes of operation therefore no new equipment would be required.

List of Abbreviations

AC	Autocorrelation
AEOS	Advanced Electro-Optical System
AO	Adaptive Optics
AU	Astronomical Unit
BRDF	Bidirectional Reflectance Distribution Function
CCD	Charge Coupled Device
CMOS	Complementary Metal Oxide Semiconductor
COWPOKE	Cluster Orbits With Perturbations of Keplerian Elements
DARPA	Defence Advanced Research Projects Agency
DART	Demonstration of Autonomous Rendezvous
DVA	Directed Vector Autocorrelation
EMCCD	Electron Multiplying CCD
ETS	Experimental Test Satellite
FFT	Fast Fourier Transform
FITS	Flexible Image Transport System
GEO	Geostationary Equatorial Orbit
GEODDS	Ground-based Electro-Optical Deep Space Surveillance
GPS	Global Positioning System
ICRF	International Celestial Reference Frame
IOD	Initial Orbit Determination
JCF	Jordan Canonical Form
JSpOC	Joint Space Operations Center
L1	GPS Carrier Frequency
L3CCDs	Low Light Level CCD
LEO	Low Earth Orbit
LVLH	Local Vertical Local Horizontal
MATLAB	Matrix Laboratory
MFBD	Multi Frame Blind Deconvolution

MTF	Modulation Transfer Function
MUBLCOM	Multiple Paths Beyond Line of Sight Communications
NASDA	National Space Development Agency of Japan
OD	Orbit Determination
OOI	On Orbit Inspection
OOS	On Orbit Servicing
OOS	On Orbit Servicing
QE	Quantum Efficiency
RIC	Radial, In-Track, Cross-Track frame
RSSS	Russian Space Surveillance System
SNR	Signal to Noise Ratio
SOI	Space Object Identification
SRP	Solar Radiation Pressure
SSA	Space Situational Awareness
SSN	Space Surveillance Network
TDRSS	Tracking and Data Relay Satellite System
TLE	Two Line Elements (Orbital data)
TOD	True of Date (Coordinate Frame epoch)
UoM	University of Montreal

Appendices

Appendix A

A.1 Proximity Flight Missions

The following is a list of proposed and launched technology demonstrator or operational missions flown in both LEO and GEO orbits.

Table 9 Autonomous On-Orbit Servicing and Proximity Flight Missions

Mission Name	Owner	Status	Year	Mission Orbit	Mission Type	Ref.
ETS-VII	JPN	Launched	1997	LEO	Tech Demo	[2]
XSS-10	US	Launched	2003	LEO	Tech Demo	[8]
XSS-11	US	Launched	2005	LEO	Tech Demo	[9]
DART	US	Launched	2005	LEO	Tech Demo	[10]
Orbital Express	US	Launched	2007	LEO	Tech Demo	[11]
MITEX	US	Launched	2008	GEO	Tech Demo?	[136]
Shi-Jian-12	PRC	Launched	2010	LEO	Tech Demo	-
GSSAP-1	US	Launched	2014	GEO	SSA Ops	[140]
GSSAP-2	US	Launched	2014	GEO	SSA Ops	[140]
ANGELS	US	Launched	2014	GYO*	Tech Demo	[141]
Kosmos 2254	RUS	Launched	2014	LEO	Tech Demo?	-
ROGER	ESA	Proposed	2003	GEO	Debris remed.	[138]
ConeExpress	GER	Proposed	2006	GEO	OOS-refueling	[139]
Tankersat	EUR	Proposed	c.1982	GEO	OOS-refueling	[137]
Phoenix	US	Proposed	2019	GEO	OOS-refueling	[134]
Vivisat	US	Proposed	2010		OOS-sustainment	[142]
SIS	CAN	Proposed	2010	GEO	OOS-refueling	[143]

*GYO = graveyard orbit

Appendix B

B.1 Orbit Estimation

Orbit determination is one of the most mathematically analyzed problems since the Copernican model was realized. Notable mathematicians such as Newton, Kepler, Gauss, and Laplace all made significant contributions to the science of astrodynamics. Some of the techniques that they derived bear their names to this day.

The key problem of orbit estimation is that orbital motion is inherently non-linear. Orbit propagation models are imperfect; they cannot predict far into the future or accommodate unanticipated forces such as sudden changes in Earth's atmospheric density (increased drag), thrusting or physical changes that affect a satellite's orbital trajectory. Regular monitoring and tracking of Earth orbiting objects must be performed to ensure the accuracy of the orbital catalog.

Before describing orbit estimation approaches, a table of notation table is provided to summarize the notations used in following sections (see Table 10)

1.1.2 Linearizing Orbital Motion

The dynamics of most non-linear, continuous time systems can be approximately modelled by expressing a Taylor series expansion about a reference point, in this case, an initially "guessed" orbit. This model adheres to the expansion expressed in [95]:

$$\dot{\mathbf{X}}(t) = F(\mathbf{X}, t) = F(\mathbf{X}^*, t) + \left[\frac{\partial F(t)}{\partial \mathbf{X}(t)} \right]^* [\mathbf{X}(t) - \mathbf{X}^*(t)] + O_F[\mathbf{X}(t) - \mathbf{X}^*(t)] \quad (\text{B.1})$$

and the measurements \mathbf{Y} can be modelled as

$$\mathbf{Y}_i = G(\mathbf{X}, t) = G(\mathbf{X}^*, t) + \left[\frac{\partial G(t)}{\partial \mathbf{X}(t)} \right]^*_i [\mathbf{X}(t_i) - \mathbf{X}^*t_i]_i + O_G[\mathbf{X}(t_i) - \mathbf{X}^*t_i] + \epsilon_i \quad (\text{B.2})$$

where terms with * denote a reference state such that the system can be linearized.

Table 10 Table of Notation

Variable	Description
$\dot{\mathbf{X}}$	State dynamics (nonlinear)
$\mathbf{X}(t)$	State as a function of time
$F(\mathbf{X}, t)$	Nonlinear function of state and time
$F(\mathbf{X}^*, t)$	State dynamics about a reference trajectory
$\dot{\mathbf{x}}$	Linearized state dynamics
\mathbf{x}	Linearized state
$\hat{\mathbf{x}}$	Estimated (updated) linearized state
$\mathbf{Y}=\mathbf{G}(\mathbf{X},t)$	Non-linear measurement functions
\mathbf{y}	Linearized measurement functions
\mathbf{H}	Linearized measurement sensitivity matrix
$\tilde{\mathbf{H}}_i$	Measurement Jacobian (sensitivity matrix)
\mathbf{h}	Nonlinear state estimate about nominal reference
\mathbf{P}	Covariance matrix $E(\mathbf{x}^T \mathbf{x})$
$\bar{\mathbf{P}}_{k+1}$	Propagated covariance at time t_k
\mathbf{P}_k	Covariance at time t_k
$\Phi(t, t_0)$	State transition matrix propagated between t_0, t
\mathbf{Q}	Process noise matrix
\mathbf{K}_k	Kalman Gain Matrix
\mathbf{R}_k	Measurement noise matrix
$\mathbf{W} = \mathbf{R}_k^{-1}$	Measurement weight matrix
\mathbf{A}	Dynamics matrix
\mathbf{P}	Covariance Matrix (uncertainties)
Φ	State transition matrix
ϵ_i	Noise
O_F	Neglected order of Taylor expansion (dynamics)
O_G	Neglected order of Taylor expansion (measurement)

The linearized portion of the estimate is performed by rearranging the equations as

$$\dot{\mathbf{x}} = \mathbf{F}(\mathbf{X}, t) - \mathbf{F}(\mathbf{X}^*, t) \quad (\text{B.3})$$

$$\mathbf{y} = \mathbf{F}(\mathbf{X}, t) - \mathbf{F}(\mathbf{X}^*, t) \quad (\text{B.4})$$

The linearized, state-space relationship for the orbital dynamics and measurement model is expressed by taking the difference between the measured state and the nominal (reference) state measurements, such as $\mathbf{x}(t) = \mathbf{X}(t) - \mathbf{X}^*(t)$ and $\mathbf{y}(t) = \mathbf{Y}(t) - \mathbf{Y}^*(t)$.

After ignoring terms O_F and O_G , these equations can be cast as:

$$\dot{\mathbf{x}} = \mathbf{A}(\mathbf{t})\mathbf{x}(\mathbf{t}) \quad (\text{B.5})$$

$$\mathbf{y}_i = \tilde{\mathbf{H}}_i\mathbf{x}_i + \boldsymbol{\varepsilon} \quad (\text{B.6})$$

where

$$\mathbf{A}(\mathbf{t}) = \left[\frac{\partial F(t)}{\partial \mathbf{X}(t)} \right]^* \quad (\text{B.7})$$

and

$$\tilde{\mathbf{H}}_i = \left[\frac{\partial G(t)}{\partial \mathbf{X}(t)} \right]_i^* \quad (\text{B.8})$$

Using a reference trajectory, the matrices $\tilde{\mathbf{H}}_i$ and $\mathbf{A}(\mathbf{t})$ can be computed. If the reference trajectory is close to the true orbit, then $\mathbf{x}(t)$ and $\mathbf{y}(t)$ are linearized about the reference trajectory which is suitable for relative orbit estimation.

1.2 Batch Least Squares

The venerable Batch Least Squares (BLS) algorithm has been reliably used for orbit estimation for decades. It is well-described by Tapley [95] and Vallado [65]. BLS requires an initial orbit estimate such as an Initial Orbit Determination (IOD) state estimate or a previous orbital estimate. This guess is differentially corrected to produce the updated orbital state based on the new measurements.

BLS fits all new orbital data to generate a post-processed orbital estimate. As such, BLS is not well suited for real-time applications. While BLS is very tolerant of noisy measurement data and is dependable for initial states far from the measured state, it is known to produce covariance matrices (uncertainties) that are difficult to forecast forward in time [55].

To estimate an orbit, the nominal, (reference) orbit trajectory must be propagated and measurement differences taken from the nominal orbit. The predicted orbit must be formed to produce the measurement matrix \mathbf{y} :

$$\mathbf{y} = \mathbf{Y} - \mathbf{Y}_{nominal} \quad (\text{B. 9})$$

Then, the orbit must be propagated and finite differencing performed to populate the measurement sensitivity matrix, or

$$\mathbf{H} = \tilde{\mathbf{H}}\Phi(\mathbf{t}, \mathbf{t}_k) \quad (\text{B.10})$$

A differential state update estimate is formed by computing

$$\hat{\mathbf{x}} = (\mathbf{H}^T \mathbf{W} \mathbf{H})^{-1} (\mathbf{H}^T \mathbf{W} \mathbf{y}) \quad (\text{B.11})$$

where the matrices $\mathbf{H}^T \mathbf{W} \mathbf{H}$ and $\mathbf{H}^T \mathbf{W} \mathbf{y}$ are accumulated [65] with observations prior to performing the inverse and post-multiplication. In equation B.11, \mathbf{W} denotes the measurement weights or the degree to which the data is trusted. It is a diagonal matrix consisting of the inverse of the sensor noise variances.

The state deviation $\hat{\mathbf{x}}$ is iterated until the estimator converges (normally after five to six iterations). Once convergence has been achieved, the best estimated state $\hat{\mathbf{X}}_{new}$ is updated by

$$\hat{\mathbf{X}}_{new} = \hat{\mathbf{X}}_{nom} + \hat{\mathbf{x}} \quad (\text{B.12})$$

where $\hat{\mathbf{X}}_{nom}$ is the original reference trajectory used to begin the estimation.

1.3 Kalman Filter Implementation

Batch filtering is a technique that processes entire sets of observations and produces an orbital estimate after all information is processed. Kalman Filters are sequential estimators suited for real-time applications and was selected for the OOS relative orbit estimation in this research.

A Kalman Filter (KF) is an optimal sequential estimator which combines a-priori state and covariance estimates with new measurement information. Once new measurement data is received the KF updates both the state and covariance. In contrast to BLS, the KF

needs to be initialized with both a-priori state vector and covariance matrix in order to be used.

A general description of the Kalman filter typically consists of the initialization, prediction of both state and covariance, and update steps. The model of a Kalman filter assumes that the system process noise is zero-biased with Gaussian measurement noise $\mathbf{R}(t)$. A Kalman Filter is initialized with an a-priori state and covariance

$$\hat{\mathbf{x}}(t_0) = \hat{\mathbf{x}}_0 \quad (\text{B.13})$$

$$\mathbf{P}_0 = E\{\tilde{\mathbf{x}}(t_0)\tilde{\mathbf{x}}^T(t_0)\} \quad (\text{B.15})$$

The predicted state is based on the last information is

$$\bar{\mathbf{x}}_{k+1} = \Phi_{k+1,k}\hat{\mathbf{x}}_k \quad (\text{B.16})$$

and the predicted covariance is:

$$\bar{\mathbf{P}}_{k+1} = \Phi\mathbf{P}_k\Phi^T + \mathbf{Q} \quad (\text{B.17})$$

In equation B.17, \mathbf{Q} is the process noise estimate which itself is zero biased and exhibits Gaussian behavior in nature.

The Kalman gain \mathbf{K}_k adjusts the a-prior state estimate by matrix by scaling the difference between predicted and measured observations. Kalman Gain is expressed as:

$$\mathbf{K}_k = \bar{\mathbf{P}}_k\mathbf{H}_k^T[\mathbf{H}_k\bar{\mathbf{P}}_k\mathbf{H}_k^T + \mathbf{R}_k]^{-1} \quad (\text{B.18})$$

Using the Kalman gain, the state can be updated by multiplying by the difference between the observed and predicted measurements, such as

$$\hat{\mathbf{x}}_{k+1} = \bar{\mathbf{x}}_k + \mathbf{K}_k(\mathbf{y}_k - \mathbf{H}\bar{\mathbf{x}}_k) \quad (\text{B.19})$$

The covariance matrix is similarly updated as:

$$\bar{\mathbf{P}}_{k+1} = (\mathbf{I} - \mathbf{K}_k\mathbf{H})\bar{\mathbf{P}}_k \quad (\text{B.20})$$

The form of equation B.20 is susceptible to numerical issues due to rounding error. Joseph form [131] is better suited for numerical computation of the covariance and is expressed as

$$\bar{\mathbf{P}}_{k+1} = (\mathbf{I} - \mathbf{K}_k \mathbf{H}) \bar{\mathbf{P}}_k (\mathbf{I} - \mathbf{K}_k \mathbf{H})^T + \mathbf{K}_k \mathbf{R} \mathbf{K}_k^T \quad (\text{B.21})$$

1.4 Extended Kalman Filter Implementation

An Extended Kalman Filter (EKF) is considered to be the standard for use with most non-linear estimation problems. Its implementation is similar to the conventional Kalman filter with exception that the current estimate is used as the nominal estimate [131].

$$\bar{\mathbf{x}}(t) = \hat{\mathbf{x}}(t) \quad (\text{B.22})$$

This permits the EKF to be more tolerant of initial state estimates outside the linearity region of the Kalman filter algorithm. The measurement matrix \mathbf{H} is computed around the reference trajectory in order to linearize the measurements in order to update the state. The dynamics matrix is likewise accordingly computed about the reference trajectory using finite differencing approaches to estimate the matrix.

Appendix C

C.1 EMCCD Camera Parameters

Table 11 Andor iXon 888i Specifications

Parameter	Value	units	Notes
Detector	CCD201		E2V
Digitization	16	bit	
EM gain range	1-1000	-	
Pixel pitch	13	μm	
Array dimensions	1024x 1024 (13.3x 13.3)	pixels (mm)	
Dark current	0.005	$\text{e}^- \text{pix}^{-1} \text{sec}^{-1}$	@-85°C
Well depth	80,000	e^-	
Full frame rate	26	fps	1024x1024 array
Pixel read rate (standard)	10	MHz	
Pixel read rate (EMCCD)	30	MHz	
Read noise (10MHz)	40	e^-	No EM gain
Read noise (30MHz)	130	e^-	
Read noise w/ EM gain	< 1	e^-	All read rates
Peak QE	96	%	@550 nm
PC interface	USB 3.0		

Taken from NuVu Andor iXon 888 product specification sheet [132]

Table 12 NuVu HNu LN EMCCD iXon 888i Specifications

Parameter	Value	units	Notes
Detector	-		E2V
Digitization	16	bit	
EM gain range	1-5000	-	
Pixel pitch	13	μm	
Array dimensions	1024x 1024 (13.3x 13.3)	pixels (mm)	
Dark current	0.0004	$\text{e}^- \text{pix}^{-1} \text{sec}^{-1}$	@-85°C
EM register well depth	800,000	e^-	
Full frame rate	16.7	fps	1024x1024 array
Pixel read rate (standard)	100	kHz	
Pixel read rate (EMCCD)	20	MHz	
Read noise (CCD mode)	3	e^-	@100 kHz
Read noise w/ EM gain	< 0.1	e^-	20 MHz
Peak QE	96	%	@550 nm
PC interface	Gig-E cameralink		
Liquid nitrogen reservoir	1	L	capacity

Taken from NuVu HNu LN2 product specification sheet [133]

Appendix D

D.1 Computing the cross-spectrum

An excerpt of code required to compute the cross-spectrum for a set of imagery is detailed. The following is the main processing loop for computing the cross spectrum on a stack of images. ROI (Region of interest) denotes an image matrix loaded into the Matlab workspace.

```
%Compute the cross-spectrum
Itilde      = ROI - mean2(ROI);           %Zero mean specklegrams
CS          = fft2(Itilde.*Itilde).*conj(fft2(Itilde)); %cross-spectr.
ImageSum.CS = ImageSum.CS + CS;

for i=1:LOOPS %main control loop processing for each stacked image

    DecrementAvg = 0; %reset to zero

    %Load timestamps and header information...
    %Create Frame Stacks

    Stack.CC.image = ImageSum.CC / (IMAGES_TO_AVERAGE - DecrementAvg) ;
    Stack.CS.image = fftshift(ImageSum.CS.*conj(ImageSum.CS)) /
(IMAGES_TO_AVERAGE - DecrementAvg);
    Stack.CS.cmplx = ImageSum.CS / (IMAGES_TO_AVERAGE - DecrementAvg);

    %If Statistics toolbox not available, use below
    FRAME.JDofMeasurement(FRAME.JDofMeasurement==0) = []; %kill zeros
    Stack.Frame.JDTime = mean(FRAME.JDofMeasurement);

    JBase = floor(JDate) + 0.5;
    Stack.ObsTimeMinsSinceMidnight = 60*EST_2.UTC_Offset_hrs +
1440*(Stack.Frame.JDTime - JBase);

    %%%%%%%%%%%%%%%%%%%%%%%%%%%%%%%%% ANALYSE THE STACK %%%%%%%%%%%%%%%%%%%%%%%%%%%%%%%%%

    %Solar Geocentric RA and DEC
    [solar_RA, solar_dec, solar_r] = sun_low_precision( Stack.Frame.JDTime)
;

    CSData = fftshift(Stack.CS.cmplx);

    %Form real and imaginary data components
    CSDataReal = real(CSData);
    CSDataImag = imag(CSData);
```

```

%Size of image characteristics
[Ni Mi] = size(CSDataImag);

%Basic image statistics
meanlevel = mean2(CSDataImag);
sigmalevel = mean2(CSDataImag);

ImagCenter = IsolateCenterRegion(CSDataImag,IsolateFringeWindow);
ImagGLPFx = GaussianLowPassFilter( ImagCenter, 1);
ImagACGLPF = xcorr2(ImagGLPFx);

IMAGINARY_BOXED = IsolateCenterRegion( ImagACGLPF,
IsolateFringeWindow);

%Create circular mask to equalize the Radon transform over all angle
search
[IMAGINARY_BOXED2] =
CircularMask(IMAGINARY_BOXED,NormalizedImagACFringeRadius);

IMAGINARY_BOXED2 = xcorr2(IMAGINARY_BOXED2);
IMAGINARY_BOXED2(IMAGINARY_BOXED2 < 0) = 0;           %threshold cut
IMAGINARY_BOXED3 = im2bw(IMAGINARY_BOXED2, 0.1);    %binary image

%constrain the Sobel range to a small radius
[IMAGINARY_BOXED4] =
CircularMask(IMAGINARY_BOXED3,fix(NormalizedImagACFringeRadius));

%Sobel filter
BW1 = edge(IMAGINARY_BOXED4,'sobel');

ImaginaryRadon = radon_analysis(BW1,thetaResolution/10);    %finds the
fringe orientation angle based on Sobel

%Now retrieve the profile from the autocorrelated imaginary data
fringes
Stack.CS.R.profile.Perp =
GetFringePerProfile(ImaginaryRadon.PerpAngle,ImagGLPFx);

%Estimate the width of Fourier transformed Gaussian PSF
profileinfo = abs(Stack.CS.R.profile.Perp.c);
[ SeeingFWHM_arcsec sigmaFourierProfile] = EstimateSeeing( 1.5,
ARCSECPERPIXEL, profileinfo, sizelimitN);

.....

end %i

```

D.2 Directed Vector Autocorrelation

```
function [RESULT] = DVA(I)
%Input - Image I
%Output - V, the directed vector autocorrelation

tstartTicID = tic; %performance check
[N,M] = size(I);

V = zeros(2*N-1,2*M-1); %output vector us 2N-1

    for i = 1 : (2*N-1)
        si = i-N; %shift condition on array

        for j = 1 : (2*M-1)
            sj = j-M; %shift condition on array

            for s = 1:N
                for t = 1:M
                    if (s+si < 1) || (s+si > N) || ...
                        (s < 1) || (s > N) || ...
                        (t+sj < 1) || (t+sj > M) || ...
                        (t < 1) || (t > M) %out of range conditions
                        for I(k+si,t+sj)I(k,t)
                            prod = 0;
                        else
                            %DVA code modification
                            if I(s+si,t+sj) > I(s,t) %check on direction
                                prod = 0;
                            else
                                prod = I(s+si,t+sj)*I(s,t);
                            end %DVA adjustment
                        end %if
                        V(i,j) = V(i,j) + prod;
                    end % for t
                end % for k

            end %for j
        end %for i

telapsed = toc(tstartTicID);
message = sprintf('TOTAL ELAPSED PROCESSING TIME: %g (sec) %g (min)',telapsed, telapsed/60);
disp(message);

RESULT = V;

end %function
```

References

- [1] Perek, L., "Actual Situation in the Geostationary Orbit", www.unoosa.org/pdf/pres/stsc2012/tech-48E.pdf. Accessed 11 Mar 2015.
- [2] Ellery, A., "An Introduction to Space Robotics", Springer-Praxis (2000).
- [3] National Aeronautics and Space Administration Space Shuttle Mission STS-41C Press Kit, NASA release No 84-38, March 1984, http://www.jsc.nasa.gov/history/shuttle_pk/pk/Flight_011_STS-41C_Press_Kit.pdf, accessed 28 Aug 2014.
- [4] National Aeronautics and Space Administration Space Shuttle Mission STS-41B Press Kit, NASA release No 84-4, January 1984, http://www.jsc.nasa.gov/history/shuttle_pk/pk/Flight_010_STS-41B_Press_Kit.pdf, accessed 10 Jan 2016.
- [5] Robotic Refueling Mission, NASA facts, Satellite Servicing Capabilities office, http://ssco.gsfc.nasa.gov/images/RRM_2013_Factsheet_07.pdf, accessed July 2014.
- [6] Engineering Test Satellite VII (ETS-VII), http://robotics.jaxa.jp/project/ets7-HP/ets7_e/rvd/rvd_index_e.html#FP-1, accessed June 2009.
- [7] Bonin, G., Roth, N., Armitage, S., Newman, J., Risi, B., Zee, R.E., CanX-4 and CanX-5 Precision Formation Flight: Mission Accomplished!, 29th AIAA/USU Conference on Small Satellites, SSC15-I-4 (2015).
- [8] Madison R., Micro-Satellite Based, On-orbit Servicing Work at the Air Force Research Laboratory, IEEE Aerospace Conference Proceedings, (2000), pp215-226.
- [9] XSS-11 Factsheet, accessible from <http://www.kirtland.af.mil/shared/media/document/AFD-070404-108.pdf>
- [10] NASA, "Summary of DART Accident Report", http://www.nasa.gov/pdf/148072main_DART_mishap_overview.pdf, accessed 3 Jan 2010.

- [11] Mulder, T., "Orbital Express Autonomous Rendezvous and Capture Flight Operations, part 1 of 2: Mission Description, AR&C Exercises 1,2,3," AAS Spaceflight Mechanics Meeting (2008), Galveston TX, 2008.
- [12] Soop, E., "Handbook of Geostationary Orbits", European Space Operations Center, Microcosm Inc., 1994.
- [13] "Inter-Agency Debris Mitigation Guidelines", IADC-02-01 Revision 1, September 2007
- [14] Vallado, D., Griesback, J.D., "Simulating Space Surveillance Networks", American Astronautical Society AAS 11-580
- [15] "20th Space Control Squadron",
<http://www.peterson.af.mil/library/factsheets/factsheet.asp?id=4730>, accessed 13 July 2015.
- [16] "MIT Haystack Observatory", <http://www.haystack.mit.edu/obs/mhr/index.html>, accessed 13 July 2015.
- [17] Ground Based Electro-Optical Deep Space Surveillance, Air Force Space Command Fact Sheet:
<http://www.afspc.af.mil/library/factsheets/factsheet.asp?id=3653>. Accessed 15 Jul 2015.
- [18] Scott, R. and Wallace, B., "Small-aperture optical photometry of Canadian geostationary satellites". Canadian Aeronautics and Space Journal, August 2009, Vol 55, pp. 55-67.
- [19] Hujsak, R., "A Review of Data Correlation Methods for Space Surveillance"
Available via Texas A&M,
aero.tamu.edu/sites/default/files/faculty/.../R7%20S5.3%20Hujsak.pdf. Accessed 3 Aug 2015.
- [20] Hoots, F.R., Roehrich, R.L., "Space-track Report #3, Models for Propagation of NORAD Element Sets", accessed via
<https://celestrak.com/NORAD/documentation/spacetrk.pdf>, accessed 15 July 2015.

- [21] Payne, T., “SSA Analysis of GEOS Photometric Signature Classifications and Solar Panel Offsets”, Proceedings of the AMOS Technical Conference, Maui HI., 2007.
- [22] Payne, T.E.,”GEO Cross Tag Resolution Using Color Signatures”, Texas A&M
- [23] Bedard, D., “Spectrometric Characterization of Geostationary Satellites”, AMOS Technical Conference 2012, Maui HI.
- [24] Jorgensen, K., et al, ”Reflectance Spectra of Human-made space objects”, AMOS Technical Conference 2004, Maui HI.
- [25] Hall, D., “Surface Material Characterization from Multi-band Optical Observations”, AMOS Technical Conference, Maui HI (2015).
- [26] Bedard, D., “Time Resolved Spectrometric measurements of the Galaxy 11 spacecraft”, *Advances in Space Research 2015, Under review* , (2015)
- [27] Skinner, M.A., et al.,” Time-resolved infrared spectrophotometric observations of high area to mass ratio (HAMR) objects in GEO” *Acta Astronautica*, Vol 69, Dec 2011, pp1007-1018.
- [28] Levan, P., “Discrimination of Closely-Spaced Geosynchronous Satellites –Phase Curve Analysis & New Small Business Innovative Research (SBIR) Efforts, AMOS Technical Conference 2010 Maui, HI.
- [29] Ostro, Steven., “Convex Profile Inversion of Asteroid Light curves: Theory and Applications”, *Icarus* 75-30-63, (1988).
- [30] Hall, D., Africano, J., Kervin, P., Birge, B., “Non-Imaging Attitude and Shape Determination”, SPIE (2005).
- [31] Kaasalainen, M. and Torppa, J., “Optimization Methods for Asteroid Light curve Inversion: I. Shape Determination.” *Icarus*, Vol. 153, No. 1, pp. 24–36, September 2001)
- [32] Lambert, J., "Direct Inversion of Visible and Infrared Signatures", AMOS Technical Conference 2002, Maui HI.
- [33] Bradley,B.K..and Axelrad, P.,”Light curve Inversion for Shape Estimation of GEO objects from Space Based Sensors”, *International Symposium on Space Flight Dynamics 2014*, Paper S10-3, (2014).

- [34] Calef, B., Africano, J., Birge, B., Hall, D., Kervin, P., "Photometric Signature Inversion", Proceedings of SPIE Vol 6307, 2006.
- [35] Ackermann, M., "Blind Search for Microsatellites in LEO: Optical Signatures and Search Strategies", AMOS Technical Conference 2005, Maui, HI.
- [36] Scott, R.L. "Non-resolved detection of objects performing On Orbit Servicing in Geostationary orbit", AMOS Technical Conference 2011, Maui, HI.
- [37] Hall, D., "Analysis of Faint Glints from Stabilized GEO satellites", AMOS Technical Conference, Non-Resolved Optical Characterization session, Maui, HI, (2013).
- [38] Labeyrie, A., "Attainment of Diffraction Limited Resolution in Large Telescopes by Fourier Analyzing Speckle Patterns in Star Images", Astronomy and Astrophysics, vol. 6, pp. 85-87, 1970.
- [39] Labeyrie, A., Lipson, S.G., Nisenson, P., "An Introduction to Optical Stellar Interferometry", Cambridge University Press, New York, (2006).
- [40] Washington Double Star Catalog, United States Naval Observatory, accessible via <http://ad.usno.navy.mil/wds/>.
- [41] Phelan, D., Ryan, O., Shearer, A., "High Time Resolution Astrophysics", Astrophysics and Space Library 351, Springer (2008).
- [42] Daigle, O., et al., "Extreme faint flux imaging with an EMCCD", Publications of the Astronomical Society of the Pacific, Vol 121, No 882, Aug (2009).
- [43] Docobo, J.A., Tamazian, V.S., Balega, Yuri, Y., Melikian, N.D., "EMCCD Speckle Interferometry with the 6 m Telescope: Astrometric Measurements, Differential Photometry, and Orbits", Astronomical J., Vol 140, Issue 4, pp 1078-1083 (2010).
- [44] Tokovinin, A., Cantararutti, R., "First speckle-interferometry at SOAR telescope with electron multiplication CCD", Astronomical Society of the Pacific, Vol 120, issue 864, pp 170-177 (2008)
- [45] Genet, R.M., "Portable Speckle Interferometry Camera System", Journal of Astronomical Instrumentation, Vol 2., No.2, (2013).
- [46] Law, N., "Lucky Imaging, Diffraction Limited Astronomy from the Ground in the Visible", PhD Thesis, Cambridge University (2006).

- [47] Gili, R., Prieur, J.-L., Rivet, J.-P., Vakili, F., Koechlin, L., Bonneau, D., “PISCO2: the new speckle camera for the Nice 76-cm refractor”, *The Observatory*, Vol.134, p267-273 (2014).
- [48] Teiche, A.S., Genet, R.M., “Automated Speckle Interferometry of Double Stars” *Journal of Double Star Observers*, Vol 10, No.4, October (2014).
- [49] York, D.G, Gingerich, O., Zhang,S-N, ”The Astronomy Revolution: 400 Years of Exploring the Cosmos”, CRC Press, 1st Edition, 2011.
- [50] Worden, S.P., et al, ”Observing Deep Space Microsatellites with the MMT and Large Binocular Telescope”, AMOS Technical Conference 2005, Maui HI.
- [51] Hope, D., Jefferies, S.M., Giebinck, C., ”Imaging Geo-synchronous satellites with the AEOS Telescope”, AMOS Technical Conference 2008, Maui, HI.
- [52] Drummond, J.D., Rast, R.H.,” First Resolved Images of a Spacecraft in Geostationary Orbit with the Keck-II 10 m Telescope”, AMOS Technical Conference 2010, Maui, HI.
- [53] DARPA-SN-15-38, Broad Area Announcement, “Technology solutions for passive sparse aperture imaging for space domain awareness”, https://www.fbo.gov/index?s=opportunity&mode=form&id=03a4ea98cb49cb67bf648396d80047d5&tab=core&_cview=0, accessed 13 Jul 2015.
- [54] Woffinden, D.C., Geller., D.K., “Observability Criteria for Angles-Only Navigation” *IEEE Transactions in Aerospace and Electronic Systems*, Vol. 45, No. 3. July (2009)
- [55] Tombasco, J., “Orbit Estimation of Geosynchronous Objects Via Ground Based and Space-Based Optical Tracking”, University of Colorado Department of Aerospace Engineering Sciences (2011).
- [56] Clohessy, W.H., Wiltshire, R.S., “Terminal Guidance system for satellite rendezvous” *Journal of Aerospace Sciences*, 27, no.9, 653-658,674.,1960.
- [57] Shishido, B., Brem, R., Konohia, P., Sabol, C., Luu, K., “Accuracy Assessment of the MSSS Metric Observation Data”, *Advances in the Astronautical Sciences*, Vol 119, Part III, 2004.
- [58] Observatoire Mont-Mégantic website, <http://omm.craq-astro.ca/>. Accessed 26 Jul (2015).

- [59] Orbital Express Fact Sheet,
http://archive.darpa.mil/orbitalexpress/pdf/oe_fact_sheet_final.pdf. Accessed 15 Jul 2015.
- [60] Worden, S., "Speckle Interferometry I: A Test on an Earth Orbital Satellite", AFGL-TR-82-0340, Defence Technical Information Center AD A121942. November 1982.
- [61] Beavers, W.I., Dudgeon, D.E., Beletic, J.W and Lane, M.T., "Speckle Imaging through the Atmosphere", The Lincoln Laboratory Journal, Vol 2, November 2, 1989.
- [62] Lawrence, T.W., Goodman, D.M., Johansson, E.M., and Fitch, J.P., "Speckle imaging of satellites at the U.S. Air Force Maui Optical Station", Applied Optics, Vol 31, No 29, pp 6307-6321.
- [63] Knox, K., "Image Analysis of the 2012 Pluto (Near) Occultation", AMOS Technical Conference, Maui, HI, (2013).
- [64] Advanced Electro-Optical System (AEOS), United States Air Force Fact Sheet, <http://www.kirtland.af.mil/shared/media/document/AFD-070404-028.pdf>, accessed 10 Aug 2015.
- [65] Vallado, D.A., Fundamentals of Astrodynamics and Applications, 4th ed, Microcosm Press, Hawthorne, CA, p. 389,207,396, (2013).
- [66] Montenbruck, O., Gill, E., "Satellite Orbits, Models, Methods, Applications", Springer (2001).
- [67] Kawase, S., "Real Time Relative Motion Monitoring For Co-located Geostationary satellites", Journal of the Communications Research Laboratory, Tokyo, Japan Vol. 36, No 148, (1989).
- [68] Kawase, S., "Differential Angle Tracking for Close Geostationary Satellites", Journal of Guidance, Control and Dynamics, Vol.16, No.6, Nov,-Dec. (1993).
- [69] Sawada, F., Kawase, S., "Relative Orbit Determination Experiment by Ground-Based Differential Angle Tracking", Electronics and Communications in Japan, Vol.79, No.1, 1996.
- [70] Sabol, C., McLaughlin, C., Luu, K., "The Cluster Orbits With Perturbations of Keplerian Elements (COWPOKE) Equations", AFRL-DS-PS-TR-1025, (2004)).

- [71] Sabol, C., Hill, K., McLaughlin, C., Luu, K.K., Murai, M., "Relative Orbit Determination Of Geosynchronous Satellites Using the COWPOKE Equations", Defence Technical Information Center, AFRL-SR-AR-TR-04, DTIC: 200406625 134, 1 September (2002).
- [72] Coulman, C.E., "Fundamental and Applied Aspects of Astronomical "Seeing" Annual Review Astronomy and Astrophysics, 1985, 23: 19-57 (1985).
- [73] Allen's Astrophysical Quantities, Springer-Verlag, New York, 2002. ISBN: 10.1007/978-1-4612-1186-0.
- [74] Owens, J.C., "Optical Refractive Index of Air: Dependence on Pressure, Temperature and Composition", J. Applied Optics., Vol. 6, No.1., January (1967).
- [75] Kolmogorov, A.N., In Turbulence pp 151-55. Translated SK Friedlander, L. Topper, Interscience. (1961).
- [76] Kovalevsky, J., "Modern Astrometry 2nd Edition", Springer, (2002).
- [77] Fried, D.L., "Optical Resolution through a Randomly Inhomogeneous Medium for Very Long and Very Short Exposures", Journal of the Optical Society of America, Vol. 56, No. 10. October 1966.
- [78] Masciadri, E., Stoesz, J., Hagelin, S., Lascaux, F., "Mt. Graham: Optical turbulence vertical distribution at standard and high vertical resolution", Proc SPIE, Vol 7733 1P-77331 P-12, (2010).
- [79] Roddier, F., Gilli, J.M., Vernin, J., "On the Isoplanatic Patch Size In Stellar Speckle Interferometry", J.Optics Vol 13, No.2, pp63-70, (1982)
- [80] Korff, D., "Analysis of a Method for obtaining near-diffraction limited information in the presence of atmospheric turbulence", Journal of the optical Society of America, 63,971-980 (1973)
- [81] Gili, R., Priour, J-L., "Relative Astrometric and Photometric Measurements of Visual Binaries made using the Nice 76-cm refractor in 2008", Astronomische Nachrichten, 2012, 333 (8) pp727.
- [82] Argyle, R.W., "Observing and Measuring Visual Binary Stars", Springer, Patrick Moore Astronomy Press.,(2012).

- [83] Bagnuolo, W.G, Mason, B., Barry, D.J., “Absolute Quadrant Determinations From Speckle Observations of Binary Stars”, *Astronomical J* vol., 103, No 4, April 1992.
- [84] Genet, R. M., et al, “Kitt Peak Speckle Interferometry of Close Visual Binary Stars”, *Proc. 33rd Annual Symposium On Telescope Science*, Editors. Brian D. Warner, Buchheim, R.K., Foot, J.L., Dale Mais., pp. 77-91, (2014).
- [85] Caloi, R.M., ”Estimation of Double Star Parameters by Speckle Observations Using a Webcam”, *Journal of Double Star Observations* Vol. 4, No.3, pp 111-118. Summer 2008.
- [86] Aristidi, E., Carbillet, M., Lyon, J-F, and Aime, C.," Imaging binary stars by the cross-correlation technique", *Astronomy and Astrophysics Supplement series*, vol. 125 (1997) 139-148.
- [87] Knox, K., “Measuring Close Binary Stars with Speckle Interferometry”, *Proceedings of the AMOS Technical Conference*, Maui HI., 2014.
- [88] Moffat, A.F.J., "A Theoretical Investigation of Focal Stellar Images in the Photographic Emulsion and Application to Photographic Photometry", *Astronomy and Astrophysics*, Vol. 3, p. 455, 1969.
- [89] Mason, B., "Atmospheric Dispersion and Risley Prisms", *United States Naval Observatory, Double Star Report*, No.3, 27 Jan 2003.
- [90] Sydney, P., Africano, J., Kelecy, T., ”High Precision Satellite Astrometry and Photometry”, *AMOS Technical Conference 2004*, Maui, HI.
- [91] Hejduk, M., “Satellite Detectability Modelling for Optical Sensors”, *AMOS Technical Conference 2004*, Maui HI.
- [92] Stokes, G.H., von Braun, C., Ramaswamy, S., Harrison, D., Sharma, J., “The Space Based Visible Program”, *Lincoln Lab Journal*, Vol.11, No. 2, (1998).
- [93] *Space Based Space Surveillance Mission Book*, Boeing Corporation, 2010, accessible: <http://www.boeing.com/assets/pdf/defense-space/space/satellite/MissionBook.pdf>. Accessed: 9 Aug 2015.
- [94] Maskell, P., Oram, L., ”Sapphire: Canada’s Answer to Space-Based Surveillance of Orbital Objects”, *AMOS Technical Conference*, Maui, HI, (2008).

- [95] Tapley, B.D., Schutz, B.E., Born, G.H., "Statistical Orbit Determination" Elsevier Academic Press, New York, (2004).
- [96] Hill, G., "Researches in Lunar Theory", American Journal of Mathematics, 1, 5-26, 1878.
- [97] Vallado, D.A., Alfano, S., Curvilinear Coordinates for Covariance and Relative Motion Operations, AAS 11-464, Astrodynamics Specialist Conference, Jul. 2011, Girdwood, AK.
- [98] Meeus, J., "Astronomical Algorithms, Second Edition", Willman Bell, Richmond, VA, (1998).
- [99] Spacetrack-org. Joint Space Operations center, <https://www.space-track.org>. Accessed 26 Jul (2015).
- [100] Howell, S., "Handbook of CCD Astronomy", COHRA, Cambridge University Press, (2000).
- [101] Shell, J.R., "Optimizing orbital debris monitoring with optical telescope", AMOS Technical Conference, Maui, HI, (2010).
- [102] Miller, M.G., "Noise Considerations in Stellar Speckle Interferometry", J.Opt.Soc.Am. Vol.67, No.9, September (1977).
- [103] Dainty, J.C., "Computer Simulations of Speckle Interferometry of binary stars in the photon counting mode", Monthly Notices of the Royal Astronomical Society, vol. 183, p. 223-236, Apr. (1978).
- [104] D'Donnell, K.A., Dainty, J.C., "Space-time analysis of photon limited stellar speckle interferometry", J.Opt.Soc.Am., Vol 70, No.11, November (1980).
- [105] Welsh, B.M., "Speckle imaging signal-to-noise ratio performance as a function of frame integration time", J.Optical Society of America, Vol.12, No.6, June (1995).
- [106] Hoffman, M., "A search for binary stars using speckle interferometry", Thesis (2000), Rochester Institute of Technology, Accessed from: <http://scholarworks.rit.edu/theses/6785/>.
- [107] Parry, G., "On the statistics of stellar speckle patterns and pupil plane scintillation", Optica Acta, Vol. 26, No. 5 pp 563-574 (1979)

- [108] Andor iXon Ultra 888 EMCCD, Andor (Oxford Instruments) Datasheet available from <http://www.andor.com/scientific-cameras/ixon-emccd-camera-series/ixon-ultra-888>
- [109] Wallace, B., Scott, R.L., “The DRDC Ottawa Space Surveillance Observatory”, AMOS Technical Conference 2007, Maui, HI, (2007).
- [110] Schneiderman, A.M.,Karo, D.P.,”How to build a speckle interferometer”, J. Optical Engineering, Vol. 16, No. 1, Jan-Feb (1977).
- [111] Flexible Image Transport System (FITS) Standard, NASA Goddard Space Flight Center, http://fits.gsfc.nasa.gov/fits_standard.html, Accessed 6 Aug 2015.
- [112] Scott, R.L., Ellery, E.,” An approach to ground based space surveillance of geostationary on-orbit servicing operations”, Acta Astronautica, Vol 112, Jul-Aug 2015., pp 56-68.
- [113] Artigau, E., Lamontange, R., Doyon, R., Malo, L., Queue observing at the Observatoire du Mont-Megantic 1.6-m telescope, Proc SPIE 7737 (2010).
- [114] Michel, R., Echevarria, J., Costero, R., Harris, O., The Seeing at San Pedro Mártir Observatory as Measured by the DIMM Method, RevMexAA 19, 37-40 (2003).
- [115] Scott, R.L., Ellery, E.,” An approach to ground based space surveillance of geostationary on-orbit servicing operations”, International Astronautical Congress Toronto, Sept (2014).
- [116] Oltrogge, D., Alfano, S., "COMSPOC Update and Operational Benefits" 31st Space Symposium, Colorado, CO., 2015.
- [117] De Ruitter, A., “Improving transient performance in computationally simple gyro corrected satellite attitude determination”, Proceedings of IMechE, Vol. 226 Part G: Journal of Aerospace Engineering (2011).
- [118] Ulrich, S., “Direct Adaptive Control Methodologies for Flexible Joint Space Manipulators with Uncertainties and Modelling Errors”, PhD Thesis, Carleton University, 2012.
- [119] Ogata, K., “Modern Control Engineering Fourth Edition”, Prentice Hall, New Jersey, (2002).
- [120] Kreyszig, E., “Advanced Engineering Mathematics, Seventh Edition”, John Wiley and Sons, New York, (1993).

- [121] Levesque, J.F., De Lafontaine, J., "Innovative Navigation Schemes for State and Parameter Estimation During Mars Entry", *Journal of Guidance, Control, and Dynamics*, Vol. 30, No. 1 (2007), pp. 169-184.
- [122] Scott, R.L., Ellery, E., "Speckle Interferometry Tracking of On-Orbit Servicing in Geostationary Orbit", Submitted to the *Journal of Spacecraft and Rockets* (Under Review by the AIAA, 2015).
- [123] Scott, R.L., "How the Canadian Forces can fight, and win, against twinkling stars; On-Orbit Servicing detection in geostationary orbit", Defence R&D Canada Ottawa lecture series, presented January (2015).
- [124] Scott, R.L., "Twinkle, Twinkle Little Space Robot", Carleton University graduate lecture series, presented 18 Sept (2015).
- [125] Scott, R.L., "Twinkle, Twinkle Little Space Robot", Royal Military College of Canada Physics Colloquium, presented 8 Oct (2015).
- [126] GPS at Geosynchronous Orbits, NASA Policy and Strategic Communications office, accessible at http://www.navcen.uscg.gov/pdf/gps/news/apr2010/navigator_space_receiver_info_04212010_rev4.pdf. Accessed 9 Aug 2015.
- [127] Barbee, Brent Wm, et al. "Guidance and Navigation for Rendezvous and Proximity Operations with a Non-Cooperative Spacecraft at Geosynchronous Orbit." George H. Born Symposium. (2010).
- [128] Chan, F., "Spacecraft Collision Probability", Aerospace Corporation, (2008).
- [129] Phillips, M.R., Geller, D.K., Chavez, F., "Collision Probability Estimation" 23rd AIAA/USU Conference on Small Satellites, Logan, UT,
- [130] Thiébaud, E., "Speckle Interferometry with a photon-counting detector", *Astronomy and Astrophysics*, Vol 284, pp340-348 (1994).
- [131] Crassidis, J.L., and Junkins, J.L., *Optimal Estimation of Dynamic Systems*, CRC Press, New York, 2004.
- [132] Andor iXon ultra 888 Product specification sheet. Accessible at: http://www.andor.com/pdfs/specifications/iXon_Ultra_888_EMCCD_Specifications.pdf, Accessed 13 Aug 2015.

- [133] NuVu HNu LN2 EMCCD product specification sheet: Accessible at:
<http://www.nuvucameras.com/products/>, Accessed 13 Aug 2015.
- [134] DARPA Phoenix Mission Overview: Accessible from:
<http://www.darpa.mil/program/phoenix>.
- [135] XSS-11 Microsatellite, Kirtland Air Force Based,
<http://www.kirtland.af.mil/shared/media/document/AFD-070404-107.pdf>.
Accessed 14 Aug 2015.
- [136] Caron, Ryan. "Mysterious microsatellites in GEO: is MiTEx a possible anti-satellite capability demonstration?".
<http://www.thespacereview.com/article/670/1> accessed Mar 2009
- [137] Vandekerckhove, Jean., "Tankersat - Refueling satellites in Geosynchronous Orbit", AIAA Aeronautics and Astronautics 1982.
- [138] ESA ROGER Debris remediation phase A,
<https://gsp.esa.int/documents/10192/43064675/C15706ExS.pdf/18bb5154-fa12-44f0-a240-d84672ac49d5>.
- [139] ConeXPress Orbital Life Extension Vehicle, "
http://www.esa.int/esapub/bulletin/bulletin127/bul127h_caswell.pdf" accessed
Sept 2009.
- [140] Geosynchronous Space Situational Awareness Program (GSSAP):
<http://www.afspc.af.mil/library/factsheets/factsheet.asp?id=21389>
- [141] ANGELS Fact sheet: <http://www.kirtland.af.mil/shared/media/document/AFD-131204-039.pdf>. Accessed 14 Aug 2015.
- [142] VIVISat: <http://www.vivisat.com/>. Accessed 14 Aug 2015.
- [143] Canada's Space Infrastructure Services.,
<http://www.mdacorporation.com/corporate/news/pr/pr2011031501.cfm>. Accessed
14 Aug 2015.

Biographical Sketch

ROBERT (LAUCHIE) SCOTT received his B.Eng. degree in mechanical engineering from the Technical University of Nova Scotia (Halifax, Nova Scotia) where he graduated as a Sexton Scholar in 1999. In 1999 he received a full graduate student assistance-ship to the Florida Institute of Technology (Melbourne, Florida) where he examined the interaction of Ultra-Low-Frequency Magnetospheric waves on Earth's plasma pause using data collected by the US Air Force's Combined Radiation and Release Effects Spacecraft (CRRES). He graduated with an M.S. in Space Sciences in 2001.

Mr. Scott is a Defence Scientist for Defence R&D Canada Ottawa's Space Systems and Operations Group where he conducts research in Space Situational Awareness (SSA). He developed and operationalized the Canadian Ground Based Optical robotic telescope system which achieved contributing sensor status with the US Space Surveillance Network in 2011. Mr. Scott is a mission scientist on the NEOSSat microsatellite (HEOSS) SSA mission performing space-based experiments in the tracking of Earth orbiting objects. He also conducts ground-based experiments to track and characterize objects in both low and high Earth orbit. He is a representative on NATO Space Situational Awareness scientific technical panel SCI-283 and is a Canadian representative to the Inter-Agency Debris Committee (IADC) which is committed to the remediation and reduction of space debris in Earth's orbital environment.

His research interests are in space-based SSA, ground-based electro-optical space surveillance, resident space object photometry, satellite maneuver detection, conjunction (collision) estimation, space systems development, daylight imaging and hosted payloads for space surveillance.

Mr. Scott is a licensed professional engineer in the province of Ontario. He is a member of American Institute of Aeronautics and Astronautics, the American Astronautical Society, the Sigma Pi Sigma Physics Honor Society and is a reviewer for the Canadian Aeronautics and Space Journal.